FORMULATION AND DELIVERY OF POLYMERIC NANOPARTICLE-ASSISTED VACCINE AGAINST MELANOMA

A DISSERTATION
SUBMITTED TO THE FACULTY OF
UNIVERSITY OF MINNESOTA
BY

LIN NIU

IN PARTIAL FULFILLMENT OF THE REQUIREMENTS
FOR THE DEGREE OF
DOCTOR OF PHILOSOPHY

JAYANTH PANYAM, Ph.D. (ADVISER)

APRIL, 2015

Acknowledgements

Navigating through graduate school abroad is analogous to trudging through the Minnesota winter and enjoying its beautiful summer for me. I cherish every single bitter-sweet moment and hopefully I become a better person out of this enriching experience. The journey could not be completed on my own, without input from all the exceptional people surrounding me.

Words seem to be inadequate to express my gratitude for my adviser Dr.Jayanth Panyam for his mentorship and tutelage. It would have been impossible for me to pursue a Ph.D career without his constant support and patience. His insightful guidance has sculpting effect on both my academic and personal life.

My sincere thanks go out to Dr.William Elmquist for granting me learning opportunity during my lab rotation and for being the chair of my thesis committee and reviewing my thesis. I would like to thank Dr.James McCarthy for leading me into the world of tumor biology, reviewing my thesis plus his strong support for my project and fellowship. I'm grateful to Dr. Raj Suryanarayanan for being on my final defense committee and for the great assistance on my research. Special thanks to Dr. Timothy Wiedmann for critically reviewing / editing my thesis and all the encouragement from the very beginning of my graduate study.

The thesis is also written in remembrance of Dr.John Ohlfest, who passed away on January 21, 2013 because of metastatic melanoma. His guidance and suggestions as one of my preliminary oral exam committee members has major impact on the progress of the project. His extraordinary life will have long-lasting influence on my unwavering belief in the value of pharmaceutical and biomedical research. Special thanks to Dr. Michael Olin for his significant support for me and great contribution to the project. I'm very thankful to other Dr.Olin's lab members, especially Dr.Zhengming Xiong and Dr.Junzhe Xia for their tremendous help and contribution on all the animal studies and cytokine profile analysis. I gratefully acknowledge Dr.David Ferguson at Medicinal Chemistry Department, University of Minnesota for providing the experimental drugs used in this project. Many thanks to Dr.Charles Schiaffo and Peter Larson for synthesizing the research materials.

I'm grateful to Dr.Kris Hansen for being a leader of the 3M microneedle project and her guidance on my personal development. Many thanks to Dr. Leonard Chu for coordinating the entire microneedle project and for the precious friendship. I extend my appreciation to 3M veterinary service team for all the hard work of the animal studies.

My appreciation goes to Chris Frethem of the Characterization Facility, University of Minnesota, without whom the acquisition of cryo-SEM images would be impossible. I would like to thank Dr.Martin Wessendorf and Dr.Mark Sanders of University Imaging

Center for the teaching and help on the confocal imaging. Thanks to Nisha Shah and Paul Champoux at Flow Cytometry Resource for the training and help. Many thanks to Brenda Koniar at Research Animal Resources for all the training and assistance on animal work.

My gratitude extends to the faculty, staff, graduate students and post-doc fellows in the Department of Pharmaceutics. These wonderful persons transform my graduate education experience into indelible memory. Particularly, I would like to thank all Dr.Panyam's lab members and alumni. Thanks to Dr. Komal Shahani for helping me to start the bench top work at lab. I thank Dr. Suresh Swaminathan, Dr.Alex Grill and Dr. Tanmoy Sadhukha for being good lab mates and friends for all the assistance, support and constructive discussion over these years.

I would like to acknowledge Edward G. Rippie Fellowship in Pharmaceutics, Doctoral Dissertation Fellowship and various internal funds from University Of Minnesota for providing financial support during my graduate study.

At last but not least, I'm deeply indebted to my parents, grandparents, my wife and in-laws for all the sacrifice they made that enable my pursuit of this work. The science is advanced by standing on the shoulders of the giants. My life is built on the shoulders of my family. I dedicate this thesis to my most beloved family members.

Dedication

To My Parents

Jianjin Niu, Huimin Zhang

And

My Wife Jing Wang Niu

Abstract

Poly (lactide-co-glycolide) (PLGA) nanoparticle (NP) is a widely used biodegradable carrier for drug and vaccine delivery. This thesis focused on the formulation, delivery and efficacy of PLGA NP for its potential application in melanoma immunotherapy.

To enable reliable PLGA NP formulation for clinical use such as vaccination, lyophilization is the method of choice to manufacture dry NP dosage form. A major risk of the lyophilization product development for NPs is the irreversible NP aggregation due to freezing and drying stress. Based on real-time imaging, freezing stress could be attributed to freeze-concentration of NPs. Cryo-scanning electron microscopy (cryo-SEM) revealed individual NP separately embedded in the freeze-concentrate interstitial space of the sucrose formulation, leading to corroborative support for the "particle isolation" hypothesis of cryo-protection. Various sphere packing models were investigated to guide the rational design of cryo-/lyo-protectant containing NP formulations.

To facilitate precise intradermal delivery of NP formulation for vaccination, microneedle array-mediated administration was utilized to deliver large volume of NPs into the skin. The majority of the infused PLGA NPs were retained locally. A PLGA NP vaccine formulation delivered intradermally elicited robust humoral and cellular immunity.

Antigen-loaded NP formulation triggered quicker and stronger high affinity antibody responses compared to the soluble antigen formulation.

Vemurafenib, a selective inhibitor of BRAF V600E, induces apoptotic melanoma cell death and remarkable tumor burden reduction. However, drug resistance invariably occurs. Novel TLR7/8 agonists were encapsulated in PLGA particulate formulation as immunostimulatory nanoparticles (ISNP) to boost immune response against drug-resistant melanoma. NP-mediated intracellular delivery contributed to enhanced dendritic cell activation *in vitro* and antigen-specific $CD8^+$ T cell proliferation *in vivo*. The prophylactic vaccination using NP-assisted whole tumor cell formulation prolonged the survival of mice challenged with melanoma. To take advantage of the clearance of melanoma antigens by immune system in the context of BRAF inhibition, an ISNP-assisted *in situ* whole tumor cell vaccination strategy was investigated using BRAF V600E positive mouse SM1 melanoma cells. Despite the suppressed tumor growth, no survival benefit was observed in this therapeutic vaccination model.

Table of Contents

List of Tables

List of Abbreviations

1. active pharmaceutical ingredients	API
2. activating transcription factor 4	ATF4
3. Allophycocyanin	APC
4. axillary lymph nodes	ALN
5. B cell receptors	BCR
6. bone marrow derived dendritic cells	BMDCs
7. brachial lymph nodes	BLN
8. cryo-scanning electron microscopy	cryo-SEM
9. cytotoxic T lymphocytes	CTLs
10. cytotoxic T-lymphocyte-associated protein 4	CTLA-4
11. dendritic cell	DC
12. dermal dendritic cells	dDC
13. differential interference contrast	DIC
14. Dimethyl sulfoxide	DMSO
15. Differential scanning calorimetry	DSC
16. enzyme-linked immunosorbent assay	ELISA
17. endoplasmic reticulum	ER
18. epidermal growth factor receptor	EGFR
19. extracellular signal regulated kinase	ERK
20. fetal bovine serum	FBS
21. glass transition temperature of freeze-concentrate	Tg’
22. granulocyte-macrophage colony-stimulating factor	GM-CSF
23. Hank’s balanced salt solution	HBSS
24. hepatocyte growth factor	HGF
25. histocompatability complex molecule class I	MHC I

26. high-performance liquid chromatography	HPLC
27. hollow microstructured transdermal system	hMTS
28. Human Leukocyte Antigen	HLA
29. Immunostimulatory Nanoparticles	ISNPs
30. inguinal lymph nodes	ILN
31. intramuscular	IM
32. intradermal	ID
33. kinesin family member, 2C	KIF2C
34. macrophage receptor with collagenous structure	MARCO
35. mitogen-activated protein kinases	MAPK
36. mitogen-activated protein kinase kinase	MEK
37. Monophosphoryl Lipid A	MPL-A
38. myeloid-derived suppressor cells	MDSC
39. nanoparticles	NPs
40. O-phenylenediamine	OPD
41. oncogene-induced senescence	OIC
42. Ovalbumin	OVA
43. Poly ethylene glycol	PEG
44. polylactide	PLA
45. pattern recognition receptors	PRR
46. pathogen associated molecular patterns	PAMP
47. poly(lactide-co-glycolide)	PLGA
48. polydispersity index	PDI
49. polymerase alpha subunit B	POLA2
50. polyvinyl alcohol	PVA
51. poly dimethyl siloxane	PDMS
52. programmed death 1 receptor	PD-1
53. programmed death 1 ligand	PD-L1
54. Polystyrene	PS
55. phosphatidylinositol-3-OH kinase	PI(3)K

56. Phosphate buffered saline	PBS
57. pyruvate dehydrogenase kinase 1	PDK1
58. PKR-like ER-kinase	PERK
59. Phycoerythrin	PE
60. Quality by Design	QbD
61. reticuloendothelial system	RES
62. regulatory T cells	Treg
63. sex determining region Y-box 10	SOX10
64. secreted embryonic alkaline phosphatase	SEAP
65. subcutaneous	SQ
66. Src family kinase	SFK
67. talimogene laherparepvec	T-VEC
68. transforming growth factor beta	TGF-β
69. tumor associated antigens	TAA
70. transporter associated with antigen processing	TAP
71. toll-like receptor	TLR
72. tumor-infiltrating lymphocytes	TILs
73. ultraviolet radiation	UVR
74. valine (V) in replacement of glutamate (E) at codon 600	V600E
75. vemurafenib	PLX4720
76. wheat germ agglutinin	WGA
77. X-box binding protein 1	XBP1
78. 2-[4-(2-hydroxyethyl)piperazin-1-yl]ethanesulfonic acid	HEPES
79. 4',6-diamidino-2-phenylindole	DAPI
80. 5% dextrose solution	D5W

List of Figures

Chapter One: General Introduction

1.1 Nanoparticle lyophilization formulation and mechanism of freeze-drying stress

Nanoparticles (NPs) hold great promise in a host of therapeutic applications ranging from chemotherapy to immunomodulation. The small size and tailored surface decoration confer NPs the targeted delivery capability against tumors and immune system. Poly (lactide-co-glycolide) (PLGA) is a FDA approved biodegradable polymer widely used to construct NP carrier, within which drug and vaccine can be encapsulated. PLGA NPs undergo bulk erosion via hydrolytic degradation in aqueous environment, triggering sustained release of the loaded drug from the polymeric matrix. Thus, the inherent chemical property of PLGA platform entails development of dry dosage form for its long-term storage. Specifically, one key practical issue in implementing NP-assisted vaccination is the final dosage form used in clinical settings. PLGA NP based vaccines can be stored in a dual-chamber cartridge for pre-filled injector prior to reconstitution and administration.

Removal of water by lyophilization process enables the stable formulation of active pharmaceutical ingredients (API) that are susceptible to hydrolysis, preventing progressive degradation and premature drug release from polymeric NPs. Lyophilization (freeze-drying) is often the procedure of choice for removing water during the manufacturing of nano vaccine/drug delivery systems. The lyophilization cycle is initiated by freezing the formulation, followed by sublimation of bulk frozen water during primary drying and desorption of residual water during secondary drying. An ideal

design of lyophilization formulation should preserve the original physicochemical properties of API throughout the product life cycle. To ensure reliable clinical usage of PLGA NPs, lyophilization is the preferred method to manufacture the final dosage form. However, lyophilization can cause aggregation of NPs (1), and the altered size distribution may adversely affect the NP performance. Both the freezing and drying phases of lyophilization are contributing factors in inducing stress on NPs. Chapter two of this thesis addresses the issue of NP behavior upon freezing and the effective cryo-lyoprotection. The investigation herein is intended to facilitate robust lyophilization cycle development in order to maintain critical quality attributes of PLGA NPs for reliable use in the clinical setting.

To comport with the Quality by Design formulation approach advocated by FDA, elucidation of the underlying mechanism for lyophilization-induced NP aggregation is crucial in mitigating the identified risks. On the other hand, sucrose is a commonly adopted disaccharide that provides cryo/lyo-protection to biologics drugs, vaccine and NPs. But the mechanism of amorphous disaccharide excipient for NPs cryo/lyo-protection remains elusive. Hence, in-depth imaging study is required to shed light on those issues.

Time-lapse microscopy was used to characterize the freezing process of fluorescently labeled NPs in a dynamic manner. Freezing and thawing behavior of NPs could be directly monitored *in situ* on the microscope stage. The real-time imaging study revealed that freezing stress could be attributed to the freeze-concentration of NPs. Initially, the

propagation of growing ice crystals excluded and concentrated the unfrozen fraction of NP colloidal solution. Eventually, the collision of the adjacent ice crystals sequestered the concentrated NPs in between. Consequently, irreversible aggregation ensued. Thus, the freeze-concentrated NPs gave rise to micron-sized fibrous aggregate that failed to spontaneously reconstitute as single particle solution upon reconstitution. In addition, the freeze-concentration phenomenon *per se* occurred independent of cryoprotectant presence. Nevertheless, the NP freezing damage was fully abrogated by sufficiently high concentration of sucrose.

Furthermore, cryo-scanning electron microscopy (cryo-SEM) was employed to overcome the diffraction-limited resolution of optical microscopy for resolving discrete NPs. Cryo-sectioned frozen NP formulation was observed under cryo-SEM. It was confirmed that in the absence of cryoprotectant, NPs are subject to inter-particle close contact compression during freeze-concentration. In contrast, in the presence of cryoprotectant, an interstitial space of sucrose freeze-concentrate emerged and phase-separated from the neighboring ice crystals, while NPs were separately dispersed and embedded in the sucrose interstitial domain. To our knowledge, this observation for the first time led to corroborative support for the "particle isolation" hypothesis of NP cryoprotection. Namely, the cryo-protective property of disaccharides arises from isolating individual particles in a glassy matrix, preventing jammed close contact among particles. As a result, the irreversible NPs aggregation was averted, resulting in readily re-dispersible NP formulation.

Lastly, the cryo-SEM characterization of freeze-dried NPs indicated that the configuration of NP aggregate is analogous to the geometric problem of sphere close packing. Mathematically, the volume ratio of NP cluster in relation to the surrounding sugar matrix amounts to the volume relationship between the packed spheres and the inter-sphere void fraction. There is a threshold value above which the sucrose filling in the void space begins to prevent adjacent spheres from concatenation. Various sphere packing models were investigated. It was experimentally confirmed that the random close packing model provided the best predictor of the minimal sucrose to NP ratio required for successful cryoprotection.

The findings of this project clearly demonstrate the utility of visualization techniques in delineating the freezing / drying stress during NP lyophilization. Accordingly, screening of candidate cryoprotectant and design of freeze-drying formulatioin for NP drug delivery systems could be accelerated as opposed to fully relying on an empirical approach of trial and error. The protective mechanism of effective cryoprotectant was clarified by the high resolution characterization of NP in sucrose formulation and mathematical simulation. In summary, these imaging techniques and theoretical modeling can be applied to assist the rational design of cryo/lyoprotectant containing NP formulations.

1.2 Novel route of administration for NPs: precise intradermal delivery enabled by hollow microneedle array

A key practical question in implementing NPs-assisted therapeutic vaccination for melanoma is the transdermal delivery of immunostimulatory adjuvant. Compared to the systemic administration of potent adjuvants, localized transdermal drug delivery to the surface accessible melanoma can effectively limit the systemic side effects.

The epidermis is the outermost layer of the skin that preserves internal water and prevents external material penetration, constituting the boundary between our body and exterior surrounding. Within stratum corneum, the intercellular space of the differentiated keratinocytes is filled with lipid. Hence, the stratum corneum can be conceptualized as a "brick and mortar" structure (2). With the first generation transdermal drug delivery systems, therapeutic candidates were required to possess a unique set of physicochemical properties. Namely, the molecular weight has to be low (<400 Da), while the hydrophobicity has to be high in order to achieve penetration through the tortuous intercellular route. In addition to these relatively narrow requirements, the delivery rate (dose) remained low compared to other routes of administration. As a result, early transdermal products were limited to potent drugs, such as fentanyl for chronic pain management, nicotine for smoking cessation and other hormonal products (3). Topical formulation of imiquimod indeed induces local cytokine response (4). However, many newly developed cancer vaccine adjuvants, such as ISNP or synthetic nucleic acids Toll Like Receptor (TLR) agonists CpG and Poly I:C, do not meet the size and lipophilicity

requirements. However, should a major breach occur in the epidermis induced either physically or chemically, the transport resistance dramatically decreases (5). As such, the underlying dermal layer, which is rich in capillaries and lymphatics, becomes accessible for drugs. Thus, the second generation of transdermal drug delivery technique focused on increasing the fluidity of the lipid domain by incorporating chemical penetration enhancers thereby increasing the permeability of skin to small lipophilic organic drugs (6). Nonetheless, the mechanism for the second generation drugs remains passive diffusion. It is known that NPs do not permeate through intact skin via passive diffusion due to the size of NPs and the barrier property of stratum corneum (7). Thus, delivering large hydrophilic therapeutics, including hydrophilic macromolecules and NPs, entails active driving forces.

Microneedle-mediated delivery represents a powerful technique for transdermal drug delivery. Hollow microneedle-mediated intradermal infusion of liquid formulations can enable transdermal delivery of hydrophilic large molecules and NPs (8). The current standard practice of infusing immune adjuvants into melanoma relies on intratumoral injection using conventional hypodermic syringe/needles (9). The primary advantages of the hollow microneedle array are the accuracy and reliability of delivery into the dermal layer while avoiding inadvertent delivery into the subcutaneous tissue. The thickness of human skin consisting of epidermis and dermis is in the range of 1-3 mm with the variance depending on the anatomical location. For example, the mean skin thickness of the abdomen is 1.9 mm, while the thickness of stratum corneum and cellular epidermis is

less than 0.1 mm (10). Thus, a microneedle device with a needle length less than 1.5 mm is considered a proper insertion depth for reliable delivery into the dermal layer. The direct access to the dermal resident immune cells, such as dendritic cells and Langerhans cells, constitutes another advantage of microneedle-mediated delivery. Chapter three of this thesis addresses the *in vivo* biodistribution of NPs and immune responses following microneedle-mediated intradermal delivery. This work was carried out in collaboration with the scientists at 3M, who provided the state-of-the-art hollow microneedle array.

1.3.1 Background for melanoma

Skin cancer is the most commonly diagnosed and yet most preventable cancer in the United States. As the incidence of skin cancer has steadily risen over the past three decades (11), the U.S. Surgeon General issued a call to action to prevent skin cancer in July 2014. Malignant melanoma is the most deadly form of skin cancer. Approximately 9,000 deaths from melanoma annually were projected for the U.S.(12). Historically, inoperable metastatic melanoma has been notoriously refractory to the conventional chemotherapy and radiotherapy. In 1970, the approval of dacarbazine (DTIC) to treat melanoma was based on 10%-20% overall response rate (13). However, this alkylating agent provides little overall survival benefit for late stage melanoma patients. As a result, the prognosis for metastatic melanoma remains dismal due to the lack of effective treatments.

Nevertheless, developing effective melanoma treatment appears more promising due to discoveries in tumor genetics. Specifically, mitogen-activated protein kinases (MAPK) are now recognized to be involved in the regulation of cell proliferation and survival. Moreover, the aberrant activation of MAPK signaling pathway due to gain-of-function mutation is common in human cancer (14). The MAPK signaling cascade is comprised of RAS, RAF, mitogen-activated protein kinase kinase (MEK) and extracellular signal regulated kinase (ERK). In 2002, a milestone research paper reported that about 66% of melanoma patients harbor a BRAF somatic missense point mutation at codon 600, where glutamate (E) is substituted for valine (V). This is abbreviated as BRAF V600E (15). The constitutive activation of the oncogenic BRAF driver gene fuels the unfettered proliferation of melanoma cells by providing sustained levels of growth signal to the transformed melanocyte. This seminal discovery immediately gave rise to an intensive search for selective BRAF inhibitors, which eventually resulted in the 2011 FDA approval of vemurafenib, which specifically kills melanoma cells expressing the BRAF V600E mutation (16). Further inquiry into the underlying mechanism of action uncovered that vemurafenib potently triggers endoplasmic reticulum (ER) stress. The intracellular calcium concentration is increased in response to vemurafenib treatment, up-regulating various ER stress related genes, including transcription factor X-box binding protein 1 (XBP1) and ER stress response protein activating transcription factor 4 (ATF4) (17). Simultaneously, the abundance of anti-apoptotic proteins is decreased, inducing programmed cell death (apoptosis) in sensitive melanoma cells. As a result of the targeted

BRAF inhibition, vemurafenib treatment results in high response rate and remarkable tumor shrinkage in melanoma patients harboring the mutation (18).

1.3.2 Acquired resistance to BRAF inhibitor and potential therapeutic strategies

Unfortunately, the clinical response to vemurafenib is short-lived (19). Most patients invariably experience relapse within months due to the emergence of drug resistance (20). Thus, development of an intervention to prolong patient survival and prevent evolution of drug resistant melanoma cells is highly desirable. Presently, a variety of therapeutic strategies have been proposed, based on the expanding knowledge of the biology and underlying mechanisms of BRAF mutant melanoma.

Vemurafenib induces apoptosis in sensitive melanoma cells by blocking the MAPK pathway. Paradoxically, MAPK pathway is activated in other skin cells with RAS mutations (particularly HRAS) when treated with vemurafenib. This intriguing phenomenon leads to vemurafenib-induced secondary skin tumors, such as cutaneous squamous-cell carcinomas and keratoacanthomas (21). These skin lesions are manageable; however the paradoxical vemurafenib-dependent expansion of resistant melanoma is more insidious. In a primary human melanoma xenograft model, continuous dosing of vemurafenib selects for drug-resistant melanoma. It was discovered that the incessant proliferation of drug-resistant melanoma becomes dependent on the presence of vemurafenib. In turn, the cessation of vemurafenib dosing engenders the regression of established drug-resistant tumor (22). Thus, a discontinuous vemurafenib dosing strategy

experimentally prevents the emergence of lethal drug-resistant melanoma. On the other hand, similar to the intrinsic resistance of BRAF positive colon cancer to vemurafenib, it was discovered that the epidermal growth factor receptor (EGFR) is co-opted in a subset of melanoma patients that received BRAF inhibitor therapy (23). In the absence of vemurafenib, overexpression of EGFR and enhanced TGF-β signaling in melanoma only lead to slow growth due to oncogene-induced senescence (OIC). However, in the presence of vemurafenib, the subset of melanoma cells with activated TGF-β signaling event is favorably enriched among the heterogeneous melanoma cells. This selected drug-dependent population is characterized by the suppression of sex determining region Y-box 10 (SOX10). However, the enrichment of low SOX10 and high EGFR cells is reversed by the discontinuation of vemurafenib (24). Thus, a "drug-holiday" strategy is advocated for EGFR positive melanoma patients to allow for re-gaining of drug sensitivity. However, the rational design and implementation of optimum discontinuous dosing regimen for each individual patient can be challenging in practice. Whether the selection for drug-dependent resistant cells is synchronized among multiple metastatic sites remains an open question. It was observed that while most metastatic tumors regress in response to vemurafenib, other tumors could continue to expand in the same patient. Thus, drug holiday could have a differential impact dependent on distinctive sites.

Besides the vemurafenib monotherapy regimen, combination therapies constitutes the predominant strategies under investigation. The MAPK reactivation via alternative signaling pathways bypasses the BRAF inhibition and confers acquired resistance (25).

For instance, N-RAS mutation activates CRAF, which in turn phosphorylate MEK. The CRAF-mediated MEK activation is parallel to the BRAF-driven MEK-ERK signaling transduction and circumvents BRAF inhibition (26). In addition, MAP3K8 (COT) was identified to activate ERK through MEK-dependent but RAF-independent manner (27), providing the rationale to combine BRAF inhibitor with a MEK inhibitor to mitigate acquired resistance downstream of the re-activated MAPK pathway. The combined treatment involving BRAF inhibitor dabrafenib and MEK inhibitor trametinib significantly improves the progression-free survival and has since obtained FDA approval (28). However, the combination therapy does not fully overcome the resistance problem. Cross-resistance against simultaneous application of two kinase inhibitors can still develop due to the highly heterogeneous mechanisms of resistance (29, 30).

Traditional drugs have also been re-purposed to treat BRAF V600E - harboring melanoma due to the identification of a new therapeutic target. It was discovered that copper participates in the BRAF V600E driven signaling cascade. Copper (Cu) influx (via Cu transporter 1) elevates phosphorylation of ERK through Cu-MEK1 interaction. The reduced intracellular concentration of Cu and disruption of Cu-MEK1 binding were validated to be effective in suppressing BRAF V600E signaling transduction (31). Thus, copper chelators were proposed to be another avenue to inhibit BRAF V600E positive melanoma and tumor recurrence following BRAF inhibition. In addition, the chromatin organization is potentially crucial for the BRAF driven tumorigenesis as well. It was discovered that SETDB1 cooperates with BRAF V600E to accelerate melanoma growth

and invasiveness by controlling histone H3K9 methylation (32). Thus, SETDB1 inhibitors may re-sensitize melanoma to BRAF inhibition. Apart from the oncogene driven events, energy supply is another prerequisite for the persistence and survival of melanoma. A protective mechanism guarding against malignant transformation is the oncogene-induced senescence (OIC), which modifies the metabolic pathway via suppression of pyruvate dehydrogenase kinase 1 (PDK1). BRAF driven melanomagenesis overcomes OIC through normalizing PDK1 expression. Along this line, depletion of PDK1 was shown to eliminate the subset of vemurafenib-resistant melanoma (33). Similar to the undesirable metabolic manipulation, autophagy also plays a cytoprotective role in rescuing the stressed melanoma cells. In the presence of vemurafenib, BRAF V600E binds with ER gatekeeper, GRP78, triggering PKR-like ER-kinase (PERK) -dependent ER stress and activated autophagy machinery (34). A higher level of vemurafenib-induced autophagy is correlated with shorter duration of progression-free survival. Combination therapy of autophagy inhibitor with BRAF inhibitor led to regression of resistant melanoma in a xenograft model, providing another promising therapeutic pathway. Beyond the resistance mechanisms inherent to tumor cell *per se*, the stromal cells can also render melanoma refractory to BRAF inhibitor treatment. Stromal cell-derived hepatocyte growth factor (HGF) engages its receptor, MET, and re-activates MAPK and phosphatidylinositol-3-OH kinase (PI(3)K)–AKT signaling pathway. Combination therapy that pairs HGF or MET antagonist with RAF inhibitor resulted in resistance reversal (35).

The preponderance of combination therapies arises from the consensus that BRAF driven melanomagenesis is not a singular event but a corollary of multi-faceted tumorigenic factors. Recently, a novel insight was generated in elucidating the impact of ultraviolet radiation (UVR) in a BRAF V600E specific context. In a murine model that expresses BRAF V600E in melanocytes, UVR exposure led to significant clonal expansion and increased melanoma burden. TP53 was identified as a frequently mutated tumor suppressor as a result of UVR (36). Mutated TP53 collaborates with oncogenic BRAF V600E so that melanomagenesis was accelerated. A similar collaboration between BRAF and PTEN was documented previously (37). Therefore, it is conceivable that the BRAF gain-of-function mutation and tumor suppressor genes loss-of-function mutations co-exist to foster a permissive genetic landscape for the emergence of resistant melanoma under the drug selective pressure. The ever-expanding understanding of melanoma biology both presents treatment opportunities as well as reveals additional challenges. However, considering the sobering fact that a large variety of mechanisms could be exploited by melanoma to confer fitness advantage, it almost seems inevitable that the resistance for small molecule drugs will occur over time even under multiple inhibitors. The curative treatment will likely require alternate strategies to eradicate drug resistant melanoma, with immunotherapy being a promising option.

1.3.3 Overview of current melanoma immunotherapy

The immune system performs constant immunosurveillance to suppress malignant transformation (38). A clinically apparent tumor typically has undergone three stages of

immunoediting processes encompassing “elimination, equilibrium and escape”(39). The objective of cancer immunotherapy is to recruit and facilitate the patient’s own immune system in the fight against cancer (40). Unlike chemotherapy and radiotherapy, which often destroy growing cancerous and healthy cells indiscriminately, immunotherapy primarily relies on the action of cytotoxic T lymphocytes (CTLs) to seek out and kill malignant cells selectively based on recognition of proteins expressed specifically by tumor cells (a.k.a. tumor associated antigens or TAA). Historically, metastatic melanoma has been a fertile ground for exploring experimental cancer immunotherapy partly due to the lack of other efficacious treatments. It has since been validated that metastatic melanoma contains a variety of TAA, such as MAGE and gp100, and patients possess native, albeit inadequate, anti-melanoma immunity (41). The initial breakthrough in immunotherapy arose from the discovery of CTL-associated protein 4 (CTLA-4). CTLA-4 exerts inhibitory modulation on T cells’ tumoricidal function. Consequently, blocking the CTLA-4 checkpoint releases the “brake” on the effector function of T cells (42). Cancer immunotherapy came of age in 2010, when significant efficacy of an anti-CTLA-4 antibody in the B16 melanoma mouse model was finally translated to an improved overall survival of late stage melanoma patients treated with ipilimumab (CTLA-4 checkpoint inhibitor) (43, 44). The success of ipilimumab corroborates the existence of naturally occurring yet functionally hampered T cells that target melanoma associated antigens. In addition, another inhibitory receptor of T cells, programmed death 1 (PD-1) receptor, has been validated as a novel checkpoint target (45). In response to cytotoxic T cell infiltration, melanoma up-regulates its cognate ligand PD-L1 to attenuate the T cell

assault (46). PD-1 and PD-L1 axis partially contribute to the exhaustion of anti-tumor T cells after chronic exposure to melanoma antigens, rendering T cells anergic (47). Anti-PD-1 antibody produces an objective response rate of 28% in melanoma patient (48). Furthermore, the concurrent regimen of PD-1 inhibitor and CTLA-4 inhibitor (Nivolumab plus Ipilimumab) induced more rapid and extensive tumor regression in a clinical trial (49). Again, the advances in the use of checkpoint inhibitors imply the effectiveness in potentiating naturally occurring anti-melanoma T cells. However, the checkpoint inhibition strategy typically generates a response rate of no more than one-third. The efficacy is probably partially restricted by the quantity and quality of pre-existing anti-melanoma T cells in advanced melanoma patients.

The native anti-melanoma immunity is partly manifested by the presence of tumor-infiltrating lymphocytes (TILs). Another very promising strategy relies on the *ex vivo* expanded TILs isolated from melanoma patients. In combination with IL-2 and lymphodepletion preparation, adoptive T cell transfer of the autologous TILs to patients led to a remarkable 72% objective response rate and 22% complete regression (50). The 3-year survival for patients with complete response is 100% and the 5-year survival is 93%. The durable complete response is irrespective of prior treatment history. In addition, two novel tumor specific mutations have been identified as the target antigen of TILs from two patients experiencing complete regression. Interestingly, the newly discovered mutated kinesin family member, 2C (KIF2C) antigen, and mutated DNA polymerase alpha subunit B (POLA2) antigen are all involved in cell proliferation (51).

The adoptive cell therapy represents one of the most powerful immunotherapeutic approaches against melanoma currently. However, this highly personalized protocol demands specialized expertise and facilities and this constrains its widespread implementation in hospitals. Nevertheless, this strategy illustrates the huge potential of empowering T cells in eradicating melanoma by targeting patient-specific mutated proteins.

1.3.4 Immunostimulatory nanoparticle assisted *in situ* whole tumor cell vaccination in the context of BRAF inhibition

Vaccination is an effective strategy to elicit primary T cell response against tumor neo-antigens and expand pre-existing melanoma reactive T cells via recall response (52, 53). Extensive research and numerous clinical trials with tumor vaccines using synthetic peptides derived from TAA have been conducted (54). However, a consistent survival benefit for large cohorts of patients remains elusive. Despite the overall low (~10%) response rate, the patients that do respond enjoy long-term tumor-free survival (55, 56).

There are two major limitations associated with the single TAA-targeting strategy. First, the immune system of many patients cannot react with the pre-selected antigen present in the vaccine. The recognition of pre-selected antigen by patients' immune system relies upon relevant major histocompatability complex molecule (MHC) binding to the antigen. Human Leukocyte Antigen (HLA) genotyping is necessary to ensure the proper presentation of the pre-selected peptide, restricting its utility in a diverse population.

Second, vaccine induced cytotoxic T cells fail to kill tumors that do not produce the pre-selected antigen. Resistant tumor clones could also emerge under single selection pressure through losing the targeted tumor antigen. Recently, immune reaction against multiple tumor antigens following administration of a multipeptide cancer vaccine has been shown to prolong overall patient survival (57). To this end, whole tumor cells containing the entire repertoire of TAA specific to a patient would be an ideal antigen source for creating an individualized cancer vaccine. However, generation of autologous whole tumor cell vaccine entails tumor cell collection and *ex vivo* processing in a highly personalized manner. This, in turn, poses significant technical/financial constraints in harnessing the most relevant tumor antigens for each individual in a large cohort of patients. Thus, it would be highly desirable to develop an *in situ* whole tumor cell vaccination strategy as a first line treatment.

Due to the targeted nature of vemurafenib, BRAF inhibition does not interfere with T cell proliferation and functionality (58), obviating concerns over drug-induced systemic immunosuppression. Vemurafenib also enhances MHC expression in homozygous BRAF mutation melanoma cells through type I and type II interferon dependent manner (59). The up-regulated MHC I expression in melanoma cells is conducive to the presentation of TAA for T cell immunosurveillance. The synergy between vemurafenib and killer T cell has been further substantiated by the improved efficacy of adoptive T cell therapy in mouse model (60). However, BRAF inhibition does not directly enhance melanoma immunogenicity (61). Nevertheless, the initial tumor debulking by BRAF inhibitor

transfers a significant amount of tumor antigen to immune system as antigen presenting cells phagocytose melanoma apoptotic bodies. Therefore, there is an inherent and unique opportunity to create an *in situ* whole tumor cell vaccine to accentuate T cell mediated immunity.

The overall goal of this project is to create a vaccination strategy so that patients' own immune system is recruited to fight the battle against melanoma. It is interesting to note that initial treatment with vemurafenib results in the massive killing of melanoma cells, resulting in a good supply of melanoma-associated antigens to immune system. The immune cells that scavenge the dying melanoma cells can acquire melanoma antigens and mount an immune response to the remaining tumor cells. Thus, vemurafenib treatment presents an unparalleled opportunity to create an *in situ* (on-site) whole tumor cell vaccine for each patient without the need for surgical resection and laboratory manipulation, which is a novel concept in tumor vaccination strategy. Unlike conventional chemotherapy, vemurafenib does not have any detrimental effects on the function of body's immune system. Thus, combining vemurafenib with cancer vaccination is a highly promising option to treat metastatic melanoma.

One major task in developing a cancer vaccine is to stimulate the body's immune system to respond to tumor antigens. The immune system responds aggressively only in the presence of a foreign protein; this allows the immune system to distinguish between innocuous self-antigens (proteins expressed by autologous normal cells) and dangerous

foreign antigens from pathogenic microbes. A major challenge in cancer vaccine development derives from the "self-origin" nature of tumor cells. For instance, melanoma cells dying from vemurafenib treatment undergo programmed cell death (apoptosis), a non-violent mechanism of cell death utilized by normal healthy cells as well. Typically, immune cells do not discern potential danger when they 'see' apoptotic cells as opposed to when encountering a virus infected cell. This mechanism involves specialized detectors that recognize molecular structural patterns present only in microbes. One class of these "detectors" is called Toll Like Receptors (TLR), which are strategically deployed by immune cells that patrol the body. Recent studies show that chemicals that can activate these detectors (called TLR agonists) can fool the immune system into mounting an immune response against apoptotic tumor cells.

Based on the above discussion, it is clear that using vemurafenib to induce initial tumor cell kill and then using TLR agonists to activate the immune system is an attractive strategy to treat melanoma. The final challenge is to ensure that the TLR agonist is presented along with the dying melanoma cells to ensure a robust targeted immune response. The way we approach this challenge is to deliver the TLR agonists into tumor cells using polymeric nanoparticles that have a size similar to that of a virus. Basically, this nanoparticle based artificial virus system has the size and essential molecular cues of a virus that our immune system recognizes very well.(62) We name this nanoparticle system Immunostimulatory Nanoparticles (ISNPs). ISNPs can not only activate the immune system as efficiently as a virus, but can also infiltrate melanoma cells like a Trojan horse. It is well documented that

nanoparticles preferentially accumulate within the solid tumor due to the "leaky" nature of tumor blood vessels. Once nanoparticles reach the solid tumor, they achieve cellular entry into tumor cells, mimicking virus entry into cells. Thus, ISNPs localized within dying melanoma cells could activate the immune system similar to how virus infected dying cells activate the immune system.

First, ISNPs loaded with TLR agonists were formulated and characterized successfully. Exposure of immune cells to ISNPs resulted in a strong activation of the immune cells, with concomitant secretion of proinflammatory cytokines. Second, my studies show that melanoma cells internalize targeted nanoparticles effectively. Further, vemurafenib treatment induced apoptosis in melanoma cells and the presence of ISNPs in these dying melanoma cells resulted in the activation of immune cells. In addition, by using a model protein antigen, ISNPs activated a strong cytotoxic T cell response to the model antigen in mice.

We propose *in situ* generation of a whole cell vaccine. In addition to delivery of sufficient TAA to the immune system, immunostimulatory signals are also required. Novel TLR agonists, such as TLR7/8 agonists, which stimulate a Th1 immune response featured by activation of anti-tumor CTLs are highly desirable. Therefore, we propose to use PLGA NPs carrying novel TLR7/8 agonists (developed by Ferguson lab at University of Minnesota) to enhance dendritic cell activation and modulate the immunosuppressive melanoma microenvironment. Development of ISNP is described in Chapter four of the

thesis with a focus on ISNP formulation and its adjuvant effect. We hypothesize that the ISNP-based vaccination could confer anti-melanoma immunity

In essence, inoperable metastatic melanoma is refractory to conventional chemotherapy and radiotherapy. Thus, the development of new strategies to prevent melanoma disease progression is highly significant. The key innovation of this project resides in the central concept of surgery-free, *in situ* creation of whole tumor antigen vaccine. The idea of using a highly specific anticancer agent (vemurafenib) to create *in situ* apoptotic tumor cells rich in tumor antigens, along with the targeted co-delivery of TLR agonists has not been pursued before. Previous approaches to immunotherapy have relied on either using a purified peptide antigen along with adjuvants or using a whole cell lysate created in the laboratory along with the adjuvants. Because many of the components of the therapeutic approach being pursued here are already approved for human use, we expect that the proposed approach can be rapidly translated to the clinic. We expect that combining ISNPs with other highly-specific tumor debulking strategies (photothermal ablation, targeted antibodies) will enable similar approaches to treat other (non-BRAF mutant) cancers.

Chapter Two: Visualization of Freezing Stress-induced Aggregation of Nanoparticles and Cryoprotection Using Disaccharide Excipient

2.1 Synopsis

PLGA nanoparticles (NPs) undergo both freezing and drying stress during lyophilization. The impact of freezing on NPs under various cooling rates was evaluated in this study. To elucidate the underlying mechanism of freezing stress induced aggregation, epi-fluorescence time-lapse microscopy was used to characterize the freezing process and the frozen state of NP formulations with and without sucrose. Based on images obtained in real time, the freezing stress could be attributed to freeze-concentration of NPs. Cryo-scanning electron microscopy (cryo-SEM) revealed individual NP separately embedded in the freeze-concentrate interstitial space of the sucrose formulation, leading to corroborative support for the "particle isolation" hypothesis. The random close packing model provided the best predictor of the minimal sucrose to NP ratio required for successful cryo-protection. These findings clearly demonstrate the utility of visualization techniques in delineating the freezing and drying stress that occurs during lyophilization, which can be applied to the rational design of cryo-/lyo-protectant containing NP formulations.

2.2 Introduction

Removal of water by the process of lyophilization (freeze-drying) enables the long-term storage of pharmaceutical formulations that contain active pharmaceutical ingredients (API) susceptible to hydrolysis or denaturation. The lyophilization cycle is initiated by freezing the formulation, followed by sublimation of bulk frozen water during primary drying, and completed by desorption of adsorbed water during secondary drying (63). An ideal design of lyophilization formulation and cycle should be capable of preserving the original physicochemical properties of API throughout the product life cycle (64).

The final product of a lyophilized pharmaceutical formulation is commonly referred to as a "cake", which is a structurally intact solid that is in contact with the container. The appearance of the cake is the most straightforward and convenient quality control parameter as well as being most critical in conveying the quality to the end user (65). Shrinkage or collapse of cake can be the first warning sign of poor process and/or product control. Macroscopic cracks and splits also portend problematic processes.

The internal structure of lyophilized cake contains information to guide optimization of lyophilization process. It provides crucial insight into the freezing history and micro-collapse during drying phase. The ice crystal dimension and directionality can also be informative as the formation of large ice crystals is conducive to the generation of large channels for vapor transport during primary drying. With lower vapor transport resistance, the primary drying phase is shortened leading to less manufacturing time per

batch. Micro-X-ray computed tomography (micro-CT) has been used to assess the internal structure of the cake (66); however, this approach is expensive and not widely available. Thus, identifying alternative techniques for imaging the internal structure would be of value (67).

In this study, the internal and surface structure of lyophilized cakes derived from nanoparticle (NP) formulations was characterized. The rationale is that there is little work on the mechanism of freeze-drying related NPs damage, despite the extensive literature pertaining to low molecular weight drugs, biopharmaceuticals, and vaccine products (68-70). Moreover, lyophilization is commonly used for colloidal drug carriers (1), although there is limited understanding of the precise mechanisms underlying freeze-drying stress on NP formulations. Due to the large surface area-to-volume ratio of NPs and associated increased interfacial free energy, NPs constitute a thermodynamically meta-stable system (71). According to the DLVO theory, NPs in solution can possess a sufficiently large electrostatic repulsive force to overcome Van der Waals attraction to prevent aggregation (72). However, in the solid state, particularly during the freezing and drying stages, the stability of NPs relies on other factors that are not well defined. Presently, there are conflicting reports regarding the correlation between freezing and NP stress (73). To facilitate robust lyophilization cycle development and a Quality by Design (QbD) approach (74), further research is needed to improve the mechanistic understanding of NP behavior upon freezing and drying. Therefore, epi-fluorescence and

confocal microscopy were used to evaluate the impact of freezing and freeze-drying on PLGA NPs under various cooling rates.

The inclusion of disaccharide excipients, such as sucrose and trehalose, has been the most widely adopted practice to protect biopharmaceuticals during lyophilization (75). The underlying mechanisms of protection conferred by sugar for biologic drugs are well established (76, 77). To this end, the relative scarcity of research on protection mechanism of disaccharides in NP formulations warrants further investigation. Previously, the "particle isolation" hypothesis was posited as the stabilization mechanism where NPs are separated by the unfrozen fraction of sugar excipient (78). To date, visual experimental support for this hypothesis is lacking. To test this hypothesis, the freezing stress on NPs and the structure of the sugar/NP formulation requires direct visualization by high resolution imaging techniques, and cryo-scanning electron microscopy (cryo-SEM) is recognized as a reliable technique for studying hydrated samples at high resolution (79, 80). Imaging samples in the frozen state constitutes another advantage of cryo-SEM, because artifacts arising from sample drying are largely avoided. Thus, cryo-SEM was used to characterize the stress on NPs in the freezing stage and to investigate the "particle isolation hypothesis".

2.3 Methods and Materials:

2.3.1 Fabrication of PLGA NPs and Coumarin-6-loaded PLGA NPs

PLGA NPs were synthesized using emulsion-solvent evaporation technique. Briefly, 32 mg poly (D,L-lactide-co-glycolide) (PLGA; 50:50, 0.55-0.75 dL/g inherent viscosity, LACTEL Absorbable Polymers, Birmingham, AL) was dissolved in 1 ml chloroform in a borosilicate glass container along with coumarin-6 (250 μg) (Sigma-Aldrich, St Louis, MO). The emulsion was formed with 8 ml of 2.5% polyvinyl alcohol (PVA) aqueous solution (87%-90% hydrolyzed, 30,000-50,000 Da, Sigma), and the dispersion was sonicated (20 W for 5 minutes) with a tip sonicator (Misonix Sonicator 3000) on ice bath. This emulsion was then stirred for 18 hrs at ambient conditions in a chemical hood followed by another hour under vacuum to completely remove chloroform. NPs were recovered by ultracentrifugation (Optima XPN-80 ultracentrifuge, Beckman Coulter) at 35,000 rpm for 35 min at 4 °C and then washed three times with distilled water.

2.3.2 Laser Scanning Confocal microscopy of Lyophilized Nanoparticle Formulation

The embedding of lyophilized cake was adapted from an earlier reported protocol (67) using a poly dimethyl siloxane (PDMS)-based organic silicon polymer. SYLGARD® 184 Silicone Elastomer base (Dow Corning Corporation) was mixed thoroughly with SYLGARD® 184 Silicone Elastomer curing agent at a 10:1 ratio (v/v) for 5 minutes using a polypropylene transfer pipette. Dimethylvinyl-terminated dimethyl siloxane is the

main constituent of the base, which is cross-linked upon exposure to curing agent in the presence of catalyst for hydrosilylation. According to the manufacturer's instructions, the curing proceeds at a constant rate without heat generation, and is independent of section thickness or degree of confinement.

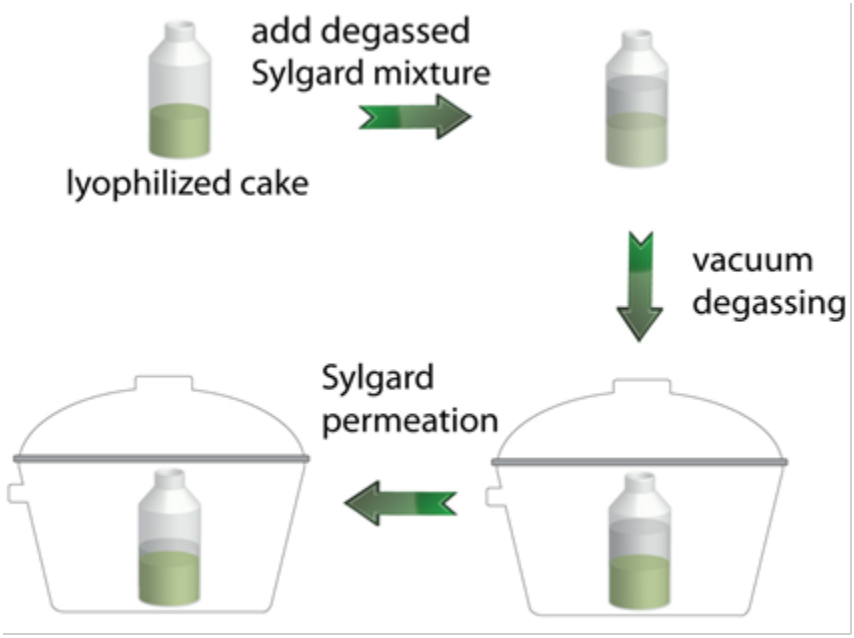

Figure 2-1. Sylgard 184 embedding of freeze-dried pharmaceutical cake

Transfer pipette was clipped to produce large tip opening for the easy transfer of extremely viscous SYLGARD® 184 into a 50 mL conical centrifuge tube. The SYLGARD® 184 mixture was degassed in a laboratory vacuum container. This degassing step was repeated several times so that the de-pressurization and re-pressurization cycles of vacuum chamber could effectively eliminate bubbles. The elastomer was then carefully decanted into a lyophilization vial, degassed in a vacuum

chamber to promote permeation of SYLGARD into cake, and cured at room temperature for 48 hrs to solidify the cake (Figure 1). Embedded cake was cross-sectioned using a razor blade and visualized under a Leica MZ FL III Fluorescence Stereomicroscope. For confocal imaging, the sample cake was further cut into thin sections (Figure 2) and mounted on a glass slide for observation under Nikon AZ100 C1si Confocal Microscope (University Imaging Center, University of Minnesota).

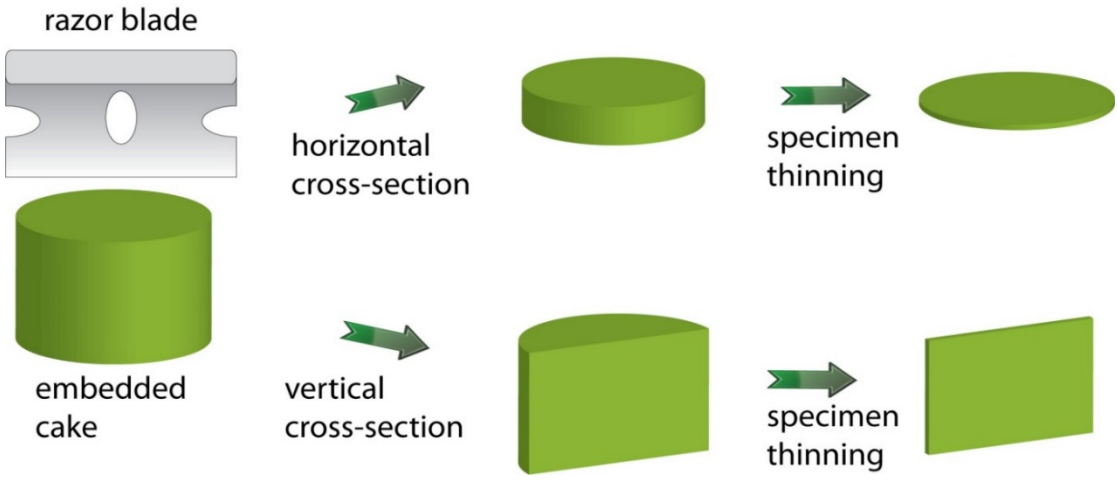

Figure 2-2.Sectioning of Sylgard 184 embedded freeze-dried pharmaceutical cake

2.3.3 Freeze-thaw stress study on NPs

For a single freeze-thaw cycle stress test, a dispersion of NPs in a microcentrifuge tube was frozen by either placing the sample in liquid nitrogen for 2 minutes, in a -80°C freezer or -20°C freezer for no more than 2.5 hrs. Thereafter, the sample was thawed at room temperature. Hydrodynamic diameter of NPs was determined using dynamic light scattering (Delsa Nano C particle analyzer, Beckman Coulter) before and after the freeze-

thaw test. PLGA NPs (30 mg/mL) as well as 100 nm and 200 nm Fluoresbrite™ YG carboxylate polystyrene nanoparticles (PS NPs; 2.6% w/v, Polysciences) were used for the freeze-thaw stress test.

2.3.4 Real-time imaging of freezing stress and cryoprotection

Imaging of freezing stress-induced changes in NP dispersion was conducted on a Carl Zeiss epi-fluorescent microscope. A volume of 10 µl of the NP dispersion was deposited on a glass microscope slide and covered with a coverslip. The slides were frozen in -80 °C freezer for 30 minutes and imaged with a fluorescent microscope within 1 minute after removal from the freezer. Field of view was chosen randomly on the slide.

For real time imaging study, 10 µl of NP dispersion, in the presence or absence of a cryoprotectant, was deposited on a glass slide and covered with a coverslip. After the slides were mounted on the microscope stage, a dry ice pellet was placed on the glass slide flanking the coverslip for *in situ* freezing (Figure 3). The thawing step was triggered by removing the dry ice pellet. Time-lapse video of freezing and thawing behavior were recorded at the maximal frame rate possible for the required exposure time of the fluorescent NPs (100-360 milliseconds per frame).

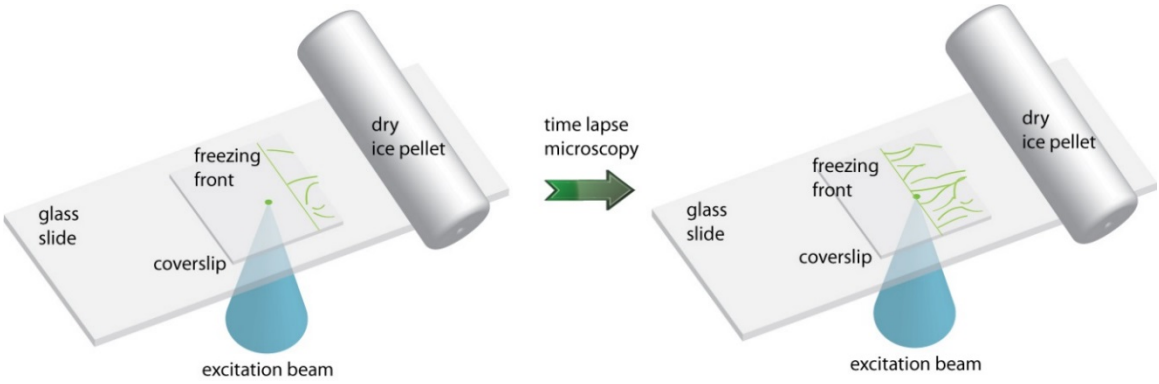

Figure 2-3. Schematic of the experimental set up for real-time imaging of freezing stress on fluorescent NPs

2.3.5 Cryo-SEM imaging of NP freeze-concentration

Before sample preparation, silicon chip specimen substrates were nicked manually to facilitate subsequent freeze-fracturing. A volume of 15µl of PLGA NP dispersion at a concentration of 1.5 mg/mL or 30 mg/mL in water or in 3% w/v sucrose was evenly spread on the substrate using a micropipette. The substrate was then placed on a pre-cooled glass slide, which had an underlying dry ice pellet. Freezing of the NP dispersion was nearly instantaneous. The frozen sample was transferred with pre-cooled forceps into a shallow liquid nitrogen container, in which the sample was mounted onto a custom-built holder and fastened with a screw to secure tight contact and correct sample orientation (Figure 4). The holder was then transferred to the Emitech K-1250 Cryopreparation System, where the silicon chip was fractured to expose a cross-sectional surface. The fractured surface was sublimated for 10 minutes at -96 °C to enhance the surface topological contrast and sputter-coated with platinum to reduce charging. Images

were acquired with a Hitachi S4700 Cold Field Emission Gun Scanning Electron Microscope at approximately -150°C. Since only the surface detail information was of interest and deep beam penetration of electrons was not beneficial, the cryoSEM was operated at a relatively low acceleration voltage of 1.5 - 2.0 kV to improve resolution and minimize charging and beam damage to the frozen samples.

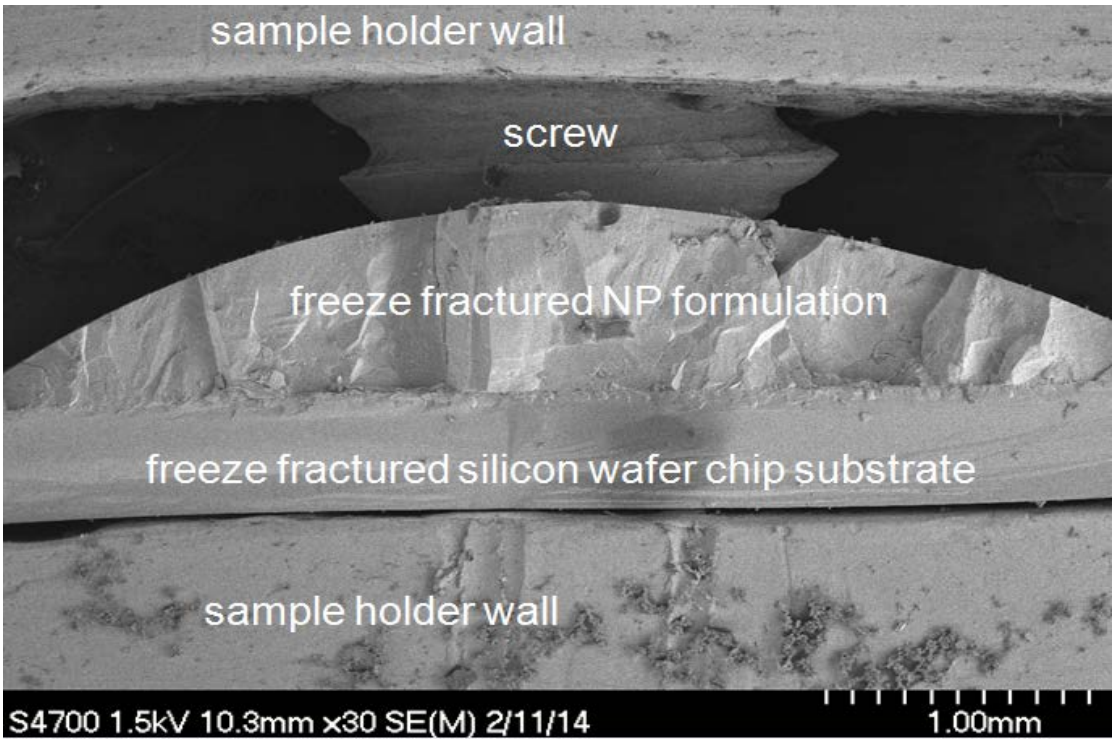

Figure 2-4.Cryo-SEM experimental set up for high resolution imaging of frozen-fractured nanoparticle formulation

2.3.6 Modulated Differential Scanning Calorimetry for determing Tg'

Thermal Analysis was conducted under constant dry nitrogen purge (50 mL/min) in a differential scanning calorimeter (Q2000, TA Instruments, New Castle, DE) equipped with a refrigerated cooling accessory module. Approximately 18 μL of NP dispersion or sucrose solution was placed into a preweighed Tzero DSC pan, and the pan was hermetically sealed with a lid using the Tzero press. The final weight was then determined. For the measurement of glass transition temperature of the maximally frozen sucrose formulation (Tg') in the presence or absence of NPs, the samples were cooled at -10 °C/min during the freezing step and held for another 10 min to ensure complete freezing. The instrument was operated in the modulated mode (temperature modulation was ± 0.75°C every 100 s) with an underlying heating rate of 1°C/min.

2.3.7 Lyophilization of NPs formulation

Lyophilization for testing the models of cryo- and lyo-protection with sucrose was performed on a shelf temperature controlled VirTisAdVantage freeze-dryer (SP Scientific, Stone Ridge, NY). The freezing steps consisted of ramping to 0°C within 30 minutes for pre-cooling and equilibration, ramping to -50°C at 0.5°C/min, and then holding at -50°C for 2 hrs. The primary drying steps consisted of ramping to -35°C and holding 24 hrs. The secondary freezing protocol was initiated by ramping to 0°C at 0.12°C / min, holding for 5 hrs, followed by ramping to 25°C at 0.25°C/min and holding for 9 hrs (Figure 5). The condenser temperature was set at -46°C throughout the cycle.

Carboxylate functionalized PS NPs (100 nm and 200 nm) were used at concentrations of 1.3%, 0.65% and 0.325%.

Lyophilized cakes of coumarin-6 loaded PLGA NPs in 1% sucrose/3% mannitol for Sylgard silicone embedding were prepared with a FreeZone 4.5 lab freeze dryer system (LABCONCO, Kansas City, MO). Sucrose was added at 1% as the amorphous excipient, and 3% mannitol was added as the crystalline bulking agent. For fast cooling, the formulation was frozen by placing it in a -80 °C freezer for 30 minutes, followed by a 60 minute annealing step at -20°C, and another segment of -80°C for 30 minutes. For slow cooling, the formulation was frozen by placing it in -20°C freezer for 4 hrs followed by a -80°C freezer for 0.5 hour. Primary drying was carried out with the condenser temperature at -45°C for 48 hrs. Secondary drying was performed under vacuum at 25°C for 12 hrs.

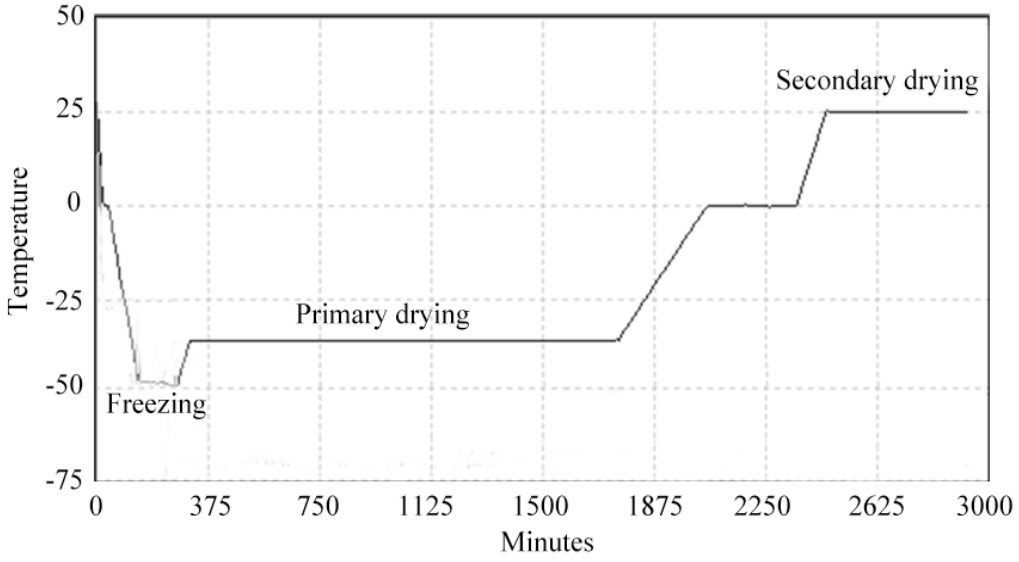

Figure 2-5.Programmed freeze-drying protocol for sucrose-nanoparticle formulation

2.4 Results and discussion:

2.4.1 Confocal imaging

Sylgard 184 silicone elastomer was used to embed the intact cake of fluorescently labeled PLGA NPs formulation as previously reported (67). Partially crystalline 1% sucrose/3% mannitol was used to demonstrate the feasibility of this embedding approach for NPs. Pharmaceutically elegant cake was achieved with a formulation containing coumarin-6 loaded PLGA NPs (Figure 6).

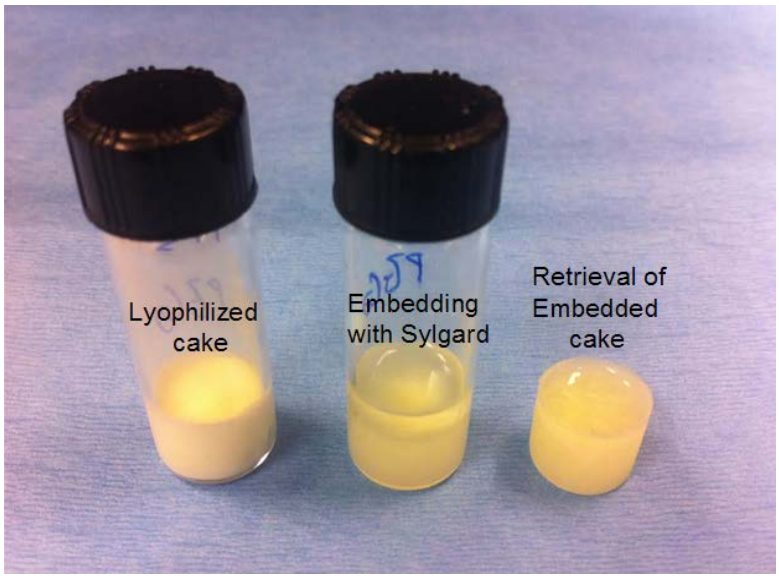

Figure 2-6. Pictures of the lyophilized cake at various stages of the embedding procedure

Figure 7 depicts the vertical cross section of the internal cake morphology. The directionality of the void spaces left by sublimated ice crystals are clearly evident and no major internal collapse is seen. Regions with higher light intensity suggested the presence of concentrated NPs, while the intervening region with lower intensity implied a lower concentration of NPs. Similar morphology was apparent from the bottom view of the cake (Figure 8). However, there was pervasive background noise due to the epifluorescent signal originating from out-of-focus optical planes. Thus, scanning fluorescence confocal imaging was used, which had significantly less background noise and enabled visualization of a much more distinct demarcation between the domains (Figure 9; horizontal zoom).

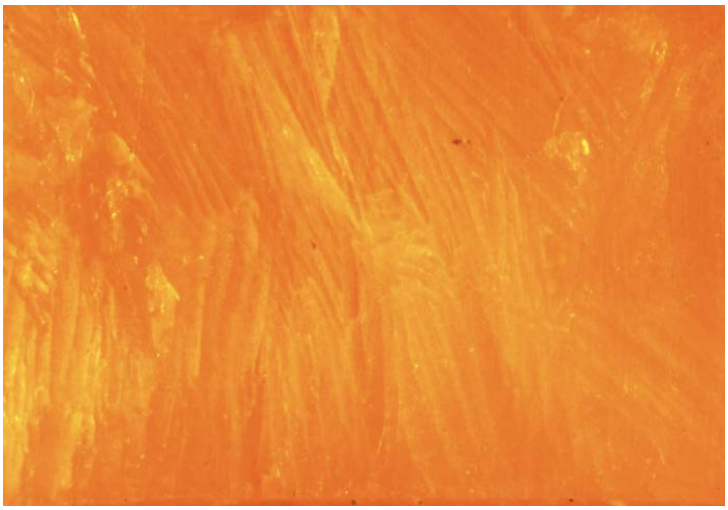

Figure 2-7. The internal morphological pattern of silicone-embedded lyophilized cake of 1% sucrose/ 3% mannitol, coumarin-6 PLGA NP formulation under a stereoscope with halogen lamp illumination.

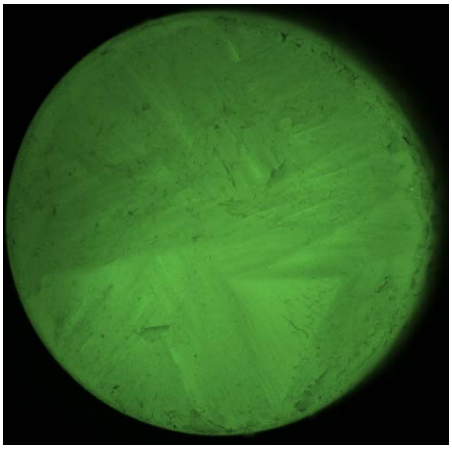

Figure 2-8. Bottom view of Sylgard silicone-embedded lyophilized cake (1.2 cm in diameter without sectioning) of 1% sucrose/ 3% mannitol PLGA NP formulation under a stereoscope in fluorescent mode.

At different cooling rates, distinctly different ice crystal patterns were obtained. Fast cooling rate coupled with an annealing step resulted in a pattern of alternating columnar shapes, reflective of different NP concentrations. Slow cooling rate resulted in a reticular meshwork, characterized by irregular ice crystals with polygonal geometry (Figure 9). Interestingly, the vertical orientation of the ice crystals seen under the fast cooling rate suggested that growth originated from the bottom of the vial, which is consistent with maximal heat conduction from the vial to the freezer shelf. In contrast, the reticular structure observed at the slow cooling rate suggests that significant supercooling occurred with ice nucleation occurring throughout the vial.

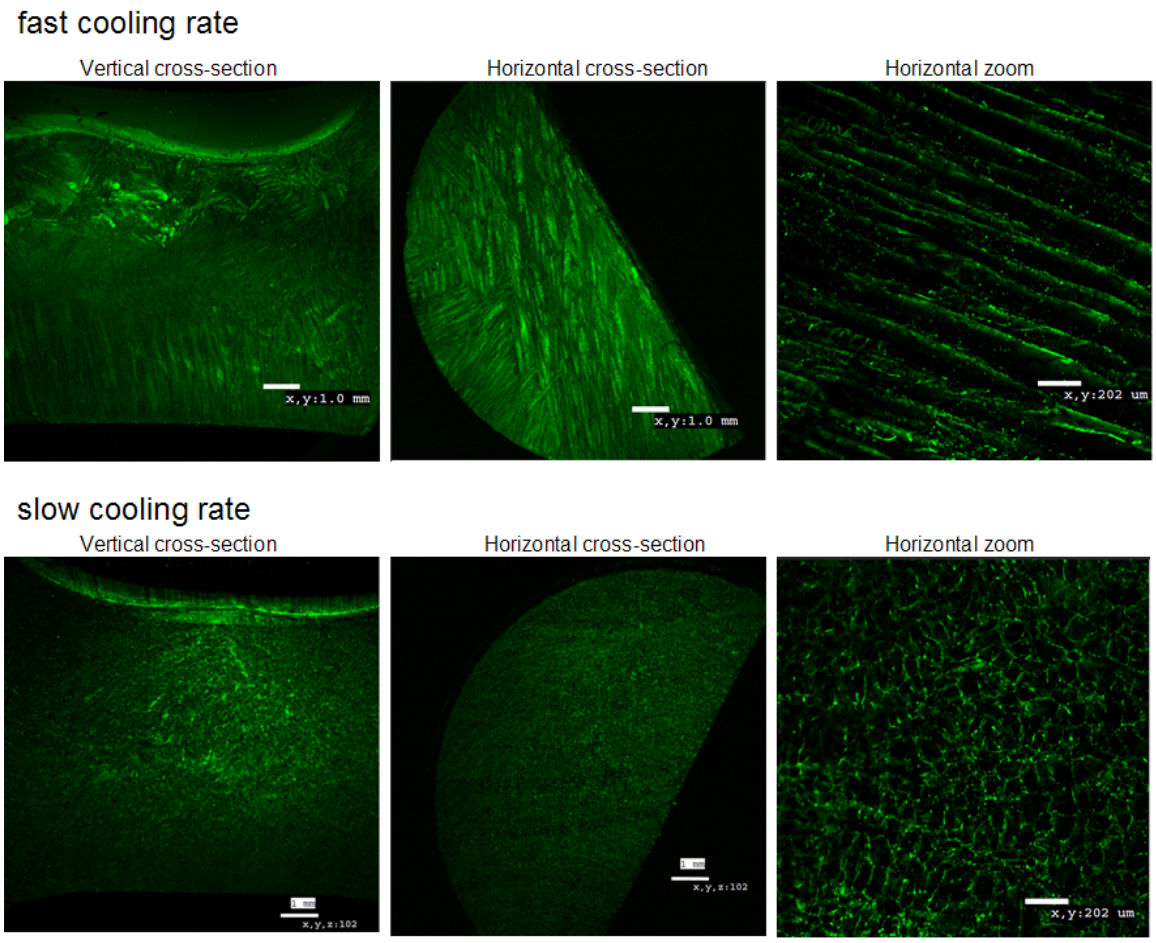

Figure 2-9. Confocal imaging of Sylgard 184 embedded lyophilized cake of coumarin-6 PLGA NPs in sucrose/mannitol formulation

In addition to obtaining images in the X-Y plane, scanning was carried out along the Z-axis, permitting reconstruction of a 3D image (Figure 10). Here too, alternating high and low intensity stripes consisting of NP-concentrated domains and the intervening NP-absent domains were evident.

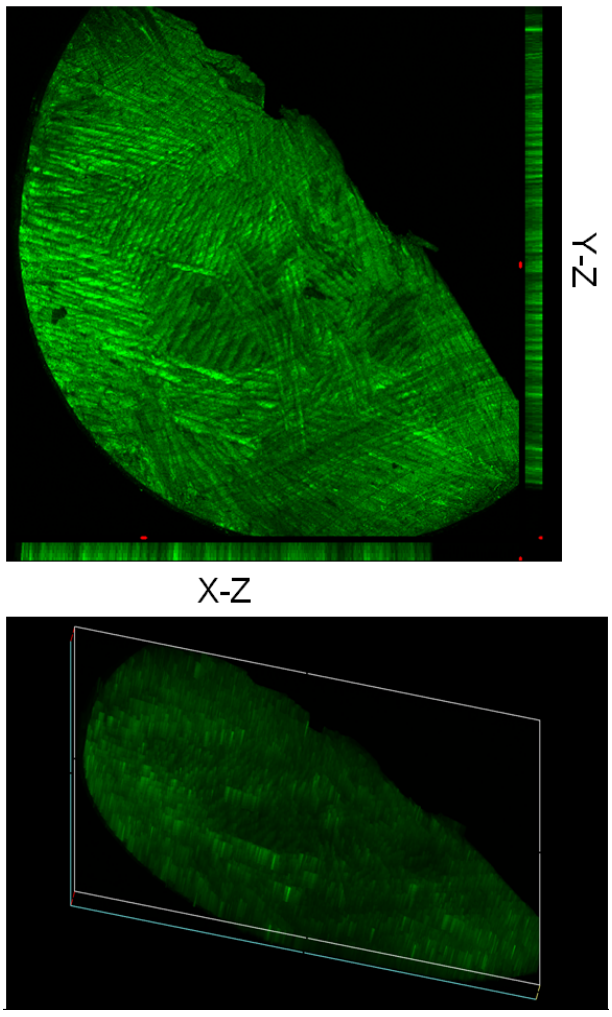

Figure 2-10. Z stack imaging of lyophilized coumarin-6 PLGA NPs cake and reconstruction of 3D structure of a lyophilized cake slice

Another common feature observed in the samples was intense fluorescence at the air/solid interface (Figure 9, vertical cross-section). The higher concentration of NPs at the surface is consistent with the expectation that NPs would be more favorably located at the surface relative to water.

With sublimation of water, counterions would be expected to be drawn to the surface of the NPs, which would neutralize the charge that existed in solution. Moreover, with removal of water, the interparticle separation distance would be decreased, resulting in an increase in the strength of the Van der Waals attractive forces. These factors would contribute to particle aggregation and poor re-dispersibility. Indeed, in the absence of the cryo-/lyoprotectant, the predominant macroscopic morphology appeared as fibrous structures with high aspect ratios. Aggregation of NPs was also corroborated by examining freeze-dried coumarin-6 fluorescent PLGA NPs in the absence of a cryo-/lyoprotectant under a fluorescent microscope. In these images (Figure 11), fibers, as long as 200 microns, and short fibers, a few microns in length, coexisted along with sheet-like structures. Finally, lyophilized PLGA NPs powder could not be spontaneously redispersed but required sonication.

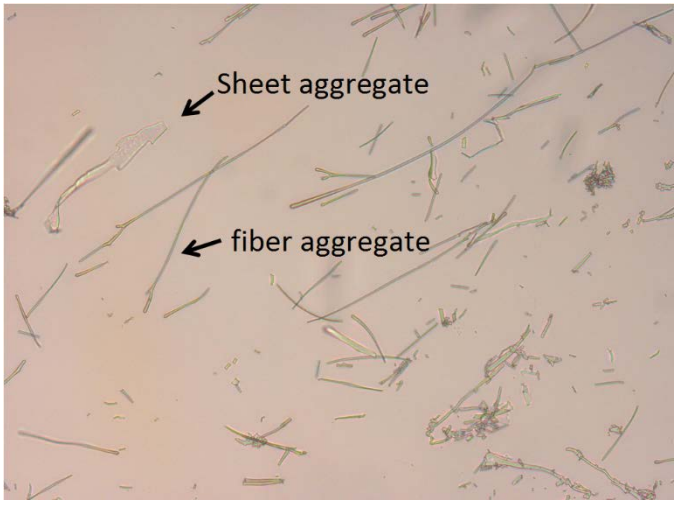

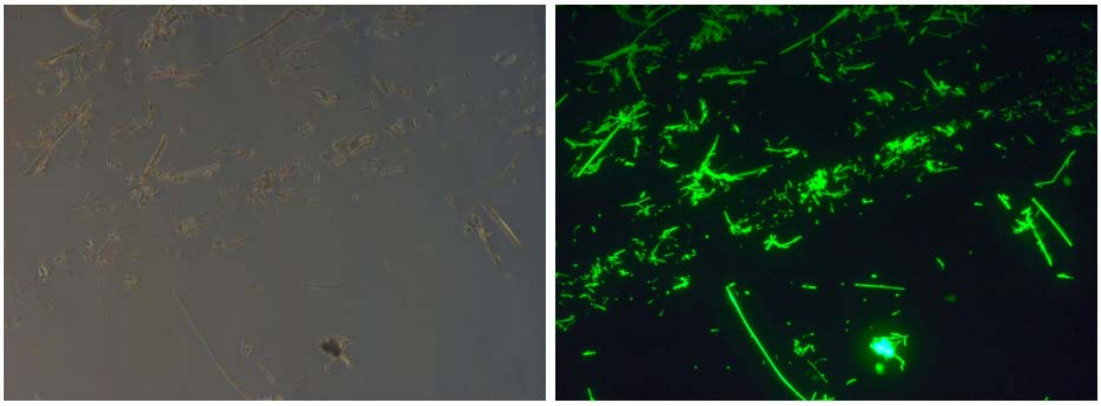

Figure 2-11. Lyophilized coumarin-6 PLGA NPs under optical and fluorescent microscopes

2.4.2 Freeze-thaw stress on PLGA NPs

The lyophilization process sequentially implements freezing and drying steps, both of which can induce stress. The mechanism of freezing stress on NPs appears to depend on cooling rate. A previous study found that quench freezing was required to circumvent the freezing damage on nanocrystals (81). On the other hand, no major damage was documented with PLGA NPs after freeze-thaw cycle (82). In our study, despite the use of liquid nitrogen to induce flash freezing, a 19% increase in the hydrodynamic diameter of PLGA NPs was observed after thawing (Figure. 12). Freezing at -80 °C resulted in a 41% increase in size. Clearly, more rapid freezing reduces the damage, but even virtually instantaneous freezing cannot prevent its occurrence.

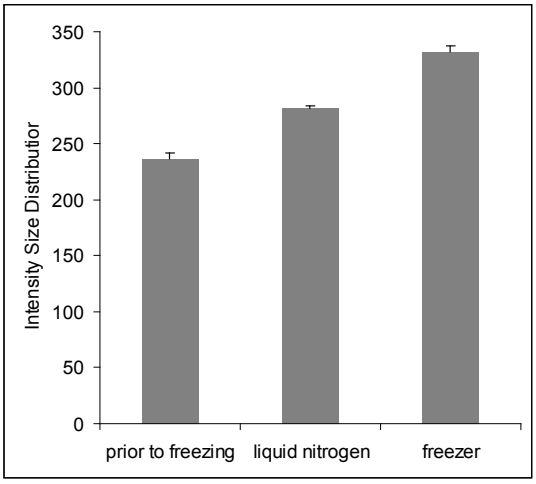

Figure 2-12. Hydrodynamic size of NPs with reconstitution of a 30 mg/mL PLGA NPs in water dispersion following exposure in liquid nitrogen or -80°C freezer

Freezing at -20 °C promoted greater aggregation, with the appearance of micron size particles in the size distribution curve (Table1). The NP size distribution curve also systematically shifted towards larger size as the cooling rate was decreased (Figure 13), coupled with an increase in the polydispersity index (PDI).

No	Data	Diameter(nm)	Polydispersity Index	D (10%) (nm)	D (50%) (nm)	D (90%) (nm)
1	np -20	575.0	0.242	204.8	440.8	1223.2
2	np -80	314.4	0.168	176.7	327.1	628.7
3	np before freeze	258.9	0.092	160.6	261.3	430.0

Table 1. Freezing induced size distribution change after -80 °C or -20 °C exposure of PLGA NPs

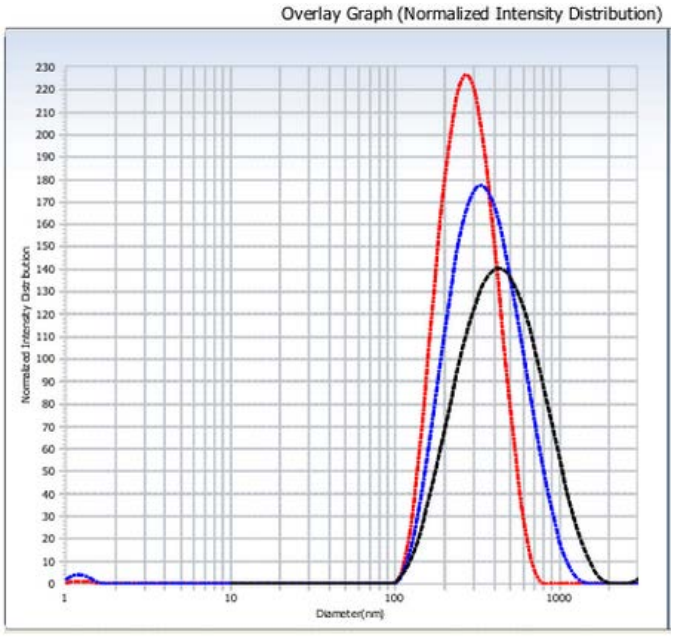

Figure 2-13. Freezing induced size distribution change after -80°C (blue curve) or -20°C exposure (black curve) for PLGA NPs dispersed in water (red curve)

It was previously reported that freezing stress-induced aggregation is dependent on the concentration of NPs (1). In our studies, PLGA NPs, in the concentration range of 1 to 30 mg/mL had approximately equivalent freezing damage (Figure 14). It may be that the final interparticle separation distance in the frozen state is similar, despite the larger separation in the aqueous dispersion. As such, equivalent aggregation is observed (Figure 15).

The efficacy of cryo-protection against NP aggregation was assessed at a number of sucrose and NP concentrations at both fast and slow cooling rates. For NP dispersion in water, at concentrations ranging from 1 to 30 mg/mL, a sugar concentration as low as 1%

(w/v) was sufficient to yield a size distribution that overlapped with the non-frozen control NPs (Figure 16). Moreover, cryo-protection was observed at both slow and fast cooling rates. Thus, relatively low concentrations of sucrose prevent NP aggregation.

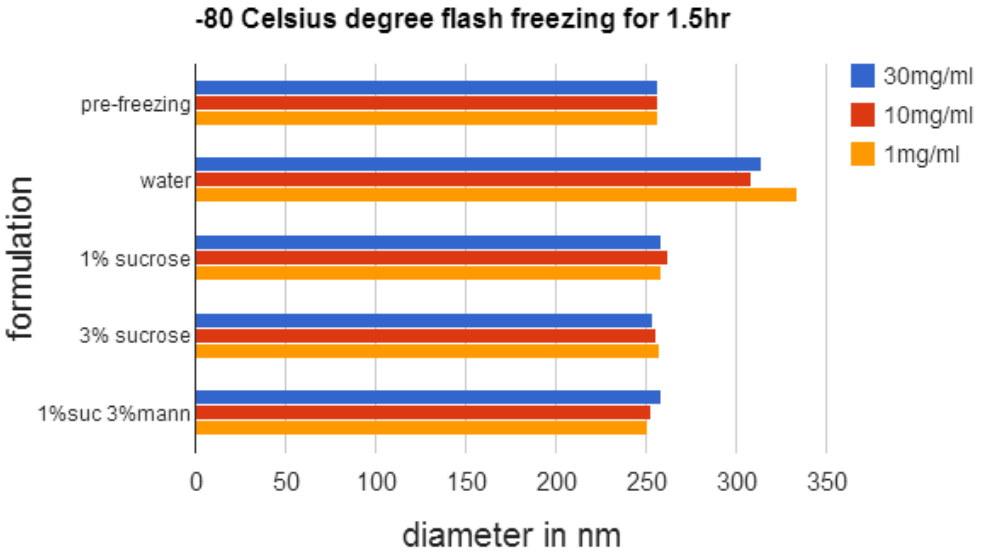

Figure 2-14. Hydrodynamic size of PLGA NPs after flash freezing at -80°C with or without cryoprotectant

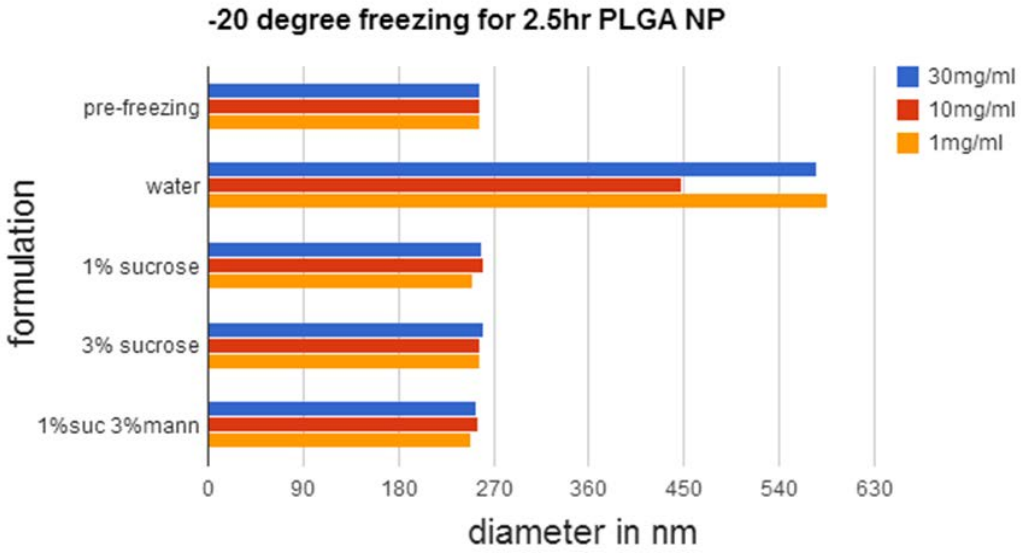

Figure 2-15. Hydrodynamic size of PLGA NPs after freezing at -20°C with or without cryoprotectant

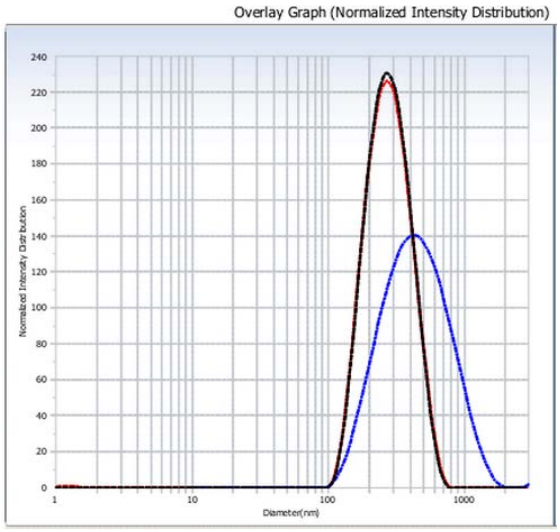

Figure 2-16. Freezing-induced size change after -20 °C freezing exposure for PLGA NPs with (black curve) or without 3% sucrose (blue curve) in comparison to original size distribution (red curve)

2.4.3 Real time imaging of freezing stress and cryoproctection on NPs

Fluorescent images of a PLGA NP dispersion held between glass planes and frozen in -80°C freezer is shown in figure 17. The image contains punctuated fluorescent signals of NPs interspersed within dark domains, which presumably are ice crystals. The darker domains were demarcated by linear or serpentine lines of intense fluorescent signal arising from concentrated NPs. The geometric patterns of freeze-concentrated NPs encompassed both parallel lines and repetitive bifurcations; of which at least two order of fractal branching was evident.

Real-time, time-lapse fluorescence images were also obtained using the above approach. Before freezing, NPs were observed to be undergoing random motion.

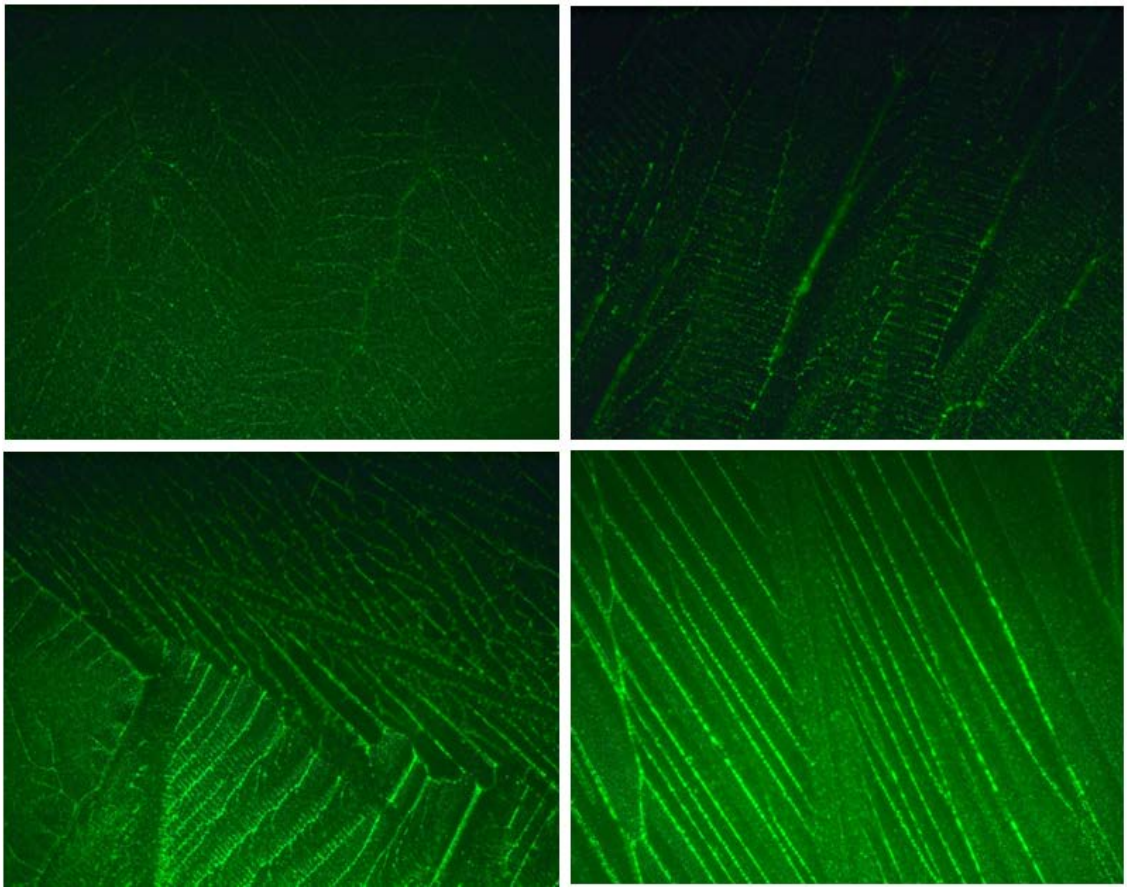

Figure 2-17. Representative fluorescent images of aqueous PLGA NP dispersion frozen on glass microscope slides at -80 °C freezer

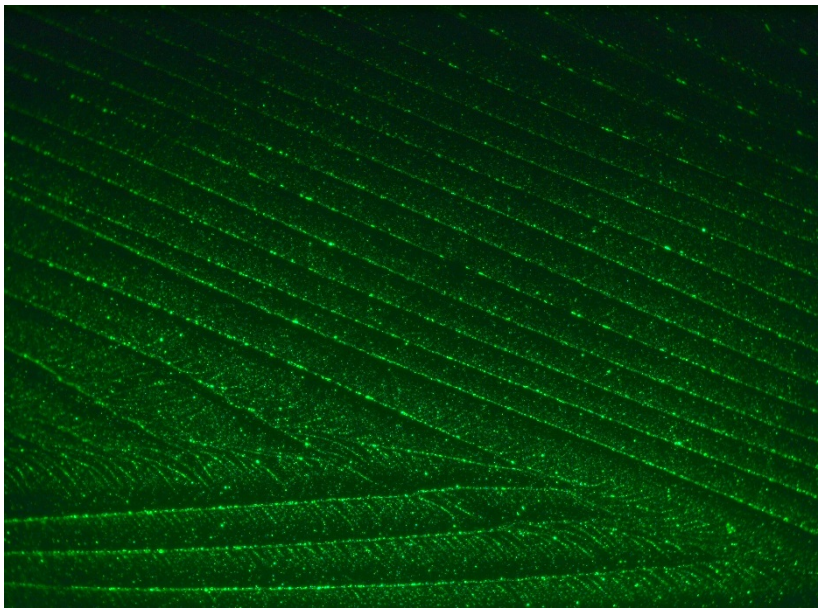

Figure 2-18. Fluorescent image of aqueous PLGA NP dispersion frozen on microscope slides upon dry ice induced in situ freezing

With freezing, NPs were squeezed in between the advancing fronts of ice crystals. This is shown in Figure 18, which consists of an alternating pattern of narrow lines with intense green fluorescent signal and darker streaks punctuated by NPs. A commercial, monodisperse PS NP formulation also showed similar behavior (Figures 19, 20, 21). As the ice crystal propagated across the slide, a majority of NPs were transiently excluded and propelled by the moving ice crystal front, until they encountered another emerging ice crystal. Because the rate of ice propagation was faster than the rate of NP displacement, NPs became immobilized in a confined space.

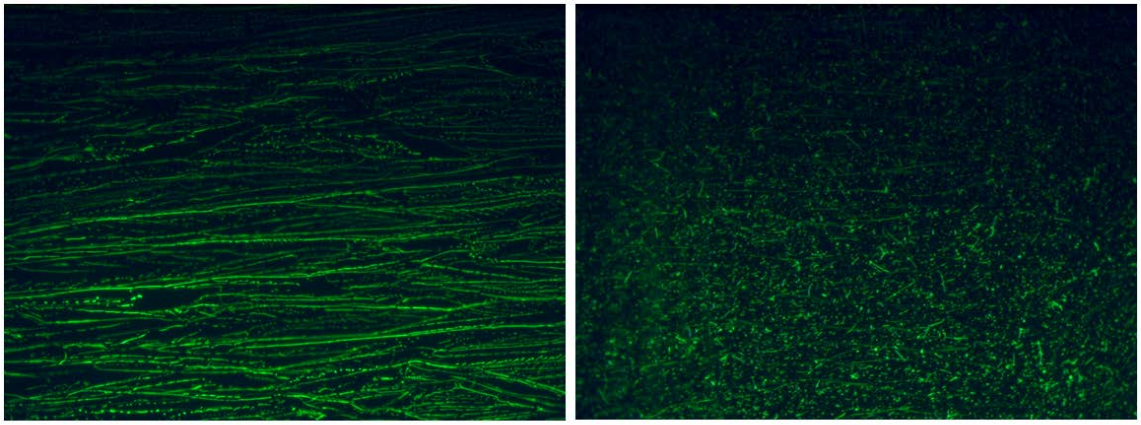

Figure 2-19. Real time microscopy of freeze-thaw behavior of 1.25 mg/mL PS NPs dispersed in water

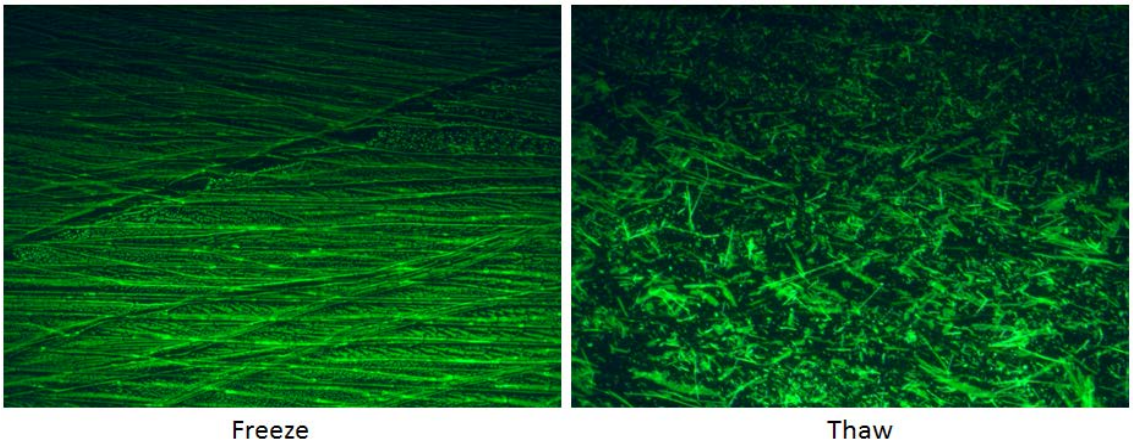

Figure 2-20. Real time microscopy of freeze-thaw behavior of 2.5 mg/mL PS NPs dispersed in water

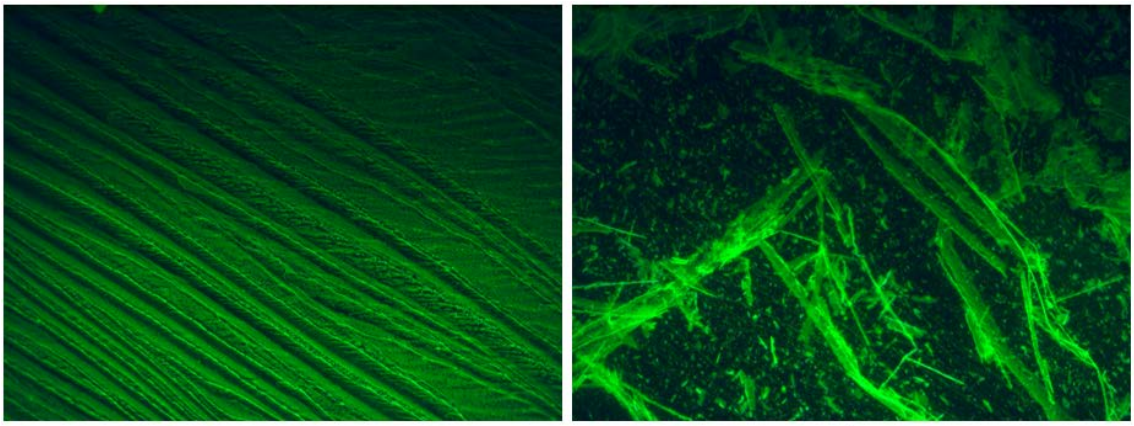

Figure 2-21. Real time microscopy of freeze-thaw behavior of 5 mg/mL PS NPs dispersed in water

In contrast to the PLGA NPs, freezing stress-induced aggregation of PS NPs was dependent on concentration. Specifically, a 2.5 mg/mL PS NPs had denser freeze-concentration than 1.25 mg/ml with the formation of larger and longer fibrous aggregates. The trend was also evident at 5 mg/mL concentration, where the sample gave rise to sheet like aggregated structure with membranous morphology (Figure 21).

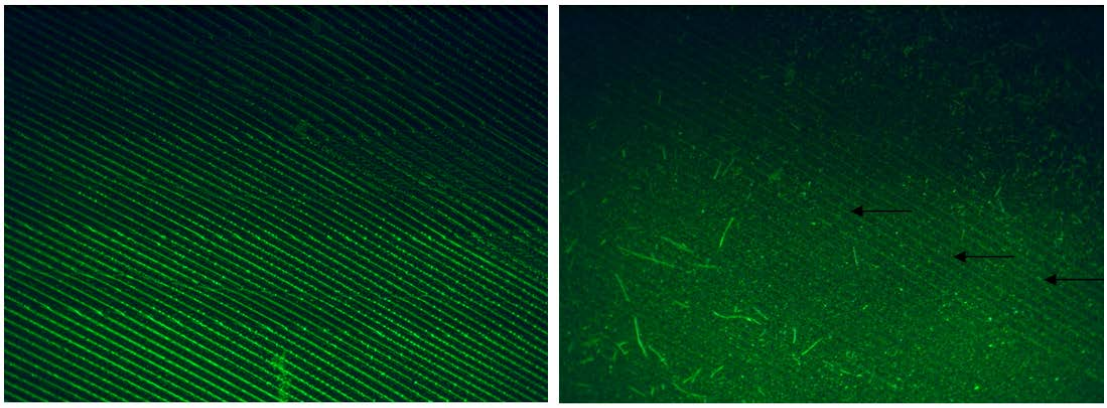

Figure 2-22. Representative images of PS NPs after freeze-thaw. Arrows indicate NPs immobilized on the slide after thawing

Upon thawing, NPs were spontaneously redispersed, with fiber-like aggregates, moving slowly under the convective force of water. However, some aggregates remained fixed in space, indicative of immobilization of NPs aggregates onto the surface of the glass substrate (Figure 22, arrows). The locations of immobilized NPs aggregates were superimposed on the locations of the freeze-concentrated NPs prior to thawing. The presence of imprinted streaks of NP aggregates on the glass slides suggests the potential role of formulation container - wall interface acting as another site for freezing stress-induced aggregation.

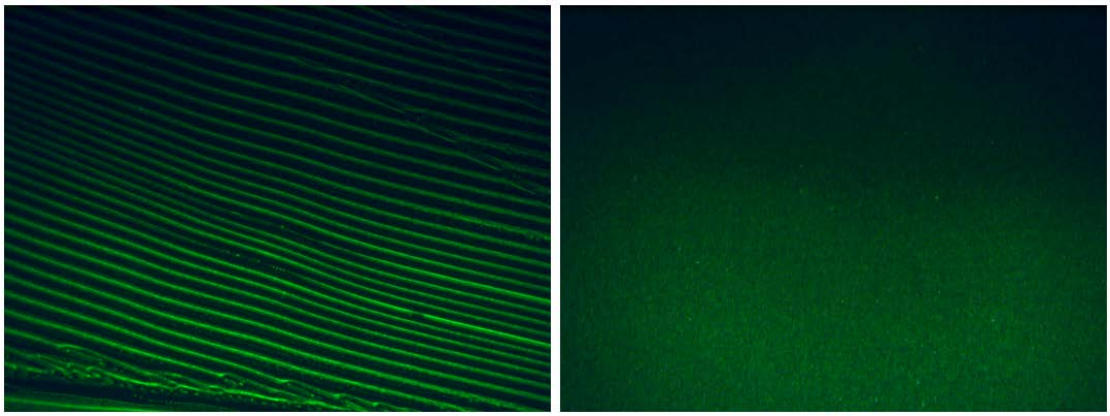

Figure 2-23. Real time microscopy of freeze-thaw behavior of 1.25 mg/mL PS NPs in 3% sucrose formulation

In the presence of a cryoprotectant, the freeze concentration processes also resulted in clear separation between ice and NPs as captured in time-elapse microscopy. Immediately following the formation of ice crystals, however, NPs remained mobile within the interstitial space between ice crystals. This was in stark contrast to the abrupt immobilization of NPs in the absence of cryoprotectant. Over approximately 1 minute, the mobility of NPs within the interstitial space rich in cryoprotectant freeze-concentrate gradually decreased until the NPs became immobile. Conceivably, the unfrozen, cryoprotectant-rich fraction was initially in a rubbery state but eventually converted into the glassy state when the glass transition temperature was reached. During thawing, NPs within the interstitial space became mobile prior to melting of ice crystals, which presumably occurred as the temperature traversed the Tg' of the maximally frozen freeze-concentrate. In the presence of a cryoprotectant, when the thawing process was

completed, a well-dispersed NPs suspension was observed, indicating successful cryoprotection.

2.4.4 Cryo-electron microscopy of freeze-concentrated NPs

The resolution of optical microscopes (including fluorescence microscope) is diffraction-limited, with the resolution in the X-Y plane generally no better than 250 nm. The freeze-concentration of NPs brought NPs so close together that the Airy disks of adjacent discrete point light source began to overlap, thus making it impossible to resolve neighboring NPs. Thus, to substantiate the interplay between freeze-concentration, aggregation and cryoprotection of NPs, an imaging technique with higher resolution was needed.

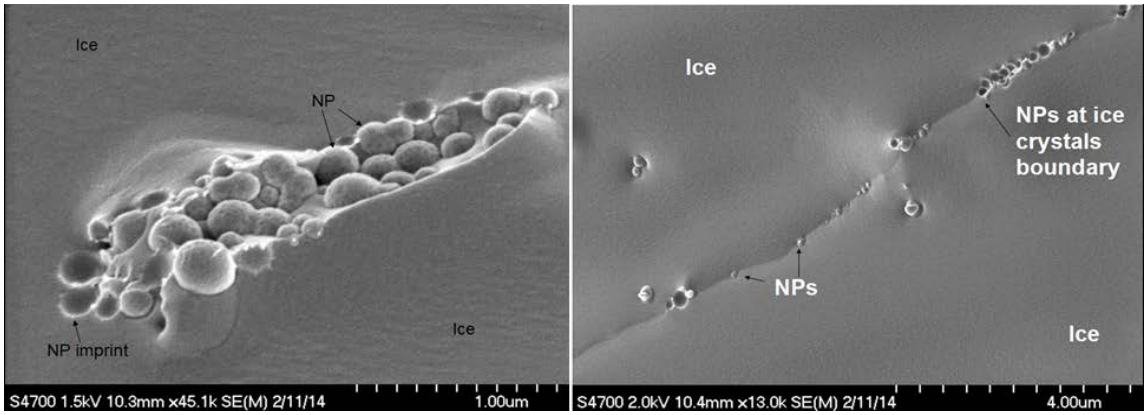

Figure 2-24. Cryo-SEM image of an aqueous 1.5mg/mL PLGA NP dispersion, after dry ice-induced freezing

The cryo-SEM sample preparation procedure for PLGA NP dispersion was in line with previous dry ice-induced *in situ* freezing procedure, favoring ice crystallization instead of vitrification. Thus, the sample preparation could recapitulate realistic freezing events with respect to pharmaceutically relevant processes. Even with a diluted PLGA NP dispersion (1.5 mg/mL), freezing resulted in clustering and linear concatenation (Figure 24). This clearly demonstrates that NPs can be in close contact so that Van der Waals force of attraction predominates. It is understandable that those clustered NPs will not be easily re-dispersed upon reconstitution unless a high-energy process (e.g., sonication) is used.

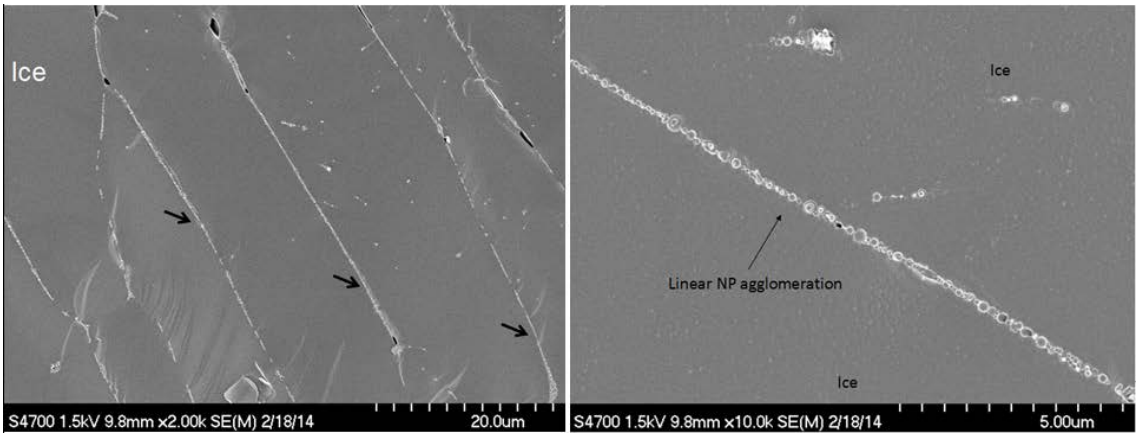

Figure 2-25. Cryo-SEM image of an aqueous 30mg/mL PLGA NP dispersion, after dry ice-induced freezing

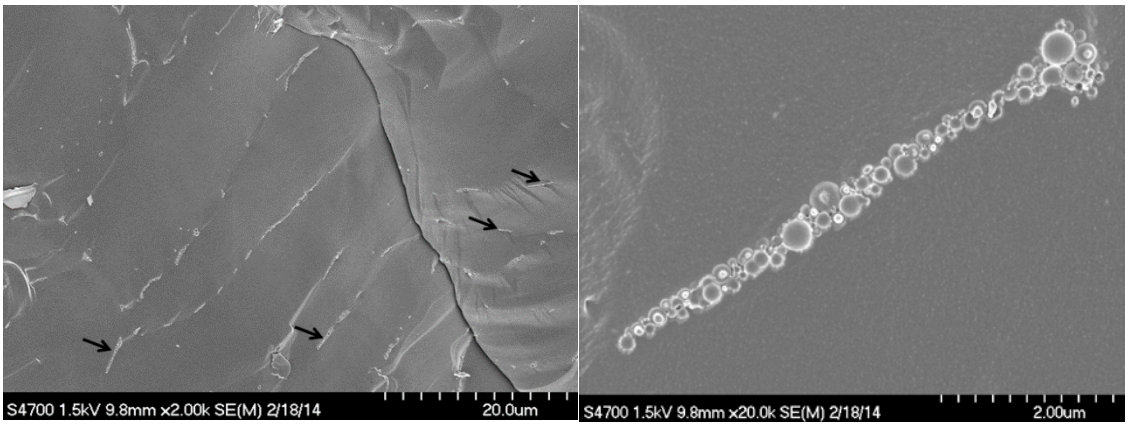

Figure 2-26. Cryo-SEM image showing the presence of fiber-like aggregates (arrows) following dry ice-induced freezing of an aqueous 30mg/mL PLGA NP dispersion

With a 30 mg/mL sample, cryo-SEM also confirmed that the high aspect ratio filamentous geometry consisted of individual NPs in between ice crystal domains (Figure 25). Long fibers with lengths longer than 20 microns, shorter fibers (Figure 26) and multi-layered aggregates (Figure 27) coexisted. Thus, cryo-SEM data affirmatively established the prominent freeze-concentration of NPs within the frozen bulk solution as a major mechanism for NP aggregation during freezing.

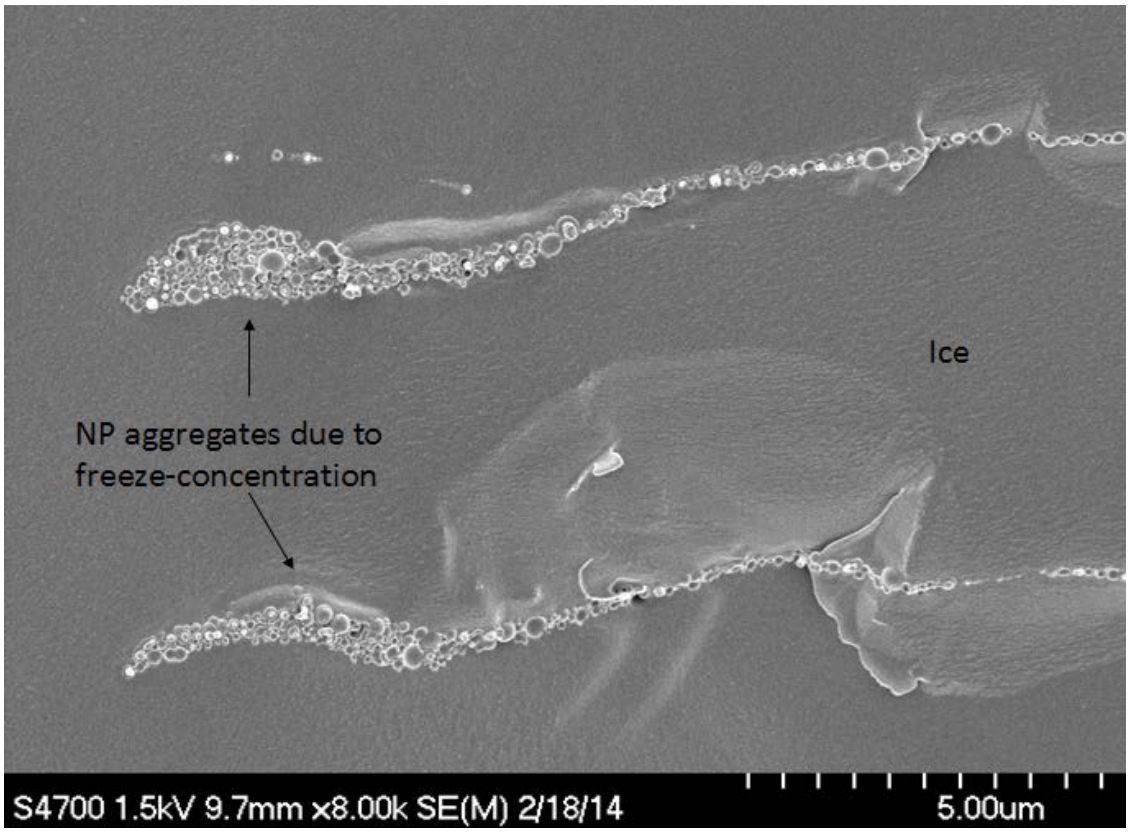

Figure 2-27. Multi-layer clustering of PLGA NPs, after dry ice-induced freezing of an aqueous 30 mg/mL dispersion

Bubbles were also observed at the frozen fractured plane. There were apparent NPs aggregates, comprising both islet and linear aggregates at the air-formulation interface, which indicates that this interface is another site for NP agglomeration (Figure 28). However, unlike the prevalent pattern of liner freeze-concentrated NP aggregation in bulk solution, islands of irregularly connected NPs were the predominant pattern within the bubbles (Figure 29).

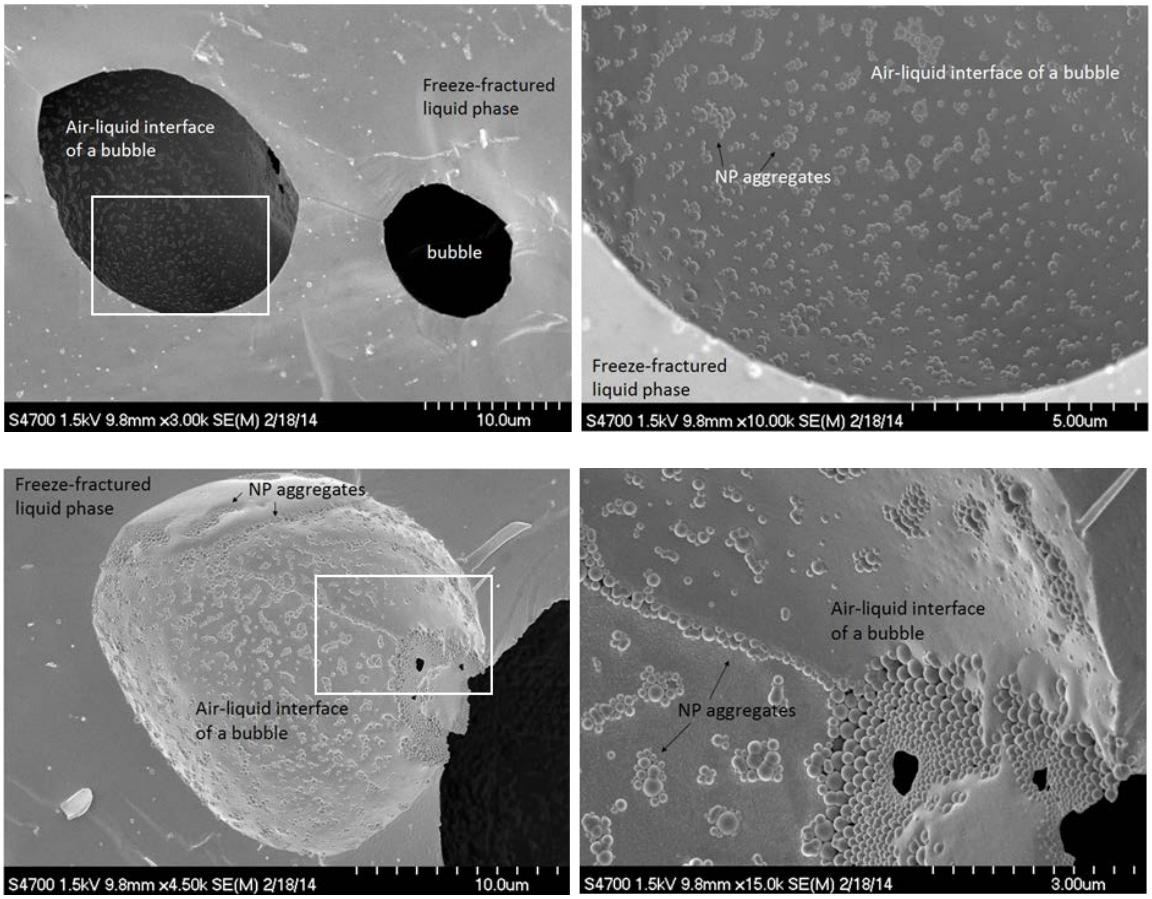

Figure 2-28. Clustering of PLGA NPs at bubble interfaces

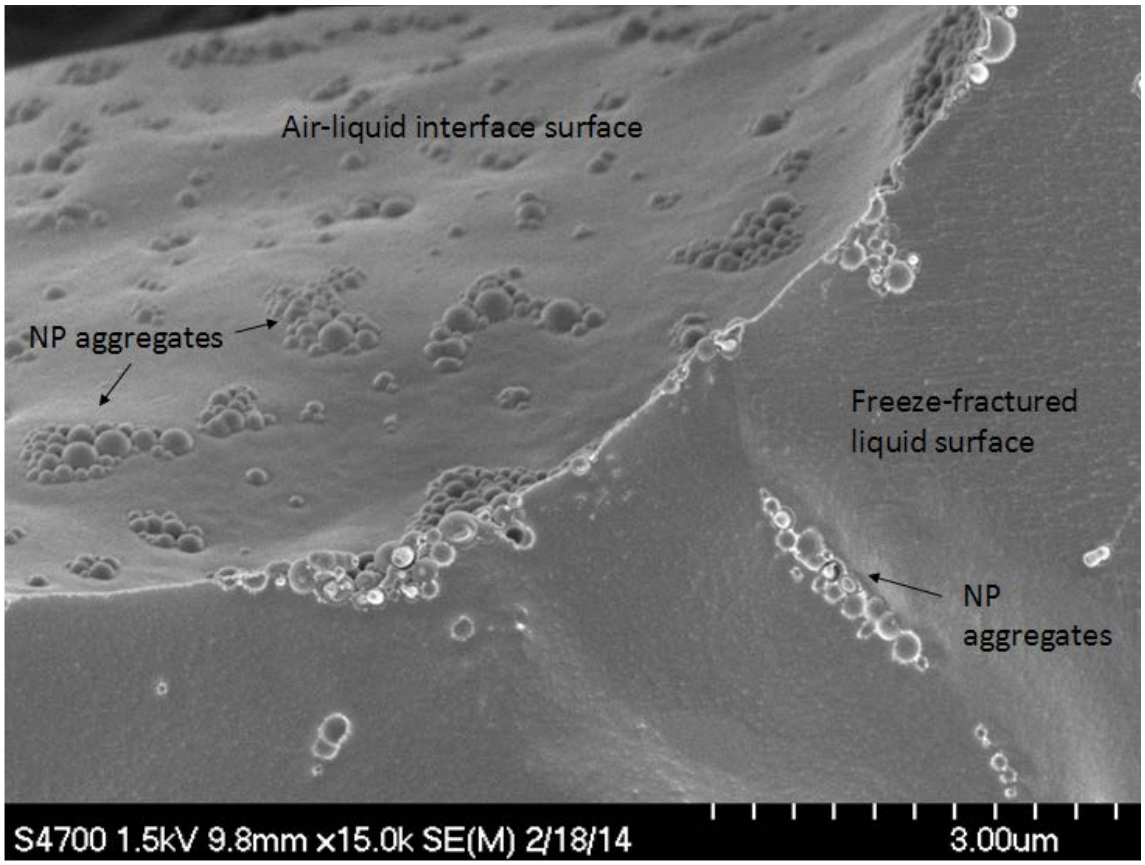

Figure 2-29. PLGA NP aggregates displayed different geometric patterns at bubble interface and bulk solution

In the presence of 3% sucrose, the freeze-concentration phenomenon persisted (Figure 30), but here was also a clear interstitial space formed between ice crystals. During the freezing stage, there was phase separation between ice crystal and freeze-concentrate of sucrose, suggesting that as freezing progressed, water molecules aligned at the boundary of growing ice lattice at the nucleating seed surface. Sucrose concentration in the remaining unfrozen fraction must necessarily increase, eventually resulting in the formation of an amorphous state in the interstitial space (Figure 31).

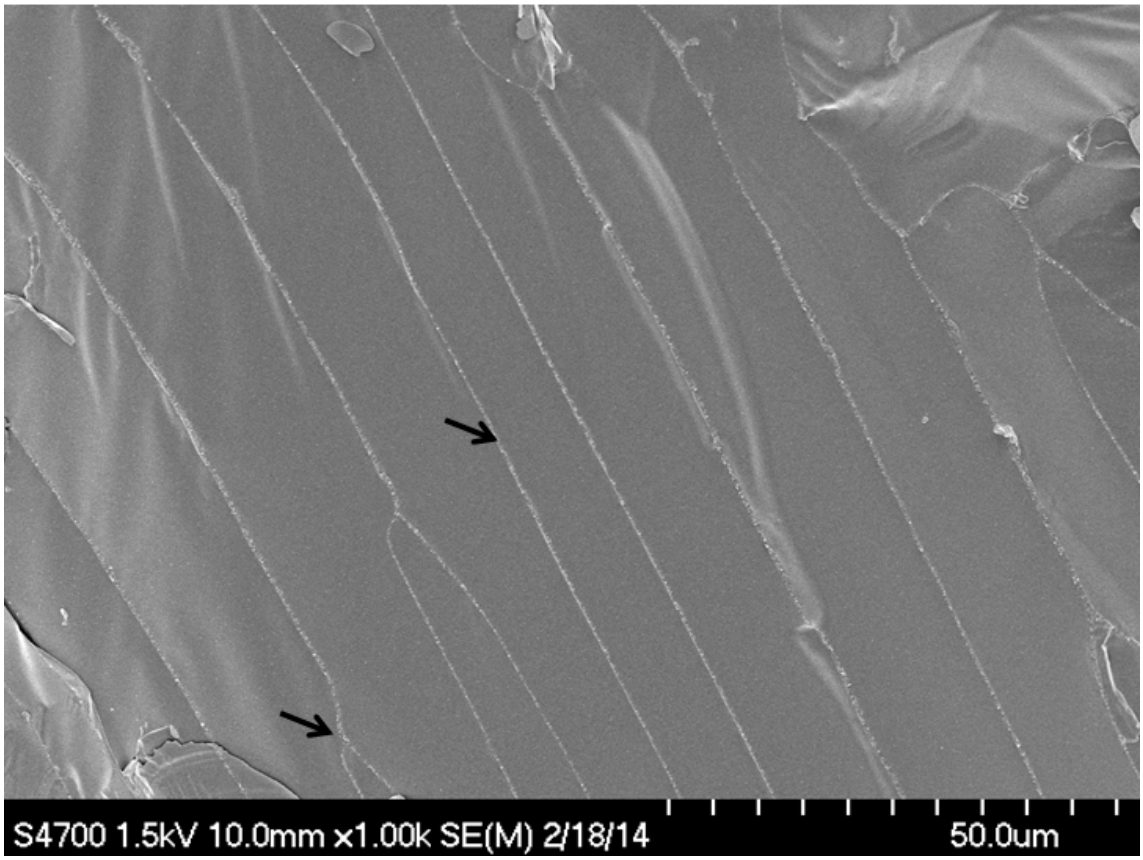

Figure 2-30. Linear freeze-concentration pattern in frozen PLGA NP formulation containing 3% sucrose

Discrete NPs were interspersed in a rivulet like interstitial domain consisting of maximally frozen freeze-concentrate of sucrose. Owing to the physical isolation of adjacent NPs via glassy sucrose, no multi-particle concatenation was observed. In essence, the freeze-concentration stress on NPs was buffered by the presence of sucrose that created a relatively large inter-particle distance. To our knowledge, this is the first direct visual evidence to support the particle isolation hypothesis.

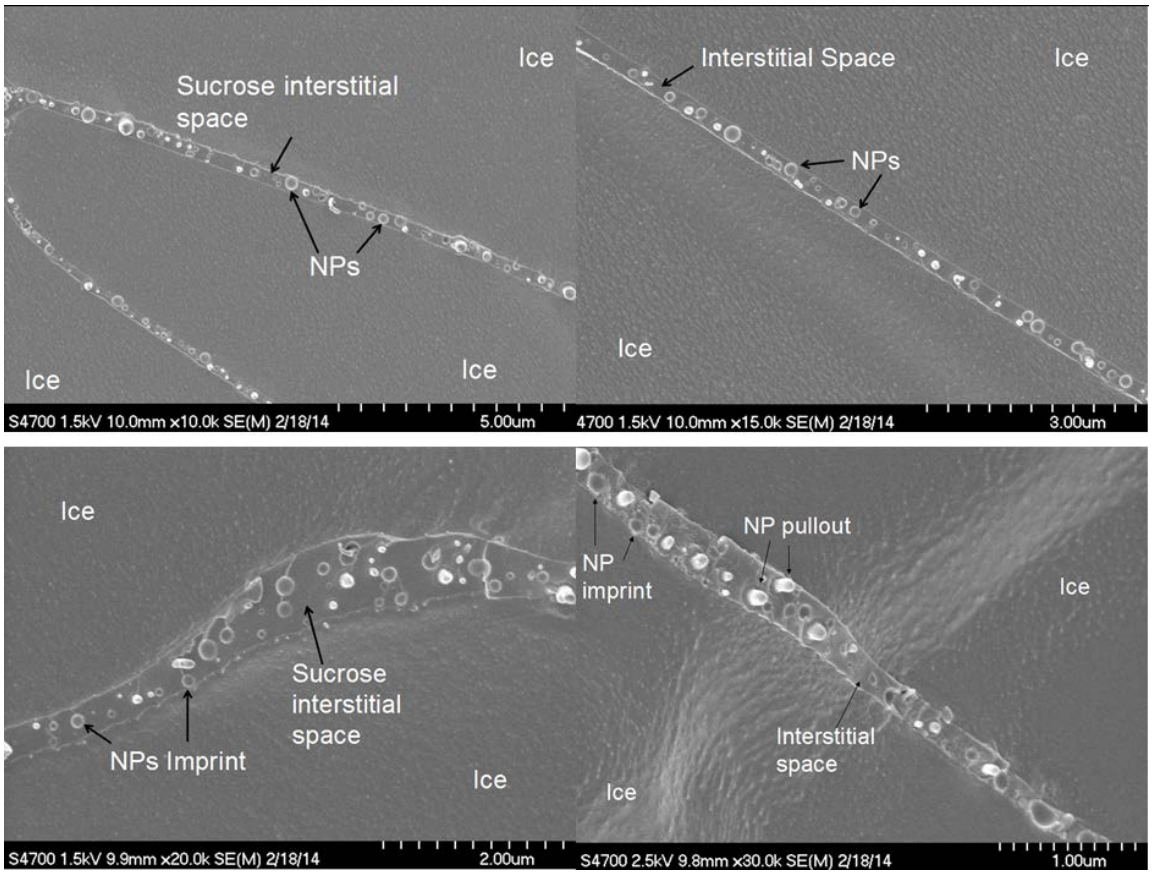

Figure 2-31. Interstitial spaces in frozen PLGA NP formulation containing 3% sucrose

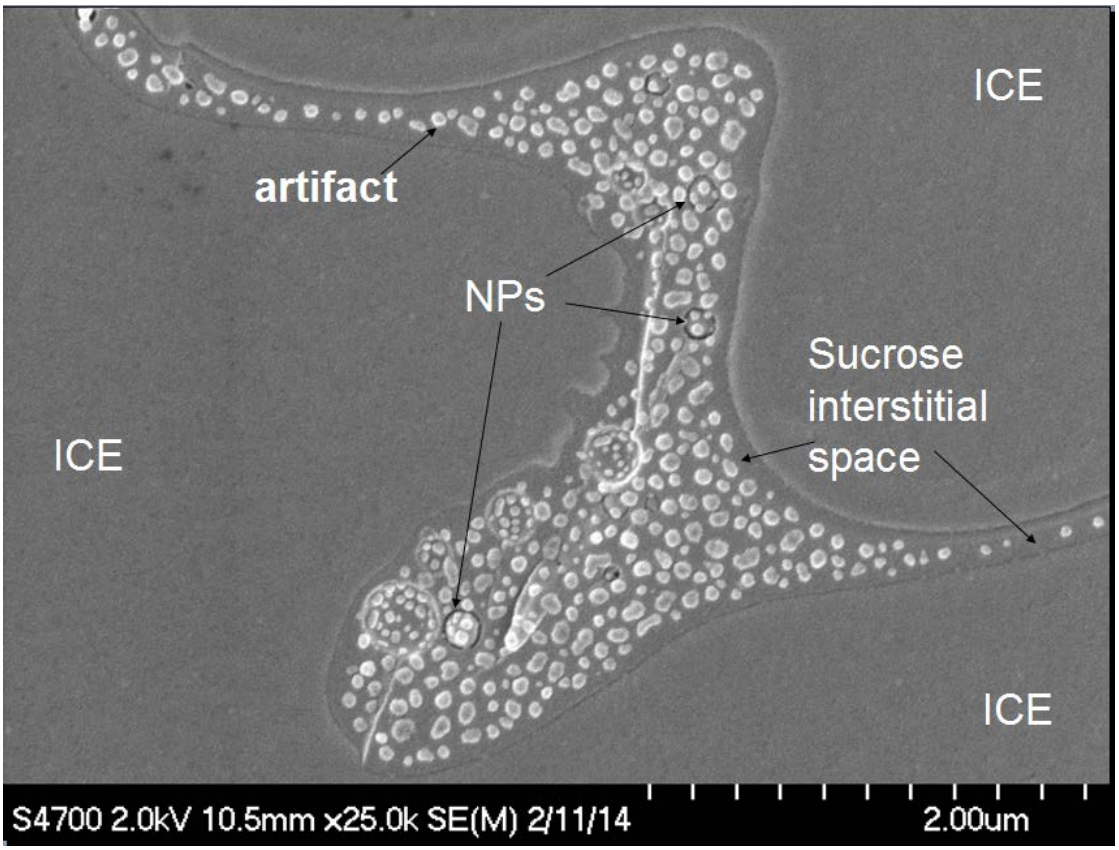

Figure 2-32. Interstitial spaces in the formulation containing 3% sucrose and 1.5 mg/mL PLGA NPs

Based on these observations, the ratio of cryoprotectant is the key to stabilizing NP. For the formulation containing 3% sucrose and 30 mg/mL PLGA NPs, the inter-particle distance within the interstitial space was estimated to be in the sub-micron range, albeit doublets of particles were occasionally observed. Lower NP concentration (1.5 mg/mL) but same 3% sucrose (Figure 32) had generally a larger inter-particle distance. Thus, a higher sucrose to NP ratio translated into a lower particle density, which was associated with better protection against NP agglomeration.

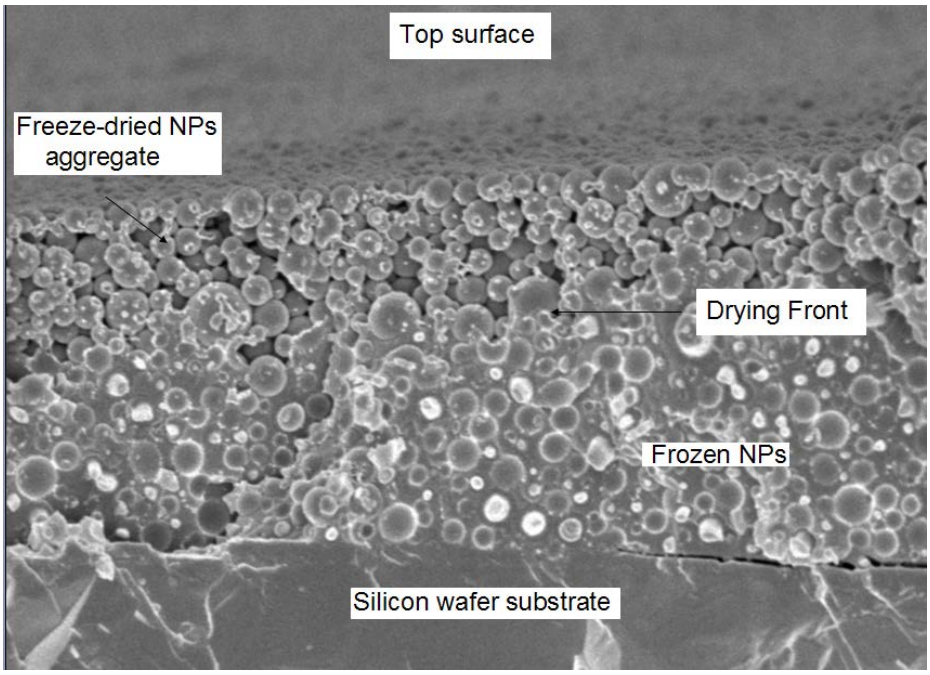

Figure 2-33. Closely packed PLGA NPs at the air-liquid-substrate tri-phase interface

Lastly, deposition of concentrated PLGA NPs formulation onto both glass slide and silicon wafer substrate led to preferential accumulation at the edge of the liquid film. Thus, the air-liquid-substrate tri-phasic interface may be another site for aggregation (Figure 33).

2.4.5 Modeling the minimal weight ratio of disaccharide to NPs necessary for efficient cryo-/lyoprotection

In light of the imaging data, interfaces emerged as the major sites for enrichment of NPs and therefore sites for NP aggregation. Formation of ice-ice and ice-container interfaces

caused spatial confinement of NPs and thereby subjected NPs to mechanical compression. In contrast, the air-formulation interfaces either at the surface or near bubbles also caused confinement of the NPs, but to a lesser extent, as expansion into air occurs more readily.

For effective protection against freeze-concentration induced aggregation, particles must be separated by either cryoprotectant or frozen water. In accordance to the particle isolation hypothesis, four theoretical models are available to estimate the minimal sugar to NP ratio required for protection.

The close packed sphere model was originally proposed by Kepler (83) (Figure 34), where the highest packing density is taken to be 0.74, leaving a void fraction of 0.26. The latter value would represent a lower limit of sugar needed to maintain particle separation. In practice, the packing of monodisperse NPs during freeze-concentration and freeze-drying will not reach the theoretical maximum. As a result, the weight ratio is underestimated. The presence of polydispersity worsens the estimate, although imperfect packing has the opposite effect. For PS NPs, the weight ratio of sugar to NPs was calculated to be 0.53 to 1.

$$V_{nanosphere} = 0.74$$

$$V_{void\ space} = 0.26$$

$$\frac{W_{sugar}}{W_{nano}} = \frac{\rho_{sugar} \times V_{void\ space}}{\rho_{nano} \times V_{nanosphere}}$$

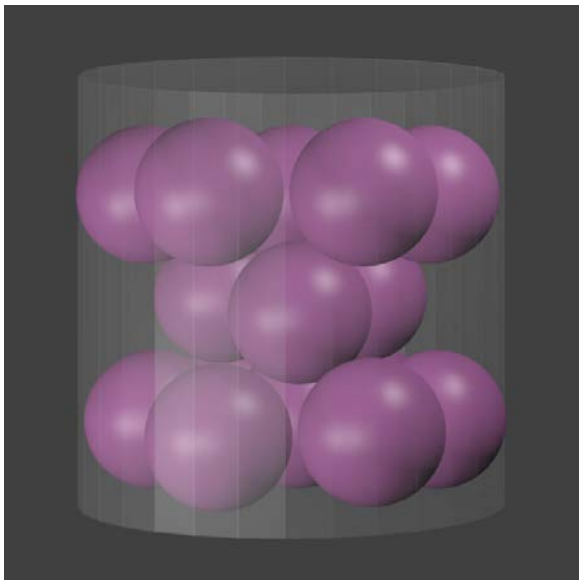

Figure 2-34. Schematic showing the model of closely packed NPs in a confined space

The “caged sphere” model entails each sphere being caged by a cube of cryoprotectant with the cube planes are tangential to the sphere surface (Figure 35). The void volume is calculated as the volume of the cube less the volume of an included sphere. The required weight ratio of sucrose to NPs would be 1.38 to 1. The “caged sphere” model should yield an appropriate estimate for NPs in a confined space as when they were phase-separated during the freezing event.

$$V_{cube} = (2r)^3$$

$$V_{nanosphere} = \frac{4\pi r^3}{3}$$

$$V_{void} = V_{cube} - V_{nanosphere}$$

$$\frac{W_{sugar}}{W_{nano}} = \frac{\rho_{sugar} \times V_{void\,space}}{\rho_{nano} \times V_{nanosphere}}$$

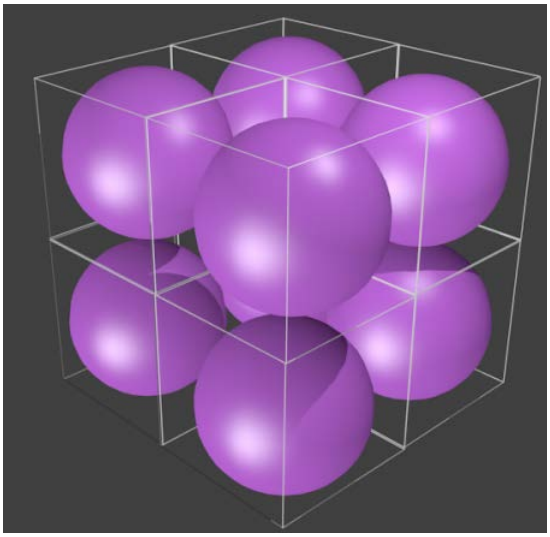

Figure 2-35. Schematic showing the model of caged NPs in a confined space

The third approach assumes a random close packing (84). Random close packing of polydisperse particles has an estimated packing density of 0.65, assuming a standard deviation of σ <20% (85). The corresponding weight ratio of sucrose to NPs would be 0.82 to 1. This approach is expected to be more accurate than Kepler's dense packing model for the freeze-concentrated NPs packed within a confined space.

$$V_{nanosphere} = 0.65$$

$$V_{void\ space} = 0.35$$

$$\frac{W_{sugar}}{W_{nano}} = \frac{\rho_{sugar} \times V_{void\ space}}{\rho_{nano} \times V_{nanosphere}}$$

The above approaches assumed that sucrose will completely fill the void space; however, this need not be the case as was observed in the frozen formulation of PLGA NPs containing 3% sucrose (Figure 36).

The last model follows the water replacement theory of lyoprotection mechanism for biologics, where lyoprotectants substitute for the protein hydration shell to preserve the native conformation of protein (86). With NPs, the polyhydroxyfunctional groups of disaccharides could function as hydrogen donors, while the carbonyl groups of PLGA or the carboxyl group of carboxylate polystyrene could act as a hydrogen acceptor. Sucrose has also been suggested to readily spread at the surface of NPs, due to the low sugar/ NP interfacial tension (78). Hence, sucrose could replace the hydration shell surrounding the NPs and thereby serve as a spacer between particles. Thus, this model is termed "sugar-coating model" (Figure 37).

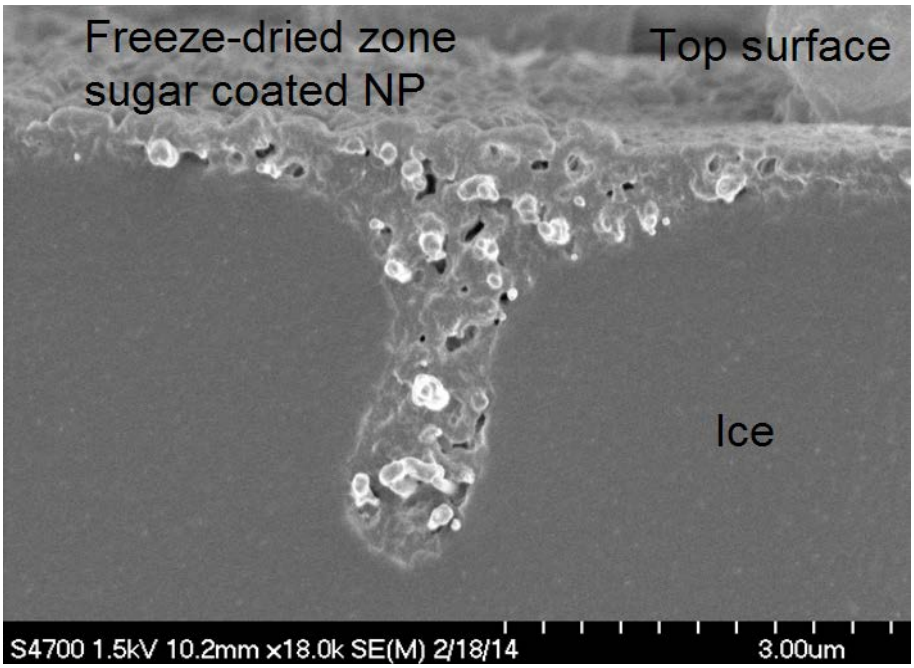

Figure 2-36. Cryo-SEM image showing the top surface of a formulation containing 30 mg/mL PLGA NPs and 3% sucrose

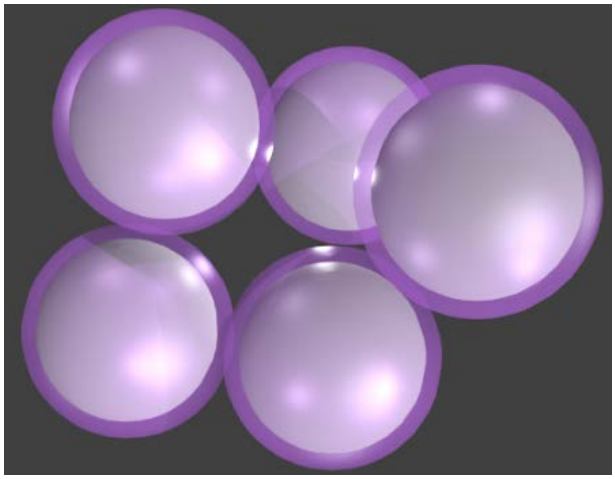

Figure 2-37. Schematic showing the model of sugar-coated NPs in close proximity

When the thickness of sugar coating layer is 20% of the radius of a monodispersed NP population (R = r+0.2r), (for instance, 20nm thickness of sucrose coated onto NPs with 200 nm diameter), the weight ratio of sugar / PS NPs would be 1.13 to 1.

$$V_{nanosphere} = \frac{4\pi r^3}{3}$$

$$V_{sugar\text{-}coating} = \frac{4\pi R^3}{3} - \frac{4\pi r^3}{3}$$

$$\frac{W_{sugar}}{W_{nano}} = \frac{\rho_{sugar} \times V_{sugar-coating}}{\rho_{nano} \times V_{nanosphere}}$$

$$\rho_{sucrose} = 1.59 \text{ g/cm}^3$$

$$\rho_{PS} = 1.05 \text{ g/cm}^3$$

The predicative capability of these models was examined by measuring the size distribution of PS NPs before and after lyophilization as a function of sucrose/NP ratio. Initially, the glass transition temperature of maximally frozen freeze-concentrate was determined. The step change in the reverse heat flow occurred at the same temperature (-33 °C ~ -34 °C) for sucrose formulation in the presence or absence of PS NPs (Figure 38). Thus, the primary drying step was performed slightly below the Tg' to prevent cake collapse. Monodisperse carboxylate PS NPs with diameters of 100 nm and 200 nm were used.

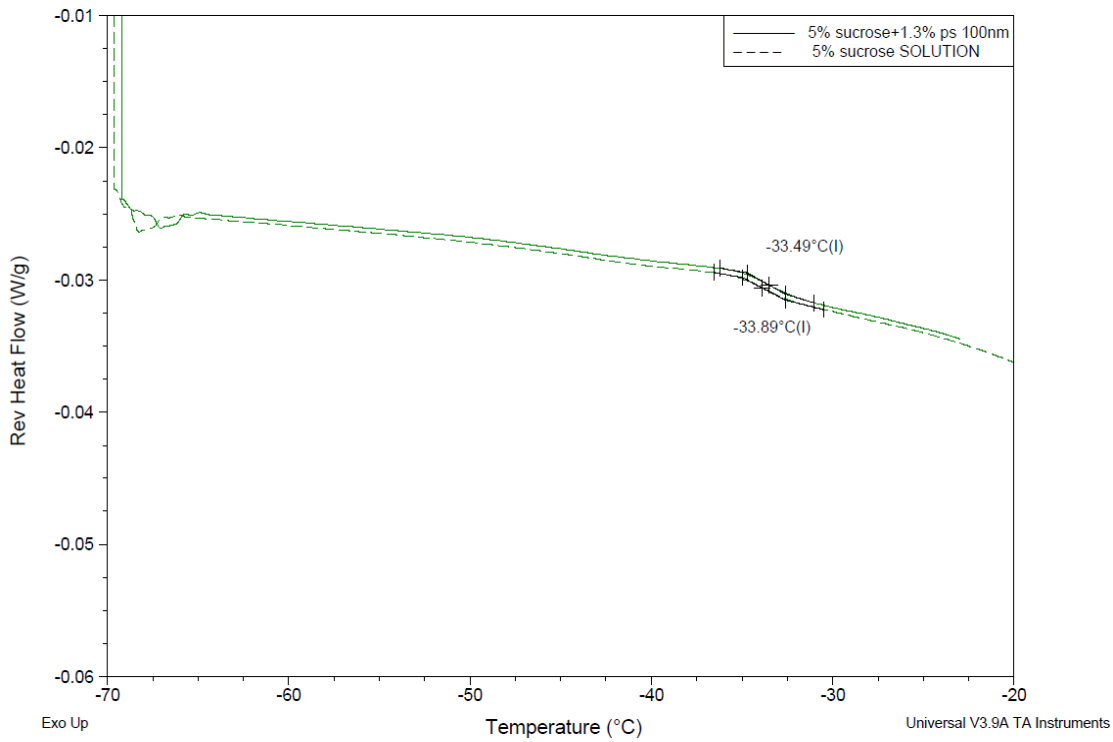

Figure 2-38. DSC heating curves of 5% sucrose with or without 1.3% Carboxylate PS NPs 100nm

Surprisingly, there was no detectable freezing stress on carboxylate functionalized PS NPs (100 nm diameter) from freeze-thaw test and real-time fluorescent microscopy study (data not shown). However, after freeze-drying the pure water formulation, more than a 300% size increase was observed. Thus, freeze-drying stress on the 100 nm PS NPs primarily originated from the drying phase. In removing water, 100 nm PS NPs formed stacks, leading to close physical contact and aggregation. As for sucrose based lyoprotection of 100 nm PS NPs, a series of formulations with increasing sucrose / NP ratios were lyophilized. Since the Kepler dense packing model (sucrose to NP ratio of 0.53:1) is the lower limit of an effective sucrose formulation, a sucrose-to-NP ratio of

0.25:1 was purposefully used as an inadequate formulation. The 0.25-1 ratio was indeed insufficient to fully prevent the formulation from freeze-drying stress. However, the mere presence of sucrose in the formulation reduced the lyophilization-induced size change to only 25% increase from the more than 300% increase observed in the absence of sucrose (Table 2). Kepler dense packing model-based ratio (0.53:1) further mitigated the freeze-drying stress, although there was still a slight increase in size. The random close packing model (sucrose to NP ratio of 0.82:1) was shown to be completely protective, generating an identical size distribution curve of NPs upon reconstitution of lyophilized formulation (Figure 39). All other models such as caged sphere model that require higher sucrose to NP ratio than 0.82-1 protected the 100 nm NPs equally well.

No	Data	Diameter(nm)	Polydispersity Index	D (10%) (nm)	D (50%) (nm)	D (90%) (nm)
1	PS100 LYO 0.82-1	101.7	0.042	70.9	100.5	143.4
2	PS100 LYO 0.53-1	105.4	0.112	64.0	106.9	174.7
3	PS100 LYO 0.25-1	125.7	0.127	75.8	129.5	223.5
4	PS100 LYO H2O	340.9	0.161	102.7	211.8	502.8
5	PS100 H2O std	102.4	0.047	71.1	101.2	144.3

Table 2. Size distribution of 100 nm carboxylate PS NPs after lyophilization under various weight ratios of sucrose to NPs

In contrast to the 100 nm PS NPs, the 200 nm PS NPs demonstrated altered size distribution after freeze-thaw test. Freeze-drying in pure water formulation resulted in more than a 500% size increase (Table 3). Similarly, the sucrose to NP ratio of 0.25:1 was again insufficient to fully prevent the formulation from freeze-drying stress, albeit significantly reducing the lyophilization stress (only a 150% size increase). Kepler dense

packing model ratio (sucrose to NP ratio of 0.53:1) further reduced freeze-drying stress, although there was still a slight (7%) size increase and higher PDI. The random close packing model (sucrose to NP ratio of 0.82:1) was shown to achieve full protection, and an identical size distribution was obtained upon reconstitution of lyophilized formulation (Figure 40). Higher ratios were all equally effective.

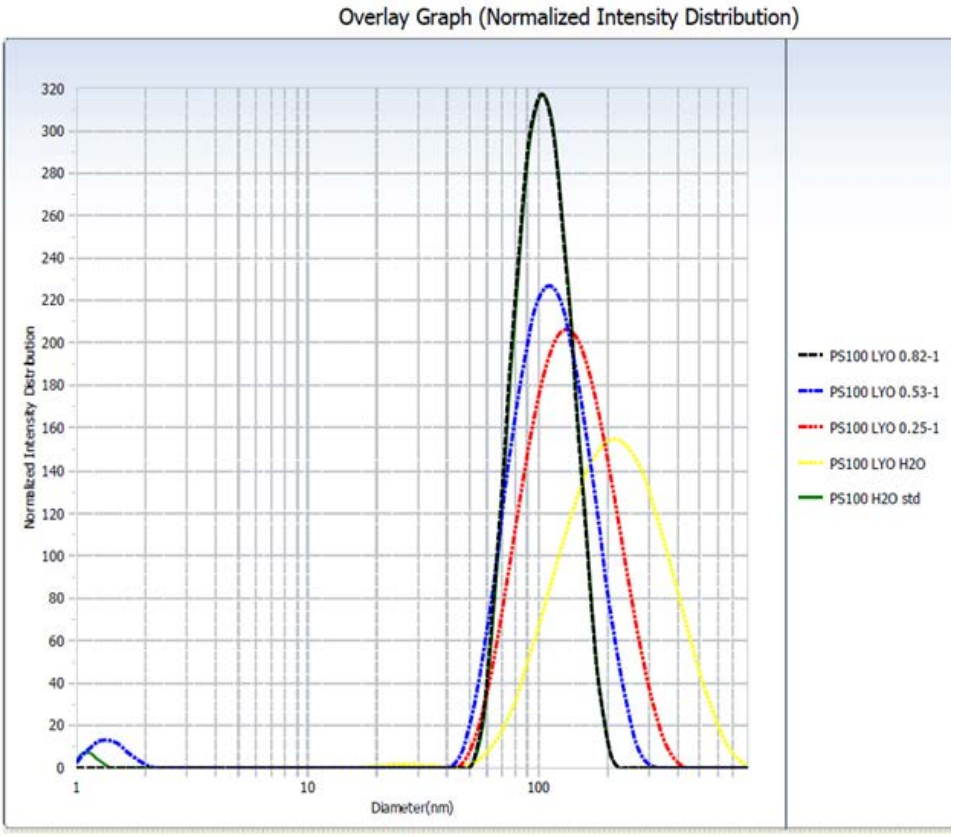

Figure 2-39. Size distribution of 100 nm carboxylate PS NPs after lyophilization with various weight ratios of sucrose to NPs: original size distribution before freezing (green curve), lyophilized in water (yellow curve), inadequate sucrose formulation (0.25:1, red curve), Kepler dense packing model (0.53:1, blue curve) and random close packing model (0.82:1, black curve)

No	Data	Diameter(nm)	Polydispersity Index	D (10%) (nm)	D (50%) (nm)	D (90%) (nm)
1	PS200 LYO 0.82-1	186.9	-0.009	150.6	183.8	225.0
2	PS200 LYO 0.53-1	202.8	0.095	127.4	205.2	334.0
3	PS200 LYO 0.25-1	301.4	0.263	156.5	284.3	534.9
4	PS200 lyo H2O	1071.6	0.429	187.9	612.1	21607.3
5	PS200 H2O STD	188.7	-0.008	152.9	185.8	226.2

Table 3. Size distribution of 200 nm carboxylate PS NPs after lyophilization with various weight ratios of sucrose to NPs

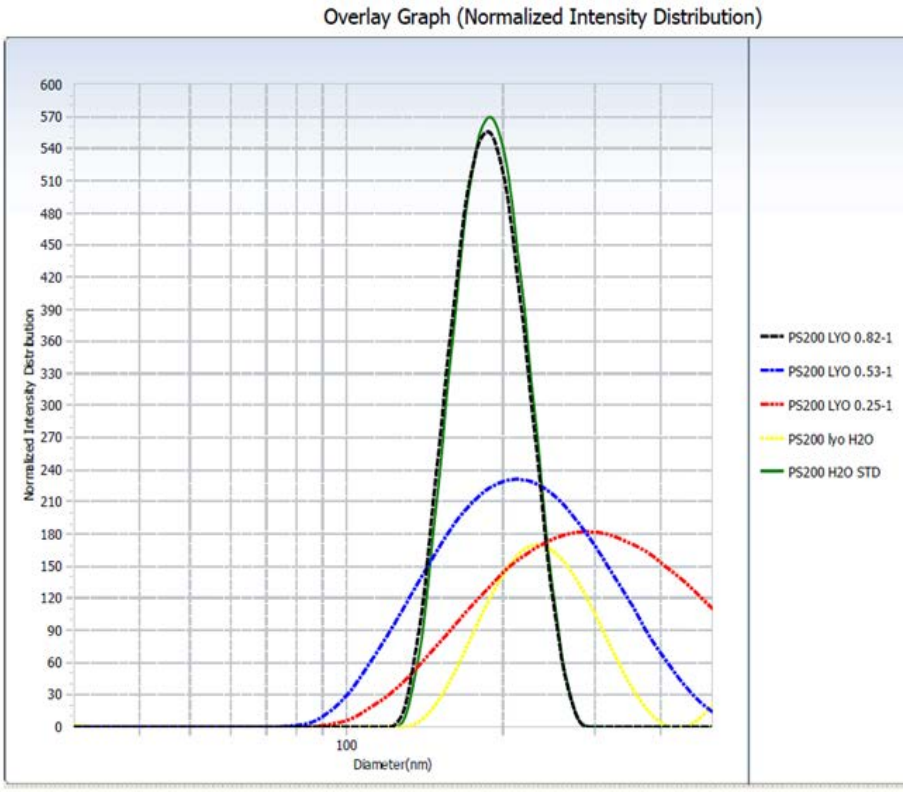

Figure 2-40. Size distribution of 200 nm carboxylate PS NPs after lyophilization with various weight ratios of sucrose to NPs: original size distribution before freezing (green curve), lyophilized in water (yellow curve), inadequate sucrose formulation (0.25:1, red

curve), Kepler dense packing model (0.53:1, blue curve) and random close packing model (0.82:1, black curve)

2.5 Discussion

In this project, the stages of freeze-drying processes were systematically investigated, including the initial *in situ* freezing by real-time microscopy, frozen samples by cryo-SEM, and final lyophilized cake by confocal imaging. The visual documentation firmly established the relationship between NP freeze-concentration and freezing stress. Freeze-concentration of NPs resulted in close physical contact, and aggregation ensued for NPs with susceptible surface chemistry. In our study, the geometric pattern of paralleled linear freeze-concentrate was generated, providing an explanation for the idiosyncratic morphology of the "fibrous" aggregates from unprotected NP formulation under fast cooling rate freezing. The freeze-concentrate morphology was reflected in the cake internal structure as well.

Most importantly, it was through the cryo-SEM study that the particle isolation hypothesis was corroborated. Sucrose will phase-separate from water into interstitial space during ice crystallization, forming a buffering zone. Discrete NPs were separated from each other and embedded in the glassy matrix comprised of the cryoprotectant (Figure 41). In addition, this visualization data provided explanation for the observed NP mobility in the interstitial space immediately before ice thawing. When the temperature was increased past the glass transition temperature Tg' of the maximally frozen freeze-

concentrate, the glassy sucrose matrix likely converted to the rubbery state. There was a step change in the viscosity of the interstitial space as evident by the increase in the NP mobility. As the temperature continued to approach the freezing point of water, water molecules began to migrate into the amorphous sucrose domain, further depressing the Tg' of interstitial space and increasing the fluidity of interstitial space as shown by NP mobility. Eventually, sucrose dissolved into aqueous medium and the viscosity of interstitial space was reduced drastically in a short period of time. Consequently, NPs could re-disperse spontaneously as individual particulates with ice melting.

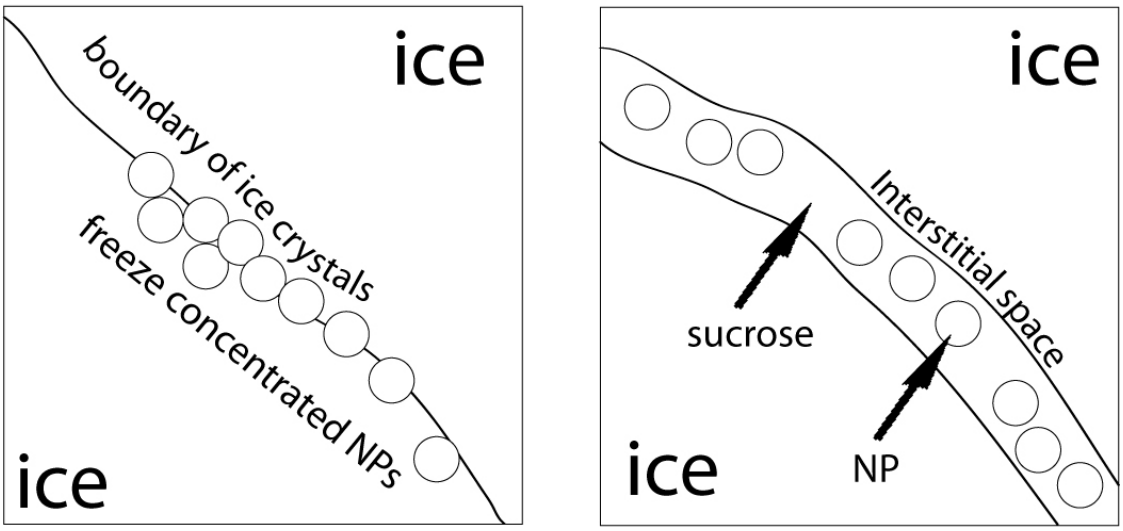

Figure 2-41. Schematic of NP freeze-concentration and cryoprotectant interstitial space

Previously, the concept of critical freezing temperature was proposed to prevent NP freezing stress. It was observed that slower cooling rate generated more severe aggregation of nanocrystal dispersion compared to extremely fast cooling rate (87).Theoretically, in the extreme scenario of fast cooling, the formation of amorphous

frozen water molecules is favored at freezing temperature below -140°C so that free NPs could be immobilized in the vitreous water network instantaneously. However, for pharmaceutically relevant processes, it is inevitable to conduct freeze-drying above the glass transition temperature of water. As a result, the initial vitreous water will eventually re-crystallize and exert stress on NPs. In other words, the attempt to circumvent the freezing damage cannot resort to extremely low temperature freezing, but can only be derived from the addition of a proper cryoprotectant.

In addition to the discovery of NP freeze-concentration in the bulk dispersion, there were other interfacial sites for NP enrichment. Our cryo-SEM also uncovered a key phenomenon of preferential accumulation of NPs in air-liquid interface within a bubble. This observation was reminiscent of 'pickering emulsions', in which microparticles and nanoparticles could act as emulsifying agents to stabilize an emulsion (87, 88). Particles with reasonable amphiphilicity could preferentially align at the water-oil interface, effectively lowering the surface tension. PLGA polymer by itself is hydrophobic. PLGA NP dispersion in water has negative charge at the electrical double layer (Zeta potential ≈ -30mV). To this end, PLGA NPs demonstrate reasonable amphiphilicity to be a particulate surfactant. It was also broadly recognized that particles have a tendency to adsorb to the air-liquid interface (89). In particular, during industrial processing, mixing, pumping and filling are all involved with creating bubbles. The accumulation and entrapment of particles at the air-liquid interface can be conducive to subsequent flocculation underneath the air-liquid interface. Our observation raises the question

regarding the role of air-liquid interface as a destabilizing locus for NPs. Caution should be exercised especially for colloidal dispersions subject to downstream freezing treatment. It had been shown that inclusion of a surfactant in virus-like particle formulation significantly improved the activity of virus like particles after freeze-drying by competing for container surface and air-water interface (90, 91). However, it's impossible to determine the timing of NP aggregation at the air-liquid interface from this study due to the ice crystallization cryo-SEM protocol as opposed to the vitrification protocol. The occurrence of NP clustering could be already existent at pre-freezing phase. Clustering could also be attributed to the freezing phase, during which propagating ice crystals at air-liquid interface squeezed NPs into isolated island of NP clusters. Nonetheless, formulation scientists should be cognizant of the air-liquid interface as a major locus for aggregation risk.

By inspecting the cake, it was found that a layer of NPs was enriched at the top surface of the formulation, which may have two possible origins. The first origin is attributable to the freezing driven event. Namely, in light of the ice crystal growth direction, this top layer of NPs was propelled by the last segment of ice crystal's upward propagation. The freeze-concentrated NPs perched on top of the outermost portion of the formulation. The second possibility could be attributed to drying driven event. That is, the freeze-dried top layer functions as a filter for discrete NP "blowout" from underneath. During freezing, some NPs can be immobilized as discrete individual NPs, which may not be well incorporated into freeze-concentrate space. Due to their light weight and lack of

embedding excipient in the surrounding, blowout could occur so that standalone NPs move upwards until entrapped by the uppermost layer. To this end, slower cooling rate may be preferable in that more thorough freeze-concentration could occur, ensuring more close association of NPs with sugar based cryoprotectant.

In the presence of disaccharide based cryoprotectant, interstitial spaces emerged between ice crystals. Despite the freeze-concentration of NPs, effective cryoprotectant prevented freezing damage by offering sufficient matrix to encapsulate NPs. A minimal amount of sugar protectant was needed to provide adequate buffering space so as to isolate discrete NPs from each other. Modeling based on sphere close packing and void space delineated the lower boundary of disaccharide cryo-/lyoprotectant design space. The modeling work was premised on our imaging findings. The closely compacted NPs in the freeze-concentrated cluster were reminiscent of the sphere packing issue (92). Mathematically, the volume ratio of NP clusters in relation to the surrounding sugar matrix amounts to the correlation between packed spheres and void fraction of the sphere close packing problem. Along the same line, the particle packing density within the sucrose interstitial space also relied on the weight ratio of sugar over NPs. With the proposed formula, minimal amount of effective cryoprotectant could be deduced readily for distinct particle systems such as PLGA NPs, PS NPs, gold particles, silica particles and iron oxide particles provided the density of the particles and cryoprotectant are known. On the other hand, the hypothetical scenario of sugar coating model is based on the hydrogen binding approach and predicted to be most applicable to the top surface enriched NPs layer,

which is located at the interface between vial air headspace and the top surface of the freeze-dried cake. The freeze-concentrated region at top surface is open-ended in comparison to the confined space of internally freeze-concentrated region in the frozen bulk solution. In the open-ended space, NP packing could be loose compared to the confined space scenario where the mechanical compression led to jamming of NPs. Moreover, there are additional rationales to justify the inquiry of "sugar-coating model" on top of the particle isolation benefit. First of all, for the core-shell construct of nano vehicle (93, 94), a sugar layer with reasonable thickness covering the entire length of corona could prevent the entanglement of long polymer chains of the shell layer on adjacent particles during both freezing and drying stages (95). Secondly, the coated sugar layer could protect the surface conjugated protein molecules such as an antibody during freeze-drying. Functional proteins are being increasingly incorporated onto nanomedicine platform to diversify the innovative applications. Both targeting moieties and immobilized enzyme have been combined into nanomedicine carrier (96, 97). It is well established that the vast majority of proteins could suffer irreversible conformation change when the water environment is stripped away (98-100). It's safe to predict that in the absence of an effective cryo-/lyoprotectant, the bioactivity of such surface molecules will likely decrease. Moreover, another noteworthy pattern observed in the cryo-SEM samples was that the width of the interstitial space was closely related to the diameter of the confined NPs, indicative of the encountering of two growing ice crystals stalled by the presence of NPs. Even if the compression has no direct impact on NP aggregation, the direct contact with ice interface could have a deleterious effect on the surface conjugated

protein (101). In this regard, inclusion of proper cryo-/lyoprotectant in the formulation is almost imperative to maximize the functionality of surface conjugated protein moiety.

Our modeling attempt dealt solely with an amorphous cryoprotectant system. As for a partially crystalline formulation, the extrapolation of the modeling results to sucrose-mannitol binary system should be interpreted with caution. Mannitol is a popular bulking agent that imparts excellent mechanical strength and easily produces a pharmaceutically elegant cake (102). It has been shown that the primary drying could even be operated at a significantly higher temperature than the Tg' of protective amorphous component because mannitol provides structure to tolerate the increased mobility of amorphous component during primary drying. During the initial freezing event, both sucrose and mannitol will phase-separate from ice as amorphous mixture into the interstitial space (103). Hence, annealing at higher temperature was necessary to increase carbohydrate mobility to fully convert the kinetically trapped amorphous mannitol into crystalline mannitol. This secondary phase-separation between amorphous sucrose and crystalline mannitol is bound to alter the organization of interstitial space and have an impact on the embedded NPs. Consequently, the predicted minimal weight ratio of amorphous sucrose over NPs may not be appropriate in a partially crystalline system and warrants further investigation.

For future study, the freeze-concentration of NPs in complex formulations requires further elucidation. NPs for diagnostic and therapeutic purposes are routinely decorated

with bio-molecules, which entail special formulation design in terms of the pH and ionic strength of the buffer system. The choice of buffer system is equally critical with respect to the NP zeta potential and colloidal stability. Polymers such as PEG and surfactants are commonly utilized to stabilize NPs (104). The impact of freeze-concentration on proteins, salts and polymers is well documented. It was recognized that during freezing, pH of sodium phosphate buffer changed significantly as a result of differential propensity of ion species to precipitate (105). The freezing triggered pH shift was dependent upon the initial pH and activity of precipitating salts (106). On the other hand, phase separation of polymers such as PVP and dextran during freeze-concentration is known. So was the effect of sugar and certain salts on inhibiting the phase separation of polymers (107). Thus, the interaction between various excipients and NPs during freeze-concentration warrants further investigation.

In summary, time-lapse microscopy was used to monitor the NP freezing behavior in real time. The technique can be adopted to streamline the formulation design for novel nano drug delivery carriers. High resolution imaging with cryo-SEM gave credence to the particle isolation hypothesis and improved the mechanistic understanding of cryoprotection for particulate systems. Confocal imaging technique provided superior imaging of internal structure of the final lyophilized cake. This chapter of the thesis attempted to address several key questions concerning the lyophilization of nanoparticulate systems, which should be useful in formulation design and lyophilization cycle development for both translational research and manufacturing of NP products.

Chapter Three: High Volume Intradermal Delivery of Polymeric Nanoparticles Using the Hollow Microstructured Transdermal System

This chapter involves the delivery of PLGA nanoparticles to the skin by a hollow microneedle system. We show that the approach allows precise delivery of a relatively large quantity of nanoparticles into the dermal space, which has potential for improving immune response to nanoparticle-based vaccine formulations.

3.1 Introduction

The fabrication of microneedles was originally conceived in 1950s. But only in the last decade has advancement in engineering and fabrication technology occurred that can allow development of safe and effective microneedle-based drug delivery systems (108). Compared to the conventional syringe needle, the microneedle has a miniaturized dimension that can diminish needle phobia in patients. The insertion depth is sufficiently shallow to avoid impinging innervated tissue, resulting in a painless injection (109). The smaller size and the associated engineering features also enable streamlined vaccination logistics including non-cold chain distribution, self-administration, mitigated sharps waste disposal and reduced needle-stick and re-use risks (110). Importantly, microneedle technology has displayed benefits such as dose-sparing vaccine delivery and unique capability of targeting dermal-resident immune cells (111, 112).

A plethora of research has documented the multifaceted advantages of nanoparticles (NPs) as diagnostic, drug and vaccine delivery systems (113-115). However, the optimal delivery mode and route of administration of NPs remain open questions for many disease states. Because the stratum corneum is only permeable to lipophilic drugs with molecular weight less than 400 Da (116), trascutaneous delivery of NPs has been deemed impractical. However, the application of microneedle technology presents an opportunity to facilitate the transdermal transport of NPs. Pretreatment with solid microneedles significantly increased the skin permeability to NPs by perforating the skin barrier (117); nevertheless, with this approach, less than 20% of DNA coated PLGA NPs traversed the skin in eight hours. NPs have also been coated onto the microneedle surface for direct delivery with skin penetration (118). Embedding in dissolvable solid microneedles constitutes another strategy (119), which involves release of NPs with dissolution of inserted microneedles.

The above studies relied on the use of solid microneedle systems, which have inherent limiting factors. For example, the intrinsic coating and encapsulation capacity of solid microneedles limit the delivery capacity. In the case of microneedle-pretreated skin, the enhanced permeation effect was more pronounced for negatively charged NPs than positively charged NPs (117). This dependency on the particle surface charge reduces the general applicability of microneedle mediated NP delivery. Moreover, the manufacturing

and coating processes can cause NP instability, requiring special optimization and adaptation for each specific NP system.

In the current study, we investigated the hollow microstructured transdermal system (hMTS; 3M) for intradermal NP delivery. As the name implies, hMTS comprises a hollow microneedle array that can deliver up to 2 mL liquid formulation into the skin. The detailed specifications of the prototype device was described by Burton, et al (120). The drug delivery mechanism involves convective mass transport driven by liquid delivery. This is inherently appealing for efficient transcutaneous NP delivery. There is theoretically no particle surface charge dependency or diffusion-limiting behavior with the pressure driven convective release of liquid. No special formulation adaption is needed, allowing delivery of any aqueous NP dispersion. Finally, the technology allows for complete delivery of the 2 mL volume at a range of delivery rates, allowing for the delivery of the entire dose in a short time.

We evaluated the use of hMTS to achieve high volume intradermal delivery of PLGA NPs in a rat model. To our knowledge, this is the first characterization of PLGA NP disposition with hollow microneedle assisted dermal delivery. The analysis focused on the local retention and systemic exposure, and the results formed the basis of developing a vaccine formulation. With vaccine administration, the resulting profiles of the humoral and cellular immune responses were compared to that resulting from conventional intramuscular (IM) injection. Given the promising results, this novel modality of

intradermal delivery for NPs could open up new avenues to improve NP-based sentinel lymph node mapping and *in situ* manipulation of the tumor microenvironment and the tumor draining lymph nodes using NPs loaded with immunomodulatory agents.

3.2 Method and Materials

3.2.1 Fabrication of PLGA NPs

Coumarin-6 loaded PLGA NPs were synthesized using the method reported in the previous chapter (Page 26). Immunostimulatory nanoparticles (ISNPs) were formulated using emulsion-solvent evaporation technique. One mg of imiquimod (Sigma-Aldrich) was weighed and dissolved in chloroform. The glass vial was subjected to 10 minutes of heating at 60°C in a water bath to facilitate the dissolution of imiquimod. Monophosphoryl Lipid A (MPL-A *Salmonella enterica* serotype Minnesota Re 595, Re mutant) (Sigma-Aldrich) was prepared as a 2 mg/mL stock solution in 80% chloroform/20% methanol. To the chloroform solution of containing imiquimod, 100 mg of PLGA and 200 μg MPL-A were added. An emulsion was formed with 8 ml of 2.5% polyvinyl alcohol (PVA) aqueous solution (87%-90% hydrolyzed, 30,000-50,000 Da, Sigma), and the dispersion was sonicated (20 W for 5 minutes) with a tip sonicator (Misonix Sonicator 3000) on ice bath. This emulsion was then stirred for 18 hrs at ambient conditions in a chemical hood followed by another hour under vacuum to completely remove chloroform. NPs were recovered by ultracentrifugation (Optima

XPN-80 ultracentrifuge, Beckman Coulter) at 35,000 rpm for 35 min at 4 °C and then washed three times with endotoxin free water.

Ovalbumin (OVA) loaded NPs were produced using a double emulsion-solvent evaporation technique. PLGA (100 mg) was dissolved in 1 ml of chloroform. OVA (5 mg) was dissolved in 200 μL PBS and added into PLGA chloroform solution. A primary emulsion was created by sonicating the mixture at 5.0 power setting (~15 W) for 30 seconds. A secondary emulsion was then generated in 8 ml of 2.5% PVA solution under sonication (20 W for 5 minutes) on an ice bath. This emulsion was stirred for 18 hours at ambient conditions and then for 1 hour under vacuum. NPs were recovered by ultracentrifugation (35,000 rpm for 35 minutes at 4°C) and then washed three times with Hyclone^{TM} endotoxin-free, cell culture grade water (Thermal Scientific). OVA loading in NPs was characterized by dissolving PLGA NPs in 0.1 N NaOH for bicinchoninic acid assay (Pierce™ BCA Protein Assay Kit, Thermo Scientific) with an OVA-based standard curve ranging from 2 mg/mL to 25 μg/mL concentrations.

An *in vitro* release study was conducted in PBS supplemented with 0.05% NaN_3 at 37°C in an oscillatory shaker. One mL of NP suspension in the release buffer was collected at each time point. NPs were separated from release buffer using an ultrafiltration centrifugal tube with molecular weight cut-off value of 50,000 Da (Millipore). NP-free release buffer was collected and freeze-dried. Reconstitution in smaller volume was

applied to achieve concentrated OVA samples. Released OVA was quantified by BCA kit.

3.2.2 Biodistribution study of intradermally delivered PLGA NPs using hollow microneedle array

Crl:CD(SD) rats were used to study the biodistribution of PLGA NPs following various routes of administration. Rats were anesthetized by isoflurane. Hair on the flank of the rats was clipped and the shaved site was wiped clean. Intradermal delivery was enabled by a plastic, hollow microneedle array with 18 microneedles (900 microns needle length) manufactured by 3M (St Paul, MN). The hollow microneedle device used in this experiment was comprised of a needle array, microfluidics chamber, tubing connection and adhesive ring (Figure 3-1). The hollow microneedle array was mounted onto a hand-held applicator (120). The skin in the flank region was stretched and backed by a plastic block platform to flatten the skin against a solid substrate. The microneedle array was applied to the skin by triggering the actuator of the applicator. Insertion of the needle array into intradermal space was achieved due to the forceful ejection from the spring-driven applicator. The attachment of the device onto rat skin was maintained by an adhesive ring. Two slices of adhesive tape were used to reinforce the device attachment during the entire course of delivery (Figure 3-2). Five mg of coumarin-6 loaded PLGA NPs in 1 mL 5% dextrose solution (D5W, USP) was delivered intradermally. The delivery was conducted at constant rate of 4 mL/hour via a programmed syringe pump.

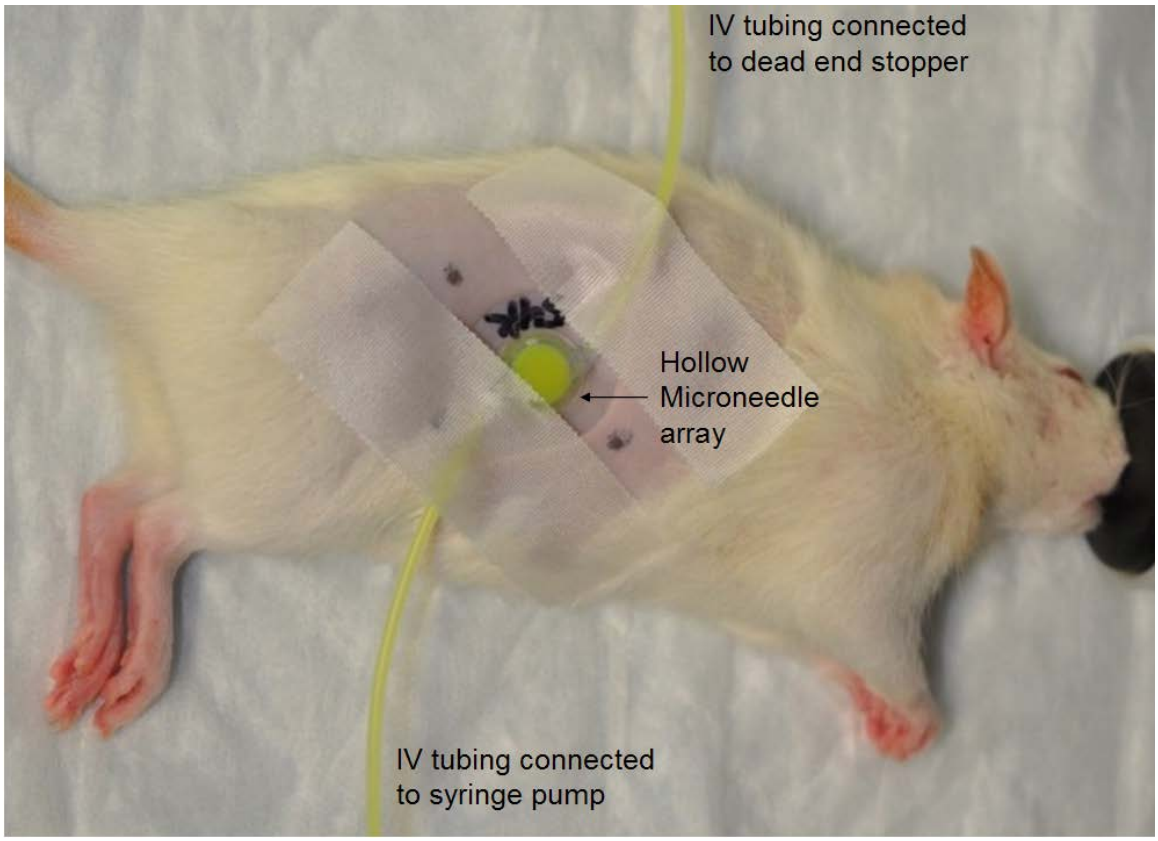

Figure 3-1.Set-up used for intradermal delivery of PLGA NPs via hollow microneedle array

Figure 3-2. The attachment of hollow microneedle array on rat skin.

At various times after delivery, blood was withdrawn by cardiac puncture into an anti-coagulation vial. The rats were sacrificed and the axillary lymph nodes, inguinal lymph nodes, liver, spleen, kidney, heart, lung, brain, pancreas and skin at infusion site were all collected. Organs were placed in borosilicate glass tubes on ice and weighed. Unprocessed organs were stored at -80°C freezer until processed. Deionized water was added into thawed organs to fully submerge the organ before homogenization (1 mL for lymph node samples and 3 mL for other samples). The organs were homogenized in glass tubes for 3 to 5 minutes using the Omni Tip^{TM} homogenizing kit equipped with plastic generator probes (Omni International). Homogenized tissue samples were pre-cooled in a refrigerator followed by freezing at -20°C freezer overnight and -80°C freezer for 1 hour before lyophilization. The gradient cooling was utilized to prevent the glass vial from

cracking due to the large volume of rat tissue sample and expansion during freezing. Homogenized samples were freeze-dried using a lab freeze dryer (FreeZone 4.5 freeze dry system, Labconco) for 48 hrs. The dehydrated samples were fragmented using a transfer pipette tip to facilitate extraction. Four mL of diethyl ether was added to the glass tubes, and the tubes were hermetically capped and placed on a rotary shaker at room temperature overnight. Following centrifugation at 2,000 rpm for 20 minutes, 2 ml of the supernatant was transferred into a microcentrifuge tube for secondary centrifugation at 13,500 rpm for 10 minutes. The supernatant (1.4 mL) was transferred into another microcentrifuge tube for solvent evaporation in a 50°C water bath. The residue was reconstituted with 1 mL methanol by vortexing. For HPLC analysis of coumarin-6, the mobile phase consisted of acetonitrile (ACN) and sodium 1-heptanesulfonate aqueous solution (1 g/L, 0.0045M/L), which was run in the isocratic mode at 75 : 25 ratio and a flow rate of 1 mL/min. The retention time of coumarin-6 was about 6 minutes. 1-heptane sulfonate was used to assist ion-pair chromatography. The ion-pair interacts with reverse-phase column for separation and sharp HPLC peak. A Beckman Coulter HPLC system, (Fullerton, CA) equipped with System Gold 125 solvent module, System Gold 508 auto-injector, FP-2020 plus fluorescence detector (JASCO Inc., Easton, MD) and a C-12 Synergi MAX-RP column (4.6 × 150 mm; 4 μm particle size, Phenomenex), was used. Two mg coumarin-6 was weighed in a microcentrifuge tube and dissolved in 1 mL chloroform to give a 2 mg /mL (2 μg/uL) stock solution. This stock solution was serially diluted to obtain the standard solutions that were used to generate a standard curve.

3.2.3 Generation of bone marrow-derived dendritic cells (BMDCs)

Wild type C57BL/6 mice (6 to 12 months old) were euthanized by carbon dioxide asphyxiation. The hind leg region was disinfected by spraying 70% ethanol. Leg bones from the hip joint were separated, and the muscle and associated connective tissue was surgically removed. The intact mouse tibia and femur bones were disinfected by submerging into 70% ethanol for 5 minutes on ice. All remaining procedures were carried out under sterile conditions. Mouse leg bones were transferred into laminar flow cell culture hood. Tibia and femur bones were rinsed twice with cold PBS buffer and cut open at the both ends to access the bone marrow. Mouse bone marrow precursor cells were flushed from tibia and femur by injecting PBS buffer using a 25 gauge needle inserted into the bone lumen. Bone marrow was transferred into a sterile cell strainer with 70 micron Nylon Mesh (Fisherbrand, Fisher Scientific). Rubber syringe plunger was used to gently dissociate the bone marrow tissue. The single cell suspensions were diluted with PBS and centrifuges at 1,000 rpm for 7 minutes. One mL of Hybri-Max™ Red Blood Cell Lysing Buffer (Sigma-Aldrich) containing 8.3 g/L ammonium chloride in 0.01 M Tris-HCl buffer was added into the pellet to eliminate erythrocytes through osmotic shock. The pellet was gently mixed for 1 minute followed by dilution with 20 mL PBS buffer. This was repeated, if complete RBC lysis was not achieved. Alternatively, red blood cells could also be eliminated via brief exposure to pure water treatment using endotoxin free cell culture grade water for 10 seconds. Precursor cells were cultured in 100 X 15 mm untreated Petri Dish (BD Falcon) at 1X 10^6 cells/mL density within RPMI 1640 medium supplemented with 10% FBS, 20 ng/mL granulocyte-

macrophage colony-stimulating factor (GM-CSF) (PeproTech, Rocky Hill, NJ) and 50 μM 2-mercaptoethanol (Sigma-Aldrich, St. Louis, MO) for 6 days to generate immature BMDCs. Medium was changed once at Day 3.

3.2.4 Flow cytometry for BMDCs treated with NPs

Aliquots containing one million BMDCs were placed in a 24-well cell culture plate. For NP treatments, blank PLGA NPs or ISNPs were added to the BMDCs at 0.2 mg/mL final concentration for 24 hours. At the end of the incubation, all the cells were collected including adherent cells, which were dislodged by 5-minute treatment with non-enzymatic cell dissociation solution (Sigma-Aldrich, St. Louis, MO) to preserve the cell surface markers. BMDCs were dispensed into assay tubes and washed twice with PBS before incubation with 100 μL FACS buffer (1X PBS buffer supplemented with 1% BSA and 0.05% sodium azide) at 4°C for at least 10 minutes to block non-specific binding. FcγIII and FcγII receptors on BMDCs were blocked by incubating with FACS buffer supplemented with rat anti-mouse CD16/CD32 (Mouse BD Fc Block™) for 5 minutes to prevent non-specific antibody binding via Fc receptors. Subsequently, dual staining for BMDCs was carried out by pairing a PE labeled hamster anti-mouse CD11c antibody (Clone: HL3) with another FITC labeled antibody against co-stimulatory markers, such as FITC-labeled rat anti-mouse CD86 (Clone: GL1) or FITC-labeled rat anti-mouse CD40 (Clone: 3/23) or FITC-labeled rat anti-mouse I-A/I-E (Clone: 2G9) on ice for 30 minutes. Antibody isotype control tube was stained with FITC-labeled rat IgG2a, Kappa isotype control and PE-labeled hamster IgG1, Lambda 1 isotype control. Stained cells

were washed twice with 2-3 mL FACS buffer and then suspended in 0.5 mL FACS buffer for data acquisition on BD FACSCalibur flow cytometer. The first gate encompassed the major population cluster based on forward scattering (cell size) and side scattering (cell internal granularity). Compensation was conducted with single stained mature BMDCs cells. The BMDCs were further gated for CD11c positive population. Flow cytometry data were analyzed by FlowJo software.

3.2.5 Vaccination protocol

Two doses of vaccine (prime and boost) were administered to Crl:CD(SD) rats three weeks apart either by intramuscular (IM, hind leg thigh muscle) injection using conventional syringe or by intradermal (ID) delivery using the hMTS microneedle array. All the formulations used for the priming vaccination dose contained 2 mg of ISNPs loaded with both the TLR4 agonist MPL-A and the TLR7 agonist imiquimod as the adjuvant. Antigen was given either in the form of soluble OVA solution or OVA encapsulated PLGA NPs at an equivalent dose of OVA (16 μg). The booster vaccination dose only contained 10 μg OVA in the form of either soluble OVA or OVA loaded NP. There was no ISNP adjuvant component in the booster dose. Blood collection was carried out three weeks after each dose. Aliquots of serum were frozen at -80°C freezer until subsequently assayed. Spleens were harvested at the end of the experiment (three weeks after the booster dose) for splenocyte isolation.

3.2.6 The enzyme-linked immunosorbent assay (ELISA) for serum antibody response

Immulon® 2 HB (Thermo Scientific) is a clear polystyrene microplate optimized for antigen-down ELISA study. The surface chemistry of Immulon® 2 HB is suitable for probing serum samples to mitigate non-specific immunoglobulin binding, while maintaining reasonable capacity for satisfactory antigen coating. During manufacturing, the surface of Immulon® 2 HB is treated with corona discharge irradiation processes to generate high-energy oxygen ions that could be incorporated into the polystyrene polymer chain, conferring hydrophilicity to the plate surface. Unlike more hydrophobic Maxisorp plate specially designed for high antibody binding capacity (600 ng IgG/cm2), Immulon® 2 HB plate exhibits intermediate hydrophobicity and IgG binding power (400 ng IgG/cm2). Since this study employs an ELISA format with antigen-coated plate and sera samples, we choose Immulon® 2 HB microplate to optimize the signal to noise ratio of this ELISA study. The pI value of OVA is approximately 4.5. The universal ELISA bicarbonate-carbonate based buffer at pH 9.6 was used as the coating buffer; under which OVA exists as negatively charged protein. Presumably, a combination of both hydrophilic and hydrophobic interactions plays a major role in the passive adsorption of OVA onto the surface of Immulon® 2 HB microplate. To create 1,000 ml of a 0.05M bicarbonate buffer solution, 3.2676 g sodium bicarbonate (0.0389 M $NaHCO_3$) and 1.176 g sodium carbonate (0.0111 M Na_2CO_3) were mixed in 1 L DI water. One or two drops of pure HCL were added for fine adjustment to pH 9.6 using a pH meter (Accumet Basic). Immulon® 2 HB Flat Bottom MicroTiter® Plates were coated with 10 μg/ml

OVA in pH 9.6 carbonated buffer (100 μl per well) overnight at 4°C in a moist chamber. Then the plates were washed three times with washing buffer (PBS with 0.05% Tween-20) the next morning. Non-specific binding was blocked by adding 200 □L blocking buffer (PBS with 1% casein) per well for 1 hour at 37°C. Serial dilutions of serum samples were done in 1% casein-PBS blocking buffer. Diluted samples were added to the wells and incubated (100 μL per well) for 1.5 hours at 37°C. Plates were washed four times with washing buffer. For urea ELISA, the washing protocol consisted of 10 minutes of washing with 7M urea followed by three more washings with ordinary washing buffer. Goat anti-rat IgG2a-HRP and goat anti-rat IgG1-HRP (AbD Serotec, Raleigh, NC) were diluted in blocking buffer and 100 μL of either solution was added to each well. Detection antibody was incubated at room temperature for 1.5 hours followed by washing four times. O-phenylenediamine (OPD) substrate (100 μL per well) was developed for 15 min at room temperature followed by addition of 100 μL stop solution (2M HCL). The optical density was determined using a ELx800 Absorbance Microplate Reader (Bio-Teck, Winooski, VT) and KCjunior software.

3.2.7 Surface plasmon resonance for OVA specific binding of serum antibodies

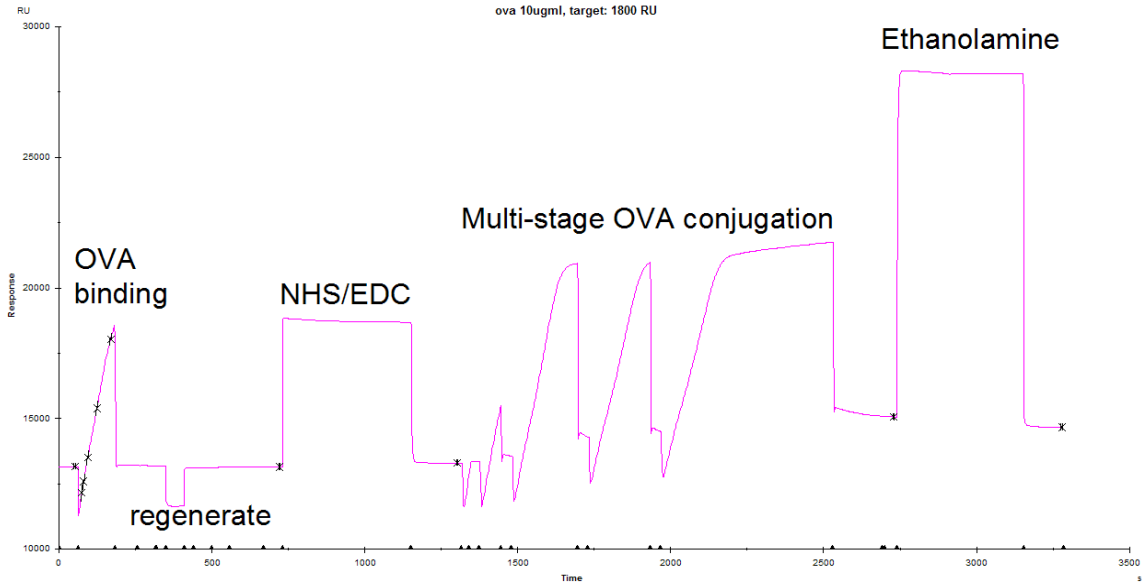

Figure 3-3. CM-5 chip surface preparation protocol that achieved 1500 response unit (RU) following OVA conjugation.

The SPR study was run on a Biacore 2000 instrument (GE healthcare). The built-in automatic immobilization method was used to prepare the surface of CM5 Biacore sensor chip (Figure 3-3). The pI of OVA is 4.5. Thus, OVA was dissolved in 10 mM acetate buffer (pH 4.2) at 10 µg/mL concentration to facilitate protein association with the carboxymethylated dextran matrix. The pre-concentration of OVA onto chip surface matrix increases conjugation efficiency. NHS-EDC was utilized to activate the chip surface. The immobilization protocol was programmed for1800 response units of OVA conjugation level via amine coupling. The extra free reactive NHS-ester groups were blocked by 1M ethanolamine. Pooled rat sera samples from each group were diluted in PBS buffer to 10 X, 20X, 30X, 45X, 67.5X dilutions. The assay was performed in direct

binding mode with an unconjugated blank channel as reference. Sample injection time was 2 minutes, and dissociation phase was 9.5 minutes at a flow rate of 30 μL/min. After each run, the chip surface was regenerated with 10 mM glycine-hydrogen chloride (pH 2.0) for 18 seconds followed by 10 mM glycine- hydrogen chloride (pH 1.7) for 12 seconds. The SPR data were analyzed with BIAevaluation 4.0 software.

3.2.8 ELISPOT assay for splenocyte IFN gamma response

At the endpoint of the vaccination study, rat spleens were collected with aseptic technique for cultured ELISPOT assay. Spleens were crushed using a plunger rubber end within a 70 micron cell strainer in a Petri dish. Splenocytes were pooled from rats that received the same vaccination treatment. The single cell suspension obtained was diluted with PBS buffer and centrifuged at 1,200 rpm for 7 minutes. Red blood cells were eliminated by brief exposure to endotoxin-free, cell culture-grade water for 10 seconds, followed by dilution with 30 mL PBS. If the erythrocyte lysis was incomplete, this step was repeated. Splenocytes were dispensed into 24-well cell culture plates at 3 million cells/mL density. Recall response was triggered by culturing splenocytes in the presence of 10 μg/ml OVA antigen in cell culture media for 6 days. One mL fresh cell culture medium was supplied at day 4. Rat IFN-γ ELISpot^{PLUS} kit (Mabtech, Cincinnati, OH) was used according to manufacturer's instruction. PVDF Elispot plate was pretreated with 70% ethanol briefly to assist wetting. Capture antibody for IFN-γ was coated by incubating the wells in 100 μL antibody (15 μg/mL in sterile PBS) overnight at 4°C in a

moist chamber. Splenocytes (6 X 10^5 per 200 μL) were added to wells for 24 hours in a 37°C 5% CO_2 incubator. Captured cytokine was detected by a biotin-labeled anti-IFN-γ antibody followed by addition of streptavidin-horseradish peroxidase (HRP). The spots were developed by 3,3',5,5'-tetramethylbenzidine (TMB) substrate and enumerated by a CTL ImmunoSpot plate reader (Cellular Technology Limited, Shaker Heights, OH).

3.3 Results

3.3.1 Intradermal delivery of PLGA NPs by hollow microneedle array

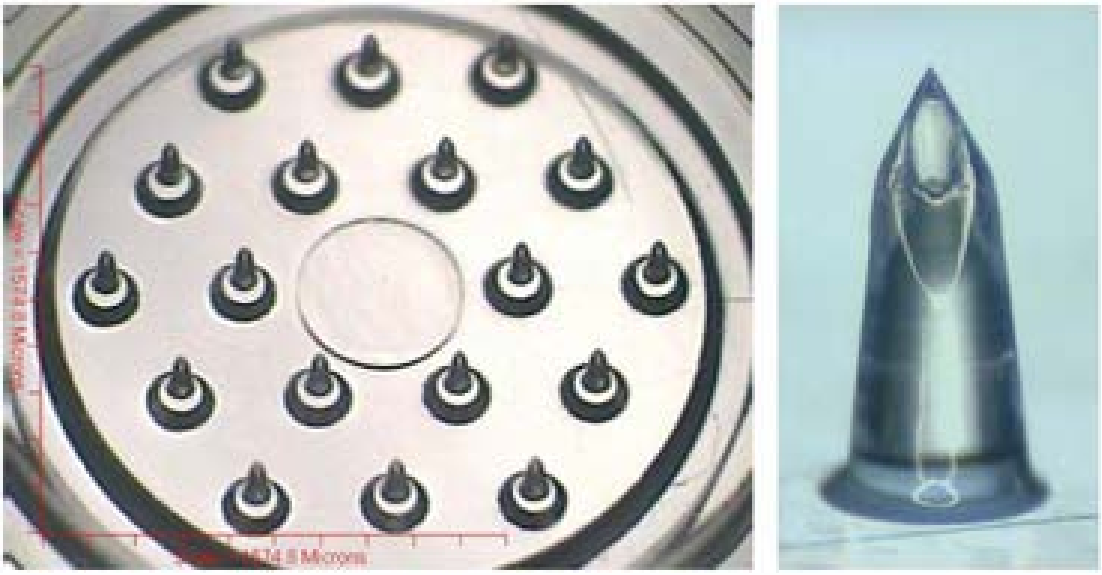

Figure 3-4. 3M's Hollow MTS and the hollow microneedle close-up.

3M's hMTS is shown in figure 3-4. Coumarin-6 was encapsulated into PLGA NPs at a loading of 5.47 μg/mg NPs (121). The average hydrodynamic diameter of coumarin-6

loaded NPs was 260.7 nm (Figure 3-5). The inner diameter of the mini-hypodermic needle was in the range of 10 - 40 microns.

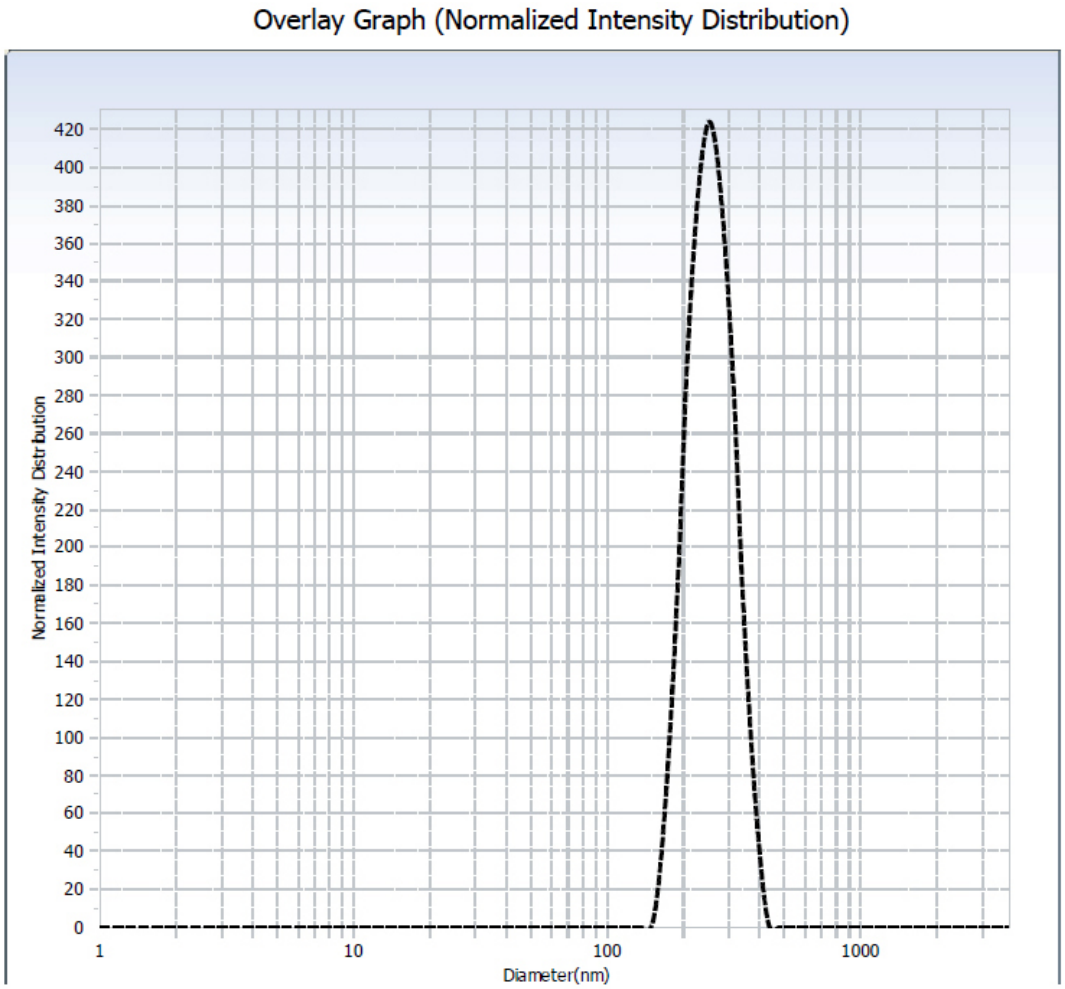

Ave. Diameter(nm)	Polydispersity Index	D (10%) (nm)	D (50%) (nm)	D (90%) (nm)
260.7	0.156	187.0	242.7	316.6

Figure 3-5. Size characterization of coumarin-6 loaded PLGA NPs by dynamic light scattering.

PLGA NPs dispersed at 5 mg/ml in 5% dextrose solution (D5W USP) was negatively charged with a Zeta potential of -6.75 mV. One mL of the formulation was administered at a constant rate over 15 minutes through hMTS. The back pressure of the syringe pump tended to increase primarily at the early phase of delivery. Nevertheless, the delivery was completed at a relatively stabilized high pressure thereafter. Upon removal of microneedle array, the imprint of the microneedles in the skin was visible (Figure 3-6). The injection site showed a wheal with a whitish boundary mirroring the dimension of the microneedle patch. But the wheal was different from the characteristic elevated bleb following Mantoux technique for manual intradermal injection (122). On the periphery, there was a larger circular imprint reflective of the skin contact with the adhesive ring. The geometric pattern of microneedles array design was reproducibly printed on the skin infusion site. Each individual needle generated a corresponding focal point with visible accumulation of NPs in the top layers of skin. In between those discrete focal points, there were diffusive patches of tracer NPs suggestive of intradermal diffusion and/or convective transport of NPs during the delivery phase. However, the distribution of these patches was not uniform.

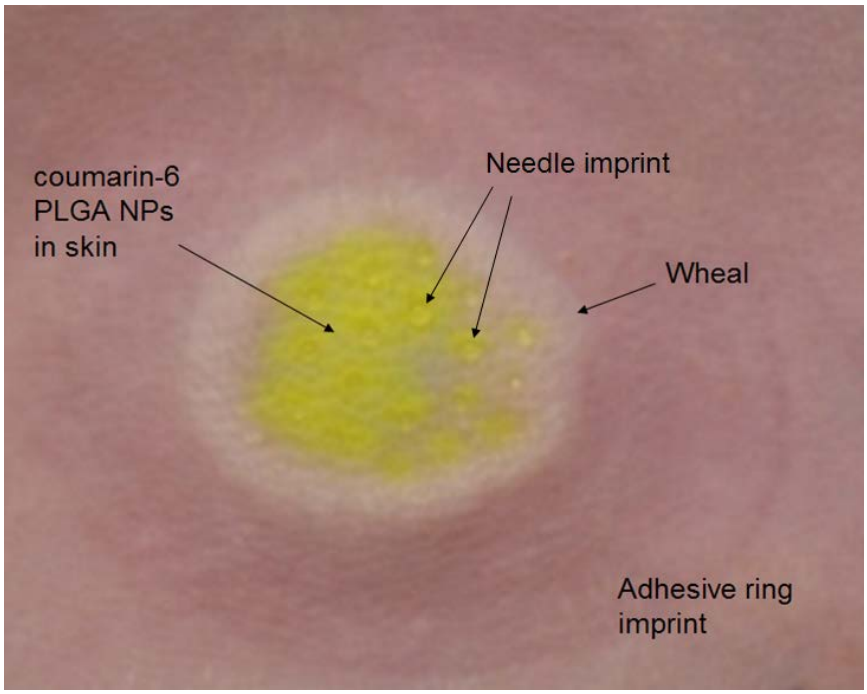

Figure 3-6. Picture of 5 mg fluorescent PLGA NPs delivered into rat skin immediately after hollow microneedle array removal.

Typically the skin surface was devoid of liquid immediately after microneedle array removal, indicating successful deposition of the entire NP dose directly into the epidermal and dermal layers of the skin. Occasionally, there was liquid residue (Figure 3-7), but once the moisture was removed by gauze, no liquid oozed from the injection site. The needles remained straight and intact with insertion and retraction.

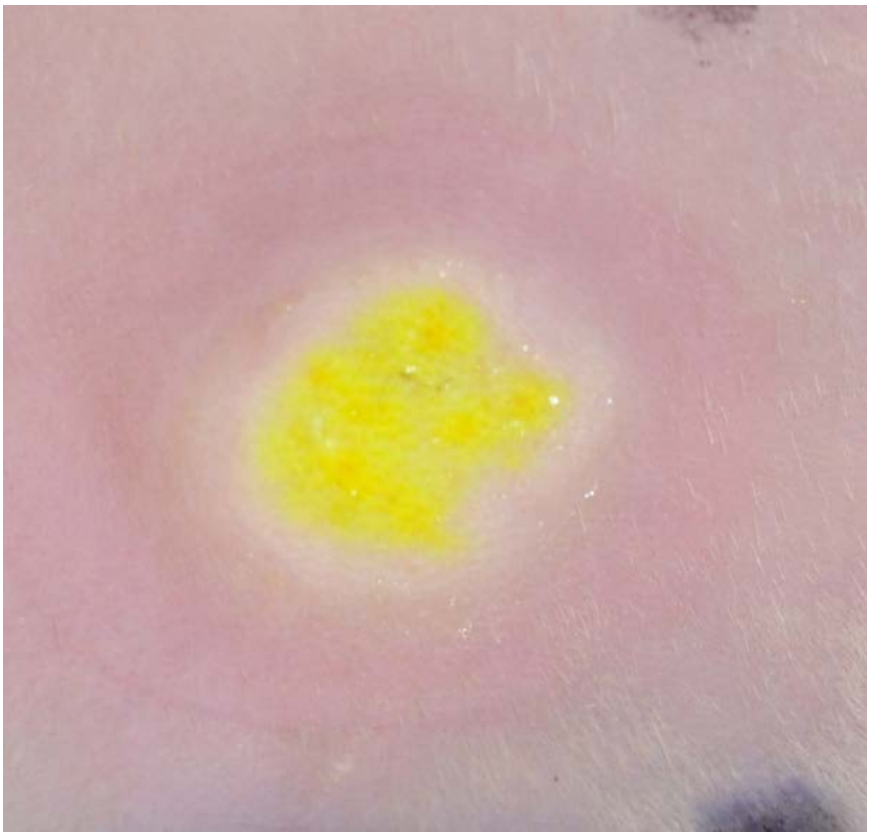

Figure 3-7. Representative picture of intradermal depot of 5 mg fluorescent PLGA NPs immediately after hollow microneedle array removal.

Skin harvested following necropsy had trace of the PLGA NP depot after 48 hours, but the size of the patch in the top layers of skin shrank significantly compared to 1-6 hours post-infusion. The diffusive pattern of the patch became more punctate at 48 hours. Underneath the injection site, there was a palpable swollen “pouch” like structure with edematous hydrogel texture at 1 hour, which largely resolved by 24 hours. NPs were visible in the enlarged hydrogel “pouch”.

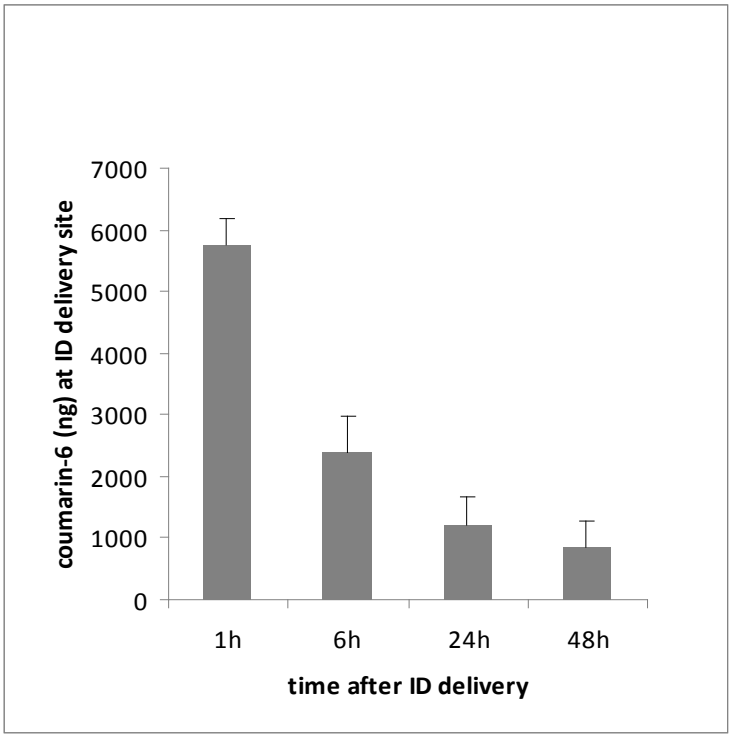

Figure 3-8. Sustained presence of PLGA NPs at the intradermal injection site.

Previously, the average depth of penetration for hMTS reached 600 μm in a pig skin model (120), which can be compared to the 800 μm thickness of the combined rat dermal and epithelial layers (123). Thus, the needle tip orifices were predicted to be located within the dermis. However, in this study, NPs not only reached the dermis but also the hypodermic domain. Analysis of the excised skin revealed that a significant amount of coumarin-6 was retained locally over at least 48 hours (Figure 3-8).

3.3.2 High volume intradermal delivery of NPs by hollow microneedle array generates a burst transit through draining lymph nodes

Previously, it was proposed that the intradermally delivered drugs gain access to the systemic compartment via lymphatic transport (120). In order to elucidate the role of lymphatics in the disposition of intradermally administered NPs, relevant lymph nodes were collected in relation to the intradermal infusion site. Rat axilla contains two sets of lymph nodes that provide lymph drainage for skin at the flank and upper trunk (124). For this study, the string of four axillary lymph nodes (ALN) and the string of three brachial lymph nodes (BLN) under the armpit were expected to be responsible for the superficial lymph drainage (Figure 3-9). In contrast, inguinal lymph nodes (ILN) drains superficial region of hind leg and buttock. ILN were collected as a non-draining lymph node control.

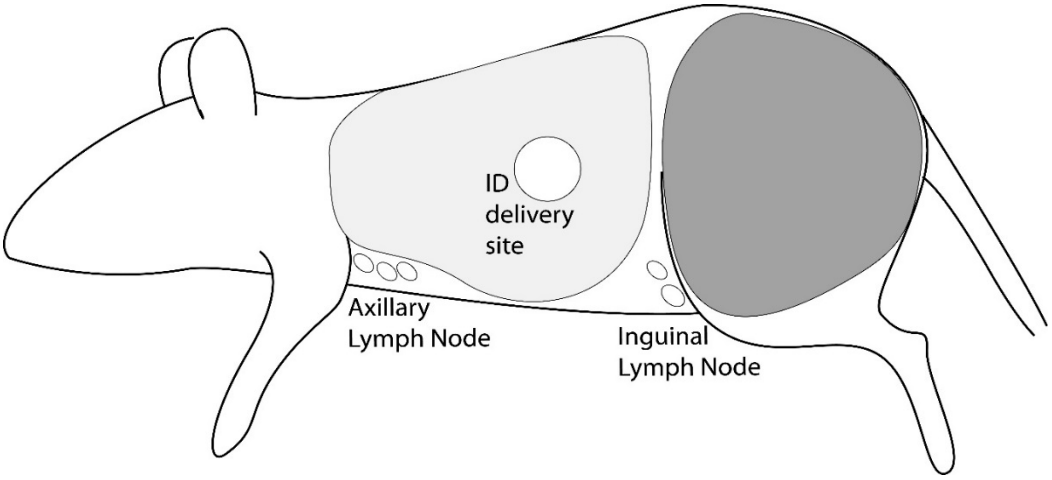

Figure 3-9. Map of draining lymph nodes for skin in rats (adapted from "Patterns of lymphatic drainage in the adult laboratory rat") (124). The axillary lymph node (ALN)

drains the light gray color region from the flank, while inguinal lymph node drains the dark gray color region.

Following intradermal administration, coumarin-6 concentration was significantly higher ($P<0.01$) in ALN than in ILN for early time points (both 1h and 6h) (Figure 3-10). At 1-hour, the coumarin-6 concentration at ALN was 88-fold higher compared to ILN control, suggesting the intradermally delivered agents were transported via its attendant draining lymph nodes as opposed to the irrelevant non-draining lymph nodes. No difference in ALN/ILN concentration ratio was observed with the IV delivery. This data provided direct evidence corroborating the critical role of draining lymph nodes in drug disposition via hMTS ID administration.

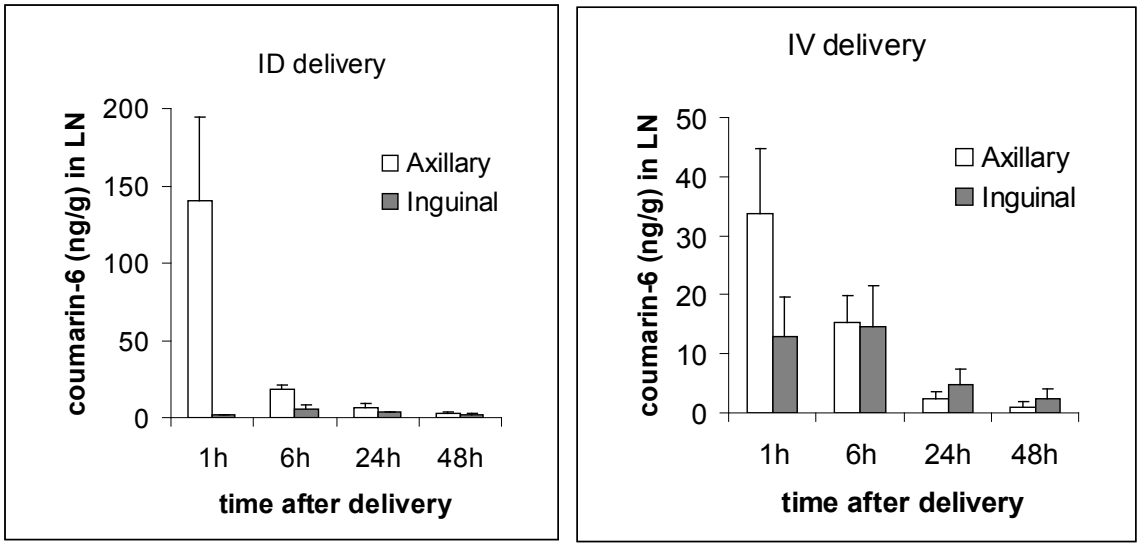

Figure 3-10. Coumarin-6 concentration normalized for ALN and ILN tissue weight after delivery of 5 mg PLGA NPs by ID or IV administration.

ID route of administration was also compared to the conventional subcutaneous injection. First, intradermal delivery of NPs resulted in significantly higher exposure in draining ALN in comparison to the non-draining ILN, confirming the central role of draining lymph node in the transport of hMTS delivered agents (Figure 3-11). Second, coumarin-6 concentration in ALN was 91-fold higher for the ID group than for the SQ group ($P<0.01$) at 30 minutes after administration. Thus, intradermal delivery of NPs by hollow microneedle array created a unique burst transit through draining lymph nodes at early time, which was absent from the SQ injection.

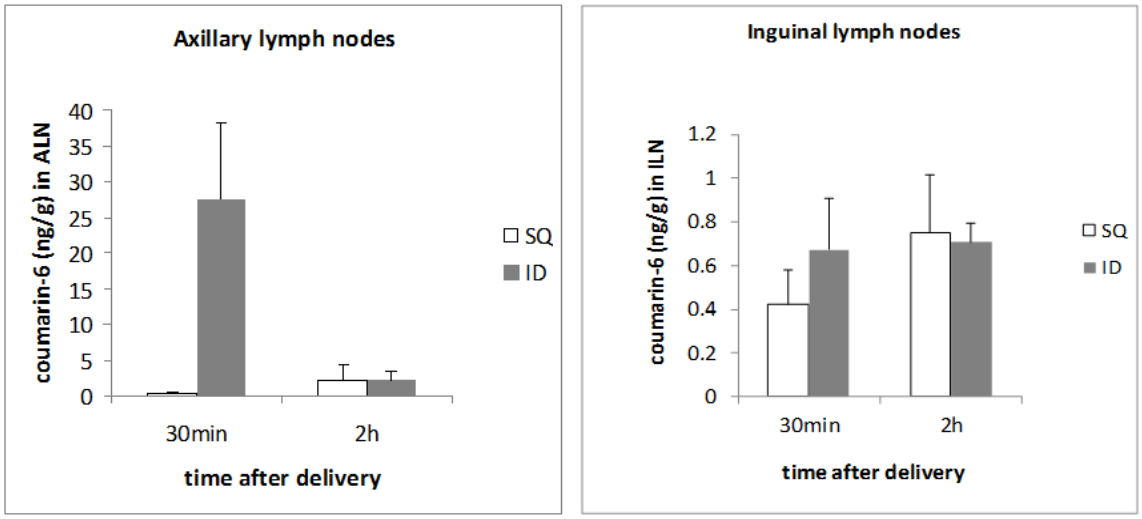

Figure 3-11. Coumarin-6 concentration normalized for ALN and ILN tissue weight after delivery of 5 mg PLGA NPs via intradermal (ID) or subcutaneous (SQ) administration.

3.3.3 The local retention of PLGA NPs subsequent to intradermal delivery amounted to limited systemic exposure and bioavailability

The distribution of PLGA NPs following hMTS delivery was analyzed in several organs (125). At 1-hour time point, the coumarin-6 concentration in liver after ID administration was only 5% of that achieved after IV bolus administration of an equivalent dose of PLGA NPs (Figure 3-12). Similarly, the coumarin-6 concentration in blood and spleen after ID administration was only about 14% of those following IV administration. Given the difference in the blood concentration-time profile, intradermal delivery resulted in limited systemic exposure of PLGA NPs.

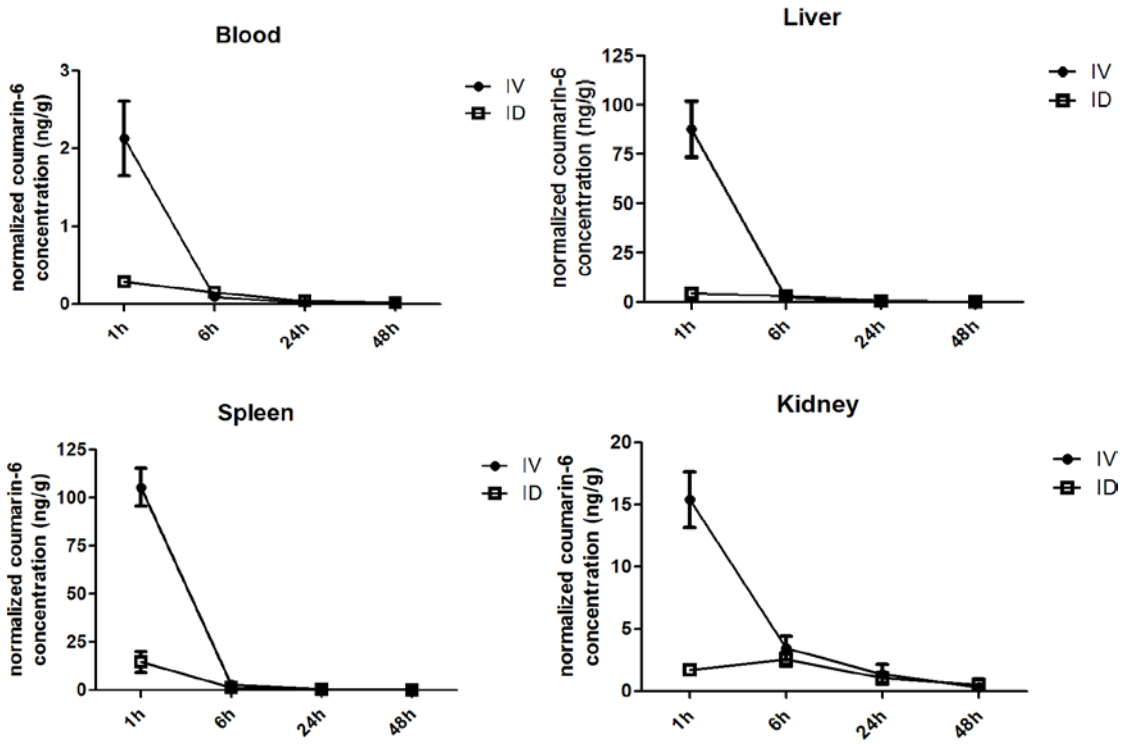

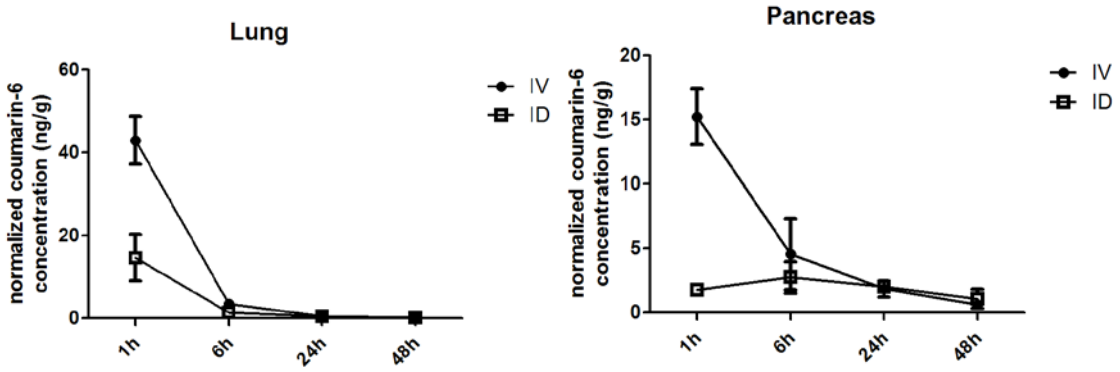

Figure 3-12. Concentration-time profile in major organs after administration of 5 mg coumarin-6 PLGA NPs via intradermal (ID) or intravenous (IV) route.

In addition, the coumarin-6 concentration against was normalized with the organ specific extraction efficiency to estimate the absolute amount of coumarin-6 in each organ and overall biodistribution profile. At 1 hour post-ID delivery, the systemic exposure was less than 1% of the total dose (Table 1), indicating the majority of coumarin-6 PLGA NPs was retained at the site of infusion. Despite the relatively limited systemic exposure, ALN showed disproportionately large accumulation of coumarin-6. The absolute amount of coumarin-6 in ALN was on par with the NPs in blood circulation and even higher than in spleen, a much larger organ than ALN. Thus, draining lymph nodes can serve as a key portal to the systemic dissemination of intradermally-delivered nanoparticles.

organ	extraction efficiency (EE)	coumarin-6(ng/g)	coumarin6 normalized by EE	organ weight estimate (g)	Coumarin6 in each organ (ng)	Percentage of total dose (%)
Blood	0.18	0.29	1.57	18.00	28.30	0.10
Liver	0.42	4.39	10.43	9.00	93.88	0.34
Spleen	0.59	14.59	24.78	0.60	14.87	0.05
Kidney	0.50	1.70	3.42	2.20	7.52	0.03
Lung	0.57	14.59	25.64	1.48	37.94	0.14
ALN	0.68	140.19	204.90	0.13	26.64	0.10
ILN	0.59	1.59	2.71	0.04	0.11	0.00
Pancreas	0.67	1.78	2.64	0.93	2.46	0.01
Brain	0.50	0.88	1.77	1.77	3.14	0.01
Heart	0.58	1.91	3.27	0.96	3.14	0.01
Skin	0.20	3364.00	16884.41	1.43	24144.71	88.28

Table 1. Biodistribution of coumarin-6 in major organs after ID delivery of PLGA NPs.

3.3.4 Intradermal administration of ISNPs elicit robust humoral immune response

To evaluate vaccination feasibility, a previously reported immunostimulatory nanoparticle (ISNP)-based adjuvant system was used (126). The formulation consisted of TLR4 agonist, MPL-A, and TLR7 agonist, imiquimod, co-encapsulated in PLGA NPs.

Initial studies probed ISNPs' potency in stimulating professional antigen presenting cells *in vitro*.

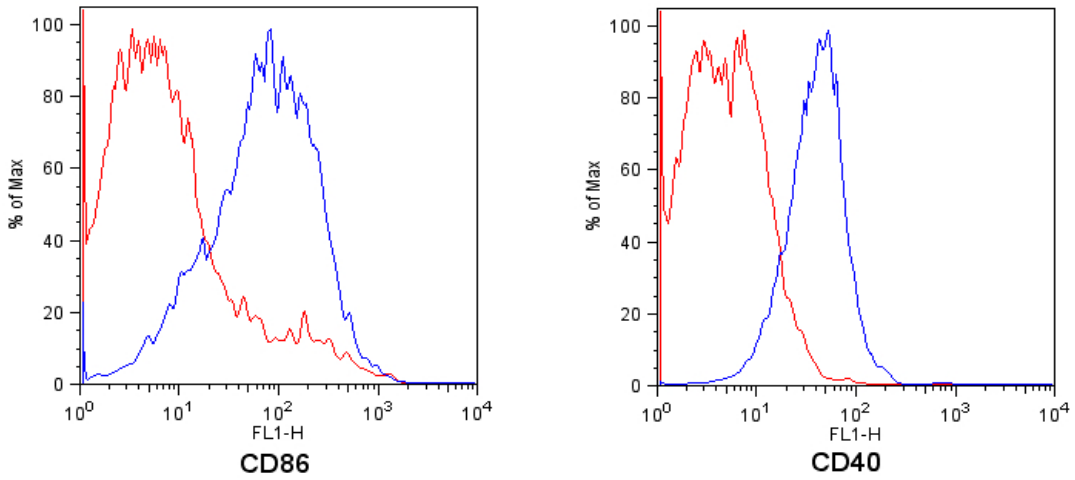

Figure 3-13. Representative histogram of flow cytometric analysis for in vitro CD11c+ BMDC maturation in response to ISNPs stimulation (Red curve: immature BMDC; Blue curve: BMDCs treated with ISNPs).

ISNPs efficiently led to the maturation of BMDCs, as shown by the remarkable shift in CD86/CD40 expression for the entire CD11c positive immature BMDCs (iDC) population by flow cytometry (Figure 3-13). The mean fluorescent intensity of CD86 and CD40 expression levels increased by 4-fold and 5-fold, respectively, after stimulation with ISNPs for 24 hours (Figure 3-14). The up-regulation of MHC II expression level was also statistically significant ($P<0.01$) after co-incubation with ISNPs. However, in the absence of TLR agonists loading, blank PLGA NPs did not activate BMDCs. Thus, ISNPs constituted a potent TLR based adjuvant component for vaccine formulations.

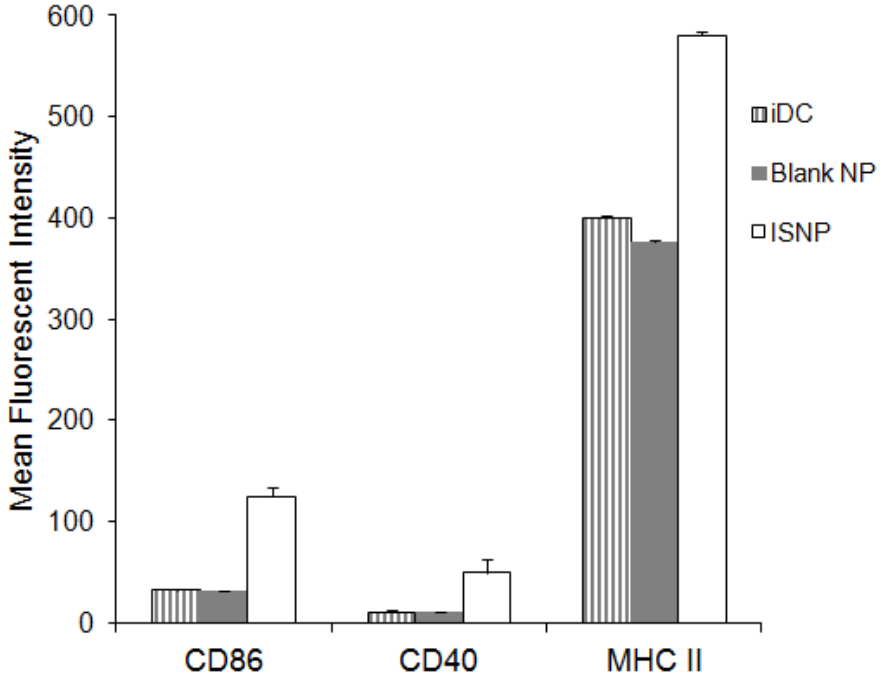

Figure 3-14. Upregulaton of BMDC activation markers after co-incubation with 0.2 mg/mL ISNPs for 24 hours.

Ovalbumin (OVA) was used as the model antigen in the *in vivo* vaccination efficacy study, where two types of vaccine formulations were tested. OVA was administered either as a soluble protein or loaded in NPs at equivalent doses. Two mg of ISNP was the fixed adjuvant component for both formulations. ISNPs were combined with 16 μg of OVA antigen as the final vaccine formulation. For OVA loaded NPs, OVA was encapsulated into separate PLGA NPs (32 μg/mg OVA loading) rather than into ISNPs. The OVA loaded NPs demonstrated a burst release of 18% *in vitro* within 24 hours followed by a slow secondary sustained release of 43% by day 15 (Figure 3-15).

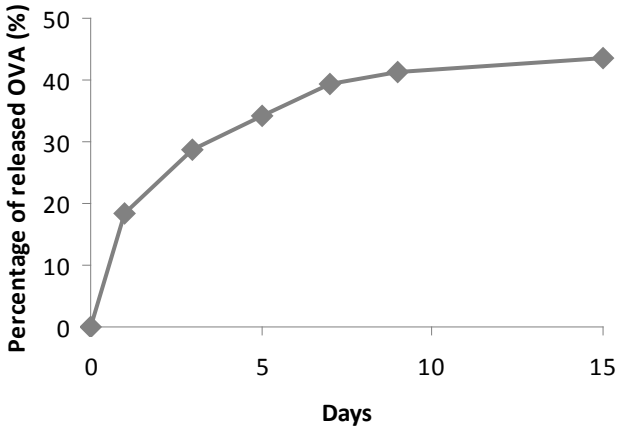

Figure 3-15. Release kinetics of OVA from PLGA NPs in PBS at 37°C.

IgG1 is the predominant IgG subtype that accounts for more than 60% of total IgG (127). ELISA was used to quantify the OVA-specific IgG1 after vaccination. ISNPs promoted a strong antigen-specific antibody response in all groups. Specifically, 3 weeks after the priming dose, all the groups showed intense OVA-specific antibody signal (OD ≥ 1) even after a 9,000-fold dilution of serum (Figure 3-16).

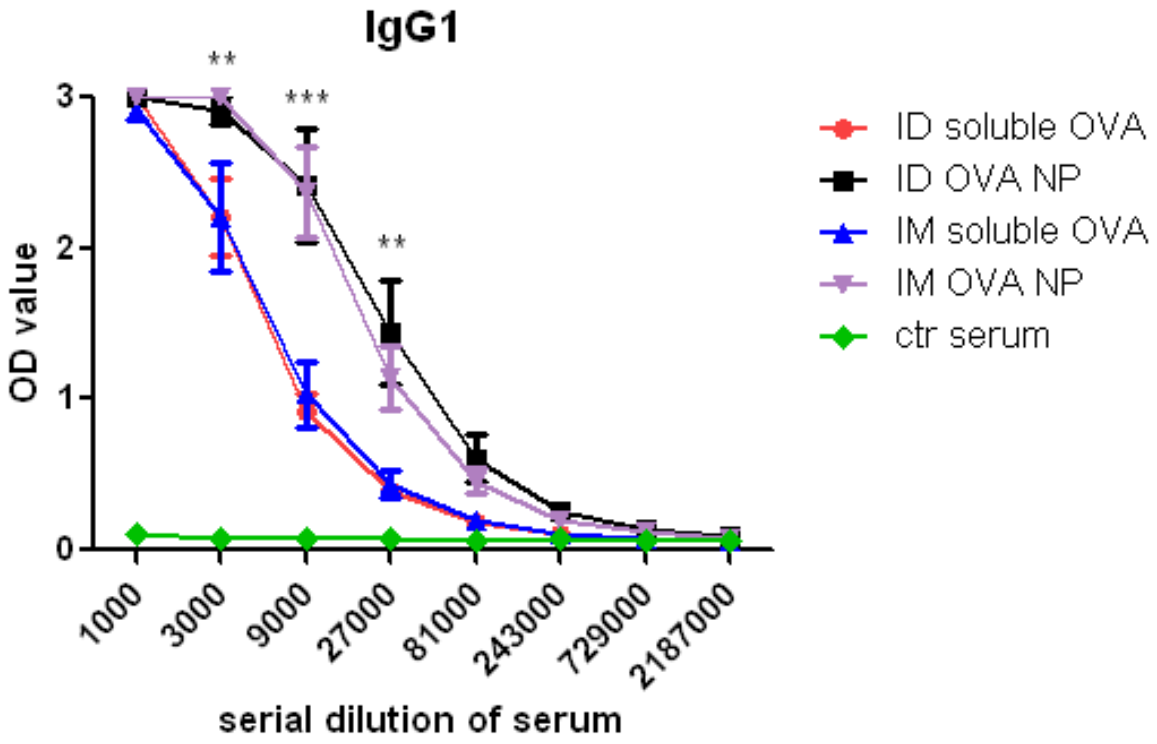

Figure 3-16. OD value of post-priming ELISA for serum OVA-specific IgG1.

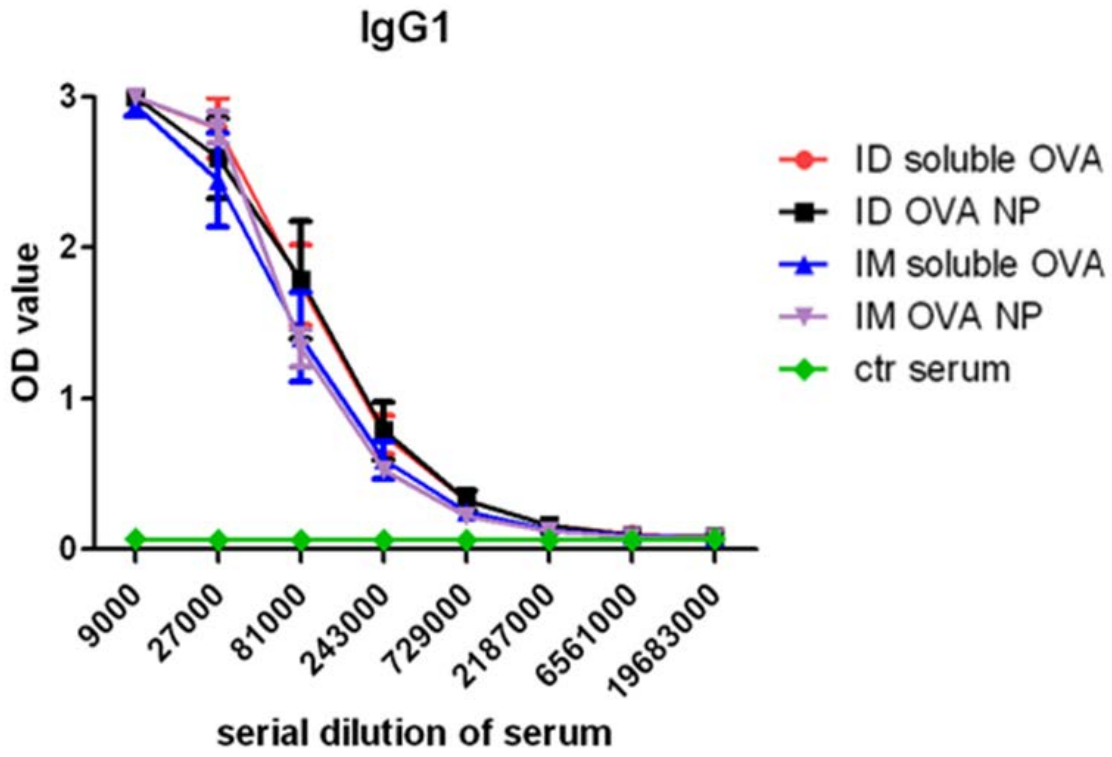

Figure 3-17. OD value of post-booster ELISA for serum OVA-specific IgG1.

Compared to the soluble antigen, NP-encapsulated OVA triggered a significantly stronger IgG1 antibody response three weeks after the priming dose regardless of the administration route, suggesting that the physical state of antigen has a major impact on the humoral response. Furthermore, three weeks after the booster dose of vaccination (six weeks after priming), there were even stronger anti-OVA IgG1 responses among all the groups (Figure 3-17). Interestingly, OVA-specific IgG1 levels of all groups became comparable three weeks post-booster, reaching an antibody titer plateau (Figure 3-18). Therefore, at the later times, the ELISA data implied that ISNPs-based vaccine formulation produced similar OVA-specific IgG1 response independent of antigen format and administration route. However, the advantage of OVA loaded NPs formulation over

soluble OVA formulation resided in the faster kinetics in mounting IgG1 antibody production as shown by the stronger response after the first priming dose.

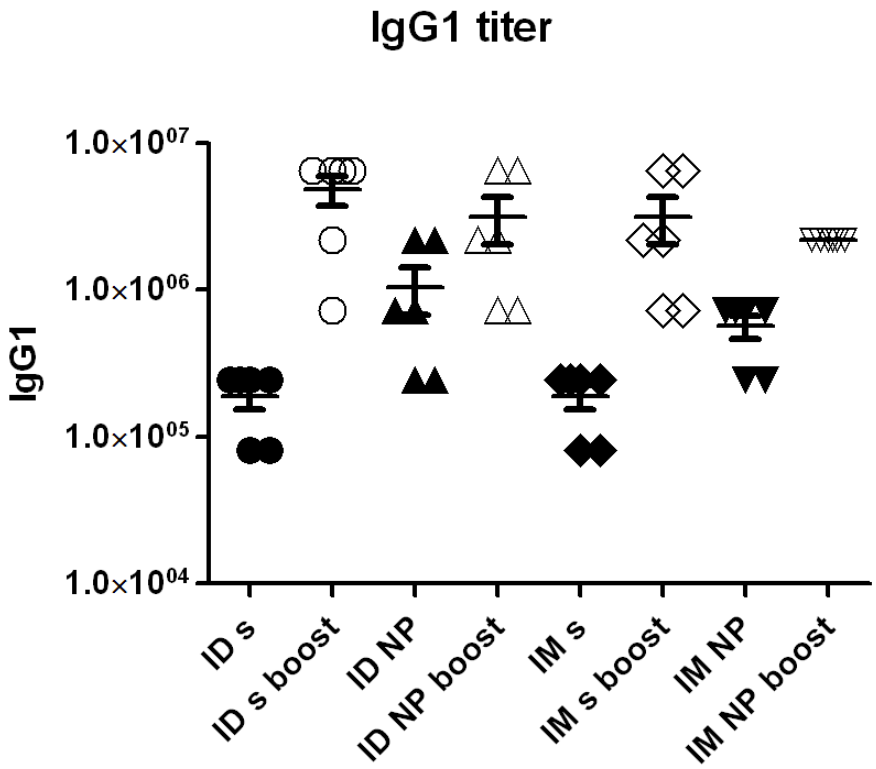

Figure 3-18. OVA specific IgG1 antibody titer (solid symbols: post-priming; open symbols: post-boost, the threshold for deciding antibody titer was set with OD value >=0.1 and OD value was > 2 standard deviations above the mean of pre-vaccinated sera control sample.)

3.3.5 Intradermal deposition of antigen-loaded NP vaccine formulation triggers the strongest IgG2a response

IgG2 is another crucial subtype that accounts for about 30 % of total IgG population (127). The overall IgG2a response was weaker than IgG1 based on ELISA, which was not unexpected considering the relative abundance of IgG1 and IgG2a. However, the OVA-NP formulation delivered via IM route produced higher post-priming OD value than the two cohorts receiving soluble OVA formulation (Figure 3-19). Importantly, OVA-NPs delivered intradermally via hMTS resulted in the highest post-priming IgG2a signal among all experimental groups, suggesting a unique feature of the OVA-NP formulation delivered by hMTS. Furthermore, in contrast to the IgG1 response kinetics, which eventually plateaued for all groups after booster, the augmented IgG2a response with OVA NP formulation was maintained even after the booster dose (Figure 3-20), while the IgG2a responses in all other groups became comparable (Figure 3-21).

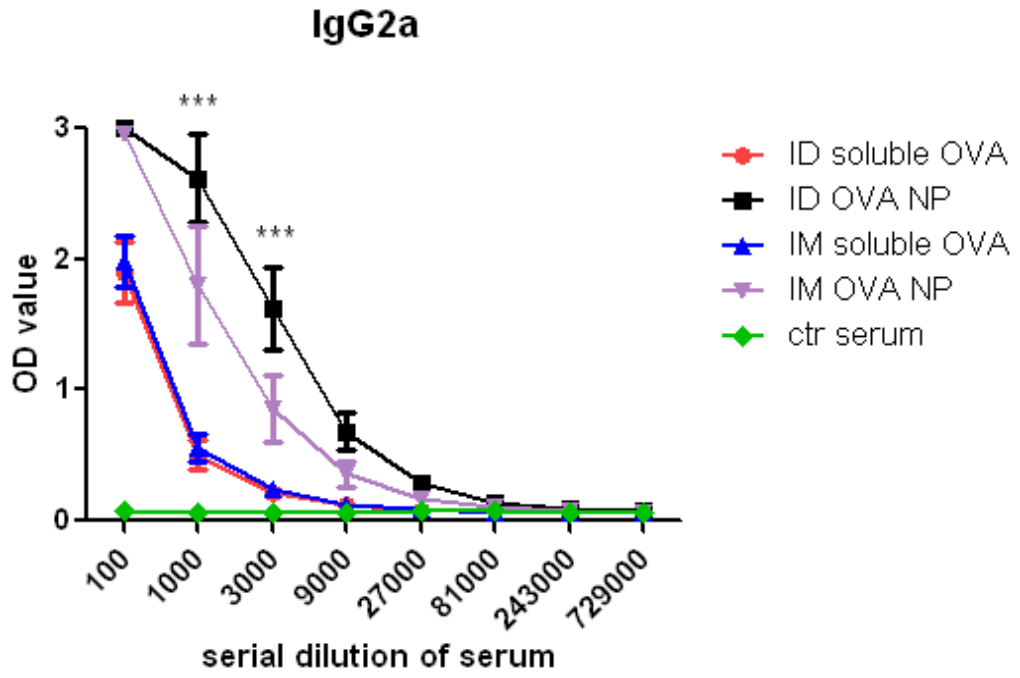

Figure 3-19. OD value of post-priming ELISA for serum OVA-specific IgG2a.

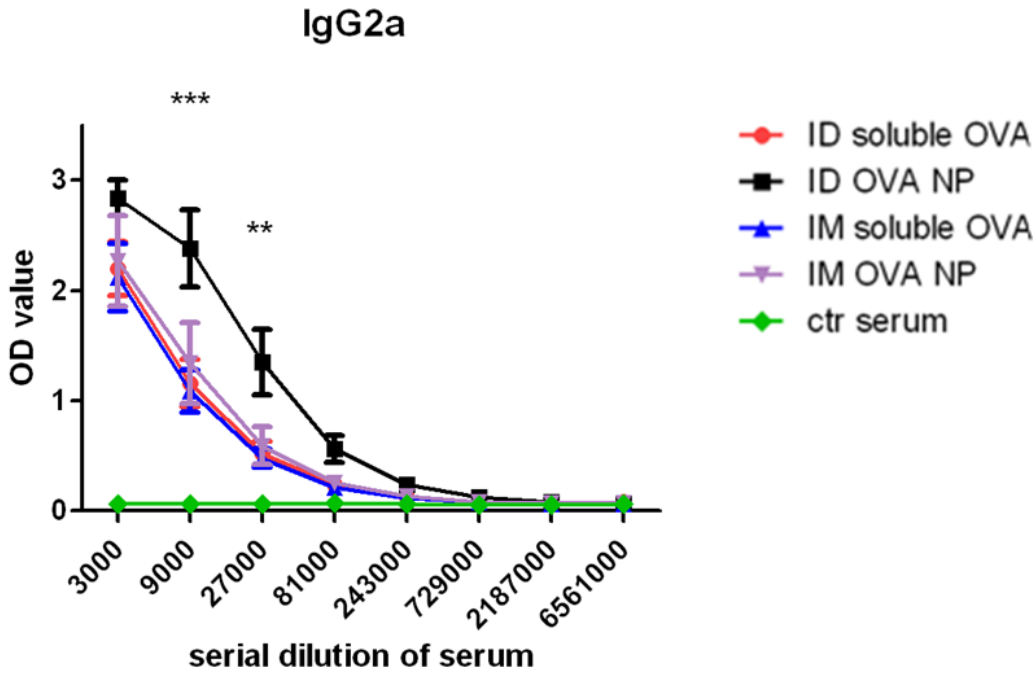

Figure 3-20. OD value of post-booster ELISA for serum OVA-specific IgG2a.

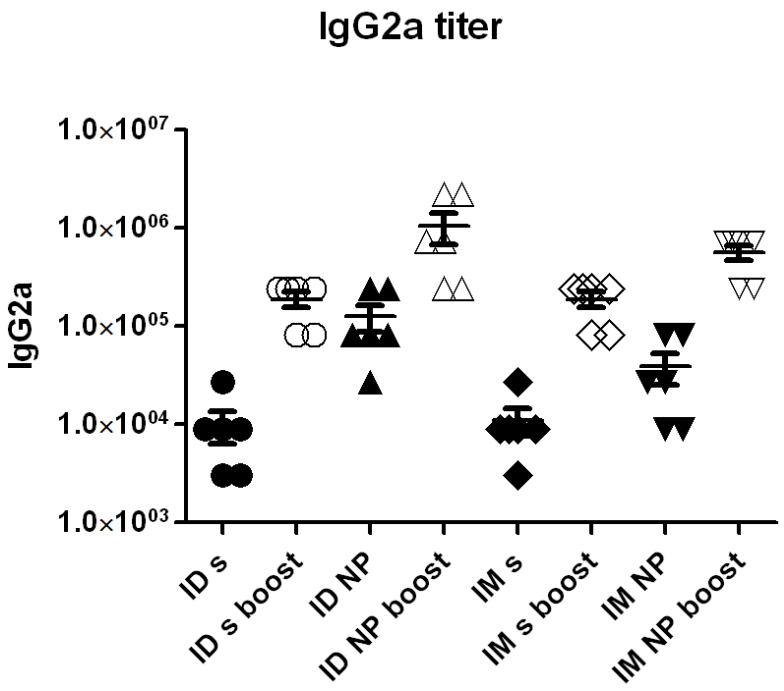

Figure 3-21. OVA specific IgG2a antibody titer (solid sign: post-priming; open sign: post-boost, the threshold for deciding antibody titer was set with OD value >=0.1 and OD value was > 2 standard deviations above the mean of pre-vaccinated sera control samples).

3.3.6 Antigen loaded NPs formulation promoted antibody affinity maturation

In order to monitor the progress of antibody affinity maturation, a modified ELISA with a stringent urea-washing step was used to analyze the avidity (combined affinity) of serum antibody. The 7M urea should disrupt weak antibody-antigen interactions (128), stripping away loosely bound OVA-specific antibodies. For instance, only 32% of post-priming antibodies remained bound after urea washing for rats immunized with soluble OVA

formulations (Figure 3-22). Even though conventional ELISA showed that the antibody titer was sufficiently high, it was deduced from urea ELISA that two-thirds of antibodies induced by soluble OVA formulation were low affinity antibodies. Conversely, 56% of post-priming IgG1 antibodies with OVA-NP vaccination were retained after urea washing and were categorized as high affinity antibodies. Thus, OVA antigen delivered in NP formulation promoted antibody affinity maturation and created higher affinity IgG1 with swifter kinetics compared to soluble antigen. There was no statistically significant difference between the ID and IM route. This discrepancy in IgG1 affinity was solely dependent on antigen formulation and independent of administration route.

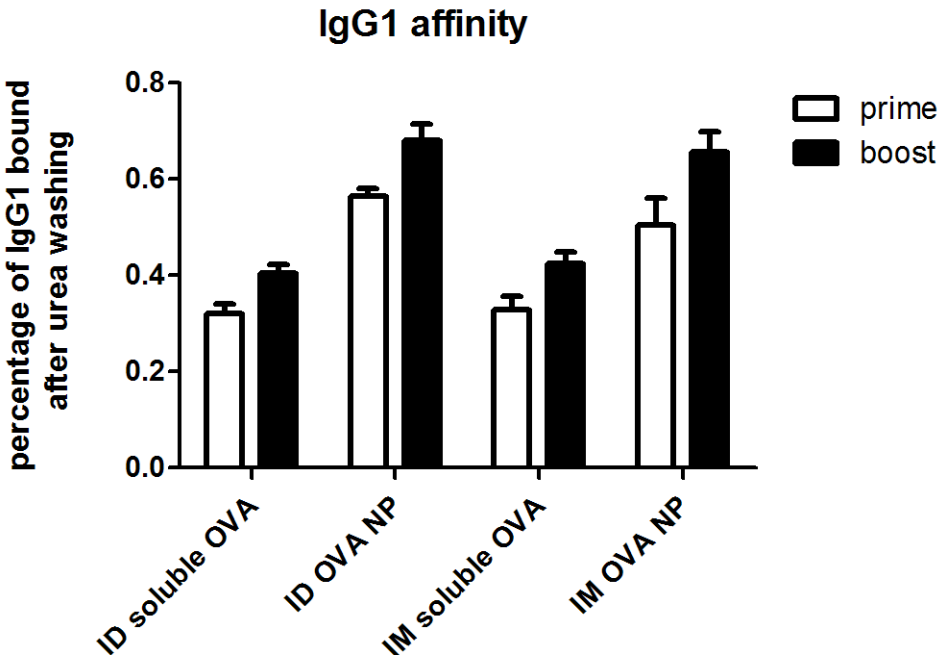

Figure 3-22. Urea ELISA for assessing the IgG1 antibody affinity.

The classical trend of antibody affinity maturation after a booster dose was observed in all vaccinated groups, indicating that IgG1 antibody affinity continued to improve over

time. However, despite the aforementioned fact that IgG1 titers of all vaccinated groups reach a titer plateau after the booster dose, NPs formulation generated higher affinity antibodies. Sixty-eight percent of post-booster antibodies were high affinity antibodies for NP formulation, while only 40% of the post-booster antibodies showed high affinity binding for soluble formulation. In fact, the post-booster affinity of soluble formulation groups (40% high affinity) was still lower than the post-priming affinity of NPs formulation groups (56%). Thus, a single dose of NP formulation can produce superior antibodies in terms of affinity within just three weeks in comparison to what could be achieved in six weeks with a soluble formulation.

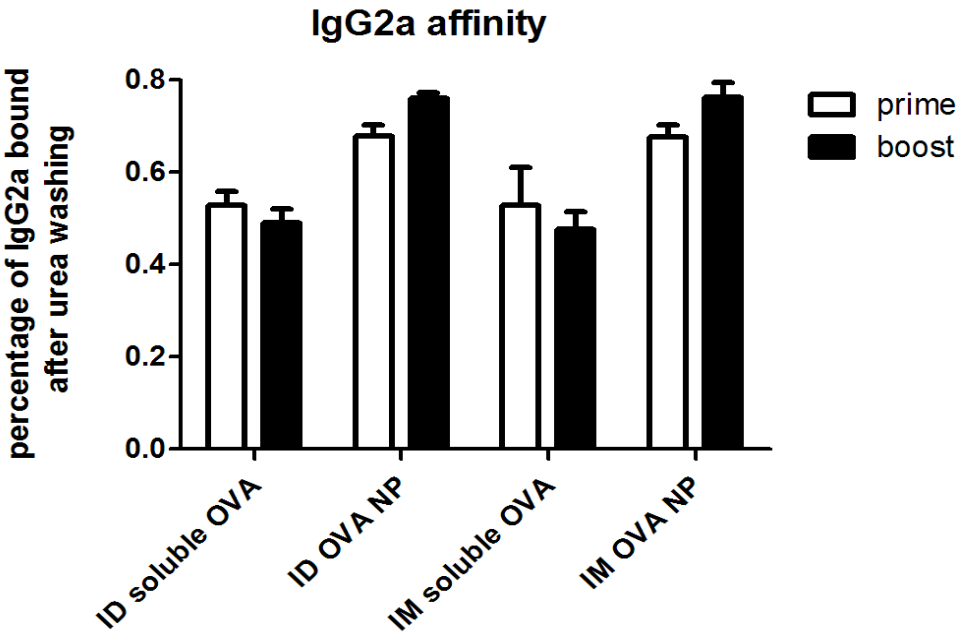

Figure 3-23. Urea ELISA for assessing the IgG2a antibody affinity.

As for the IgG2a, the affinity solely relies on antigen formulation and is independent of the administration route. Fifty-three percent of post-priming IgG2a antibodies subsequent to soluble OVA vaccination was high affinity antibodies compared to the 68% following OVA NP vaccination (Figure 3-23). Interestingly, there was no IgG2a affinity maturation after booster reinforcement for soluble OVA formulation. But in OVA NPs vaccinated cohorts, the IgG2a affinity continued to increase. Up to 76% of IgG2a antibodies were classified as strongly bound antibodies after the booster dose.

3.3.7 Antigen loaded NPs and soluble antigen formulations display distinct antigen-antibody binding behaviors in Surface Plasmon Resonance study

To further understand the serum antibody response in relation to vaccination regimen, SPR was adopted to complement the ELISA data. The antigen OVA was covalently conjugated onto the surface of CM5 Biacore chip. After introducing serum sample, the differential response between the antigen conjugated channel and the un-conjugated control channel could be monitored as a reflection of formation of antibody-antigen complex at the chip surface. Conversely, during the elution phase, antibody-antigen complex became progressively dissociated.

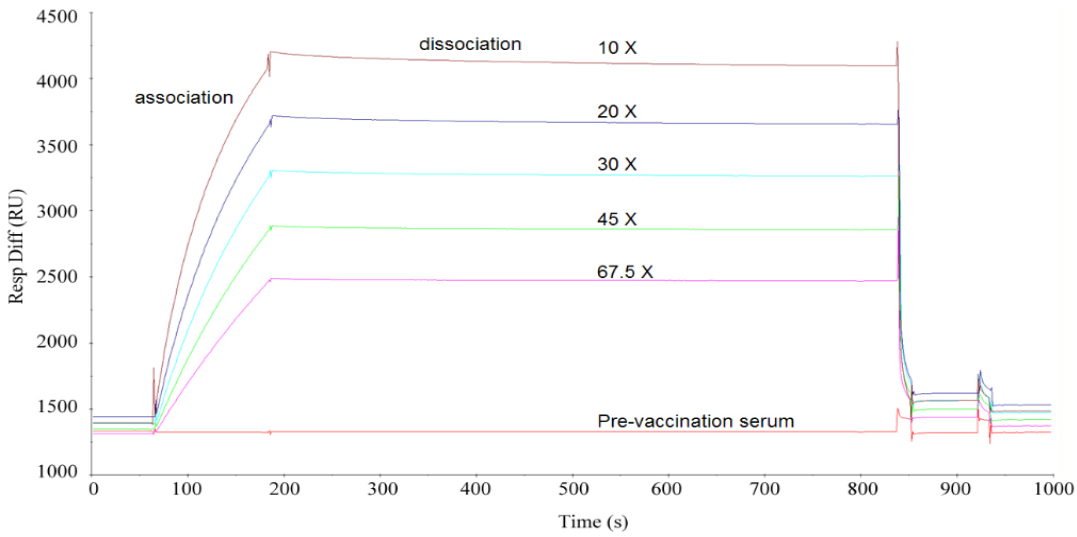

Figure 3-24. Binding response of post-booster serum from rats vaccinated with soluble OVA via ID route. Pooled sera were serially diluted (67.5X, 45X, 30X, 20X, 10X) and compared to pre-vaccination serum samples.

A strong SPR effect due to antigen-specific binding was observed in a dose-dependent manner. The magnitude of association signals were inversely related to the serum dilution factor (Figure 3-24). A classical profile of SPR response was indicative of the successful recognition of OVA antigen conjugated on the chip microfluidic surface by serum antibodies. However, cohorts immunized with soluble OVA formulation surprisingly gave rise to stronger antibody binding signals than the OVA NPs formulation (Figure 3-25), which was inconsistent with the ELISA data. This discrepancy could be attributed, at least partly, to the chemical modification of OVA antigen during chemical conjugation to the chip surface. It is possible that antibody binding epitope on OVA was altered chemically so that a negative impact on antibody-antigen binding was observed. To this

end, we also speculated that antibodies may recognize distinct epitopes of the same OVA antigen depending on the antigen format of the vaccine formulations.

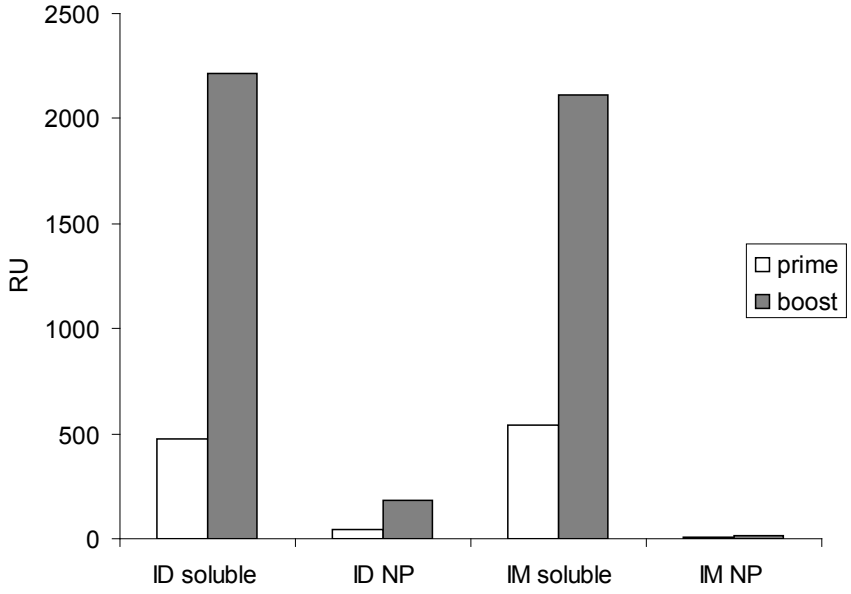

Figure 3-25. Binding response (RU) at the end of association phase for sera diluted by 20-fold.

The dissociation rate constant, Kd, of the antibodies was estimated to be on the order of 10^{-5} (1/s) by a global fitting model, suggesting the presence of high affinity antibodies. More than 96% of antibodies remained bound after 9.5 minutes elution (Figure 3-26), and the bound antibodies had to be removed by a strongly acidic eluting buffer (pH<2.0) to fully regenerate the chip surface for subsequent samples analysis.

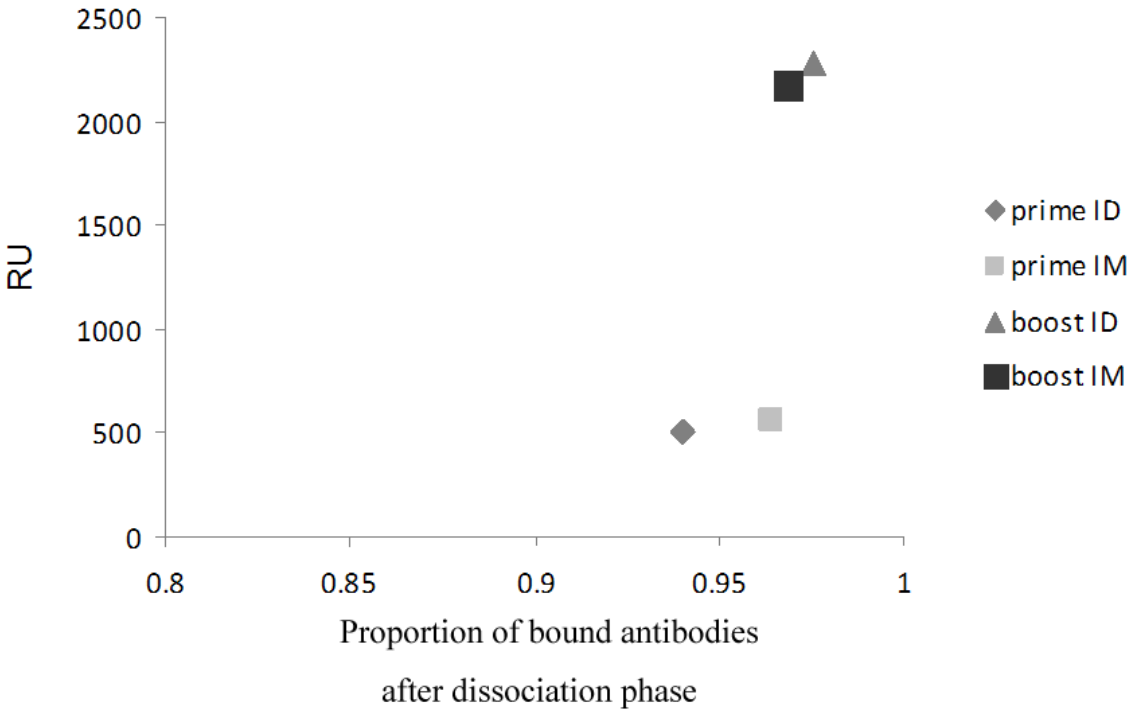

Figure 3-26. Response unit of associated antibody-antigen complex plotted against the proportion of remaining bound antibodies after dissociation phase (20-fold dilution of sera from ID-delivered soluble OVA formulation group).

3.3.8 Intradermal delivery ISNPs enhances Th1 response

The Th2 response is an evolutionarily conserved response to protect against helminthes and extracellular microbes, and conventional vaccine formulations with aluminum-based adjuvants predominantly stimulate Th2 response. In contrast, the Th1 response is critical for immunity against intracellular pathogens and malignancy. IgG2a is widely considered a surrogate biomarker for Th1 response, while IgG1 is a biomarker for Th2 response (129). The relative strength of Th1/Th2 response could therefore be assessed from the

IgG1/IgG2a antibody titer ratio (130). In this study, the IgG1 response was in general more robust than the IgG2a response (IgG1/IgG2a titer ratio>1) after priming (Figure 3-27). Intradermal delivery of OVA NP formulation displayed outstanding ability to induce IgG2a antibodies, leading to the lowest IgG1/IgG2a ratio among all groups. Thus, this novel modality of vaccination demonstrated the highest relative strength of Th1 response.

After the booster dose, all groups showed a trend for enhancement of IgG2a titer and a reduced IgG1/IgG2a ratio, indicating that the IgG2a antibody class switching was lagging behind IgG1. Nonetheless, after booster dosing, intradermal NP vaccine formulation still exhibited the lowest IgG1/IgG2a ratio in favor of skewing the immunity towards Th1 response. Interferon gamma (IFN γ) is the major Th1 polarizing cytokine secreted by T helper cells to influence the fate of antigen-specific B cells. Splenocytes were harvested at the end of the study to evaluate the secretion of IFN γ and enumerated by ELISPOT assay (Figure 3-28). Robust systemic cellular immunity was revealed in all groups as manifested by the large population of IFN γ positive splenocytes (Figure 3-29). Intradermal delivery of NPs formulation by hMTS demonstrated a significantly stronger IFN γ response, substantiating that this modality of vaccine formulation delivery induced a more balanced Th1/Th2 response.

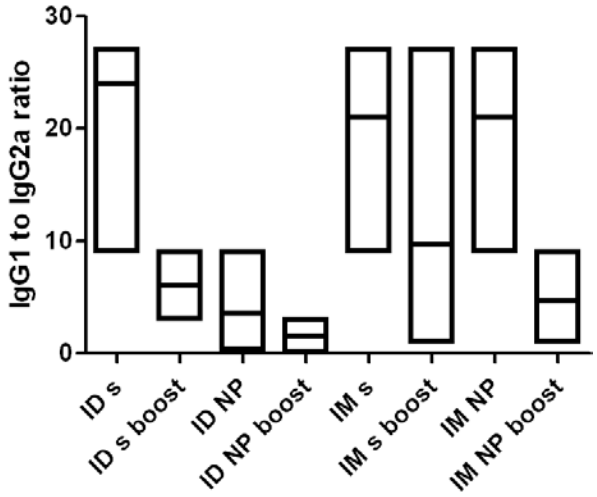

Figure 3-27. IgG1 over IgG2a antibody titer ratio range of vaccinated rats.

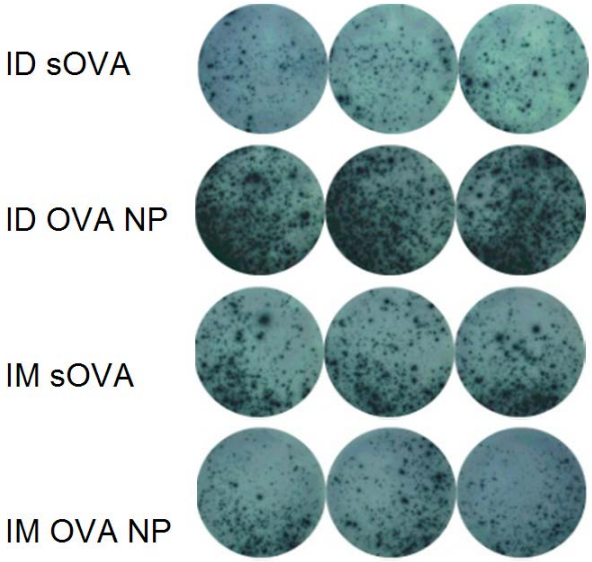

Figure 3-28. Representative image of developed ELISPOT wells containing splenocytes at 60,000 cells / well concentration.

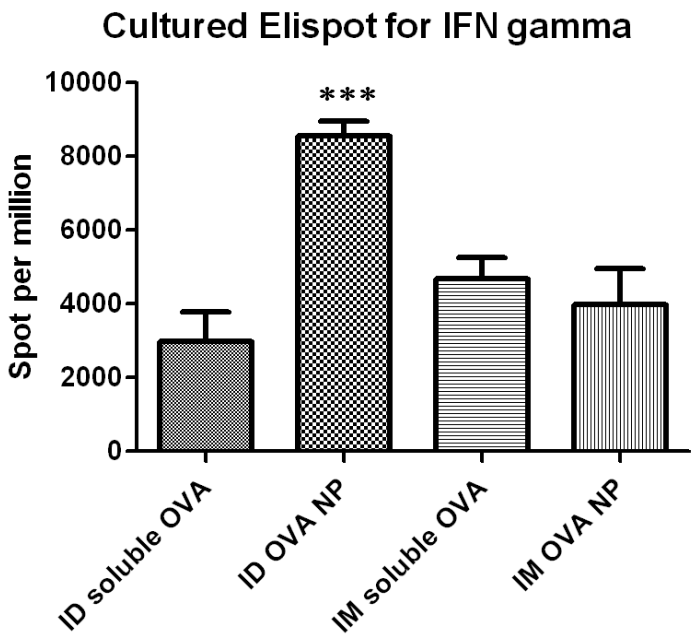

Figure 3-29. Enumerated splenocytes secreting IFN gamma in the cultured ELISPOT assay.

3.4 Discussion

The route of administration is critical for drug delivery, because it affects the bioavailability, adsorption, distribution, metabolism and clearance of drugs (131). NPs have been administered by IV injection route (132) as well as through intramuscular, subcutaneous and pulmonary routes. Recently, injection of NPs into lymph nodes for immunization and oral route for systemic delivery of Fc-targeted NPs via FcRn mediated transepithelial trafficking has been reported (133, 134).

We explored a novel hollow microneedle system for delivering PLGA NPs. The mass balance estimation of locally retained NPs in the skin was in agreement with the visual

inspection that large quantities of NPs were embedded in the infusion site. The high local retention rate is likely the corollary of the size of PLGA NPs. It was reported that radio-colloidal particles with a 50 to 100 nm size distribution drain optimally within the interstitial space, while sizes larger than 200 nm is inefficiently drained into lymphatics (135). Similarly, 100 nm NPs drain much more poorly than the 25 nm counterparts (136). During ID delivery, the syringe back-pressure was observed to increase, suggesting that the infused NPs encountered transport resistance and that the delivery rate was faster than the drainage rate. However, continued increase in syringe back pressure may also be indicative of occlusion at the injection site. Accumulated PLGA NPs could cluster into local micro-depots. The increased size of aggregated NPs could further reduce the dissemination of NPs. The non-uniform diffusive patch of fluorescently-labeled NPs was suggestive of the differential resistance of each needle in the microneedle array. Presumably, needles with early build-up of NP depot will have higher delivery resistance and probably smaller diffusive patch adjacent to the needle. The pore size of the interstitial space and extracellular matrix could be a major limiting factor that determines the transport resistance. For future study, the hMTS mediated intradermal delivery of sub-100 nm NPs would be of great interest to address the correlation between particle size and local retention. It is predicted that smaller NPs will exhibit a pharmacokinetic profile similar to that of the hMTS delivered biologics drugs, which have higher systemic bioavailability following ID delivery.

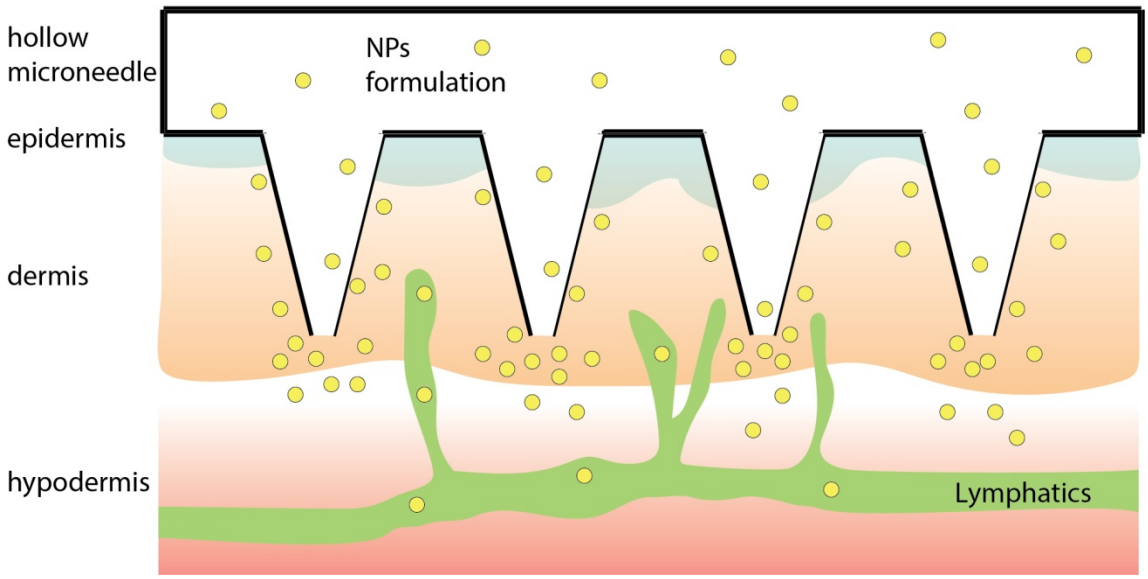

Figure 3-30. Schematic graph for ID delivery of PLGA NPs via hMTS

The clearance of IV administered NPs relies on liver and spleen resident phagocytic cells, which together constitute the reticuloendothelial system (RES) (137). In stark contrast, the high local retention and limited systemic bioavailability of ID administered PLGA NPs appeared to shift the clearance from the RES to the local, attendant draining lymph nodes (Figure 3-30). Resident phagocytes and extravasated inflammatory monocytes may also have participated in the clearance of NPs. Although not addressed in this study, any local inflammation caused by NPs can significantly alter the extracellular matrix of skin (138). Specifically, the elevated vascular permeability and mobilized immune cells could affect the fate of intradermal NPs, which would depend on whether they were immunostimulatory or immune-inert.

The significant burst transit through draining lymph nodes with the microneedle array is a unique phenomenon. The ID and SC delivery differed in two significant ways. First, the lymphatic anatomy in the dermal layer is distinct from the subcutaneous space. The dermis is equipped with the superficial lymphatic plexus and a dense network of lymph capillaries (139). Thus, the terminal lymphatic vessels from the dermis converge into larger collecting lymphatic vessels. This greater lymph-collecting capability could contribute to the swift transit of ID-delivered agents through afferent lymphatic vasculatures and eventually into draining lymph nodes. Second, hMTS infusion was pressure-driven by syringe pump over 15 minutes but the subcutaneous injection was an instantaneous bolus injection. The pressure driven process offered sustained high interstitial pressure. Lymphatic endothelial cells are connected to the interstitium via anchoring filaments. Elevated interstitial pressure and expansion of the interstitium can lead to widening of lymph lumens by mechanically pulling on anchoring filaments (140, 141). This pressure gradient drives convective flow across permeable lymphatic endothelial lining.

However, a caveat with the current study is the dissimilarity between rodent and human skin, which could be overcome by using minipigs that have a dermal structure more comparable to humans (142). For future investigations, it would be of interest to co-administer hyaluronidase via hMTS delivery. Hyaluronidase has been shown to remodel the basic structure of interstitial space, significantly increasing the pore size of the extracellular matrix and bioavailability (143, 144), which could alter the disposition of ID

delivered NPs. Lymph eventually drains into blood circulation at the thoracic duct and the subclavian vein. It is conceivable that smaller NPs in conjunction with hyaluronidase could potentially render ID route an attractive alternative to the IV injection of NPs to achieve systemic delivery of NPs.

Lymphatic mapping for sentinel lymph nodes of malignant cutaneous melanoma is important for detecting potential metastasis from the primary melanoma site and is one of the most reliable prognostic factors for long term survival prediction. Visualization of dynamic lymphoscintigraphy of collecting lymph vessel and sentinel lymph nodes has been assisted by the use of radio-colloidal particles. For example, technetium-99m radiopharmaceutical agents in the volume of 0.05 – 0.2 mL were manually injected into dermal and subdermal domain using 25 gauge syringe at 4 to 8 locations near melanoma lesion (145). Oncogenesis of melanoma originates from the melanocytes located at the lower level of epidermis (stratum basale), and thus intradermal injection of tracer dye that drain through the same upper lymphatic plexus utilized by melanocytes is ideal to recapitulate a potential metastatic pathway for cancerous cells. The intratumoral and peritumoral multi-point injection practice could be further streamlined with a microneedle array to achieve efficient and reliable delivery of radio-colloidal particles. In addition, the delayed imaging test at two and half hours post-injection can be accelerated due to the quick lymphatic drainage in the dermal domain via hMTS delivery relative to the hypodermal domain.

hMTS could also enhance lymph node targeting by NPs. A novel ‘albumin hitchhiking’ design approach for molecular vaccine comprising a hydrophobic albumin binding moiety and adjuvant/peptide component has demonstrated superior lymph node targeting property when administered subcutaneously (146). Given that ID delivery using microneedles promoted a much stronger burst transit into draining lymph nodes compared to subcutaneous injection in our study, it is conceivable that the combination of lymph node targeting agents may further improve the quick access to draining lymph nodes. Moreover, microneedle mediated vaccine delivery is conducive to the direct engagement with Langerhans cells and dermal dendritic cells (dDC), which facilitate the transportation of acquired NPs into draining lymph nodes.

Antigen-loaded NPs elicited better antibody response than the soluble antigen formulation. The use of NPs can enable the sustained release of antigen both at a tissue level (depot in skin) and at a cellular level (NPs in dDCs). In contrast, soluble antigens likely transit through draining lymph nodes quickly. The more rapid elimination of soluble antigens can result in lower effective antigen concentrations during the course of humoral immunity, encompassing initiation, clonal expansion, affinity maturation and maintenance for long term memory. Creation of intradermal vaccine depots comprised of NP formulation elicited faster kinetics of IgG1 humoral immune response. This is especially advantageous in a pandemic context in that a single dose of vaccination with NP formulation could potentially confer protective immunity much more quickly.

On the other hand, since all priming vaccine formulations contained the same TLR adjuvant component, the appearance of high affinity antibodies suggested that antigen presented in the NP format *per se* accelerated affinity maturation at an earlier time point post-vaccination. The improvement in antibody quality could be the corollary of NP format at both the level of the individual particle and the level of the local depot. In terms of NP trafficking, NPs could transit as individual particles directly through the lymphatics into the draining lymph node, gaining access to lymph node resident phagocytes and B cells. In addition, dDC could also internalize NPs in the dermis and transport NPs into draining lymph nodes. For NPs that directly encounter B cells, B cells differentiate monovalent binding of cognate antigen from multivalent binding of cognate antigen via B cell receptors (BCR) on the surface of the B cell. BCR clustering due to multivalent engagement with antigens is critical in assembling the most efficient signaling event for B cell activation. Both Syk and Src family kinase (SFK) are required for B cell activation with monovalent binding, while in the presence of multivalent binding the requirement for robust SFK engagement is significantly lowered so that the sensitivity of B cells increases dramatically (147). The spatial configuration of spherical nanoparticles presents antigen in a three dimensional format. In theory, the highly repetitive multivalent antigen presentation on the surface of nanopartices enables the simultaneous binding with multiple BCRs and the clustering of BCRs into microdomain of immunological synapse on the interface between B cell membrane and nanoparticle. In addition, it was reported recently that mobility of antigens constitutes another crucial aspect in inducing BCR clustering and B cell activation (148). In terms of future

nanoparticulate vaccine platform design, surface decoration with antigen tethered to the mobile polyethylene glycol corona could confer further benefit in triggering B cell activation compared to the passively adsorbed antigen on the surface of nanoparticulate in that the adsorbed antigen is essentially immobilized and less accommodating to move with binding BCR in the process of BCR microcluster formulation.

ELISA is the classical gold standard for monitoring efficacious vaccination reactions. SPR is a relatively new technique that supplements the ELISA study. One interesting observation in this project was the discordant conclusions drawn from ELISA and SPR studies. The antigen-loaded NPs performed better than the soluble antigen counterpart in every aspect probed in the ELISA format. The advantage of OVA-loaded NPs formulation was multifaceted: high antibody titer could be induced early and higher avidity antibodies were attained with single dose vaccination in a shorter time frame and the highest IgG2a response was only elicited by antigen loaded NPs via ID delivery powered by hMTS. However, the SPR gave the opposite result characterized by a lower binding response following immunization with antigen loaded NPs than with soluble antigen formulation. Several distinctions in ELISA and SPR experimental design may account for the discordant results. First of all, the ELISA focused on the specific detection of the most essential and abundant components of humoral immunity, IgG1 and IgG2a, while the SPR format did not exclude the binding of other immunoglobulin classes, such as the low affinity IgM. Nonetheless, we attribute the discrepancy between ELISA and SPR data primarily to the difference in the involved epitopes. It is speculated

that that soluble antigen formulation elicited antibodies that recognized distinct epitopes compared to the antibodies triggered by the antigen-loaded NPs. Owing to the SPR chip surface preparation procedure, the antigen OVA was chemically modified by amine coupling. In the SPR study, the amino acid epitopes with reactive primary amine such as lysine were altered permanently and this could have reduced the binding of serum antibodies to the antigen. In the ELISA format, antigen epitopes were not chemically modified and thus represented the unaltered native epitopes. It has been reported that the acylation of epsilon amino groups of lysine in OVA has severe impact on its conformation (149). To this end, spatial epitopes containing lysine residues were predicted to be the predominant epitopes involved in NP-triggered antibodies, which may not be necessarily true for the soluble antigen-triggered antibodies. This observation raised the question of the correlation between vaccine antigen presentation formats and immunodominant spatial epitope. Depending on whether or not T cells are involved in antigen recognition and B cell activation, antigens could be categorized into T cell-independent antigen and T cell-dependent antigen. In other words, B cell clones could either directly engage certain antigens or indirectly engage them through assistance from T helper cells. T cell-independent antigens are typically characterized by a polymeric nature with repetitive units and resistance to degradation for long term persistence. These requirements are met by the antigen-loaded NP format, raising the potential of converting an otherwise T-dependent antigen into T-independent antigen via association with NP format. Thus, there could be expansion of B cell clones that only engaged the antigen associated with NPs rather than the soluble antigen format. This discrepancy illustrated

the importance of antigen presentation format in influencing the responsiveness of B cell repertoire subsequent to vaccination. For instance, the current central topic of vaccine design concentrates on the induction of broadly neutralizing antibodies against just a few highly conserved epitopes for HIV and influenza virus mutant strains (150). However, the induction of broadly neutralizing antibodies turned to be elusive by conventional vaccine formulation, while self-assembly virus like NPs have shown promise as an enabling technique for eliciting desired antibodies against specific epitopes (151). Thus, this observation warrants in-depth research that delves into the epitope mapping with respect to the special design of each novel nanoparticulate vaccine platform.

Finally, it was found that ID delivery of antigen-loaded NP formulation enhanced the relative strength of Th1 response, leading to a more balanced Th1/Th2 immunity following vaccination. Specific subsets of skin-resident immune cells were identified to be associated with Th1 or Th2 polarizing functionality (152, 153). In this regard, the implications of this technique are significant in that this may potentially pave the way for creation of local controlled release depot into superficially accessible melanoma lesions, modulating immunosuppressive microenvironment of tumor and tumor draining lymph nodes, especially in the context of a combination strategy involving *in situ* melanoma cancer vaccine and T cell checkpoint inhibitors. Melanomas harbor the highest somatic mutation prevalence among a wide range of cancer types due to the chronic exposure of ultraviolet light (154). Presumably, the mutated melanoma associated tumor antigens will be readily available as potential targets for cancer immunotherapy. An increasing body of

evidence support the hypothesis that delivering immunomodulatory agents directly into accessible melanoma lesion could induce local and systemic anti-tumor immunity against injected and distant uninjected tumors (9). Amgen's investigational oncolytic virus talimogene laherparepvec (T-VEC) succeeded in meeting the primary endpoint of achieving a durable response rate in the Phase III clinical trial for unresectable III B-IV stage metastatic melanoma patients (155). Sixty-four percent of injected melanoma tumors showed a size reduction of more than 50%. On the other hand, surgically implanted cancer vaccine tablet in the format of PLGA scaffold loaded with tumor associated antigen has shown great promise in instigating antitumor immunity (156). The clinical trial of a cancer vaccine tablet formulation is currently underway (157). The current study provides an alternative delivery option for biodegradable material-based cancer vaccine formulation, supplanting the surgical implantation of a vaccine tablet with intradermal deposition of particulates using the microneedle array.

Conclusion

A hollow microneedle array was used as a novel transdermal delivery modality for precision delivery of a large volume of NPs. The majority of injected NPs were retained locally. A unique burst transit through draining lymph nodes was documented but led to the limited systemic exposure. A PLGA NP vaccine formulation delivered intradermally via hollow microneedle elicited robust humoral and cellular immunity. Antigen-loaded NPs formulation triggered quicker, stronger and better quality antibody responses compared to the soluble antigen formulation. When compared to IM injection in rats, the

unique combination of a NP formulation and the ID route of administration led to an enhanced Th1 immune response, which is considered essential for effective induction of anti-viral and anti-tumor immunities.

Chapter Four: Immunostimulatory Nanoparticles Assisted Whole Tumor Cell Vaccination against Melanoma

4.1 Introduction

60% of melanoma patients harbor an oncogenic driver gene BRAF V600E (158). Vemurafenib (PLX4720) is the first FDA approved selective BRAF inhibitor, which blocks the aberrantly activated MAPK signaling pathway (159). Owing to this targeted mechanism of action, vemurafenib leads to a high clinical response rate for BRAF V600E positive metastatic melanoma patients and remarkable tumor shrinkage among responders initially (160). Nevertheless, despite its groundbreaking success in revolutionizing melanoma treatment, resistance invariably emerges in a few months subsequent to the BRAF inhibitor therapy (161-164). Among various combination therapies under investigation to eliminate the resistant melanoma, cancer immunotherapy in conjunction with BRAF inhibition is one of the proposed strategies (165-167). Recently, it was reported that on top of the drug-induced apoptosis of melanoma cells (168), host immunity also contributes to the efficacy of BRAF inhibitor. The ratio of cytotoxic T lymphocytes (CTL) / regulatory T cell (Treg) is significantly elevated. However, in spite of the altered tumor-infiltrating leukocytes profile, it has been suggested that vemurafenib does not directly increase tumor immunogenicity (169). To this end, in order to promote the generation of strong anti-melanoma immunity,

therapeutic intervention that potentially boosts tumor immunogenicity in the context of BRAF inhibition warrants further study.

Dendritic cell (DC) is the most important professional phagocyte and antigen presenting cell that dictates the nature of immune response following its encounter with antigens (170). Either immunity or tolerance could be induced, depending on the context of antigen acquisition(171). Hence, DC is instrumental in coordinating cancer immunotherapy (172). DC based cellular therapy Sipuleucel-T is the first FDA approved cancer vaccine that confers survival benefit for metastatic prostate cancer patient (173). DC is pulsed with recombinant prostate cancer related antigen *ex vivo* prior to vaccination procedure. On the other hand, the ability of DC in processing antigens derived from apoptotic cells has been well recognized (174-176). With respect to melanoma treatment, the BRAF targeted therapy engenders massive scale of apoptotic cell death and substantial tumor debulking (177). As DCs scavenge dying melanoma cells and tumor associated antigens (TAA), there is a unique opportunity of creating a whole cell cancer vaccine *in situ*. However, phagocytic clearance of autologous apoptotic cells can be sub-immunogenic and even tolerogenic (178), especially within the immunosuppressive tumor microenvironment. It is well established that the presence of myeloid-derived suppressor cells (MDSC) or Treg cells foster a milieu undesirable for eliciting anti-melanoma immunity (179-181).

In this regard, during the DC's acquisition of TAA, it is imperative to activate DC and reverse immunosuppression in order to maximize the tumor immunogenicity. DC undergoes activating maturation procedure and orchestrates immunogenic responses upon detection of the "danger signals". Toll Like Receptor (TLR) family is an archetypical pattern recognition receptors (PRR) that recognized conserved pathogen associated molecular patterns (PAMP) (182). The presence of TLR agonist within phagosomal cargo results in DC maturation and preferential presentation of antigens derived from the same phagosome to T cells (183). Along the same line, it has been shown that the proper co-delivery of TAA and TLR agonists is critical in terms of producing optimum anti-tumor immunity for the rational design of cancer vaccine (184-186).

TLR7 and TLR8 are intracellular receptors for single-stranded RNA. The engagement of TLR7/8 with their ligands instigates DC via MyD88 signaling pathway, triggering the release of pro-inflammatory cytokines (187, 188). Imidazoquinoline is one prototype of synthetic compound that stimulates TLR7/8 signaling pathway. Imiquimod and resiquimod are the most widely used small molecule TLR7/8 agonists (189). Recently, a series of novel imidazoquinoline analogues were synthesized at University of Minnesota. Several promising candidate drugs demonstrated stronger potency in activating TLR7/8 than imiquimod and resiquimod. However, small molecule TLR agonists have to traverse cell membrane and endo-lysosomal membrane to reach the intended site of action (190). In addition, due to the low molecular weight, imidazoquinoline derivatives have high diffusion coefficient in aqueous solution. The quick diffusion and drainage *in vivo* is

unfavorable in terms of reaching and maintaining therapeutic concentration over extended period. Because the co-localization of TLR agonist and tumor antigen within DC is a crucial determinant for the success of adjuvant based cancer immunotherapy, special formulation is required to enable the application of small molecule TLR7/8 agonists in cancer immunotherapy, especially for generating *in situ* whole tumor cell vaccine.

Hence, poly lactic-co-glycolic acid (PLGA) nanoparticle (NP) formulation for novel TLR7/8 agonists was investigated. We named the PLGA NP loaded with TLR agonist as immunostimulatory nanoparticle (ISNP). PLGA is a FDA approved biodegradable polymer that has been utilized as versatile delivery vehicle for small molecule drugs, proteins and nucleic acid (191). The progressive degradation and erosion of PLGA NP give rise to the sustained drug release kinetics (192). NP delivery system enhances the intracellular delivery efficiency and the drug retention in tumor matrix (193, 194). In this study, the interplay between DC and polymeric particles was evaluated. In particular, the intracellular localization of NP within DC potentially contributes to the improved delivery and efficacy of TLR7/8 agonists. In addition, the potency of ISNP in eliciting TAA-specific T cell response and profile of cytokine production *in vivo* was characterized. On the other hand, it is shown herein that DCs cross-present TAA from apoptotic BRAF V600E melanoma cells. The cross-presentation of TAA was augmented in the presence of ISNP. Thus, ISNP was used as the adjuvant component for *ex vivo* prepared prophylactic apoptotic tumor cell vaccine to protect against melanoma

challenge. In the end, in combination with BRAF inhibitor, a preliminary study was conducted to test the therapeutic vaccination strategy on BRAF V600E melanoma bearing mice. The efficacy of ISNP assisted *in situ* whole tumor cell vaccination was evaluated.

4.2 Materials and Method

4.2.1 Production of PLGA NPs

Blank PLGA NPs and coumarin-6 loaded PLGA NPs were synthesized by protocol described in the previous chapter (Page 26).

ISNPs were created using emulsion-solvent evaporation technique similarly. One mg of 522 or 3 mg of 528 or 5 mg of 520 were dissolved in chloroform within a glass vial. The glass vial was subjected to 10 minutes of heating at 60°C in a water bath to facilitate the dissolution of 522 and 528. Monophosphoryl Lipid A (MPL-A Salmonella enterica serotype Minnesota Re 595, Re mutant) (Sigma-Aldrich) was prepared as a 2 mg/mL stock solution in 80% chloroform/20% methanol. To the chloroform solution of containing TLR7/8 agonist, 100 mg of PLGA were added. For dual TLR agonists loaded ISNP, 200 μg MPL-A were added as well. The emulsion was formed with 8 ml of 2.5% polyvinyl alcohol (PVA) aqueous solution (87%-90% hydrolyzed, 30,000-50,000 Da, Sigma), and the dispersion was sonicated (20 W for 5 minutes) with a tip sonicator (Misonix Sonicator 3000) on ice bath. This emulsion was then stirred for 18 hours at

ambient conditions in a chemical hood followed by another hour under vacuum to completely remove chloroform. NPs were recovered by ultracentrifugation (Optima XPN-80 ultracentrifuge, Beckman Coulter) at 35,000 rpm for 35 min at 4°C and then washed three times with endotoxin free water. The ISNPs were stored in the lyophilized form.

To characterize TLR7/8 agonist loading in ISNPs, the drug in approximately 1 mg ISNP was extracted with 1 ml methanol overnight. The concentration of TLR7/8 agonist was characterized by HPLC. A Beckman Coulter HPLC system (Fullerton, CA) equipped with System Gold 125 solvent module, System Gold 508 auto-injector, FP-2020 plus fluorescence detector (JASCO Inc., Easton, MD) and Eclipse C-18 reverse-phase HPLC column (Agilent product, 4.6 × 150 mm; 4 μm particle size) was used. The mobile phase consisting of 50% (v/v) acetonitrile, 50% (v/v) ammonium acetate buffer pH 4.0 was run with isocratic mode at a flow rate of 1 ml per minute. Acetate buffer was made by dissolving 145 mg ammonium acetate and 0.62 ml glacial acetic acid in 500ml water. The fluorescence detector was set at 260nm for excitation and 340 nm for emission. One mg TLR7/8 agonist was weighed in a microcentrifuge tube and dissolved in 1 ml DMSO to give a 1 mg/mL concentration stock solution. Serial dilutions were performed to generate a standard curve. For *in vitro* release study, TLR7/8 agonist loaded ISNPs were dispersed in 5 ml PBS release buffer. The total TLR7/8 agonist concentration was kept below 15% of its aqueous solubility to maintain sink condition. Release buffer was incubated in a 37°C shaker. Release buffer was sampled at various time points by dialysis via

MicroKros polysulfone hollow fiber filtration device with a molecular weight cut off value of 50 kD (Spectrum Labs, Rancho Dominguez, CA). The filtrate was lyophilized and extracted with methanol for HPLC analysis.

Ovalbumin (OVA) loaded NPs were produced using a double emulsion-solvent evaporation technique. PLGA (100 mg) was dissolved in 1 ml of chloroform. For OVA co-loaded ISNPs, PLGA was dissolved in 1 ml chloroform supplemented with 1 mg 522 or 5 mg 520 or 200 μg MPL-A. OVA (5 mg) was dissolved in 200 μL PBS buffer and added into PLGA chloroform solution. A primary emulsion was created by sonicating the mixture at 5.0 power setting for 30 seconds. A secondary emulsion was then generated in 8 ml of 2.5% PVA solution under sonication (20 W for 5 minutes) on an ice bath. This emulsion was stirred for 18 hours at ambient conditions and then for 1 hour under vacuum. NPs were recovered by ultracentrifugation (35,000 rpm for 35 minutes at 4°C) and then washed three times with Hyclone™ endotoxin free cell culture grade water (Thermal Scientific). OVA loading in NPs were characterized by dissolving PLGA NPs in 0.1 N NaOH for bicinchoninic acid assay (Pierce™ BCA Protein Assay Kit, Thermo Scientific)

4.2.2 Interaction between polymeric particles and DC

JAWSII mouse DC cell line was purchased from ATCC (ATCC® CRL-11904™). JAWSII cells were maintained in alpha minimum essential medium supplemented with 10% fetal bovine serum (FBS) and 5 ng/ml murine GM-CSF (PeproTech, Rocky Hill,

NJ). The JAWSII cells were allowed to grow to 40-50% confluency in a 24-well cell culture plate. Cross-linked poly (styrene/2% divinylbenzene) microsphere with 4.16 μm mean diameter (Bangs Laboratory, Fishers, IN) was added into cell culture plate. Phagocytosis of microsphere by JAWSII cells was monitored under a Carl Zeiss fluorescent microscope. For NP-DC interaction study, bone marrow derived dendritic cells (BMDCs) were generated according to protocol described in the previous chapter (page: 90). One million of Day 6 BMDCs were seeded into 24-well cell culture plate. Coumarin-6 loaded PLGA NPs were added at 0.2mg/ml final concentration for two hours. At the end of the co-incubation, all cells were collected including adherent cells by 5-minute treatment of non-enzymatic cell dissociation solution (Sigma-Aldrich, St. Louis, MO). Untreated BMDCs were collected as control. BMDCs were dispensed into flow cytometry assay tubes and washed twice with PBS. BMDCs were re-suspended in 0.5 mL FACS buffer (1X PBS buffer supplemented with 1% BSA and 0.05% sodium azide) for flow cytometry analysis.

4.2.3 Confocal imaging for the intracellular localization of PLGA NP within BMDCs

MatTek glass bottomed petri dishes (NO.1.5 coverslip thickness 0.16-0.19 mm) were coated with poly-lysine. Poly-lysine stock solution (25 mg/mL) was diluted in cell culture grade endotoxin free water to achieve 100 μg/ml working concentration. 200 μl poly-lysine working solution was dispensed onto the coverslip bottomed petri dish for pretreatment. The coated petri dish was kept at incubator for 30 minutes followed by two washing with endotoxin free water and air-dried briefly within laminar flow cell culture

hood. Day 6 BMDCs (0.1 Million) were seeded onto the dish in 3 mL RMPI-1640 medium with 10% FBS overnight for attachment. For morphological characterization study, triple color labeling was carried out to highlight nucleus, lysosome and cell membrane (Figure 4-1). BMDCs was incubated with 1 μM 4',6-diamidino-2-phenylindole (DAPI) and 50 nM lysotracker green in complete cell culture medium for 30 minutes within a cell culture incubator. BMDCs were further incubated with 5 μg/mL wheat germ agglutinin-tetramethylrhodamine conjugate (WGA) in Hank's balanced salt solution (HBSS) for another 10 minutes. The culture medium was replaced with pre-cooled phenol red free RPMI-1640 supplemented with 50 nM lysotracker green and 10 mM HEPES. The petri dish was kept on ice and covered with foil prior to live cell confocal imaging. Olympus Fluoview 1000 inverted scanning laser confocal microscope was used to conduct live cell imaging. 100X oil immersion lens (Numerical Aperture: 1.3) was chosen as objective lens under 2.5 X digital zoom. Images were taken at a size of 512 X 512 pixels (50.589 μm- 50.589 μm; 0.099 μm per pixel) with 20 μs/pixel dwelling time using line sequential one-way direction scanning mode. Raw data images were processed by Olympus Fluoview viewer 2.0 software.

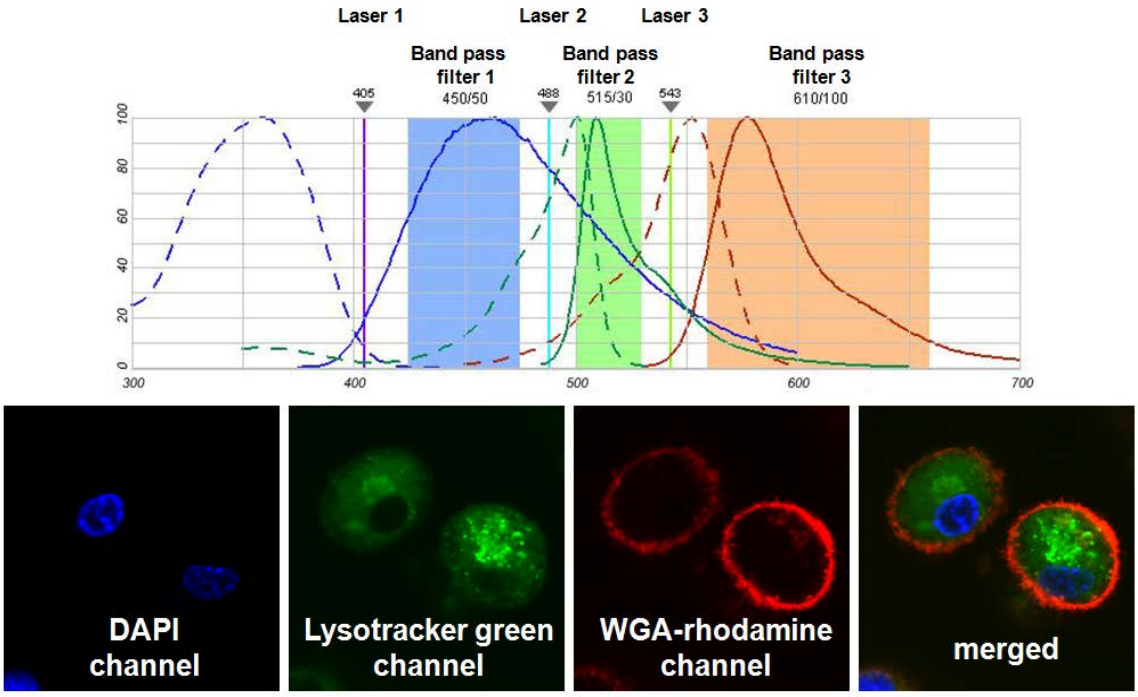

Figure 4-1. Confocal imaging filter sets for BMDCs characterization encompassing nucleus, lysosome and cell membrane.

To study the intracellular localization of coumarin-6 labeled PLGA NPs within BMDCs, 0.1 mg coumarin-6 PLGA NPs were added per dish for two hours. Medium was aspirated and the petri dish was washed once with fresh medium. BMDCs were incubated with 50 nM lysotracker red in complete culture medium for 30 minutes. The cell culture medium was replaced with pre-cooled phenol red free RPMI-1640 supplemented with 50 nM lysotracker red and 10 mM HEPES. The petri dish was kept on ice and covered with foil prior to live cell confocal imaging (Figure 4-2).

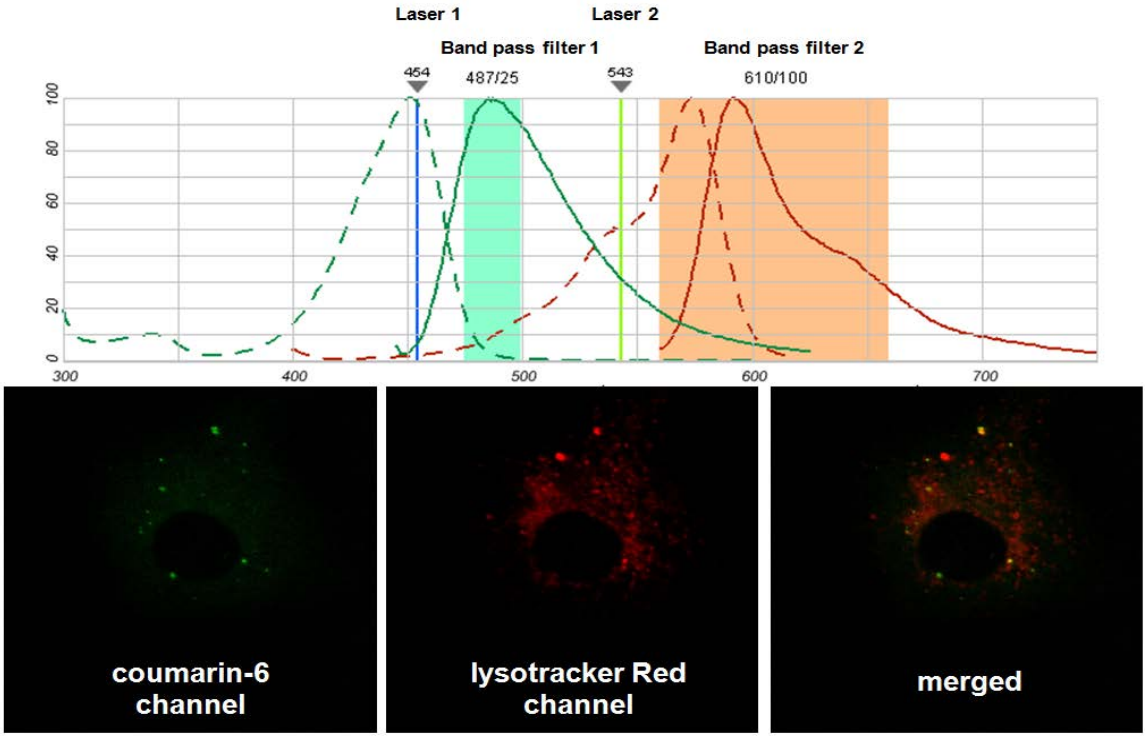

Figure 4-2. Confocal imaging filter sets for probing the intracellular localization of coumarin-6 loaded PLGA NPs in relation to the endo-lysosome.

4.2.4 Reporter cell line for assessing the activity of TLR7 agonist formulation

HEK-Blue™-mTLR7 Cell was used as the murine TLR7 reporter cell. The assay was carried out according to manufacturer's instruction (InvivoGen, San Diego, CA). Agents that activate mouse TLR7 signaling pathway trigger the release of the secreted embryonic alkaline phosphatase (SEAP) into cell culture medium supernatant. Reporter cells were seeded at 50,000 per well density into 96-well plate one day before treatment. Blank PLGA NP and 522 loaded ISNPs were provided at 0.1 or 0.3 mg/mL final concentration for stimulation. The loading of 522 ISNPs were 1 μg 522/mg NP in both 522 single agent

loaded ISNP and 522/MPL-A dual agents loaded ISNP. Free 522 drug in soluble format was tested at concentrations ranging from 0.1 μg/mL to 10 μg/mL. Treatments were prepared in 100 μl DMEM culture medium and added into 96-well plate at the second day. After 24 hours incubation, QUANTI-Blue™ substrate was used for color development. 20 μL of cell culture supernatant was added into 200 μL QUANTI-Blue™ for colorimetric assay.

4.2.5 Flow cytometry for activated BMDCs

One million of Day 6 BMDCs aliquots were placed into a 24-well cell culture plate. For NPs treated groups, blank PLGA NPs or ISNPs were added into the cell culture medium at 0.1 or 0.3 mg/mL final concentration for 24 hours. Free drugs in soluble format were added at doses equivalent to that of loaded in ISNP formulations. At the end of the incubation, all cells were collected including adherent cells, which were dislodged by 5-minute treatment using non-enzymatic cell dissociation solution (Sigma-Aldrich, St. Louis, MO) to preserve the cell surface markers. BMDCs were dispensed into assay tube and washed twice with PBS before incubation with 100 μL FACS buffer at 4°C for at least 10 minutes to block non-specific binding in general. FcγIII and FcγII receptors on BMDCs were blocked by incubating with FACS buffer supplemented with rat anti-mouse CD16/CD32 (Mouse BD Fc Block™) for 5 minutes to prevent non-specific antibody binding via Fc receptors. Subsequently, dual staining for BMDCs was carried out by pairing a PE labeled hamster anti-mouse CD11c antibody (Clone: HL3) with another

FITC labeled antibody against co-stimulatory markers, such as FITC rat anti-mouse CD86 (Clone: GL1) or FITC rat anti-mouse CD40 (Clone: 3/23) on ice for 30 minutes. Antibody isotype control tube was stained with FITC rat IgG2a, Kappa isotype control and PE labeled hamster IgG1, Lambda 1 isotype control. Stained cells were washed twice with 2-3 mL FACS buffer and then suspended in 0.5 mL FACS buffer for data acquisition on BD FACSCalibur flow cytometer. The first gate encompassed the major population cluster based on forward scattering (cell size) and side scattering (cell internal granularity). Compensation was conducted with single stained mature BMDCs cells. The BMDCs were further gated as CD11c positive population. Flow cytometry data were analyzed by FlowJo software.

4.2.6 Apoptotic cell death of SM1 cells induced by BRAF inhibition

SM1 cell line and SM1-OVA cell line are generous gifts from Dr.Antoni Ribas lab at University of California, Los Angeles. Both cell lines were maintained in RPMI-1640 cell culture medium supplemented with 10% FBS and penicillin/streptomycin. For viability study, the CellTiter 96® AQueous non-radioactive cell proliferation assay was used according to the manufacturer's instruction (Promega, Madison, WI). The assay solution consists of a tetrazolium compound MTS and an electron coupling reagent phenazine methosulfate (PMS). The substrate can be converted to a formazan product by viable cells. SM1 cells were seeded into 96-well cell culture plate at 30,000 cells per well density in 50 μL medium. Vemurafenib (LC Laboratories, Woburn, MA) was dissolved in DMSO at 15 mg/mL as stock solution and diluted into cell culture medium at various

working concentrations ranging from 20 μM to 10 nM. SM1 cells were cultured for 72 hours before the substrate color development. 20μl per well of MTS/PMS solution was added for one hour incubation. The absorption was acquired at the wavelength of 490nm using a microplate reader.

4.2.7 *In vitro* cross-presentation of OVA by BMDCs

Day 6 BMDCs were seeded at one million per well density in 24-well cell culture plate. BMDCs were pulsed with soluble OVA protein at 15 μg/ml final concentration or OVA loaded NPs with equivalent protein dose for two days. Positive control BMDCs were pulsed with 10 mg/ml OVA and 1 μg/ml LPS. For monitoring the cross-presentation of tumor associated antigen, SM1-OVA cells were seeded at density of 1 million per well in 6-well plate. SM1-OVA cells were treated with 15 μM vemurafenib for three days to induce apoptosis. Non-adherent apoptotic SM1-OVA cells were collected and washed with PBS twice. Apoptotic cells were co-incubated with day 6 BMDCs in the absence or presence of 0.2 mg/ml 522 loaded ISNP for 48 hours. For flow cytometric assay, BMDCs were stained using PE labeled anti-mouse CD11c and APC labeled anti-mouse H-2Kb bound to SIINFEKL antibody (eBioscience, clone: 25-D1.16) to identify the $CD11c^+$ BMDC population that displays MHC I/OVA peptide complex.

4.2.8 *In vivo* study on the induction of CTL response via ISNP vaccine formulations

C57BL/6J mice were purchased from Jackson Laboratories and maintained in specific pathogen-free facilities at the research animal resources at the University of Minnesota. Mice were immunized with formulations such as 2 mg of OVA loaded NP, OVA/522 co-loaded ISNP, OVA/520 co-loaded ISNP or OVA/MPL-A co-loaded ISNP. The vaccine formulations were injected subcutaneously at thigh region, which drains to inguinal lymph node. 50μl of solution was injected at left thigh subcutaneously and 50μl of solution was injected at right thigh at the same time. Vaccination schedule consisted of five doses in total for each mouse, namely first four consecutive days in a row and a final booster at day 6. There were four mice per group for each experimental treatment. Mouse total bloods were collected at Day7. For flow cytometric analysis of circulating OVA-specific $CD8^+$ T cells, a Becton Dickinson Canto three-laser flow cytometer was used for data acquisition. Anti-mouse CD8α-Pacific Blue (clone 53-6.7) was purchased from eBioscience. A SIINFEKL/Kb dextramer-PE was used for detection of SIINFEKL/Kb-binding $CD8^+$ T cells (Immunodex). For whole-blood staining, 50 μl blood was obtained via orbital bleed and placed in 100 μl of heparin supplemented PBS. Five μl of SIINFEKL/Kb dextramer was added to blood and incubated at room temperature for 10 minutes, and 1 μl (0.5 mg) anti-mouse CD8 antibody was added to cells and incubated for an additional 20 minutes at room temperature. Blood was lysed by adding 1 ml 1:10 dilution lysis buffer (BD Pharmingen), incubated for 10 minutes at room temperature, centrifuged twice and re-suspended in 100 μl PBS. Flow cytometry data was analyzed with FlowJo software (Tree Star, Inc.).

For tumor lysate vaccine formulation, SM1-OVA tumor cell lysates were prepared by dissociating cells with non-enzymatic dissociation solution (Sigma), washing twice with PBS, re-suspending in 500 μl PBS, and freezing initially by placing in −80°C freezer overnight. Cells were further lysed by five cycles of freezing in liquid nitrogen and thawing in a 56°C water bath. Cell debris was pelleted by centrifugation at 14,000 rpm and the protein concentration of the supernatant was determined using a Bradford assay. Pellets were re-suspended and lysates were stored at −80°C until use. Each vaccine formulation was prepared on the day of vaccination and consisted of 65 μg protein tumor lysate with or without ISNPs. For NP containing vaccine formulations, 2 mg blank PLGA NP, 2 mg 522 ISNP containing 1.8 μg 522 and 2 mg 520 ISNP containing 39.7 μg 520 were used respectively.

4.2.9 Preventative vaccination with apoptotic B16 cells vaccine formulations

C57BL/6J mice were purchased from Jackson Laboratories and maintained in specific pathogen-free facilities at the research animal resources at the University of Minnesota. B16 melanoma cells were irradiated (160Gy) immediately before vaccination. Apoptotic B16 melanoma cells were washed twice with PBS to eliminate serum protein from cell culture medium. One million irradiated B16 cells were combined with 2 mg PLGA NP or 2 mg 522 ISNP (1.8 μg 522) or 2mg 520 ISNP (30 μg 520) in 100 μL PBS as the whole tumor cell vaccine formulations. 50μl of vaccine formulation was injected at left thigh

subcutaneously and 50μl of solution was injected at right thigh at the same time. Three doses of vaccination were carried out with six days interval. Two days after the last booster dose, tumor challenge was initiated by intradermal injection of 5 X 10^4 B16 cells at the right flank. Tumor growth was monitored by manual measurement using a caliper. Tumor volume was calculated using the formula $V = L \times W^2 \times 0.5$.

For another parallel study monitoring cytokine profile of lymphocytes following vaccination, the same vaccination regimen was conducted. Two days after last vaccination, lymphocytes isolated from inguinal lymph nodes or splenocytes were plated at a concentration of 5×10^5 cells per well and pulsed with irradiated apoptotic B16 cells or GP100 peptide for 24 hours. After incubation, 50 μl culture supernatant was analyzed for a panel of secreted cytokines using a Th1/Th2/Th17 flow cytometric bead array according to the manufacturer's protocol (BD Biosciences).

4.2.10 *In situ* generated therapeutic tumor vaccine for BRAF mutant positive mouse melanoma

C57BL/6 strain was used as the immunocompetent melanoma bearing mouse. BRAF mutant positive melanoma was initiated via subcutaneous inoculation of one million SM1 cells. Tumor length (L) and width (W) were measured manually by caliper. Tumor volume was calculated using the formula $V = L \times W^2 \times 0.5$. Induction of SM1 apoptotic death was achieved by administering BRAF inhibitor vemurafenib (PLX-4032). Vemurafenib treatment commenced when tumors reach at least 50 mm^3 in volume. The

daily vemurafenib regimen was given in an oral dosing of 50 mg/kg once a day (P.O.). The vemurafenib formulation was made by diluting stock solution (100 mg/mL in DMSO) in diluents consisting of tween 80-ethanol-water (20:13:67) (195). Four days after starting vemurafenib regimen, single dose NP-assisted *in situ* therapeutic vaccination was generated by intratumoral injection of NP formulations. NPs were dispersed within 100 μl PBS buffer for injection. For cohorts receiving therapeutic vaccination, intratumoral injection of 2 mg PLGA NP, or 2 mg 528 loaded ISNP in 100 μL PBS was conducted. For *in situ* vaccination control group, single dose of 100 μL saline was injected intratumorally in the absence of NP formulations. Daily vemurafenib dosing was maintained throughout the whole study. For untreated vehicle control group, only tween 80-ethanol-water (20:13:67) solution without BRAF inhibitor was administered via oral gavage.

4.2.11 Evaluation on the affinity of cRGD peptide conjugated NPs for melanoma cell lines

cRGD and cRAD decorated PLGA NPs were made using a previously reported protocol (196). One mg of coumarin-6 loaded cRGD NPs and cRAD NPs was re-suspended in 0.5 mL cold serum free medium and sonicated at 5.0 power for 30 seconds. Re-suspended NPs were adjusted to a final concentration of 1 mg/mL. Human BRAF V600E positive melanoma cell line A375P is a generous gift from Dr. James McCarthy's lab at University of Minnesota. Adherent A375P cells were dislodged by pipetting forcefully. Adherent SM1 cells were dislodged by non-enzymatic dissociation buffer and 200,000

cells were transferred into a 1.5 mL microcentrifuge tube. Cells were pre-cooled in 1 mL cold complete culture medium for one hour at 4°C before adding 50 μL NP suspensions into each tube. Incubation was carried out at 4°C room on a rotational shaker for 15 minutes. Cells were transferred into flow cytometry tube for two washing with 4 mL PBS. After each washing, cells were centrifuged at 1,000 rpm for 5-minute. The final cell pellet was re-suspended with 1ml complete cell culture medium and incubated at incubator for another 15 minutes. Cells were centrifuged and washed with FACS buffer once before flow cytometric analysis for coumarin-6 fluorescence.

4.3 Results

4.3.1 The interaction between DC and polymeric particles

Professional phagocytes play a key role in responding to the invading pathogens. After the encounter with foreign subjects, DC is the type of professional phagocyte that determines the following immune responses by bridging innate and adaptive immunity. Firstly, in order to understand the interaction between DC and polymeric particles, JAWS II DC cells and polystyrene microparticles were co-incubated *in vitro*. DC began to phagocytose immediately after the introduction of particles. Randomly dispersed particles were enriched into DC cellular space within 24 hours (Figure 4-3), illustrating DC's dramatic ability in clearing particles. In fact, phagocytosed particles eventually occupy a significant proportion of the cellular space once DC removed most free particles.

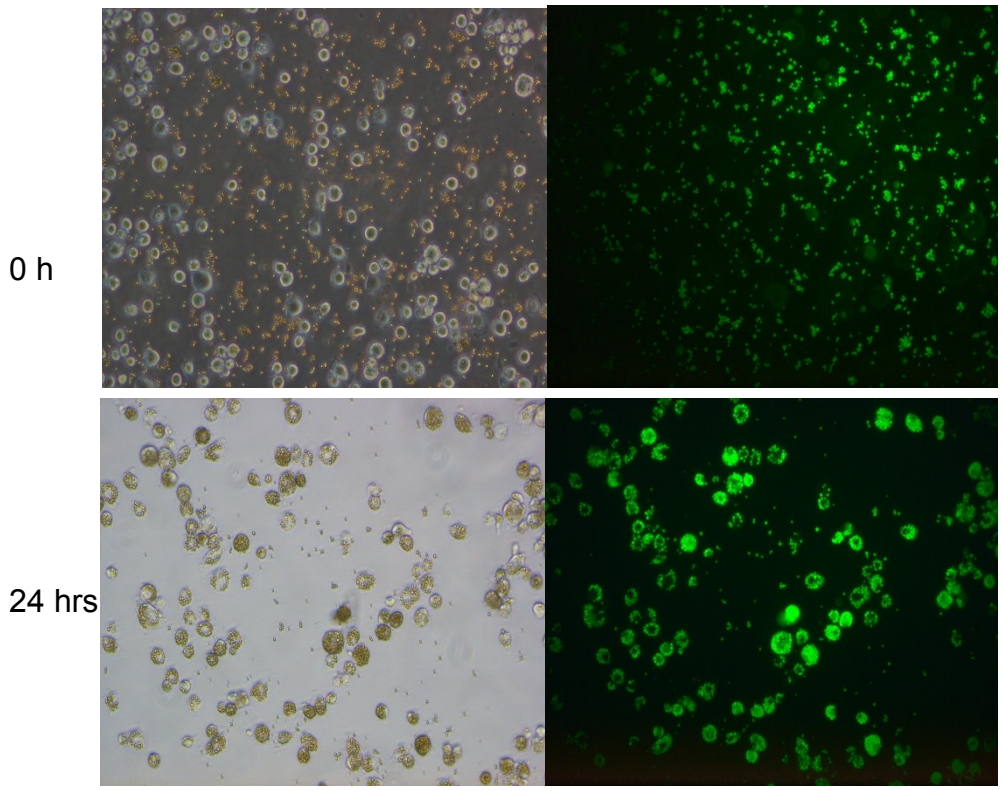

Figure 4-3. The phagocytic capability of JAW II DC in clearing fluorescent polystyrene microparticles.

Likewise, *in vitro* interaction between polymeric NP and DC was also investigated. After two hours co-incubation of BMDCs with coumarin-6 loaded PLGA NPs, a significant shift in fluorescent intensity was observed for the entire $CD11c^{+}$ BMDCs population by flow cytometry (Figure 4-4). A gate was drawn to define coumarin-6 high cell events, 90.5% of BMDCs was categorized as coumarin-6^{hi} compared with the 1.9% of untreated BMDCs population due to background auto-fluorescent signal, suggesting that BMDCs internalize PLGA NP efficiently. In addition, a population shift in side scattering was

indicative of the elevated granularity of BMDCs as a result of the increased intracellular particulate content.

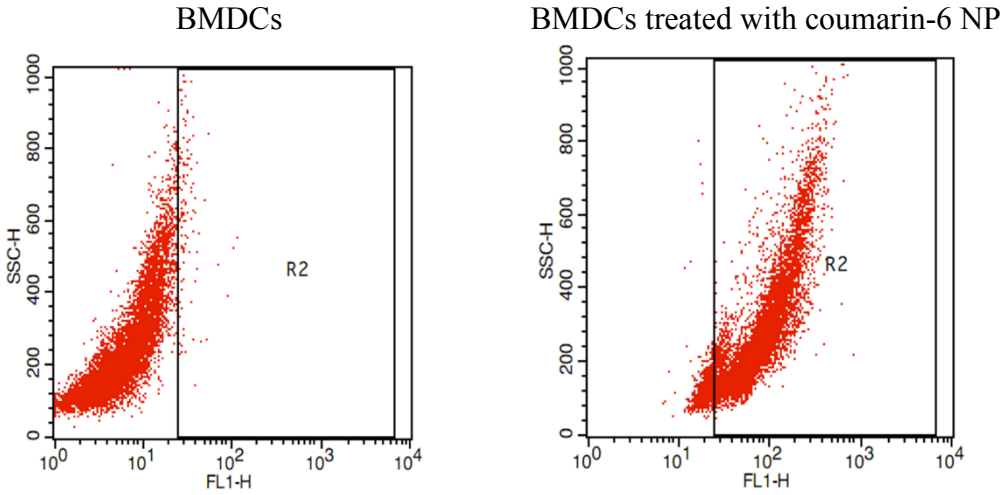

Figure 4-4. Representative dot plot of flow cytometric analysis for BMDCs incubated with 0.2 mg/ml coumarin-6 labeled PLGA NPs for two hours. Fluorescent intensity (FL1-H) was plotted against side scattering (SSC-H).

Live cell confocal imaging was conducted to confirm the internalization and interrogate the intracellular distribution of PLGA NP. Firstly, the morphology of BMDCs was probed for the validity of live cell imaging study. The brief exposure of sialic acid with Rhodamine labeled WGA delineated the contour of BMDCs' cell membrane. Corrugated and ruffled cell membrane was present, which is in agreement with the hallmark of the classical "veiled" DC morphology (Figure 4-5).

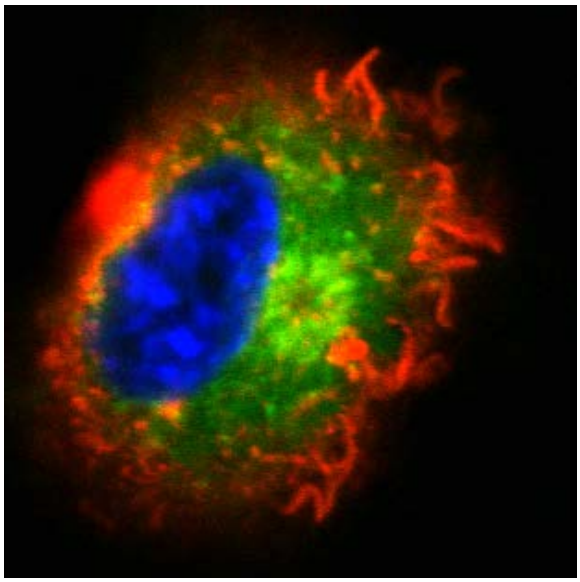

Figure 4-5. Confocal imaging was conducted for live BMDCs. Nucleus, lysosome and cell membrane were stained with DAPI, lysotracker green and rhodamine-WGA respectively.

Uptake of PLGA NP in BMDCs was corroborated. Vertical optical sectioning of adherent BMDCs via confocal microscopy proofed the presence of PLGA NPs within BMDCs cytosol. After two hours of co-incubation with BMDCs, a proportion of coumarin-6 loaded PLGA NPs was found to be yellow spots in the merged image (Figure 4-6), suggesting that PLGA NPs partially co-localized with acidic endo-lysosomal compartment. In contrast, the rest of the NPs were in their original green fluorescence. Thus, PLGA NPs were also located either in the cytoplasm or other non-acidic compartments.

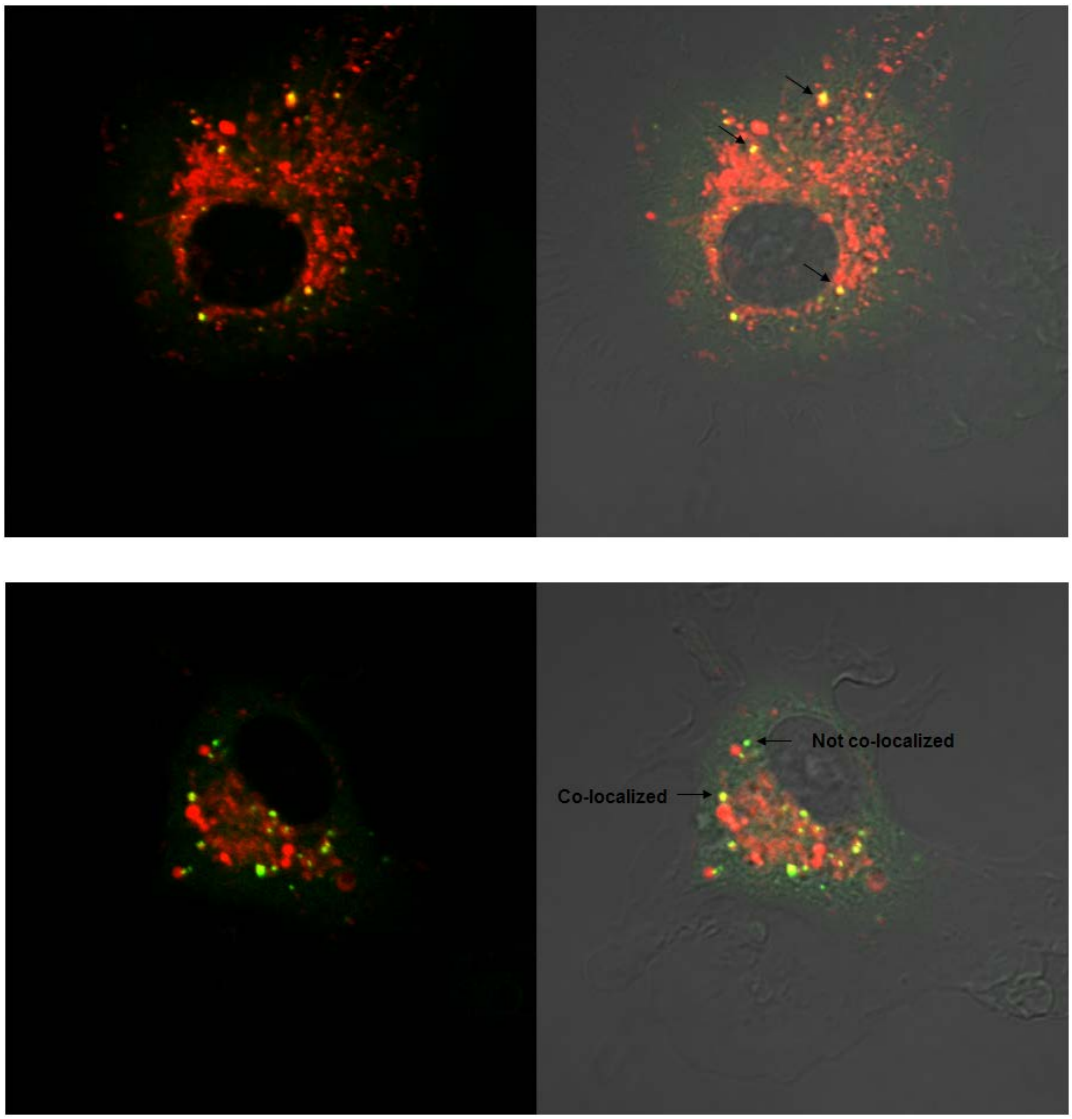
Not co-localized
Co-localized

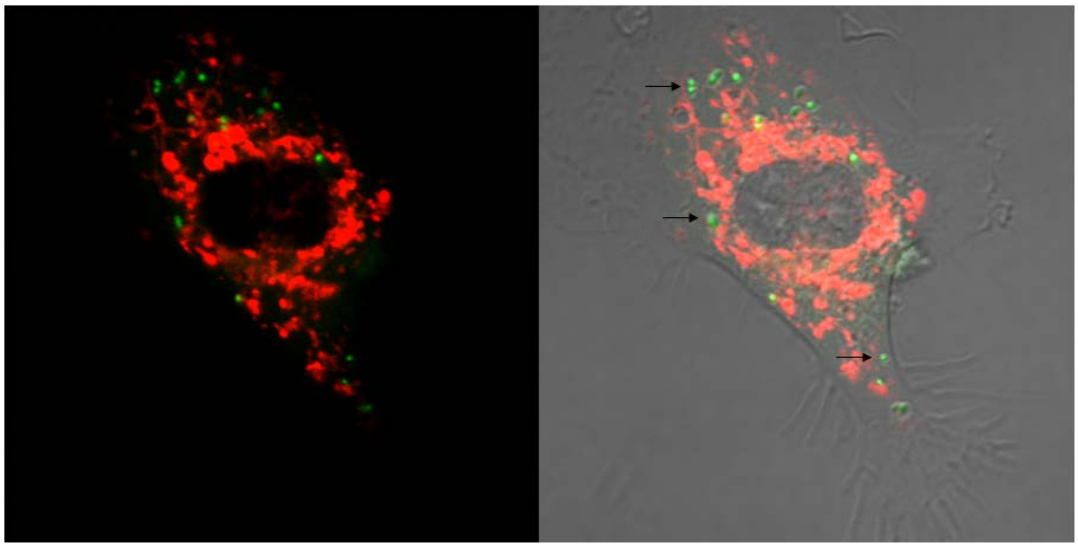

Figure 4-6. Live cell confocal imaging was conducted to study the intracellular distribution of PLGA NP within BMDCs. PLGA NPs were labeled with coumarin-6 (green fluorescent). Endo-lysosome was stained with lysotracker red. Right panel images were superimposed on differential interference contrast (DIC) images. Arrows highlight the representative intracellular NPs.

4.3.2 PLGA NP formulation for small molecule TLR7/8 agonists

Based on our imaging study, PLGA NP gained prompt access to the intracellular space of DC and endo-lysosomal compartment efficiently. In order to further improve the TLR7 agonist drug delivery efficiency, a novel candidate TLR7 agonist coded 522 was loaded into PLGA NP as 522 ISNP formulation. We hypothesized that PLGA NP could boost the efficacy of imidazoquinoline analogues by delivering sustained drug release directly at the luminal side of endo-lysosome. Firstly, 522 was encapsulated into single TLR7 agonist loaded ISNP at a loading quantity of 1 μg 522/mg ISNP. The average size of 522

was 207nm with a 0.129 polydispersity index and negative surface charge similar to blank PLGA NPs (Zeta Potential: -31.94 mV in water). Meanwhile, 522 was co-encapsulated with MPL-A to form the dual TLR agonists loaded ISNP. The loading of 522 in the dual TLR agonists loaded ISNP was identical to that of the single TLR7 agonist loaded ISNP.

The activity of 522 in ISNP formulations was evaluated in a HEK-293 reporter cell line expressing mouse TLR7. Blank PLGA NP and MPL-A single TLR4 agonist loaded ISNP as negative controls did not activate the reporter cell line, while free 522 drug in soluble format, 522 ISNP and 522/MPL-A dual agonists ISNP activated reporter cell line in a dose dependent manner. Compared to the equivalent dose of free drug, ISNP formulations slightly augmented the efficacy of 522 at a low concentration of 0.1 mg/mL, but not at higher concentration of 0.3 mg/mL (Figure 4-7).

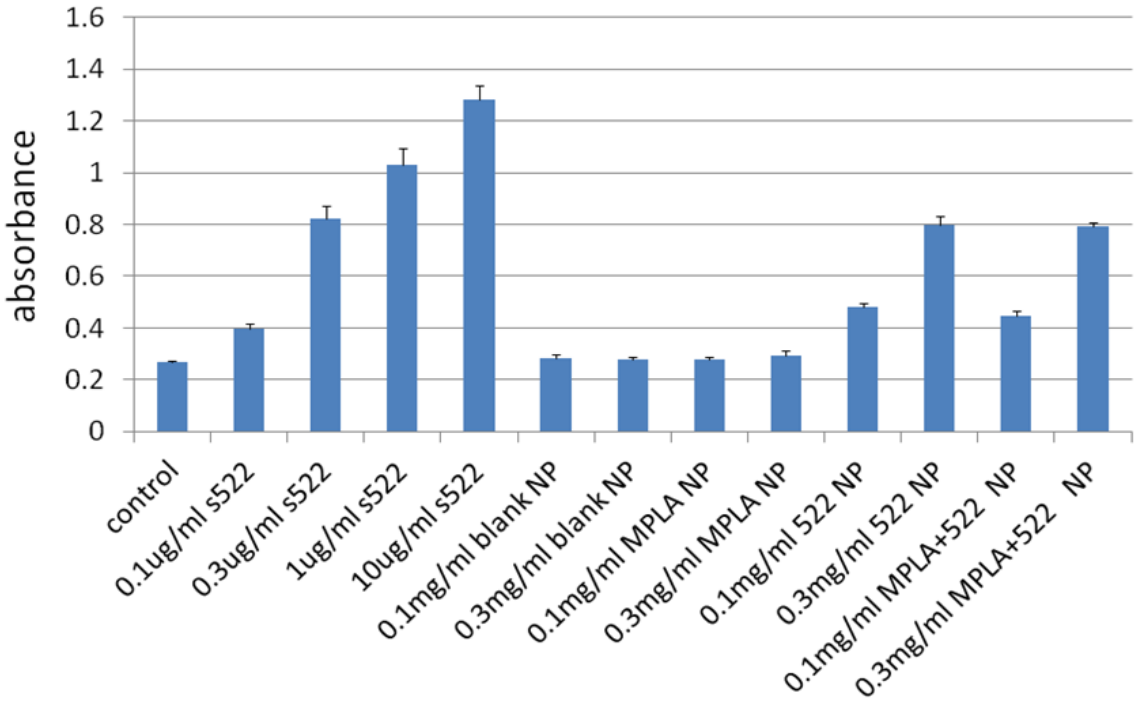

Figure 4-7. The potency of 522 loaded ISNP formulations and free 522 drug in soluble format (s522) at equivalent dose were screened using a mouse TLR7 reporter cell line. The loading of 522 in NP formulations is 1 μg 522/ mg NP. Activation of TLR7 by its agonist triggers the expression of secreted embryonic alkaline phosphatase (SEAP), which converts substrate QUANTI-Blue™ into purple/blue color.

In contrast, BMDCs demonstrated differential responsiveness towards free 522 drug and 522 loaded ISNP formulations. First of all, 522 activated BMDCs as shown by the up-regulation of the co-stimulatory molecules CD40 (Figure 4-8) and CD86 (Figure 4-9). However, unlike the mouse TLR7 reporter cell line (Figure 4-7), the activation of BMDCs via free drug format demonstrated little dose dependency between 0.1 μg/ml and 1 μg/ml 522 concentrations, potentially reaching an efficacy plateau at this dose range.

But 522 loaded ISNP led to dose dependent activation and stronger up-regulation of CD40 and CD86 compared to the free drug at equivalent dose. In fact, 522 ISNP format at 0.1 mg NP/mL (0.1 μg 522/mL) dosing concentration outperformed tenfold higher concentration of 522 free drug (1 μg 522/mL) in terms of co-stimulatory molecules up-regulation, suggesting that intracellular TLR7 agonist delivery via ISNP improved DC activation and conferred dose-sparing effect. In addition, dual TLR agonists loaded ISNP resulted in the maximum *in vitro* up-regulation of co-stimulatory molecules, indicating that simultaneously engaging multiple TLR receptors translated into more robust BMDCs activation.

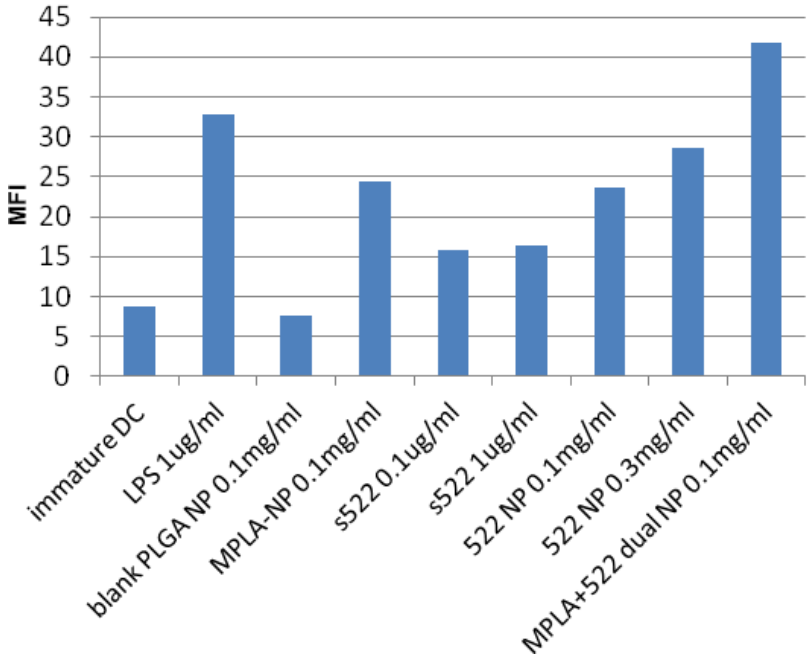

Figure 4-8. Mean fluorescent intensity of co-stimulatory molecule CD40 expression on BMDCs stimulated with either 522 ISNP formulations or free drug (s522) at equivalent dose by flow cytometry. The loading of 522 in NP formulations is 1 μg 522/ mg NP.

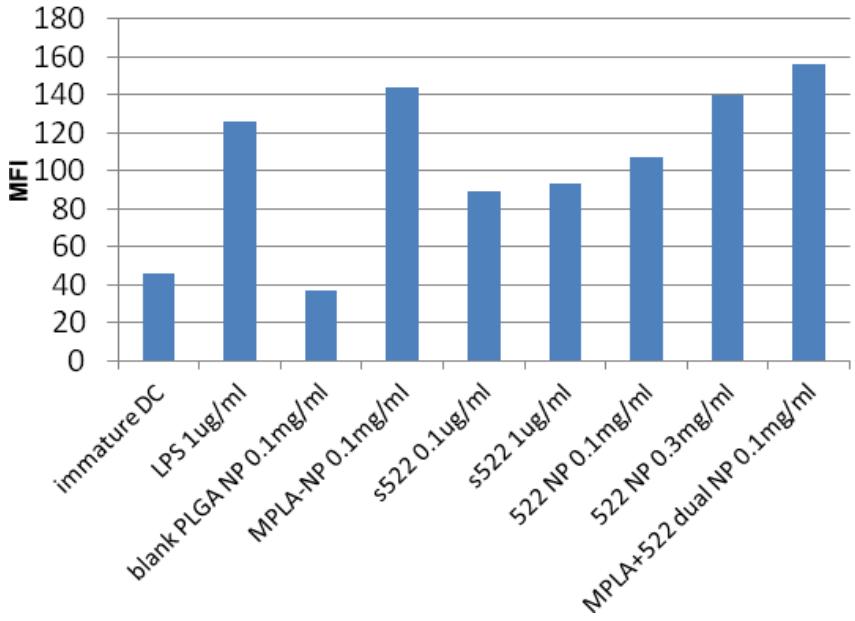

Figure 4-9. Mean fluorescent intensity of co-stimulatory molecule CD86 expression on BMDCs stimulated with either 522 ISNP formulations or free drug (s522) at equivalent dose by flow cytometry. The loading of 522 in NP formulations is 1 μg 522/ mg NP.

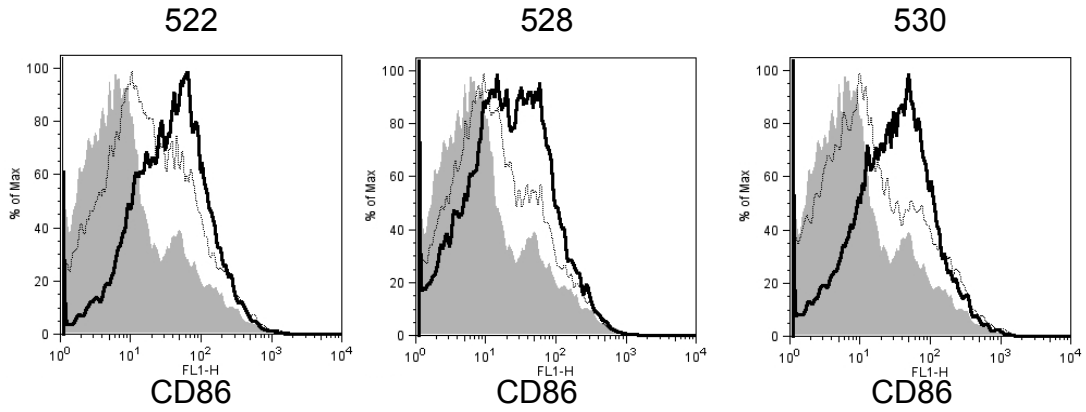

Figure 4-10. Representative flow cytometric histograms of co-stimulatory molecule CD86 expression on BMDCs stimulated with either ISNP formulations or free drug at equivalent dose. (Legend: grey shade denotes isotype control. Thin solid line denotes soluble drug. Thick solid line denotes equivalent dose of drug in ISNP.)

Meanwhile, the same dose sparing and efficacy boosting capability of ISNP formulations were repeatedly demonstrated across a series of TLR7/8 agonists. 522 contained a chiral carbon in the structure and existed as a racemic mixture. 528 is the chirally active enantiomer of the 522 racemic mixture. Similar to 522 ISNP, 528 loaded ISNP induced stronger co-stimulatory molecule expression on BMDCs than equivalent dose of free drug (Figure 4-10). Likewise, the ISNP formulations of 520 and 530 also augmented their efficacy in stimulating BMDCs compared to the equivalent dose of free drug.

On the other hand, in order to improve the limited loading of 522 and 528 in ISNP formulations, novel TLR7/8 agonists with higher hydrophobicity such as 520 were

synthesized at University of Minnesota. In general, the 522 loading was in the range of 0.9 to 1 μg drug/ mg ISNP, while the 528 loading was no more than 4 μg drug / mg ISNP. The loading of hydrophobic compound was improved significantly and a loading of 19.8 μg drug / mg ISNP was achieved for 520 ISNP formulation. In addition, the *in vitro* release profile of ISNPs was assessed. More than 40% of the loaded 528 was released in the first hour followed by a slower secondary release phase (Figure 4-11). More than 80% of 528 was released within 24 hours. The 520 release profile also consisted of the initial burst release phase and the secondary phase with slower release. However, only one thirds of the loaded 520 was released after 6 days *in vitro* (Figure 4-12).

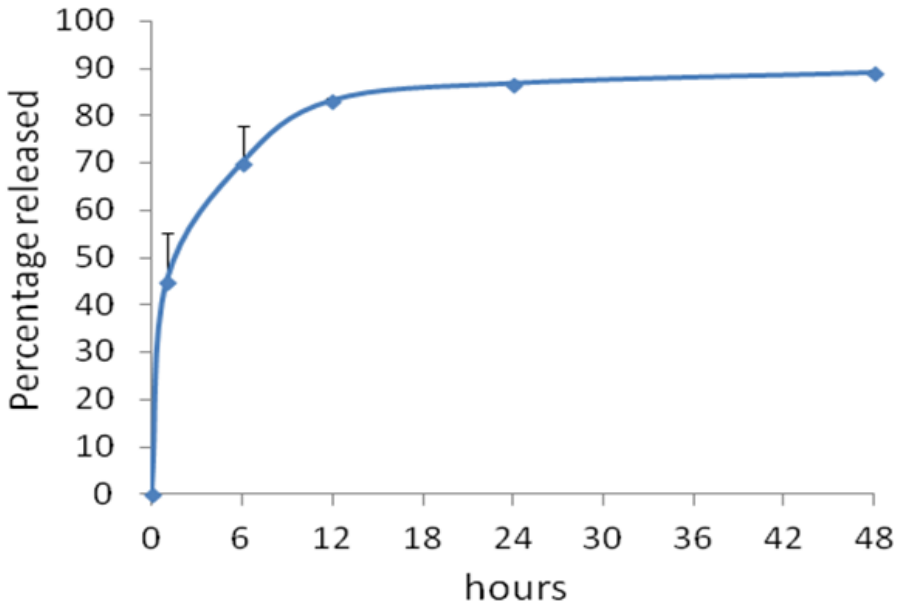

Figure 4-11. *In vitro* release profile of 528 loaded ISNP.

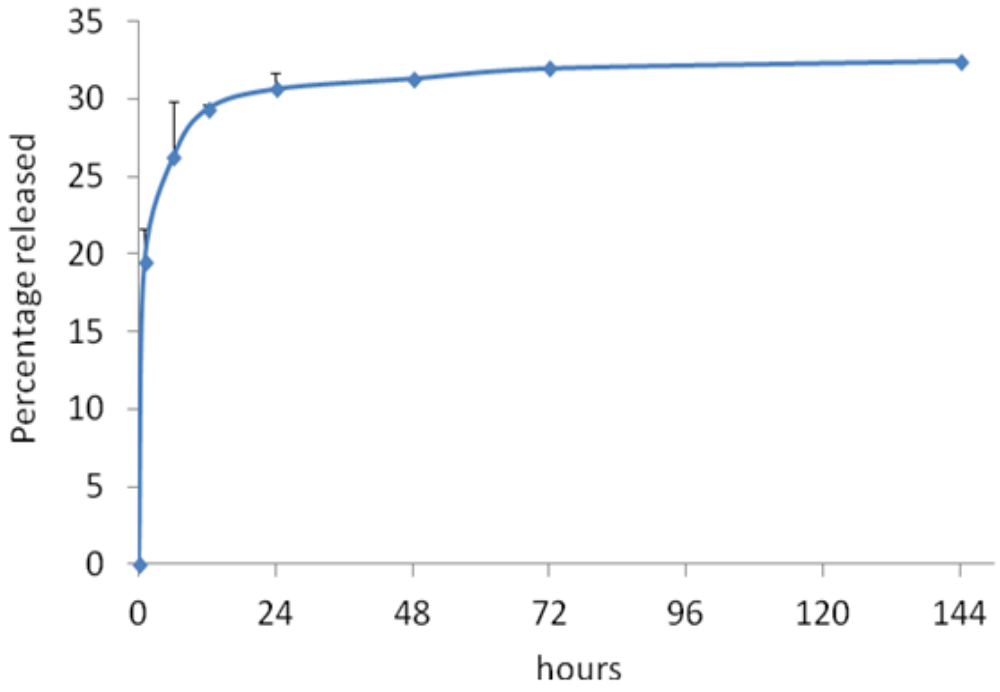

Figure 4-12. *In vitro* release profile of 520 loaded ISNP.

4.3.3 ISNPs promote antigen cross-presentation *in vitro*

SM1 is a BRAF V600E harboring murine melanoma cell line syngeneic to immunocompetent C57/B6 mice (197). SM1-OVA cell is its derivative cell line expressing OVA as a model tumor associated antigen. In order to assess DC-apoptotic cell interaction in the presence of ISNP, vemurafenib were used to trigger the apoptosis of SM1 cells. The SM1 cell line is semi-resistant to the vemurafenib mediated BRAF inhibition as shown by the viability-drug concentration curve (Figure 4-13). High concentration of vemurafenib at (>10 μM) was required to inhibit 90% of SM1 cells.

Thus, SM1-OVA cells were treated with 15 μM vemurafenib for the DC co-incubation study.

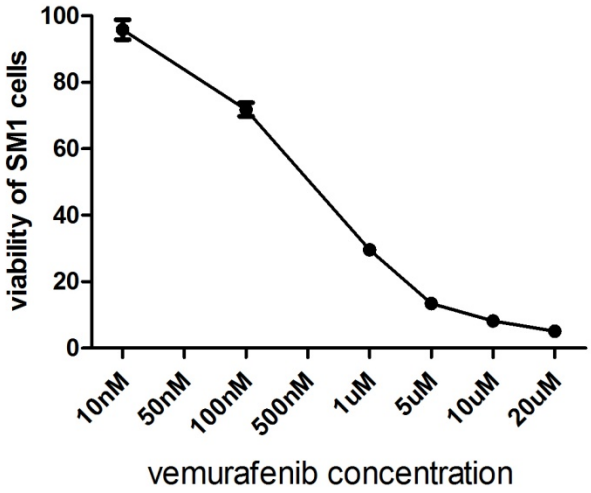

Figure 4-13. Effect of BRAF inhibitor vemurafenib on the viability of SM1 cells.

DC cross-presentation of antigen is instrumental in priming CTL proliferation, a key step in creating *in situ* vaccination against BRAF V600E melanoma. OVA derived peptide SIINFEKEL is the immune dominant T cell epitope processed by DC and mounted onto MHC I for cross-presentation to CTL. DC acquired tumor associated antigen OVA from apoptotic SM1-OVA cells, as demonstrated by the presentation of SIINFEKL on MHC I (Figure 4-14). In the presence of 522 ISNP, the cross-presentation of OVA from apoptotic cells was further enhanced (Figure 4-15). On the other hand, for OVA loaded NP formulation, the presence of TLR agonists promoted the cross-presentation efficiency significantly (Figure 4-14). All the OVA ISNPs consistently generated stronger cross-presentation than the OVA NP. 522 possessed the highest ability in facilitating this

process, illustrating the importance of DC activation and TLR engagement in mobilizing cross-presentation machinery.

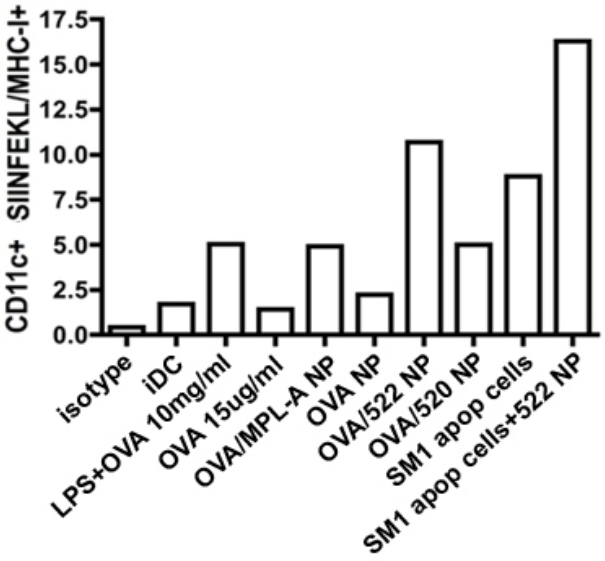

Figure 4-14. The percentage of CD11c+ BMDCs that cross-present OVA derived peptide SIINFEKL on MHC I.

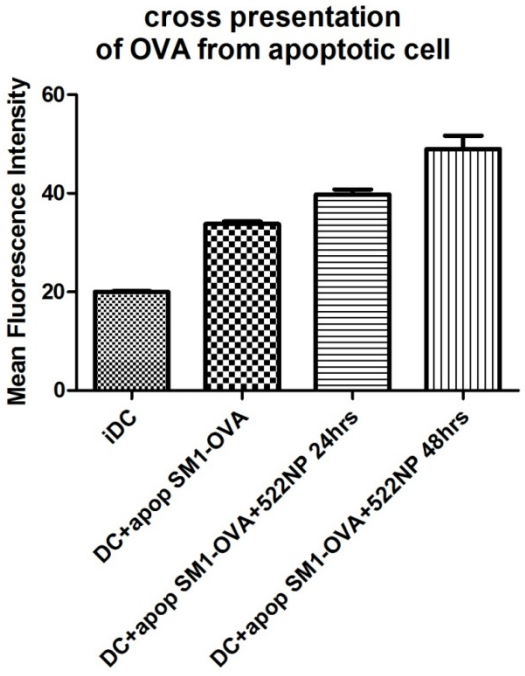

Figure 4-15. Cross-presentation of tumor associated antigen from apoptotic SM1-OVA cells by BMDCs in the presence or absence of 522 ISNP.

4.3.4 ISNP formulations engendered robust CTL response *in vivo*

Cytotoxic $CD8^+$ T cell is an important type of effector T cell that engaged in immune surveillance against malignant cells. The ability of ISNPs in priming $CD8^+$ killer T cell *in vivo* was assessed by vaccinating C57B6 mice. Firstly, OVA was used as model antigen and encapsulated into PLGA NPs in the presence or absence of TLR agonist co-loading. It was shown that both OVA/522 ISNP and OVA/520 ISNP successfully elicit robust OVA-specific $CD8^+$ T cell proliferation (Figure 4-16). Approximately 6% of $CD8^+$ T cell population from peripheral blood was OVA-specific T cells following OVA/522 ISNP

vaccination (Figure 4-17). The adjuvant potency of TLR7/8 agonist loaded ISNPs were comparable to that of the positive control using OVA/MPL-A ISNP. Since the immune response was monitored in an antigen specific manner, the significant presence of OVA-specific $CD8^+$ T cell in blood implied that OVA antigen in the NP formulations was successfully acquired, processed and cross-presented by DC. On the other hand, compared to OVA-NP without TLR agonist, ISNPs elicited significantly higher percentage of OVA-specific circulating CTL ($P<0.05$), suggesting that the novel TLR7/8 agonist loaded ISNPs potently activated DC *in vivo* in terms of promoting CTL expansion. In addition, during necropsy of ISNPs vaccinated mice, there was clear inguinal lymph node enlargement suggestive of the lymphocyte proliferation at draining lymph node.

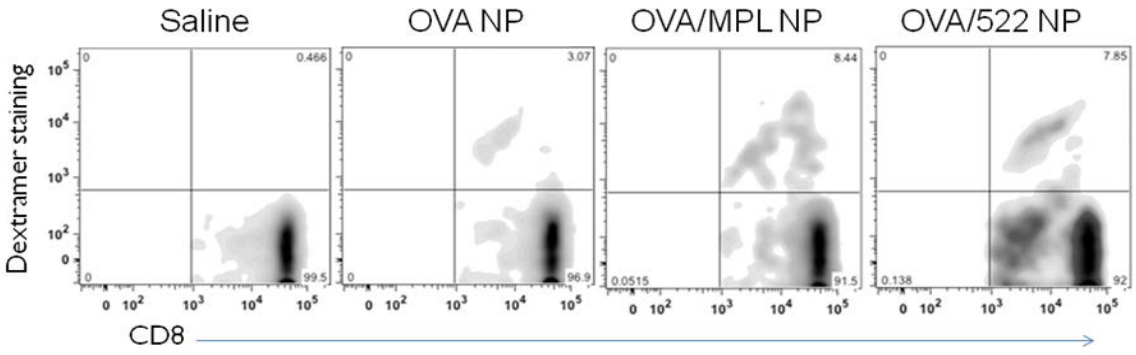

Figure 4-16. Representative flow cytometry plots for stained OVA-specific CD8+ T cells. Fluorescent labeled dextramer of SIINFEKEL based p-MHC I complex was used to monitor the systemic $CD8^+$ T cell response after immunization with various OVA loaded NP formulations

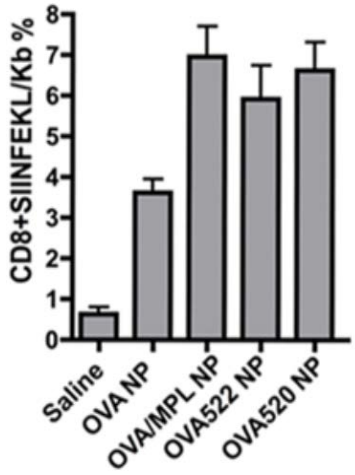

Figure 4-17. Percentage of circulating CD8+ T cells recognizing OVA derived peptide SIINFEKEL after vaccination with various OVA loaded NP formulations.

In order to test whether tumor associated antigens could be acquired by DC *in vivo* for T cell priming in the presence of NPs. A proof of concept study was carried out using SM1-OVA cell lysate combined with ISNPs as vaccine formulations. C57B6 mice were immunized with freeze-thaw generated SM1-OVA cell lysate with either blank PLGA NP or ISNPs. Vaccinated mice demonstrated the significant presence of OVA specific $CD8^+$ T Cell in blood, implying that the DCs acquire melanoma cell derived OVA antigen and cross-prime T cells (Figure 4-18). TLR agonists loaded ISNPs triggered a higher but statistically non-significant percentage of OVA-specific circulating CTL compared to the blank PLGA NP (Figure 4-19).

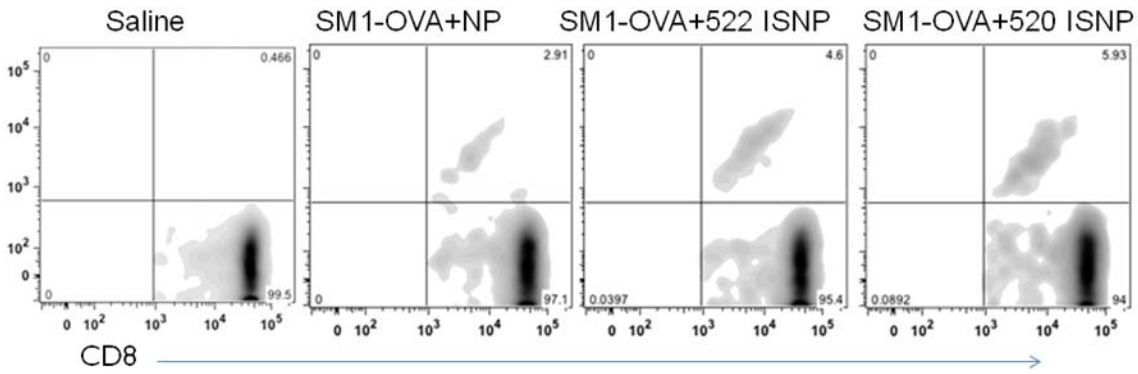

Figure 4-18. Representative flow cytometry plots for stained OVA-specific $CD8^+$ T cells. Fluorescent labeled dextramer of SIINFEKEL based p-MHC I complex was used to monitor the systemic CD8+ T cell response after SM1-OVA lysate immunization with various NP formulations.

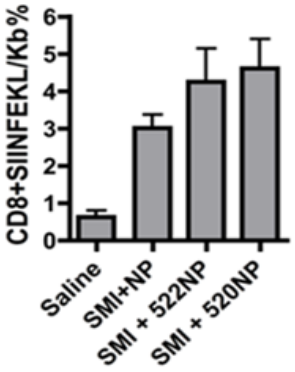

Figure 4-19. Percentage of circulating OVA-specific $CD8^+$ T cells after vaccination with SM1-OVA lysate and NP formulations.

4.3.5 NP-assisted whole tumor cell vaccine formulations differentially protected mice from B16 melanoma challenge

Apoptotic cells are eliminated by professional phagocytes. However, the attendant default interpretation of apoptotic cell death by immune system is tolerogenic instead of immunogenic. Vemurafenib treatment led to programmed cell death for BRAF V600E mutation positive melanoma cells. Professional phagocytes such as DCs could potentially acquire TAA during this procedure. In an effort to test whether introduction of ISNP during apoptotic tumor cell death event could convert the otherwise tolerogenic procedure into immunogenic event, X-ray irradiated apoptotic B16 cells were used as a surrogate whole tumor cell vaccination model. Apoptotic B16 cells generated *ex vivo* were combined with either blank PLGA NP or various ISNP formulations to immunize C57BL/6 mice preventatively before B16 tumor challenge. First of all, the tumorigenesis was delayed in all the vaccinated cohorts (Figure 4-20). For unvaccinated mice, it took on average 13.6 days to develop a superficially visible melanoma at the site of tumor cell injection. For 520 ISNP vaccinated group, the appearance of tumor was postponed for 3.6 days, while 6 days delay was observed for the blank NP group. There was one mouse fully protected from B16 melanoma challenge from the 528 ISNP vaccinated cohort. No superficial melanoma ever developed for this mouse up to 90 days. The rest of 528 ISNP vaccinated mice showed a 4.9 days delay in tumorigenesis.

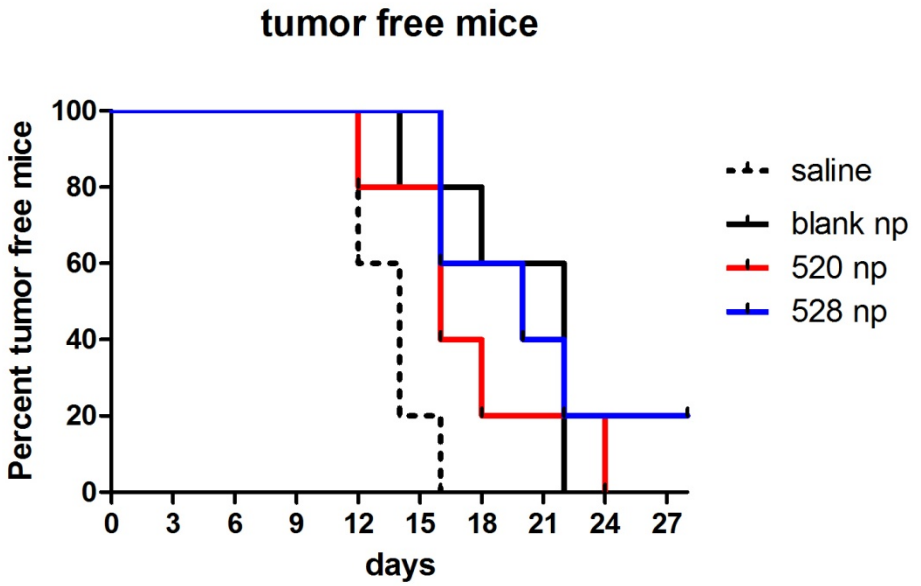

Figure 4-20. Percentage of mice that was free of visible melanomagenesis over time.

Mice that received prophylactic vaccination with apoptotic B16 cell formulations demonstrated differential B16 melanoma growing kinetics from unvaccinated mice (Figure 4-21). The time of progressing from superficially visible melanoma lesion to palpable tumor (>200 mm^3) was less than 6 days for unvaccinated mice. But 4 mice from blank PLGA NPs vaccinated mice took 12 days for this initial phase of tumor growth, 3 out of these 4 mice took 18 days for the initial tumor volume expansion. Preventative vaccination in the presence of blank PLGA NP doubled the median survival days of unprotected mice (52 days over 25 days) and conferred statistically significant survival benefit (P=0.011) (Figure 4-22). Intriguingly, in ISNP vaccinated groups including both 520 ISNP and 528 ISNP, only 20% of the mice showed significantly delayed tumor growth kinetics and prolonged survival. 528 ISNP increased median survival slightly (30

days over 25 days) and only provided marginal survival benefit (P=0.029). 520 ISNP failed to prolong survival in this model.

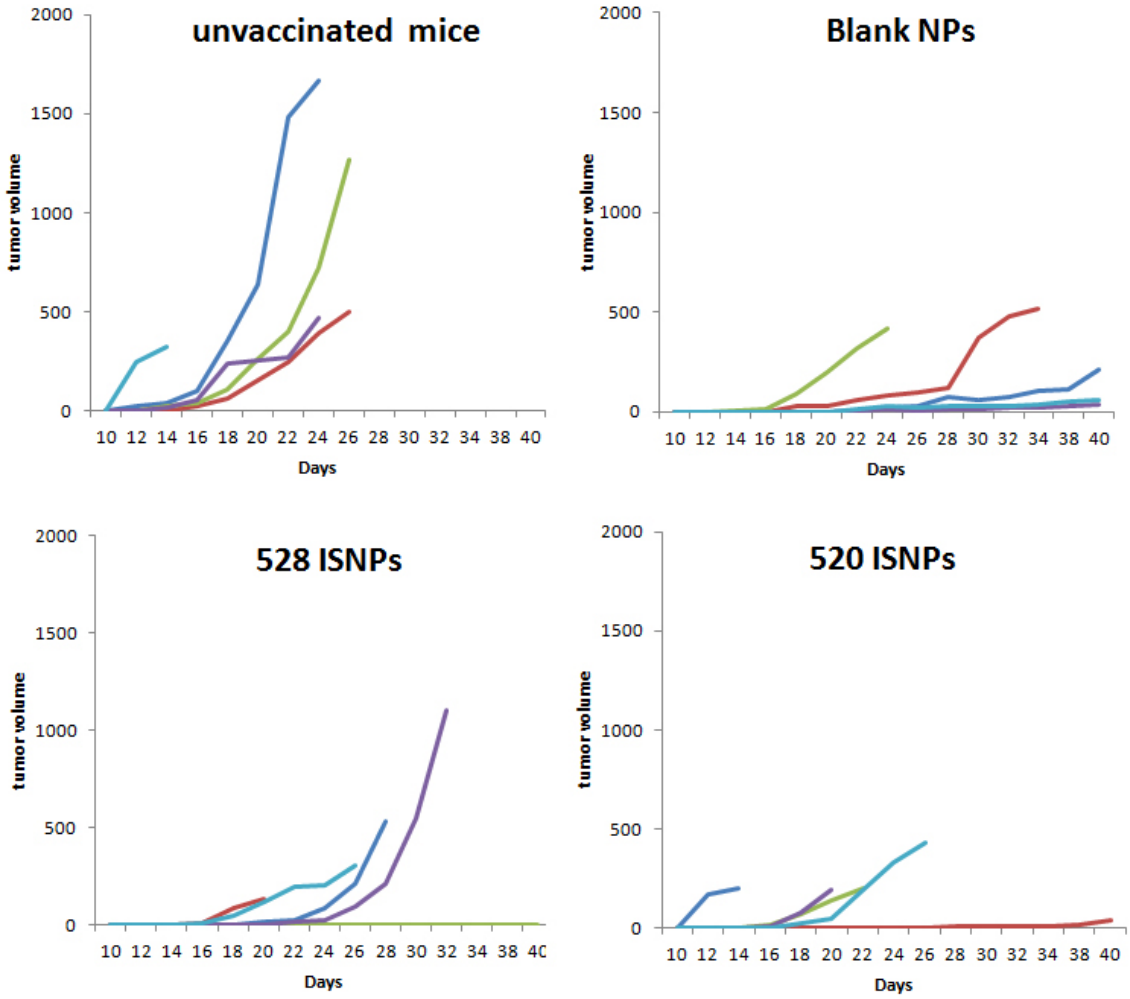

Figure 4-21. Tumor growth kinetics of B16 melanoma challenged mice with or without preventative cancer vaccination

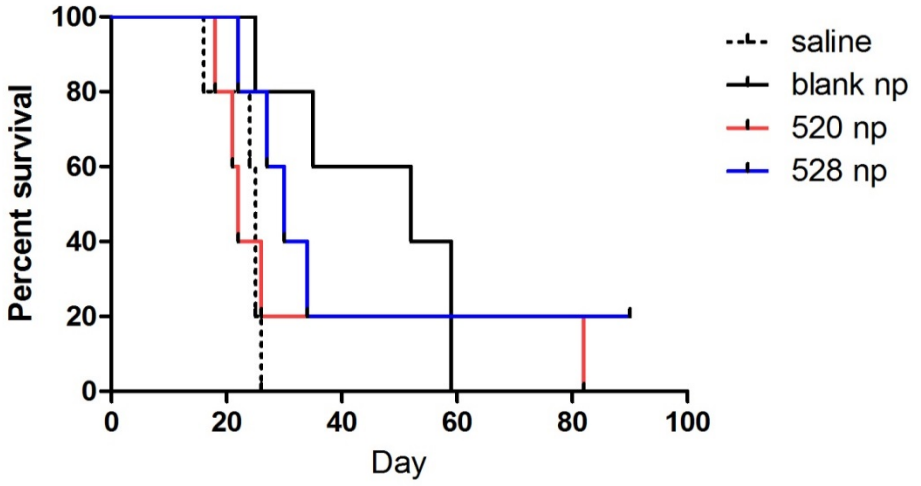

Figure 4-22. Survival of mice challenged with B16 melanoma with or without preventative vaccination (N=5). The statistical analysis was calculated with Log-rank (Mantel-Cox) test.

4.3.6 Blank PLGA NP and ISNPs produced differential local and systemic cytokine profile

Subsequent to the vaccination with various apoptotic B16 cell formulations, the local and systemic inflammatory cytokine profile was monitored. IFN-γ is the pivotal Th1 polarizing cytokine, which is crucial in $CD8^+$ T cell's effector function in combating malignancy. Firstly, 528 ISNP formulation triggered significantly higher IFN-γ and TNF-α cytokine response by lymphocytes isolated from local draining lymph node than other groups (Figure 4-23). In contrast, the enhanced local IFN-γ and TNF-α secretion by 520 ISNP and blank PLGA NP were moderate compared to the cancer vaccine comprising of only apoptotic B16 cells. 520 ISNP and PLGA NP were comparable with respect to IFN-

γ and TNF-α response. In addition, the introduction of PLGA NPs and ISNPs showed elevated IFN-γ and TNF-α response in spleen as well. Interestingly, it was the blank PLGA NP that demonstrated the highest splenocyte IFN-γ response, while the remarkable induction of IFN-γ local response by 528 ISNP was not mirrored in spleen.

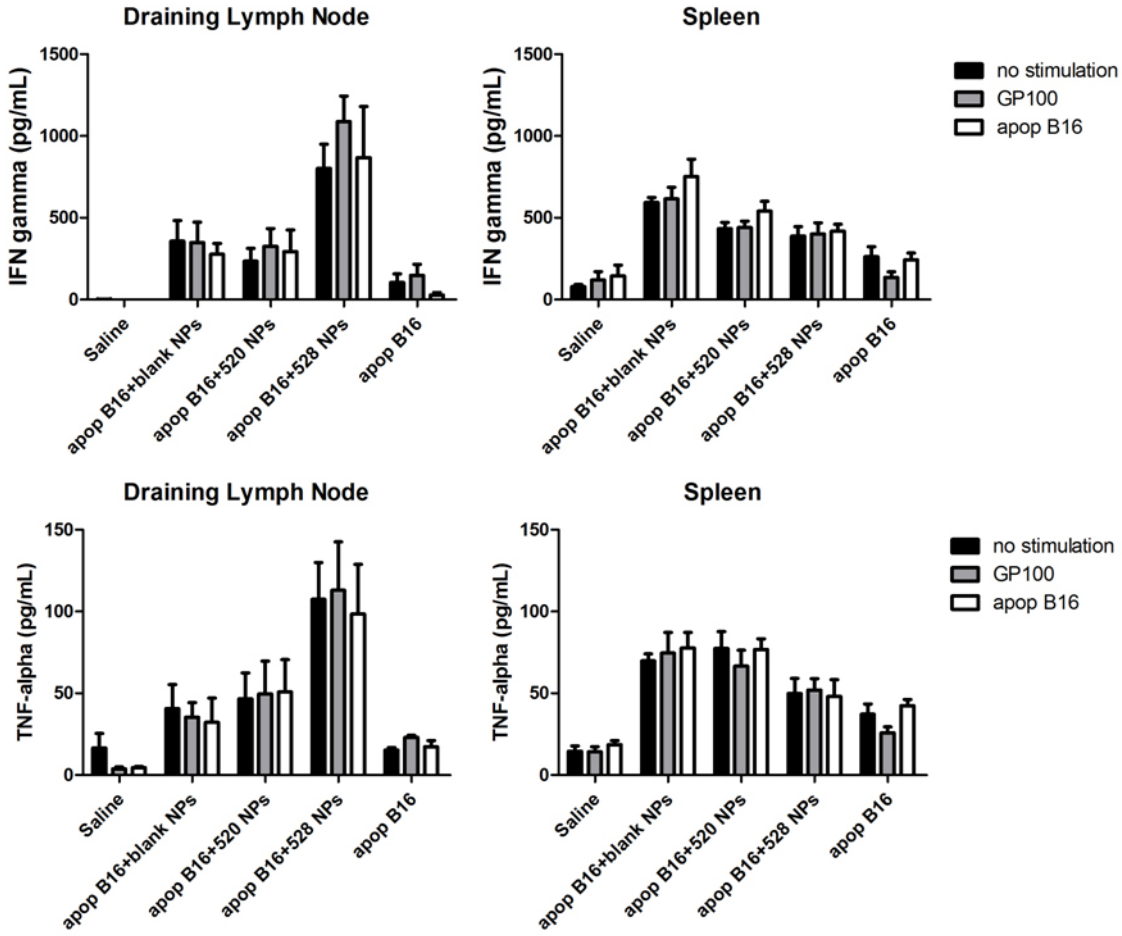

Figure 4-23. Secretion of IFN-γ and TNF-α from draining lymph node lymphocytes or splenocytes. Cells were isolated from vaccinated mice and stimulated *ex vivo*. The tumor

associated antigen was provided in the format of either irradiated apoptotic B16 cells or recombinant GP100 antigen.

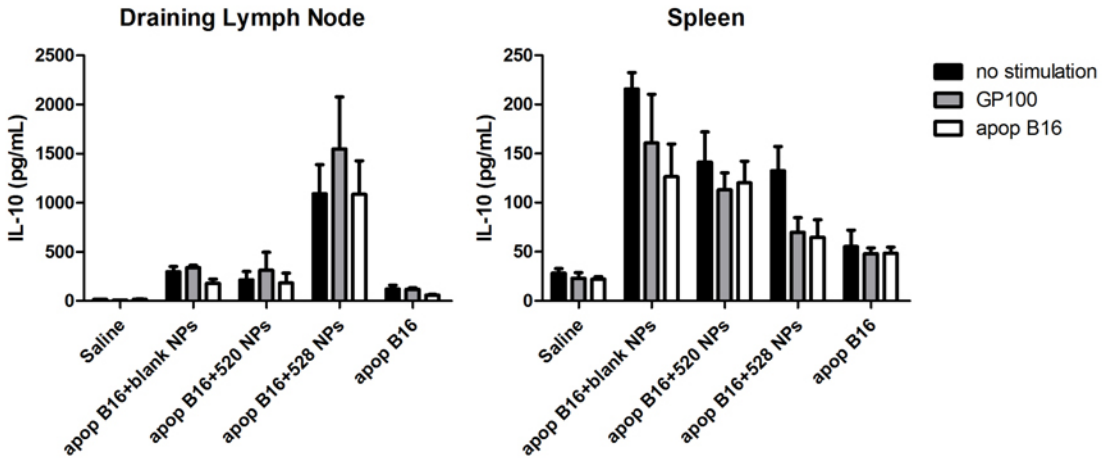

Figure 4-24. Secretion of IL-10 from draining lymph node lymphocytes or splenocytes. Cells were isolated from vaccinated mice and stimulated *ex vivo*. The tumor associated antigen was provided in the format of either irradiated apoptotic B16 cells or recombinant GP1

Despite the fact that 528 ISNP demonstrated outstanding capability in instigating stimulatory cytokine response locally, 528 ISNP also elicited dramatic local release of Th2 skewing cytokine IL-10 (Figure 4-24). However, this effect was only limited to draining lymph node and not obvious in spleen. In contrast, the blank NP formulation led to stronger IL-10 secretion in spleen in comparison to the apoptotic B16 cells alone.

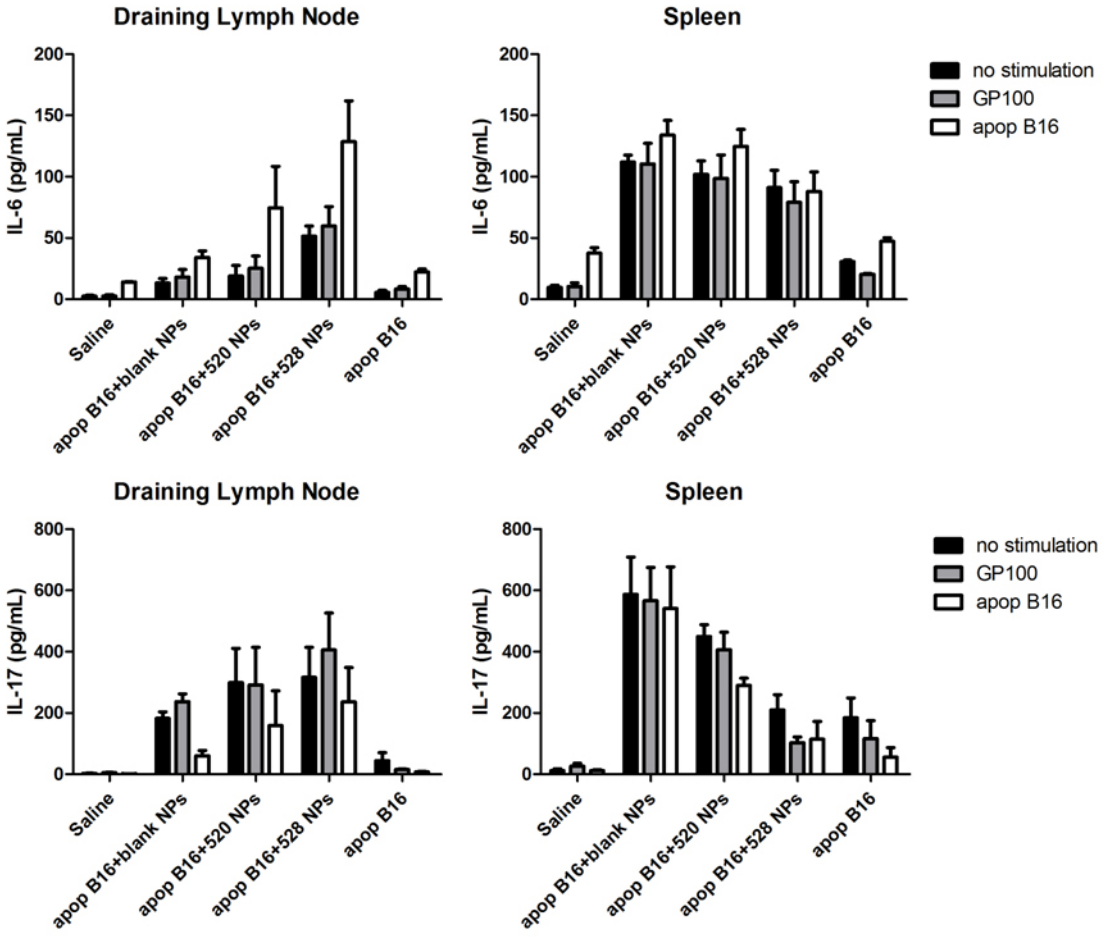

Figure 4-25. Secretion of IL-6 and IL-17 from draining lymph node lymphocytes or splenocytes. Cells were isolated from vaccinated mice and stimulated *ex vivo*. The tumor associated antigen was provided in the format of either irradiated apoptotic B16 cells or recombinant GP100 antigen.

IL-6 was another common inflammatory cytokine. Similarly, 528 ISNP gave rise to the strongest local IL-6 boost among all groups, but in the spleen the IL-6 enhancement were comparable among all NPs vaccinated groups. As for the cytokine instrumental to Th17 response, 528 ISNP only boost local IL-17 response over apoptotic cells alone but not in

the spleen. In contrast, blank PLGA NP augmented IL-17 response both in spleen and draining lymph node. Interesting, blank PLGA NP induced the highest IL-17 response in spleen among all groups, indicating a potentially adjuvant effect and pro-inflammatory role of PLGA *per se*.

4.3.7 ISNP assisted *in situ* vaccination of melanoma in the context of BRAF V600E inhibition

Immunocompetent C57BL/6 wide type mouse was used to test the efficacy of *in situ* vaccination for BRAF V600E positive SM1 melanoma. In the context of BRAF inhibition, vemurafenib-induced apoptotic BRAF V600E melanoma cells could potentially serve as the most representative tumor associated antigen repertoire for DC presentation. NP based formulation was injected directly into pre-established SM1 tumor matrix to modify the tumor microenvironment with saline injection as control group. Firstly, oral dosing of vemurafenib alone significantly inhibited the tumor growth and reduced tumor volumes compared to the untreated vehicle control group (Figure 4-26). Intriguingly, despite the slower tumor growth kinetics and reduced tumor size, BRAF inhibition in conjunction with saline intratumoral injection subsequently led to necrotic tumor with skin ulcer and premature death of a subpopulation of tumor bearing mice. There was no survival benefit observed for this regimen. Similarly, blank PLGA NP or 528 loaded ISNP in combination with vemurafenib inhibited tumor growth. It took no more than 5 days for untreated SM1 tumor to reach 500 mm^3. In contrast, it took at least 12 days for mice treated with blank NP and at least 16 days for 75% mice treated with

528 ISNP to reach the 500 mm^3 tumor size. However, SM1 tumor necrosis and ulceration were apparent in 75% of mice treated with *in situ* vaccination, leading to premature death (N=4, PLX+saline group N=3). As a result, the median survival was only improved for 4 days in blank NP treated mice and 8.5 days in 528 ISNP treated mice. There was no statistically significant survival benefit observed by NP assisted *in situ* therapeutic vaccination for this experiment (Figure 4-27).

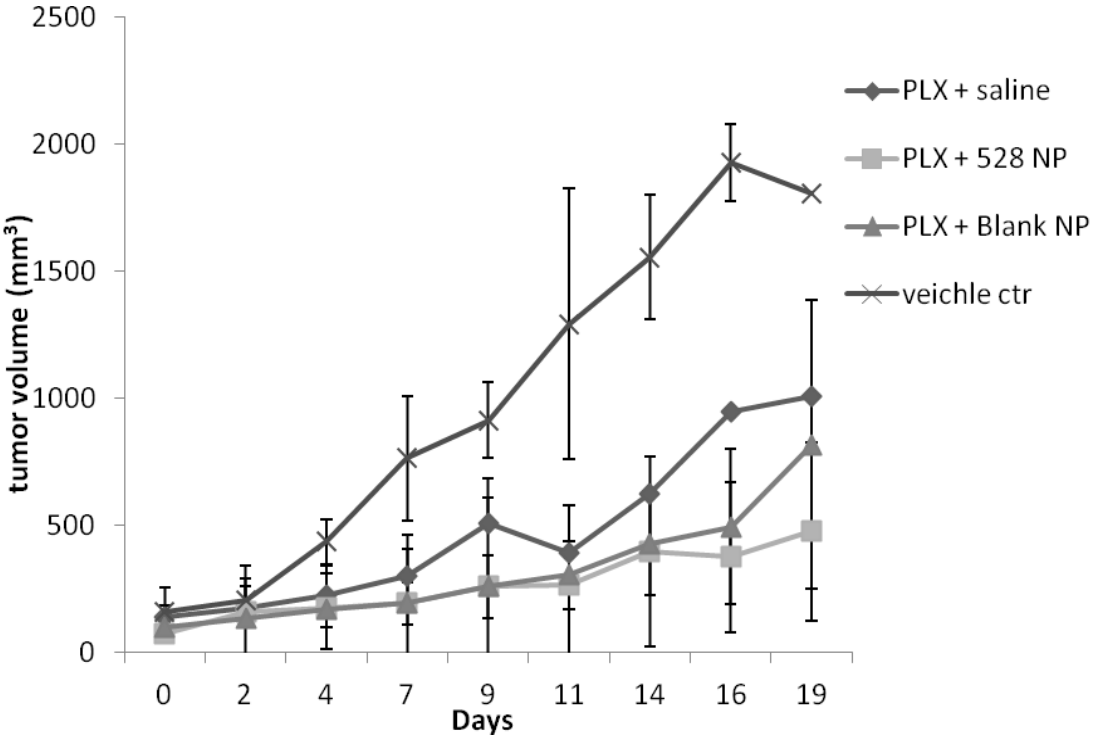

Figure 4-26. Tumor growth kinetics of SM1 melanoma bearing mice after NP-assisted in situ vaccination in the context of BRAF inhibition. (Day 0 denotes the commencement of PLX or vehicle administration)

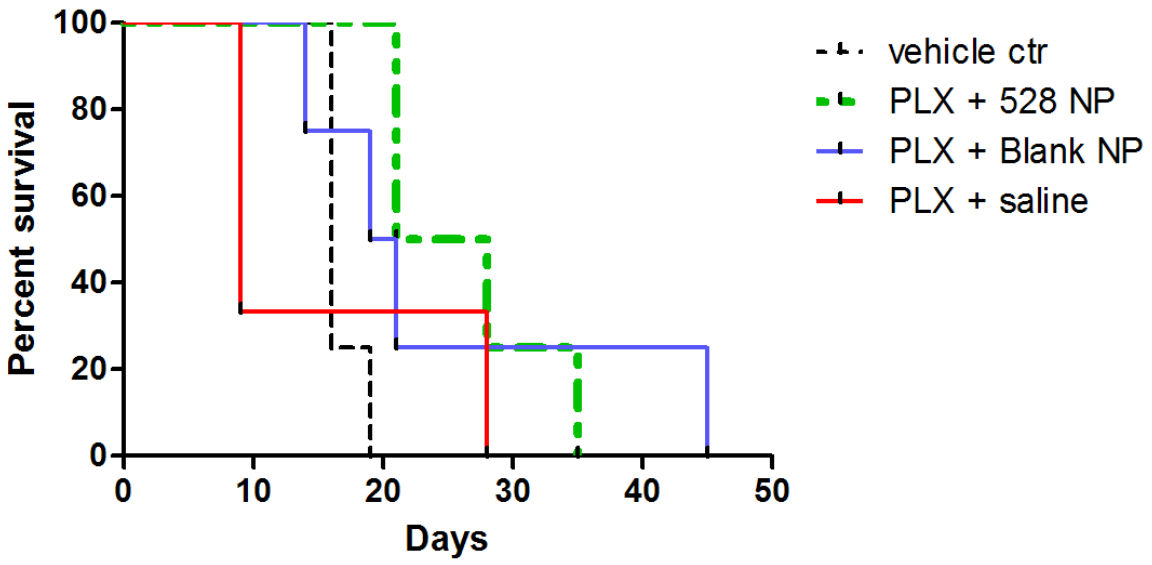

Figure 4-27. Survival plot of SM1 melanoma bearing mice after NP-assisted *in situ* vaccination in the context of BRAF inhibition.

4.3.8 Integrin αV/β3 targeted NP improved melanoma targeting property

Integrin αV/β3 has been discovered to be over-expressed in melanoma (198, 199). We confirmed that there is integrin αV/β3 expression on the surface of BRAF V600E positive melanoma cell line A375P (data not shown). cRGD peptide is a short cyclic peptide that selectively binds integrin αV/β3. The surface of PLGA NP was functionalized by PLA-PEG block co-polymer with maleimide terminal group. cRGD peptide as targeting moiety was conjugated to the reactive pegylated PLGA NPs via maleimide-thiol chemistry. A binding study was conducted to evaluate the interaction between the targeted NPs and integrin αV/β3 expressing melanoma cells. It was shown that after 15 minutes initial co-incubation of NPs with melanoma cell in 4°C that inhibit active endocytosis, a side population with significantly higher fluorescent signal emerged for

cells treated with cRGD functionalized NPs (Figure 4-28). The mean fluorescent intensity of melanoma cells was elevated as well compared to the cells treated with cRAD control peptide functionalized NPs ($P<0.01$) (Figure 4-29).

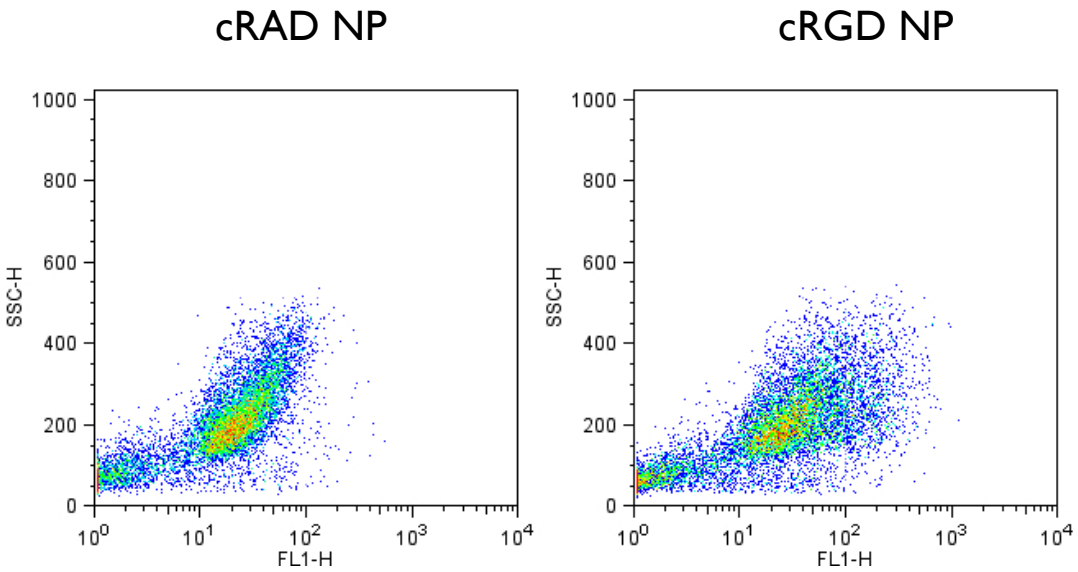

Figure 4-28. Representative flow cytometry dot plot for fluorescence high side population of A375P cells co-incubated with cRGD NPs. Fluorescent intensity (FL1-H) was plotted against side scattering (SSC-H).

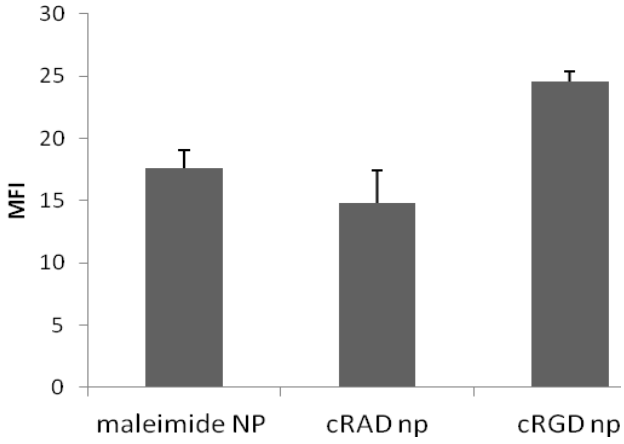

Figure 4-29. Mean fluorescent intensity of A375P cells co-incubated with coumarin-6 loaded functionalized NPs.

Similarly, cRGD functionalized NPs also demonstrated affinity for mouse melanoma cell line SM1 compared to cRAD NPs ($P<0.01$) (Figure 4-30). The proportion of the side population in cRGD NPs treated cells (14.9%) was more than doubled than the cRAD NPs treated cells (6.67%) (Figure 4-31). Thus, cRGD conjugated NP showed higher affinity for melanoma cells expressing integrin αV/β3. The availability of melanoma targeting NPs platform could potentially facilitate NPs retention in melanoma matrix for future studies.

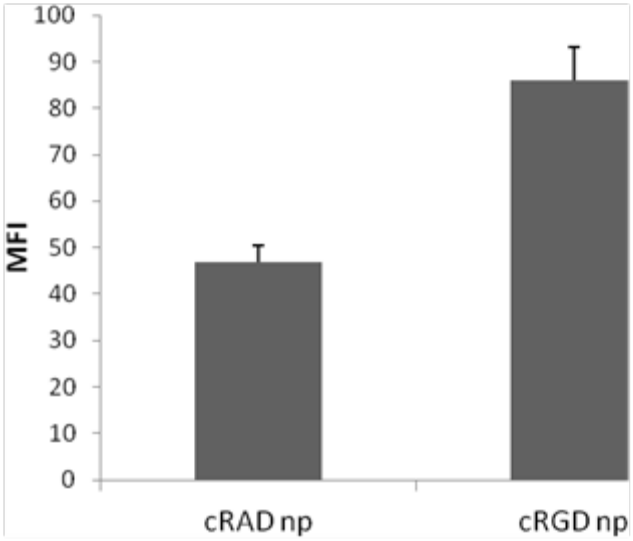

Figure 4-30. Mean fluorescent intensity of SM1 cells co-incubated with coumarin-6 loaded functionalized NPs.

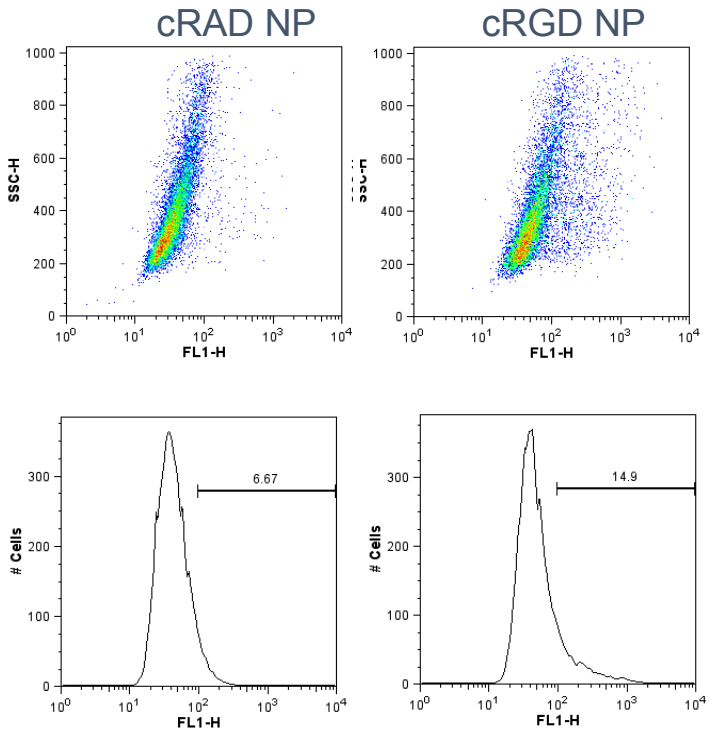

Figure 4-31. Representative flow cytometry dot plot and histogram for fluorescence high side population of mouse melanoma SM1 cells co-incubated with cRGD or cRAD NPs.

4.4 Discussion

Our microscopy imaging data demonstrated the rapid phagocytosis of polymeric microparticles by DC *in vitro* and remarkable capacity of DC in clearing large quantities of polymeric particles. Within hours, it was obvious that previously randomly dispersed microparticles in the cell culture plate were enriched into the intracellular space of DCs. DCs routinely perform sentinel function in terms of up-taking materials from its surrounding. The underlying mechanism of efficient particle up-taking is likely to be

dichotomous. Firstly, serum proteins, such as immunoglobulin and other opsonins that adsorbed on the particle surface promote phagocytic activity of DC (200). The opsonized particles initiate DC phagocytosis via Fc receptors and other scavenger receptors (201, 202). Secondly, macrophage receptor with collagenous structure (MARCO) was recently shown to be responsible in the up-taking of negatively charged particles by inflammatory phagocyte in an opsonization-independent pathway (203-205). MARCO is expressed in monocyte and monocyte derived DC. In response to tumor cell lysate pulsing, MARCO expression in DC is up-regulated (206). The blocking of MARCO on tumor lysate pulsed DC via a non-ablative anti-MARCO antibody does not eliminate $MARCO^+$ DC but only modulate DC morphology and migratory property. The manipulated $MARCO^+$ DC improves tumor reactive T cell activation and anti-melanoma immunity (205). The polymeric particles as vaccine carrier could serve as an alternative strategy for passive $MARCO^+$ DC-targeted delivery and manipulation especially for the proposed *in situ* melanoma vaccine. However, whether or not the DC migratory ability is compromised by particle overburden remain yet to be studied.

Similar to the observed microparticle-DC interaction, DCs acquire NPs as efficiently. Our flow cytometry study and live cell confocal imaging data proofed the efficient internalization of PLGA NPs by BMDCs within two hours of co-incubation. With respect to intracellular distribution, there were partially overlapped signals between fluorescent NPs and endo-lysosome. Namely, PLGA NPs were located in both cytosol and endo-lysosomal compartment. The cellular machinery involved in PLGA NPs internalization is

likely to be multi-faceted. The presence of PLGA NPs in the acidic endo-lysosomal compartment suggested that endocytic pathways could play a significant role in the internalization of PLGA NPs. Both phagocytosis and endocytosis could contribute to the robust up-taking of NPs by DC (207). Immature DCs also demonstrate constitutive sampling capabilities characterized by constant macropinocytosis (208), which is a validated mechanism for NPs up-taking by macrophage (209). Internalized NPs are initially contained in early endosome. Translocation into multivesicular bodies, late endosome and lysosome is the typical trafficking trajectory for NPs (210). It's unlikely that negatively charged PLGA NPs could achieve direct cellular entry in the absence of positively charged cell penetrating peptide (211). Thus, the presence of undecorated PLGA NPs in DC cytosol suggested escape of NPs from endocytic vesicles. It was reported that PLGA NPs could rapidly escape endo-lysosomal compartment via surface charge reversal in smooth muscle cells. Within acidic environment, the anionic surface charge was converted to cationic so that PLGA NPs traverse endocytic vesicle membrane and enter into cytoplasm (121). This partial localization of NPs within DC cytosol suggested that PLGA NPs escape endocytic compartments in professional phagocytes as well.

The intracellular fate of up-taken NPs has major implications for DC-targeted drug delivery. TLR7 and TLR8 are crucial intracellular detectors of pathogen derived ssRNA. The biogenesis of TLR7/8 originated from endoplasmic reticulum (ER) followed by trafficking via Golgi apparatus into the luminal side of endo-lysosome. One key finding

of this project is that the PLGA NP formulation of TLR7/8 agonists enhanced their drug delivery and efficacy. Imidazoquinoline derivative 522 as free drug reached an efficacy plateau in terms of activating BMDCs. However, the NP formulation overcome this efficacy ceiling and boosted the CD86 and CD40 up-regulation significantly. This augmentation in DC maturation is attributed to the intracellular delivery of NP formulation. In particular, TLR7 agonists were directly introduced into the site of action within endo-lysosome via the NP carrier. However, the enhancement may not be fully accounted for by the increased drug lysosome concentration alone. The formation of DC "phagocytic synapse" with particulate subject alters signaling platform organization (212), potentially enhancing the BMDCs' responsiveness to TLR7/8 agonists. On the other hand, for non-professional phagocytes, such as a HEK TLR7 reporter cell line, our data showed that NP formulation only slightly augments the efficacy of 522 at a low concentration of but not at higher concentration. Previously, model imidazoquinoline molecule modified with a fluorescent moiety was used to elucidate the cellular distribution of TLR7/8 agonist. It has been demonstrated that imidazoquinoline drugs such as imiquimod and resiquimod reach the site of action via a two-phase process. Firstly, imidazoquinoline permeates cell membrane via passive diffusion. Then, TLR7/8 agonists preferentially accumulate in $LAMP^+$ endo-lysosome in a pH dependent manner (190). The protonation of imidazoquinoline weak base was proposed to entrap the drug in acidic compartment (213). In this study, at low 522 total concentration, internalization of 522 ISNP probably delivered more 522 into endo-lysosome than passive diffusion of free drug, while at high concentration treatment, free drug alone may sufficiently accumulate

within endo-lysosomal lumen at equilibrium. Our data illustrated that NP formulation could have differential impact on imidazoquinoline drug delivery for professional phagocyte and non-immune cell type.

Our data showed that ISNP vaccine formulation elicit robust antigen-specific $CD8^+$ T cell response *in vivo*, which is probably the corollary of strong DC activation. Not only up-regulated co-stimulatory molecules CD86 and CD40 facilitate CD8+ T cells priming, but DC cross-presentation of antigen to T cells also plays a pivotal role in this effect. Cross-presentation is initiated by internalization of exogenous antigen. Acquired antigens are transported from phagocytic and endocytic vesicles into cytosol for proteasome processing (cytosolic pathway). Eventually processed antigen epitopes are transported by transporter associated with antigen processing (TAP) into ER for complexing with MHC I (214). Alternatively, acquired antigens are processed and loaded onto MHC I in phagolysosome (vacuolar pathway). Our data revealed that the cross-presentation of antigen can be augmented via antigen loaded ISNPs. 522 ISNP provided the strongest ability in boosting cross-presentation. Moreover, the cross-presentation of TAA derived from vemurafenib-induced apoptotic melanoma cells was also increased by 522 ISNP. The enhancement is primarily attributed to the potent TLR7 activation. TLR7 agonist drives cross-presentation in DC via a type I IFN dependent mechanism (215), which dictates the success of eliciting cellular immunity by TLR7 adjuvant-based vaccine formulation (216). In addition, the improved antigen delivery is also likely to contribute to the efficient cross-presentation. For antigen-loaded NPs, antigen delivery could be

directly improved. For the formulation consisting of NP and apoptotic cell or lysate, TAA adsorption on NP could indirectly improve antigen delivery. First of all, NPs assist in the antigen internalization by BMDCs compared to the soluble format. *In vivo*, injected soluble antigen drains efficiently through the porous lymphatic vessels and local concentration drops quickly. In contrast, NP formulations promote local retention and antigen persistence for dermal DCs up-taking, further improving the passive targeting of DC intracellular delivery. Once acquired, antigen loaded ISNP is either located in the lysosome or escape from endo-lysosomal compartment into cytosol. The sustained release from these locations would increase antigen delivery for both the cytosolic pathway and vacuolar pathway of cross-presentation.

Professional phagocytes constantly sample their surroundings and participate in maintaining tissue homeostasis. Phagocytes constitutively undertake pinocytosis and live cell nibbling (217). In addition, phagocytes also play an active role in clearing apoptotic and necrotic cells during normal turnover and abnormal cell death. Melanoma cells contained malignant cell derived proteins that could be acquired by immune system as TAA. It has been established that the immune response subsequent to apoptotic cells clearance is generally in favor of toleration rather than immunity. Thus, reversal of the immunosuppressive microenvironment is desirable with respect to effective cancer immunotherapy. One key finding of this study is that the NP-based adjuvant system elicited inflammatory cytokines during clearance of apoptotic tumor cells. In comparison to apoptotic cells alone, the addition of 528 ISNP triggered significantly stronger

inflammatory cytokine release including IFN γ, TNF α, IL-6 and IL-17 from lymphocytes in the draining lymph nodes. In particular, IFN γ is a pleiotropic type II interferon. Engagement of STAT1 signaling pathway via IFN γ led to direct growth arrest of various melanoma cell lines (218). Furthermore, IFN γ performs an immunopotentiating function to facilitate CTL mediated melanoma rejection(219). However, the remarkable induction of local IFN γ by 528 ISNP did not translate into the strongest protective immunity against B16 melanoma in our study probably due to the strong local secretion of IL-10. IL-10 is a prominent Th-2 skewing cytokine with immunoregulatory function. With respect to the B16 melanoma model, IL-10 has been identified as an undesirable cytokine in that it directly promotes melanoma cell proliferation in addition to its inhibitory action on macrophage function (220). In contrast, blank PLGA NP induced much lower local IL-10 response and moderately produced pro-inflammatory cytokines in spleen. We ascribe the strongest protection of blank NP formulation in our study to this unique cytokine profile. In addition, despite that fact that blank NP does not activate BMDCs *in vitro*; previously there has been report on the adjuvant property of PLGA particulate due to the activation of NALP3 inflammasome and IL-1β *in vivo*(221). Thus, in the future, the choice of optimal adjuvant component for rational design of cancer vaccine entails careful consideration and deeper understanding of tumor immunology. Therapeutic agents that counteract inhibitory mechanisms of immune system are likely to be beneficial to fully realize the potential of cancer vaccine.

The intratumoral injection has been the most commonly implemented administration route for oncolytic virus-based melanoma immunotherapy in B16 model and clinical trials. Localized administration of Newcastle disease virus therapy in combination with CTLA-4 checkpoint inhibitor led to the induction of anti-melanoma immunity even in distant un-injected tumors and provides to date the most impressive therapeutic efficacy in B16 model (222). Intratumoral administration of Amgen's investigational oncolytic virus talimogene laherparepvec (T-VEC) has demonstrated efficacy in the Phase III clinical trial for unresectable III B-IV stage metastatic melanoma patients (223). ISNP could possibly serve as a non-viral adjuvant component to instigate anti-melanoma immunity *in situ*. SM1 cell line is one of the first murine BRAF V600E cell line compatible with immunocompetent mouse model. However, there is still limitation of SM1 in the evaluation of the proposed *in situ* cancer vaccination strategy. Firstly, the engraftment rate of subcutaneously injected SM1 cells in C57BL/6 strain was limited compared to the well-established B16 melanoma model. Only 60% of mice (15 out of 25 mice) challenged with SM1 cells established tumor, the rest of the mice either never developed tumor at all or developed tiny palpable nodule which disappeared eventually. Secondly, the timing of tumorigenesis subsequent to SM1 cell injection was highly variable, ranging from two weeks to four weeks for the appearance of tumors. For SM1 tumor bearing mice, in the absence of BRAF inhibition, the tumors continued to grow into intact large tumor (close to 2000 mm^3 until sacrifice). But for tumor bearing mice that receive both vemurafenib and intratumoral injection of NPs or saline, skin ulceration and necrotic tumors were observed, leading to premature death. Thus, the practicality of

intratumoral injection for SM1 model remained to be determined in future study. Thereafter, an optimized mouse BRAF melanoma model is required to fully recapitulate the melanoma debulking after BRAF inhibition in clinics. Exploration of more suitable mouse model for *in situ* created BRAF V600E melanoma vaccine could pave the way for in-depth research on the combinatorial approach of BRAF inhibition and immunotherapy.

Chapter Five: Summary and Future Directions

5.1 In summary

The goal of this thesis is to develop PLGA NP based formulation for investigational vaccination strategy against melanoma. Key practical issues that enable the application of PLGA NP formulation for translational research were addressed, including the lyophilized dosage form and device-mediated intradermal delivery. ISNP was generated as immune adjuvant to potently activate innate immune system. The potential application of ISNP in melanoma immunotherapy was evaluated.

Chapter Two of the thesis strived to clarify several key questions concerning the lyophilization of NP formulations. Sound translational research and clinical application of NP-assisted vaccination depends on the availability of a reliable dosage form that preserves critical product attributes of NPs. Freezing stress on NPs was confirmed at various cooling rate, leading to increased NP size distribution. Several imaging techniques were employed to elucidate the underlying mechanism of freezing stress and cryoprotection. Time-lapse fluorescence microscopy was used to monitor the NP freezing behavior in real-time. The freezing-induced NP aggregation damage was correlated with freeze-concentration of NPs. Freezing behavior of NPs in the presence of sucrose could also be observed directly. Thus, this technique can be adopted to screen candidate cryoprotectants and streamline the formulation design for nano-drug delivery carriers.

Our cryo-SEM study provided direct visualization support to NP freeze-concentration and, most importantly, the "particle isolation" hypothesis for effective cryoprotection. Namely, the protective property of sucrose arises from separating individual particles in a glassy matrix within the interstitial space to prevent close contact and aggregation of NPs. In addition, confocal imaging technique provided superior imaging of internal structure of the final lyophilized cake, which should be applicable in optimizing formulation design and lyophilization cycle development for manufacturing robust NP products.

Chapter Three of the thesis focused on the precise delivery of high volume dose of NP formulation into the skin. The feasibility of hollow microneedle-mediated delivery of NPs was confirmed. Biodistribution study revealed the retention of NPs at the site of intradermal infusion and the formation of a local depot with potential for sustained drug release. It was found that draining lymph nodes play a crucial role for the systemic access of intradermally administered NPs. In addition, the adjuvant potency of ISNPs was validated in this study, generating high titer of antigen-specific antibody response in all vaccinated rats. Compared to the soluble antigen, not only the antigen loaded NP formulation demonstrated faster kinetics in mounting antibody response, but the avidity of the antibodies was also better as shown by urea ELISA, indicating quicker affinity maturation. Vaccination with antigen encapsulated NP formulation via intradermal microneedle array uniquely resulted in the highest IgG2a titer among all experimental groups. Intradermal delivery of NP formulation elicited the highest relative strength of

Th1 response, which was further confirmed by the secretion of Th1 cytokine IFN γ by splenocytes upon antigen recall response.

Chapter Four of the thesis explored the potential application of ISNPs in cancer immunotherapy. The interplay between PLGA NPs and DC was interrogated. NPs were internalized by DCs efficiently, gaining access to both the cytosol and endo-lysosomes. ISNP formulations augmented DC activation *in vitro* compared to the soluble drugs. In the presence of ISNPs, cross-presentation of both a model antigen OVA and antigen derived from apoptotic cells was enhanced, which translated into stronger antigen-specific $CD8^+$ T cell priming after vaccination. ISNPs induced distinctive cytokine profiles, characterized by high local IFN γ and IL-10 response. NP-assisted whole tumor cell vaccine was shown as a promising preventative cancer immunotherapy by prolonging survival after tumor challenge. The proposed ISNP assisted *in situ* vaccination in the context of first line treatment via BRAF inhibition was investigated preliminarily using the SM1 mouse melanoma model.

5.2 Future directions

Formulation design for NPs decorated with bio-molecules necessitates special consideration with respect to the pH and ionic strength of the buffer system. It was recognized that during freezing, pH of sodium phosphate buffer changed significantly due to ion precipitation(105). On the other hand, NPs are routinely functionalized with PEG. It is well known that polymers such as polyvinylpyrrolidone (PVP) and dextran

undergo phase separation during freeze-concentration (224). Thus, the interaction between various excipients and NPs during freeze-concentration warrants an in-depth follow-up study.

For future studies, microneedle-mediated intradermal delivery of sub-100 nm NPs would be of great value to probe the correlation between particle size and local retention (225). It is predicted that smaller NPs will likely to have higher systemic bioavailability, opening up the possibility of administering NPs via intradermal route as an alternative to the intravenous route. The co-administration of hyaluronidase may further promote the dissemination of locally infused NPs (226).

Lack of a reproducible, syngeneic, BRAF mutant melanoma model is a key issue. Availability of humanized mice could potentially address this issue. Severely immunodeficient mice with defects in the interleukin-2 receptor common γ-chain could be engrafted with human immune system (227). Humanized mice can be engrafted with human BRAF melanoma (more easily available) and can thus be used to test the combination of BRAF inhibition with ISNP mediated immunotherapy.

Reference:

1. Abdelwahed W, Degobert G, Stainmesse S, & Fessi H (2006) Freeze-drying of nanoparticles: Formulation, process and storage considerations. *Advanced Drug Delivery Reviews* 58(15):1688-1713.
2. Pegoraro C, MacNeil S, & Battaglia G (2012) Transdermal drug delivery: from micro to nano. *Nanoscale* 4(6):1881-1894.
3. Langer R (2004) Transdermal drug delivery: past progress, current status, and future prospects. *Advanced Drug Delivery Reviews* 56(5):557-558.
4. Chollet JL*, et al.* (1999) Development of a Topically Active Imiquimod Formulation. *Pharmaceutical Development and Technology* 4(1):35-43.
5. Prausnitz MR & Langer R (2008) Transdermal drug delivery. *Nat Biotech* 26(11):1261-1268.
6. Karande P, Jain A, Ergun K, Kispersky V, & Mitragotri S (2005) Design principles of chemical penetration enhancers for transdermal drug delivery. *Proceedings of the National Academy of Sciences of the United States of America* 102(13):4688-4693.
7. Zhang W*, et al.* Penetration and distribution of PLGA nanoparticles in the human skin treated with microneedles. *International Journal of Pharmaceutics* 402(1-2):205-212.
8. Kim Y-C, Park J-H, & Prausnitz MR. Microneedles for drug and vaccine delivery. *Advanced Drug Delivery Reviews* 64(14):1547-1568.
9. Zamarin D*, et al.* Localized Oncolytic Virotherapy Overcomes Systemic Tumor Resistance to Immune Checkpoint Blockade Immunotherapy. *Science Translational Medicine* 6(226):226ra232.
10. Sandby-Moller J, Poulsen T, & Wulf HC (2003) Epidermal thickness at different body sites: relationship to age, gender, pigmentation, blood content, skin type and smoking habits. (Translated from eng) *Acta Derm Venereol* 83(6):410-413 (in eng).
11. Linos E, Swetter SM, Cockburn MG, Colditz GA, & Clarke CA (2009) Increasing Burden of Melanoma in the United States. *J Invest Dermatol* 129(7):1666-1674.
12. Chapman PB*, et al.* Improved Survival with Vemurafenib in Melanoma with BRAF V600E Mutation. *New England Journal of Medicine* 364(26):2507-2516.
13. Sun W & Schuchter LM (2001) Metastatic melanoma. (Translated from eng) *Curr Treat Options Oncol* 2(3):193-202 (in eng).
14. Inamdar GS, Madhunapantula SV, & Robertson GP. Targeting the MAPK pathway in melanoma: Why some approaches succeed and other fail. *Biochemical Pharmacology* 80(5):624-637.

15. Davies H, *et al.* (2002) Mutations of the BRAF gene in human cancer. *Nature* 417(6892):949-954.
16. Bollag G, *et al.* Vemurafenib: the first drug approved for BRAF-mutant cancer. *Nat Rev Drug Discov* 11(11):873-886.
17. Beck D, *et al. Vemurafenib Potently Induces Endoplasmic Reticulum Stress-Mediated Apoptosis in BRAFV600E Melanoma Cells* pp ra7-ra7.
18. Sosman JA, *et al.* Survival in BRAF V600E-Mutant Advanced Melanoma Treated with Vemurafenib. *New England Journal of Medicine* 366(8):707-714.
19. Jang S & Atkins MB. Which drug, and when, for patients with BRAF-mutant melanoma? *The Lancet Oncology* 14(2):e60-e69.
20. Su F, *et al.* Resistance to Selective BRAF Inhibition Can Be Mediated by Modest Upstream Pathway Activation. *Cancer Research* 72(4):969-978.
21. Su F, *et al.* (RAS Mutations in Cutaneous Squamous-Cell Carcinomas in Patients Treated with BRAF Inhibitors. *New England Journal of Medicine* 366(3):207-215.
22. Das Thakur M, *et al.* Modelling vemurafenib resistance in melanoma reveals a strategy to forestall drug resistance. *Nature* 494(7436):251-255.
23. Prahallad A, *et al.* Unresponsiveness of colon cancer to BRAF (V600E) inhibition through feedback activation of EGFR. *Nature* 483(7388):100-103.
24. Sun C, *et al.* Reversible and adaptive resistance to BRAF (V600E) inhibition in melanoma. *Nature* 508(7494):118-122.
25. Finn L, Markovic S, & Joseph R. Therapy for metastatic melanoma: the past, present, and future. *BMC Medicine* 10(1):23.
26. Nazarian R, *et al.* Melanomas acquire resistance to B-RAF(V600E) inhibition by RTK or N-RAS upregulation. *Nature* 468(7326):973-977.
27. Johannessen CM, *et al.* COT drives resistance to RAF inhibition through MAP kinase pathway reactivation. *Nature* 468(7326):968-972.
28. Flaherty KT, *et al.* Combined BRAF and MEK Inhibition in Melanoma with BRAF V600 Mutations. *New England Journal of Medicine* 367(18):1694-1703.
29. Gowrishankar K, *et al.* Acquired Resistance to BRAF Inhibition Can Confer Cross-Resistance to Combined BRAF/MEK Inhibition. *J Invest Dermatol* 132(7):1850-1859.
30. Atefi M, *et al.* Reversing Melanoma Cross-Resistance to BRAF and MEK Inhibitors by Co-Targeting the AKT/mTOR Pathway. *PLoS ONE* 6(12):e28973.
31. Brady DC, *et al.* Copper is required for oncogenic BRAF signalling and tumorigenesis. *Nature* 509(7501):492-496.
32. Ceol CJ, *et al.* The histone methyltransferase SETDB1 is recurrently amplified in melanoma and accelerates its onset. *Nature* 471(7339):513-517.

33. Kaplon J, *et al.* A key role for mitochondrial gatekeeper pyruvate dehydrogenase in oncogene-induced senescence. *Nature* 498(7452):109-112.
34. Ma X-H, *et al.* Targeting ER stress-induced autophagy overcomes BRAF inhibitor resistance in melanoma. *The Journal of Clinical Investigation* 124(3):1406-1417.
35. Straussman R, *et al.* Tumour micro-environment elicits innate resistance to RAF inhibitors through HGF secretion. *Nature* 487(7408):500-504.
36. Viros A, *et al.* Ultraviolet radiation accelerates BRAF-driven melanomagenesis by targeting TP53. *Nature* 511(7510):478-482.
37. Dankort D, *et al.* (2009) BrafV600E cooperates with Pten loss to induce metastatic melanoma. *Nat Genet* 41(5):544-552.
38. Smyth MJ, Dunn GP, Schreiber RD, James P. Allison GD, & Frederick WA (2006) Cancer Immunosurveillance and Immunoediting: The Roles of Immunity in Suppressing Tumor Development and Shaping Tumor Immunogenicity. *Advances in Immunology*, (Academic Press), Vol Volume 90, pp 1-50.
39. Dunn GP, Old LJ, & Schreiber RD (2004) The Three Es of Cancer Immunoediting. *Annual Review of Immunology* 22(1):329-360.
40. Lizee G, *et al.* Harnessing the Power of the Immune System to Target Cancer. *Annual Review of Medicine* 64(1):71-90.
41. Sang M, *et al.* Melanoma-associated antigen genes - An update. *Cancer Letters* 302(2):85-90.
42. Leach DR, Krummel MF, & Allison JP (1996) Enhancement of Antitumor Immunity by CTLA-4 Blockade. *Science* 271(5256):1734-1736.
43. Hodi FS, *et al.* Improved Survival with Ipilimumab in Patients with Metastatic Melanoma. *New England Journal of Medicine* 363(8):711-723.
44. Robert C, *et al.* Ipilimumab plus Dacarbazine for Previously Untreated Metastatic Melanoma. *New England Journal of Medicine* 364(26):2517-2526.
45. Keir ME, Butte MJ, Freeman GJ, & Sharpe AH (2008) PD-1 and Its Ligands in Tolerance and Immunity. *Annual Review of Immunology* 26(1):677-704.
46. Spranger S, *et al.* Up-Regulation of PD-L1, IDO, and Tregs in the Melanoma Tumor Microenvironment Is Driven by CD8+ T Cells. *Science Translational Medicine* 5(200):200ra116.
47. Baitsch L, *et al.* Exhaustion of tumor-specific CD8+ T cells in metastases from melanoma patients. *The Journal of Clinical Investigation* 121(6):2350-2360.
48. Topalian SL, *et al.* Safety, Activity, and Immune Correlates of Anti-PD-1 Antibody in Cancer. *New England Journal of Medicine* 366(26):2443-2454.
49. Wolchok JD, *et al.* Nivolumab plus Ipilimumab in Advanced Melanoma. *New England Journal of Medicine* 369(2):122-133.

50. Rosenberg SA*, et al.* Durable Complete Responses in Heavily Pretreated Patients with Metastatic Melanoma Using T-Cell Transfer Immunotherapy. *Clinical Cancer Research* 17(13):4550-4557.
51. Lu Y-C*, et al.* Efficient Identification of Mutated Cancer Antigens Recognized by T Cells Associated with Durable Tumor Regressions. *Clinical Cancer Research* 20(13):3401-3410.
52. Hacohen N, Fritsch EF, Carter TA, Lander ES, & Wu CJ. Getting Personal with Neoantigen-Based Therapeutic Cancer Vaccines. *Cancer Immunology Research*.
53. Tsuji T, Altorki NK, Ritter G, Old LJ, & Gnjatic S (2009) Characterization of Preexisting MAGE-A3-Specific CD4+ T Cells in Cancer Patients and Healthy Individuals and Their Activation by Protein Vaccination. *The Journal of Immunology* 183(7):4800-4808.
54. Boon T, Coulie PG, Eynde BtJVd, & Bruggen Pvd (2006) HUMAN T CELL RESPONSES AGAINST MELANOMA. *Annual Review of Immunology* 24(1):175-208.
55. Chiang CL-L, Benencia F, & Coukos G. Whole tumor antigen vaccines. *Seminars in Immunology* 22(3):132-143.
56. Parmiani G*, et al.* (2002) Cancer Immunotherapy With Peptide-Based Vaccines: What Have We Achieved? Where Are We Going? *Journal of the National Cancer Institute* 94(11):805-818.
57. Walter S*, et al.* Multipeptide immune response to cancer vaccine IMA901 after single-dose cyclophosphamide associates with longer patient survival. *Nat Med* 18(8):1254-1261.
58. Comin-Anduix Ba*, et al.* The Oncogenic BRAF Kinase Inhibitor PLX4032/RG7204 Does Not Affect the Viability or Function of Human Lymphocytes across a Wide Range of Concentrations. *Clinical Cancer Research* 16(24):6040-6048.
59. Sapkota B, Hill CE, & Pollack BP. Vemurafenib enhances MHC induction in BRAF homozygous melanoma cells. (Translated from Eng) *Oncoimmunology* 2(1):e22890 (in Eng).
60. Koya RC*, et al.* BRAF Inhibitor Vemurafenib Improves the Antitumor Activity of Adoptive Cell Immunotherapy. *Cancer Research* 72(16):3928-3937.
61. Knight DA*, et al.* Host immunity contributes to the anti-melanoma activity of BRAF inhibitors. *The Journal of Clinical Investigation* 123(3):1371-1381.
62. Paulos CM*, et al.* (2007) Toll-like Receptors in Tumor Immunotherapy. *Clinical Cancer Research* 13(18):5280-5289.
63. Colandene JD*, et al.* (2007) Lyophilization cycle development for a high-concentration monoclonal antibody formulation lacking a crystalline bulking agent. *Journal of Pharmaceutical Sciences* 96(6):1598-1608.

64. Nail S*, et al.* (2002) Fundamentals of Freeze-Drying. *Development and Manufacture of Protein Pharmaceuticals,* Pharmaceutical Biotechnology, (Springer US), Vol 14, pp 281-360.
65. Adams GDJ & Ramsay JR (1996) Optimizing the lyophilization cycle and the consequences of collapse on the pharmaceutical acceptability of erwiniaL-Asparaginase. *Journal of Pharmaceutical Sciences* 85(12):1301-1305.
66. Parker A*, et al.* (2010) Determination of the influence of primary drying rates on the microscale structural attributes and physicochemical properties of protein containing lyophilized products. *Journal of Pharmaceutical Sciences* 99(11):4616-4629.
67. Lam P & Patapoff TW (2011) An Improved Method for Visualizing the Morphology of Lyophilized Product Cakes. *PDA Journal of Pharmaceutical Science and Technology* 65(4):425-430.
68. Chang L, Shepherd D, Sun J, Tang X, & Pikal MJ (2005) Effect of sorbitol and residual moisture on the stability of lyophilized antibodies: Implications for the mechanism of protein stabilization in the solid state. *Journal of Pharmaceutical Sciences* 94(7):1445-1455.
69. Hudson M, Cranage M, & Adams GJ (2003) Lyophilization of Vaccines. *Vaccine Protocols,* Methods in Molecular Medicine A2 - Robinson, Andrew, (Humana Press), Vol 87, pp 223-243.
70. Mockus LN*, et al.* Quality by design in formulation and process development for a freeze-dried, small molecule parenteral product: a case study. (Translated from eng) *Pharm Dev Technol* 16(6):549-576 (in eng).
71. Jiang Q & Lu HM (2008) Size dependent interface energy and its applications. *Surface Science Reports* 63(10):427-464.
72. Behrens SH, Christl DI, Emmerzael R, Schurtenberger P, & Borkovec M (2000) Charging and Aggregation Properties of Carboxyl Latex Particles: Experiments versus DLVO Theory. *Langmuir* 16(6):2566-2575.
73. Lee MK, Kim MY, Kim S, & Lee J (2009) Cryoprotectants for freeze drying of drug nano-suspensions: Effect of freezing rate. *Journal of Pharmaceutical Sciences* 98(12):4808-4817.
74. Pisano R*, et al.* Quality by design: optimization of a freeze-drying cycle via design space in case of heterogeneous drying behavior and influence of the freezing protocol. *Pharmaceutical Development and Technology* 18(1):280-295.
75. Conrad PB & de Pablo JJ (1999) Computer Simulation of the Cryoprotectant Disaccharide Trehalose in Aqueous Solution. *The Journal of Physical Chemistry A* 103(20):4049-4055.
76. Carpenter J, Chang B, Garzon-Rodriguez W, & Randolph T (2002) Rational Design of Stable Lyophilized Protein Formulations: Theory and Practice. *Rational*

Design of Stable Protein Formulations, Pharmaceutical Biotechnology, eds Carpenter J & Manning M (Springer US), Vol 13, pp 109-133.
77. Kaushik JK & Bhat R (2003) Why Is Trehalose an Exceptional Protein Stabilizer?: AN ANALYSIS OF THE THERMAL STABILITY OF PROTEINS IN THE PRESENCE OF THE COMPATIBLE OSMOLYTE TREHALOSE. *Journal of Biological Chemistry* 278(29):26458-26465.
78. Allison SD, Molina MdC, & Anchordoquy TJ (2000) Stabilization of lipid/DNA complexes during the freezing step of the lyophilization process: the particle isolation hypothesis. *Biochimica et Biophysica Acta (BBA) - Biomembranes* 1468(1–2):127-138.
79. Rossmann MG*, et al.* Reconstructing Virus Structures from Nanometer to Near-Atomic Resolutions with Cryo-Electron Microscopy and Tomography. *Viral Molecular Machines,* Advances in Experimental Medicine and Biology, (Springer US), Vol 726, pp 49-90.
80. Lengyel JS, Milne JL, & Subramaniam S (2008) Electron tomography in nanoparticle imaging and analysis. (Translated from eng) *Nanomedicine (Lond)* 3(1):125-131 (in eng).
81. Lee J & Cheng Y (2006) Critical freezing rate in freeze drying nanocrystal dispersions. *Journal of Controlled Release* 111(1–2):185-192.
82. Holzer M*, et al.* (2009) Physico-chemical characterisation of PLGA nanoparticles after freeze-drying and storage. *European Journal of Pharmaceutics and Biopharmaceutics* 72(2):428-437.
83. Zou L-N, Cheng X, Rivers ML, Jaeger HM, & Nagel SR (2009) The Packing of Granular Polymer Chains. *Science* 326(5951):408-410.
84. Anikeenko AV, Medvedev NN, & Aste T (2008) Structural and entropic insights into the nature of the random-close-packing limit. *Physical Review E* 77(3):031101.
85. Baranau V & Tallarek U. Random-close packing limits for monodisperse and polydisperse hard spheres. *Soft Matter* 10(21):3826-3841.
86. Grasmeijer N, Stankovic M, de Waard H, Frijlink HW, & Hinrichs WLJ. Unraveling protein stabilization mechanisms: Vitrification and water replacement in a glass transition temperature controlled system.), pp 763-769.
87. Binks BP & Lumsdon SO (2001) Pickering Emulsions Stabilized by Monodisperse Latex Particles: Effects of Particle Size. *Langmuir* 17(15):4540-4547.
88. Binks BP & Clint JH (2002) Solid Wettability from Surface Energy Components: Relevance to Pickering Emulsions. *Langmuir* 18(4):1270-1273.
89. Williams DF & Berg JC (1992) The aggregation of colloidal particles at the air-water interface. *Journal of Colloid and Interface Science* 152(1):218-229.

90. Shi L*, et al.* (2005) Stabilization of human papillomavirus virus-like particles by non-ionic surfactants. *Journal of Pharmaceutical Sciences* 94(7):1538-1551.
91. Lang R*, et al.* (2009) Rational Design of a Stable, Freeze-Dried Virus-Like Particle-Based Vaccine Formulation. *Drug Development and Industrial Pharmacy* 35(1):83-97.
92. Jodrey WS & Tory EM (1985) Computer simulation of close random packing of equal spheres. *Physical Review A* 32(4):2347-2351.
93. Siegwart DJ*, et al.* Combinatorial synthesis of chemically diverse core-shell nanoparticles for intracellular delivery. *Proceedings of the National Academy of Sciences*.
94. Gref R*, et al.* (2000) 'Stealth' corona-core nanoparticles surface modified by polyethylene glycol (PEG): influences of the corona (PEG chain length and surface density) and of the core composition on phagocytic uptake and plasma protein adsorption. *Colloids and Surfaces B: Biointerfaces* 18(3-4):301-313.
95. De Jaeghere F*, et al.* (2000) Freeze-drying and lyopreservation of diblock and triblock poly(lactic acid)-poly(ethylene oxide) (PLA-PEO) copolymer nanoparticles. (Translated from eng) *Pharm Dev Technol* 5(4):473-483 (in eng).
96. Minteer SD, Johnson P, Park H, & Driscoll A. Enzyme Nanoparticle Fabrication: Magnetic Nanoparticle Synthesis and Enzyme Immobilization. *Enzyme Stabilization and Immobilization,* Methods in Molecular Biology, (Humana Press), Vol 679, pp 183-191.
97. Swaminathan SK*, et al.* CD133-targeted paclitaxel delivery inhibits local tumor recurrence in a mouse model of breast cancer. (Translated from eng) *J Control Release* 171(3):280-287 (in eng).
98. Cao E, Chen Y, Cui Z, & Foster PR (2003) Effect of freezing and thawing rates on denaturation of proteins in aqueous solutions. (Translated from eng) *Biotechnol Bioeng* 82(6):684-690 (in eng).
99. Carpenter JF, Prestrelski SJ, & Arakawa T (1993) Separation of Freezing- and Drying-Induced Denaturation of Lyophilized Proteins Using Stress-Specific Stabilization: I. Enzyme Activity and Calorimetric Studies. *Archives of Biochemistry and Biophysics* 303(2):456-464.
100. Pikal-Cleland KA & Carpenter JF (2001) Lyophilization-induced protein denaturation in phosphate buffer systems: Monomeric and tetrameric β-galactosidase. *Journal of Pharmaceutical Sciences* 90(9):1255-1268.
101. Schwegman JJ, Carpenter JF, & Nail SL (2009) Evidence of partial unfolding of proteins at the ice/freeze-concentrate interface by infrared microscopy. *Journal of Pharmaceutical Sciences* 98(9):3239-3246.

102. Johnson RE, Kirchhoff CF, & Gaud HT (2002) Mannitol–sucrose mixtures—versatile formulations for protein lyophilization. *Journal of Pharmaceutical Sciences* 91(4):914-922.
103. Liao X, Krishnamurthy R, & Suryanarayanan R (2007) Influence of Processing Conditions on the Physical State of Mannitol--implications in Freeze-Drying. *Pharmaceutical Research* 24(2):370-376.
104. Al-Thabaiti SA, Al-Nowaiser FM, Obaid AY, Al-Youbi AO, & Khan Z (2008) Formation and characterization of surfactant stabilized silver nanoparticles: A kinetic study. *Colloids and Surfaces B: Biointerfaces* 67(2):230-237.
105. Kolhe P, Amend E, & K. Singh S. Impact of freezing on pH of buffered solutions and consequences for monoclonal antibody aggregation. *Biotechnology Progress* 26(3):727-733.
106. Gomez G, Pikal MJ, & Rodriguez-Hornedo N (2001) Effect of initial buffer composition on pH changes during far-from-equilibrium freezing of sodium phosphate buffer solutions. (Translated from eng) *Pharm Res* 18(1):90-97 (in eng).
107. Izutsu K-i, C. Heller M, W. Randolph T, & F. Carpenter J (1998) Effect of salts and sugars on phase separation of polyvinylpyrrolidone dextran solutions induced by freeze-concentration. *Journal of the Chemical Society, Faraday Transactions* 94(3):411-417.
108. Kim Y-C, Park J-H, & Prausnitz MR (2012) Microneedles for drug and vaccine delivery. *Advanced Drug Delivery Reviews* 64(14):1547-1568.
109. Gill HS, Denson DD, Burris BA, & Prausnitz MR (2008) Effect of microneedle design on pain in human volunteers. *Clin J Pain* 24(7):585-594.
110. Prausnitz MR (2004) Microneedles for transdermal drug delivery. *Advanced Drug Delivery Reviews* 56(5):581-587.
111. Van Damme P*, et al.* (2009) Safety and efficacy of a novel microneedle device for dose sparing intradermal influenza vaccination in healthy adults. *Vaccine* 27(3):454-459.
112. Weldon WC*, et al.* Microneedle Vaccination with Stabilized Recombinant Influenza Virus Hemagglutinin Induces Improved Protective Immunity. *Clinical and Vaccine Immunology* 18(4):647-654.
113. Phanse Y*, et al.* A systems approach to designing next generation vaccines: combining alpha-galactose modified antigens with nanoparticle platforms. *Sci. Rep.* 4.
114. Parveen S, Misra R, & Sahoo SK. Nanoparticles: a boon to drug delivery, therapeutics, diagnostics and imaging. *Nanomedicine : nanotechnology, biology, and medicine* 8(2):147-166.

115. Xie J, Lee S, & Chen X. Nanoparticle-based theranostic agents. *Advanced Drug Delivery Reviews* 62(11):1064-1079.
116. Barry BW (2001) Novel mechanisms and devices to enable successful transdermal drug delivery. *European Journal of Pharmaceutical Sciences* 14(2):101-114.
117. Kumar A*, et al.* (2012) Microneedle-mediated transcutaneous immunization with plasmid DNA coated on cationic PLGA nanoparticles. *Journal of Controlled Release* 163(2):230-239.
118. DeMuth PC, Su X, Samuel RE, Hammond PT, & Irvine DJ. Nano-Layered Microneedles for Transcutaneous Delivery of Polymer Nanoparticles and Plasmid DNA. *Advanced Materials* 22(43):4851-4856.
119. Zaric M*, et al.* Skin dendritic cell targeting via microneedle arrays laden with antigen-encapsulated poly-D,L-lactide-co-glycolide nanoparticles induces efficient antitumor and antiviral immune responses. (Translated from eng) *ACS Nano* 7(3):2042-2055 (in eng).
120. Burton S*, et al.* Rapid Intradermal Delivery of Liquid Formulations Using a Hollow Microstructured Array. *Pharmaceutical Research* 28(1):31-40.
121. PANYAM J, ZHOU W-Z, PRABHA S, SAHOO SK, & LABHASETWAR V (2002) Rapid endo-lysosomal escape of poly(dl-lactide-co-glycolide) nanoparticles: implications for drug and gene delivery. *The FASEB Journal* 16(10):1217-1226.
122. Dacso CC ed *Skin Testing for Tuberculosis. Clinical Methods: The History, Physical, and Laboratory Examinations.*), 3 Ed.
123. Ngawhirunpat T*, et al.* (2002) Changes in Electrophysiological Properties of Rat Skin with Age. *Biological and Pharmaceutical Bulletin* 25(9):1192-1196.
124. Tilney NL (1971) Patterns of lymphatic drainage in the adult laboratory rat. (Translated from eng) *J Anat* 109(Pt 3):369-383 (in eng).
125. Anselmo AC*, et al.* Delivering Nanoparticles to Lungs while Avoiding Liver and Spleen through Adsorption on Red Blood Cells. *ACS Nano* 7(12):11129-11137.
126. Kasturi SP*, et al.* Programming the magnitude and persistence of antibody responses with innate immunity. *Nature* 470(7335):543-547.
127. French MA & Harrison G (1984) Serum IgG subclass concentrations in healthy adults: a study using monoclonal antisera. (Translated from eng) *Clin Exp Immunol* 56(2):473-475 (in eng).
128. Joynson DH, Payne RA, & Rawal BK (1990) Potential role of IgG avidity for diagnosing toxoplasmosis. *Journal of Clinical Pathology* 43(12):1032-1033.
129. Mukherjee P*, et al.* (2003) TNF receptor gene therapy results in suppression of IgG2a anticollagen antibody in collagen induced arthritis. *Annals of the Rheumatic Diseases* 62(8):707-714.

130. Mountford AP, Fisher A, & Wilson RA (1994) The profile of IgG1 and IgG2a antibody responses in mice exposed to Schistosoma mansoni. (Translated from eng) *Parasite Immunol* 16(10):521-527 (in eng).
131. Qi J, Lu Y, & Wu W. Absorption, disposition and pharmacokinetics of solid lipid nanoparticles. (Translated from eng) *Curr Drug Metab* 13(4):418-428 (in eng).
132. Uner M & Yener G (2007) Importance of solid lipid nanoparticles (SLN) in various administration routes and future perspectives. (Translated from eng) *Int J Nanomedicine* 2(3):289-300 (in eng).
133. Jewell CM, Bustamante Lopez SC, & Irvine DJ. In situ engineering of the lymph node microenvironment via intranodal injection of adjuvant-releasing polymer particles. *Proceedings of the National Academy of Sciences*.
134. Pridgen EM*, et al.* Transepithelial Transport of Fc-Targeted Nanoparticles by the Neonatal Fc Receptor for Oral Delivery. *Science Translational Medicine* 5(213):213ra167.
135. Uren RF, Howman-Giles R, & Thompson JF (2003) Patterns of Lymphatic Drainage from the Skin in Patients with Melanoma. *Journal of Nuclear Medicine* 44(4):570-582.
136. Reddy ST*, et al.* (2007) Exploiting lymphatic transport and complement activation in nanoparticle vaccines. (Translated from eng) *Nat Biotechnol* 25(10):1159-1164 (in eng).
137. Li S-D & Huang L (2009) Nanoparticles evading the reticuloendothelial system: Role of the supported bilayer. *Biochimica et Biophysica Acta (BBA) - Biomembranes* 1788(10):2259-2266.
138. Weninger W, Biro M, & Jain R. Leukocyte migration in the interstitial space of non-lymphoid organs. *Nat Rev Immunol* 14(4):232-246.
139. Skobe M & Detmar M (2000) Structure, function, and molecular control of the skin lymphatic system. (Translated from eng) *J Investig Dermatol Symp Proc* 5(1):14-19 (in eng).
140. Anonymous (1993) *Interstitial-lymphatic mechanisms in the control of extracellular fluid volume* pp 1-78.
141. Negrini D & Moriondo A. Lymphatic anatomy and biomechanics. *The Journal of Physiology* 589(12):2927-2934.
142. Zheng Y*, et al.* Minipig as a potential translatable model for monoclonal antibody pharmacokinetics after intravenous and subcutaneous administration. *mAbs* 4(2):243-255.
143. Frost GI (2007) Recombinant human hyaluronidase (rHuPH20): an enabling platform for subcutaneous drug and fluid administration. (Translated from eng) *Expert Opin Drug Deliv* 4(4):427-440 (in eng).

144. Shpilberg O & Jackisch C. Subcutaneous administration of rituximab (MabThera) and trastuzumab (Herceptin) using hyaluronidase. *Br J Cancer* 109(6):1556-1561.
145. Mariani G*, et al.* (2002) Radioguided Sentinel Lymph Node Biopsy in Malignant Cutaneous Melanoma*. *Journal of Nuclear Medicine* 43(6):811-827.
146. Liu H*, et al.* Structure-based programming of lymph-node targeting in molecular vaccines. (Translated from eng) *Nature* 507(7493):519-522 (in eng).
147. Mukherjee S*, et al. Monovalent and Multivalent Ligation of the B Cell Receptor Exhibit Differential Dependence upon Syk and Src Family Kinases* pp ra1-ra1.
148. Ketchum C, Miller H, Song W, & Upadhyaya A. Ligand Mobility Regulates B Cell Receptor Clustering and Signaling Activation., pp 26-36.
149. Batra PP, Roebuck MA, & Uetrecht D (1990) Effect of lysine modification on the secondary structure of ovalbumin. (Translated from eng) *J Protein Chem* 9(1):37-44 (in eng).
150. Kwong PD, Mascola JR, & Nabel GJ. Rational Design of Vaccines to Elicit Broadly Neutralizing Antibodies to HIV-1. *Cold Spring Harbor Perspectives in Medicine* 1(1).
151. Kanekiyo M*, et al.* Self-assembling influenza nanoparticle vaccines elicit broadly neutralizing H1N1 antibodies. *Nature* 499(7456):102-106.
152. Igyarto B*, et al.* Skin-Resident Murine Dendritic Cell Subsets Promote Distinct and Opposing Antigen-Specific T Helper Cell Responses. *Immunity* 35(2):260-272.
153. Klechevsky E*, et al.* Functional Specializations of Human Epidermal Langerhans Cells and CD14+ Dermal Dendritic Cells. *Immunity* 29(3):497-510.
154. Alexandrov LB*, et al.* Signatures of mutational processes in human cancer. *Nature* 500(7463):415-421.
155. Russell SJ, Peng K-W, & Bell JC (Oncolytic virotherapy. *Nat Biotech* 30(7):658-670.
156. Ali OA, Emerich D, Dranoff G, & Mooney DJ (2009) In Situ Regulation of DC Subsets and T Cells Mediates Tumor Regression in Mice. *Science Translational Medicine* 1(8):8ra19.
157. Dolgin E. Cancer vaccines: Material breach. *Nature* 504(7480):S16-S17.
158. Nazarian R*, et al.* (2010) Melanomas acquire resistance to B-RAF(V600E) inhibition by RTK or N-RAS upregulation. *Nature* 468(7326):973-977.
159. Bollag G*, et al.* (2012) Vemurafenib: the first drug approved for BRAF-mutant cancer. *Nat Rev Drug Discov* 11(11):873-886.
160. Chapman PB*, et al.* (2011) Improved Survival with Vemurafenib in Melanoma with BRAF V600E Mutation. *New England Journal of Medicine* 364(26):2507-2516.

161. Lito P, Rosen N, & Solit DB (2013) Tumor adaptation and resistance to RAF inhibitors. *Nat Med* 19(11):1401-1409.
162. Fedorenko IV, Paraiso KHT, & Smalley KSM (2011) Acquired and intrinsic BRAF inhibitor resistance in BRAF V600E mutant melanoma. *Biochemical Pharmacology* 82(3):201-209.
163. Sun C*, et al.* (2014) Reversible and adaptive resistance to BRAF(V600E) inhibition in melanoma. *Nature* 508(7494):118-122.
164. Poulikakos PI*, et al.* (2011) RAF inhibitor resistance is mediated by dimerization of aberrantly spliced BRAF(V600E). *Nature* 480(7377):387-390.
165. Flaherty KT*, et al.* (2012) Combined BRAF and MEK Inhibition in Melanoma with BRAF V600 Mutations. *New England Journal of Medicine* 367(18):1694-1703.
166. Boni A*, et al.* (2010) Selective BRAFV600E Inhibition Enhances T-Cell Recognition of Melanoma without Affecting Lymphocyte Function. *Cancer Research* 70(13):5213-5219.
167. Wolf D, Heine A, & Brossart P (2014) Implementing combinatorial immunotherapeutic regimens against cancer: The concept of immunological conditioning. (Translated from Eng) *Oncoimmunology* 3(1):e27588 (in Eng).
168. Beck D*, et al.* (2013) *Vemurafenib Potently Induces Endoplasmic Reticulum Stress–Mediated Apoptosis in BRAFV600E Melanoma Cells* pp ra7-ra7.
169. Knight DA*, et al.* (2013) Host immunity contributes to the anti-melanoma activity of BRAF inhibitors. *The Journal of Clinical Investigation* 123(3):1371-1381.
170. Merad M, Sathe P, Helft J, Miller J, & Mortha A (2013) The Dendritic Cell Lineage: Ontogeny and Function of Dendritic Cells and Their Subsets in the Steady State and the Inflamed Setting. *Annual Review of Immunology* 31(1):563-604.
171. Ilarregui JM*, et al.* (2009) Tolerogenic signals delivered by dendritic cells to T cells through a galectin-1-driven immunoregulatory circuit involving interleukin 27 and interleukin 10. *Nat Immunol* 10(9):981-991.
172. Palucka K & Banchereau J (2012) Cancer immunotherapy via dendritic cells. *Nat Rev Cancer* 12(4):265-277.
173. Kantoff PW*, et al.* (2010) Sipuleucel-T Immunotherapy for Castration-Resistant Prostate Cancer. *New England Journal of Medicine* 363(5):411-422.
174. Blachère NE, Darnell RB, & Albert ML (2005) Apoptotic Cells Deliver Processed Antigen to Dendritic Cells for Cross-Presentation. *PLoS Biol* 3(6):e185.
175. Rovere P*, et al.* (1999) Dendritic cell presentation of antigens from apoptotic cells in a proinflammatory context: role of opsonizing anti-beta2-glycoprotein I antibodies. (Translated from eng) *Arthritis Rheum* 42(7):1412-1420 (in eng).

176. Albert ML, Sauter B, & Bhardwaj N (1998) Dendritic cells acquire antigen from apoptotic cells and induce class I-restricted CTLs. *Nature* 392(6671):86-89.
177. Joseph EW*, et al.* (2010) The RAF inhibitor PLX4032 inhibits ERK signaling and tumor cell proliferation in a V600E BRAF-selective manner. *Proceedings of the National Academy of Sciences* 107(33):14903-14908.
178. Green DR, Ferguson T, Zitvogel L, & Kroemer G (2009) Immunogenic and tolerogenic cell death. *Nat Rev Immunol* 9(5):353-363.
179. Mao Y*, et al.* (2013) Melanoma-educated CD14+ cells acquire a myeloid-derived suppressor cell phenotype through COX-2-dependent mechanisms. *Cancer Research*.
180. Weide B*, et al.* (2014) Myeloid-Derived Suppressor Cells Predict Survival of Patients with Advanced Melanoma: Comparison with Regulatory T Cells and NY-ESO-1- or Melan-A–Specific T Cells. *Clinical Cancer Research* 20(6):1601-1609.
181. Jacobs JFM, Nierkens S, Figdor CG, de Vries IJM, & Adema GJ (2012) Regulatory T cells in melanoma: the final hurdle towards effective immunotherapy? *The Lancet Oncology* 13(1):e32-e42.
182. Diebold S (2009) Activation of Dendritic Cells by Toll-Like Receptors and C-Type Lectins. *Dendritic Cells,* Handbook of Experimental Pharmacology, eds Lombardi G & Riffo-Vasquez Y (Springer Berlin Heidelberg), Vol 188, pp 3-30.
183. Blander JM & Medzhitov R (2006) Toll-dependent selection of microbial antigens for presentation by dendritic cells. *Nature* 440(7085):808-812.
184. Nierkens S*, et al.* (2008) *In vivo* Colocalization of Antigen and CpG within Dendritic Cells Is Associated with the Efficacy of Cancer Immunotherapy. *Cancer Research* 68(13):5390-5396.
185. Goldstein MJ*, et al.* (2011) *A CpG-loaded tumor cell vaccine induces antitumor CD4+ T cells that are effective in adoptive therapy for large and established tumors.* pp 118-127.
186. Cui Z, Le U, Qiu F, & Shaker D (2007) Learning from Viruses: The Necrotic Bodies of Tumor Cells with Intracellular Synthetic dsRNA Induced Strong Anti-tumor Immune Responses. (Translated from English) *Pharmaceutical Research* 24(9):1645-1652 (in English).
187. Testerman TL*, et al.* (1995) Cytokine induction by the immunomodulators imiquimod and S-27609. *Journal of Leukocyte Biology* 58(3):365-372.
188. Gilliet M, Cao W, & Liu Y-J (2008) Plasmacytoid dendritic cells: sensing nucleic acids in viral infection and autoimmune diseases. *Nat Rev Immunol* 8(8):594-606.
189. Dockrell DH & Kinghorn GR (2001) Imiquimod and resiquimod as novel immunomodulators. *Journal of Antimicrobial Chemotherapy* 48(6):751-755.

190. Russo C*, et al.* (2011) *Small molecule Toll-like receptor 7 agonists localize to the MHC class II loading compartment of human plasmacytoid dendritic cells*. pp 5683-5691.
191. Danhier F*, et al.* (2012) PLGA-based nanoparticles: An overview of biomedical applications. *Journal of Controlled Release* 161(2):505-522.
192. Körber M (2010) PLGA Erosion: Solubility- or Diffusion-Controlled? (Translated from English) *Pharmaceutical Research* 27(11):2414-2420 (in English).
193. Bertrand N, Wu J, Xu X, Kamaly N, & Farokhzad OC (2014) Cancer nanotechnology: The impact of passive and active targeting in the era of modern cancer biology. *Advanced Drug Delivery Reviews* 66(0):2-25.
194. Chou LYT, Ming K, & Chan WCW (2011) Strategies for the intracellular delivery of nanoparticles. *Chemical Society Reviews* 40(1):233-245.
195. Sparidans RW, Durmus S, Schinkel AH, Schellens JHM, & Beijnen JH (2012) Liquid chromatography–tandem mass spectrometric assay for the mutated BRAF inhibitor vemurafenib in human and mouse plasma. *Journal of Chromatography B* 889–890(0):144-147.
196. Toti US, Guru BR, Grill AE, & Panyam J (2010) Interfacial Activity Assisted Surface Functionalization: A Novel Approach To Incorporate Maleimide Functional Groups and cRGD Peptide on Polymeric Nanoparticles for Targeted Drug Delivery. *Molecular Pharmaceutics* 7(4):1108-1117.
197. Koya RC*, et al.* (2012) BRAF Inhibitor Vemurafenib Improves the Antitumor Activity of Adoptive Cell Immunotherapy. *Cancer Research* 72(16):3928-3937.
198. Woods D*, et al.* (2001) Induction of β3-Integrin Gene Expression by Sustained Activation of the Ras-Regulated Raf–MEK–Extracellular Signal-Regulated Kinase Signaling Pathway. *Molecular and Cellular Biology* 21(9):3192-3205.
199. Li X*, et al.* (2001) Integrin αvβ3 mediates K1735 murine melanoma cell motility in vivo and in vitro. *Journal of Cell Science* 114(14):2665-2672.
200. Thiele L, Diederichs JE, Reszka R, Merkle HP, & Walter E (2003) Competitive adsorption of serum proteins at microparticles affects phagocytosis by dendritic cells. *Biomaterials* 24(8):1409-1418.
201. Sobota A*, et al.* (2005) Binding of IgG-Opsonized Particles to FcγR Is an Active Stage of Phagocytosis That Involves Receptor Clustering and Phosphorylation. *The Journal of Immunology* 175(7):4450-4457.
202. Canton J, Neculai D, & Grinstein S (2013) Scavenger receptors in homeostasis and immunity. *Nat Rev Immunol* 13(9):621-634.
203. Getts DR*, et al.* (2014) Therapeutic Inflammatory Monocyte Modulation Using Immune-Modifying Microparticles. *Science Translational Medicine* 6(219):219ra217.

204. Arredouani MS*, et al.* (2005) MARCO Is the Major Binding Receptor for Unopsonized Particles and Bacteria on Human Alveolar Macrophages. *The Journal of Immunology* 175(9):6058-6064.
205. Matsushita N, Komine H, Grolleau-Julius A, Pilon-Thomas S, & Mulé J (2010) Targeting MARCO can lead to enhanced dendritic cell motility and anti-melanoma activity. (Translated from English) *Cancer Immunol Immunother* 59(6):875-884 (in English).
206. Grolleau A, Misek DE, Kuick R, Hanash S, & Mule JJ (2003) Inducible Expression of Macrophage Receptor Marco by Dendritic Cells Following Phagocytic Uptake of Dead Cells Uncovered by Oligonucleotide Arrays. *The Journal of Immunology* 171(6):2879-2888.
207. Cho N-H*, et al.* (2011) A multifunctional core-shell nanoparticle for dendritic cell-based cancer immunotherapy. *Nat Nano* 6(10):675-682.
208. West MA, Prescott AR, Eskelinen E-L, Ridley AJ, & Watts C (Rac is required for constitutive macropinocytosis by dendritic cells but does not control its downregulation. *Current Biology* 10(14):839-848.
209. Weissleder R, Nahrendorf M, & Pittet MJ (2014) Imaging macrophages with nanoparticles. *Nat Mater* 13(2):125-138.
210. Treuel L, Jiang X, & Nienhaus GU (2013) New views on cellular uptake and trafficking of manufactured nanoparticles. *Journal of The Royal Society Interface* 10(82).
211. Madani F*, et al.* (2011) Mechanisms of Cellular Uptake of Cell-Penetrating Peptides. *Journal of Biophysics* 2011.
212. Goodridge HS*, et al.* Activation of the innate immune receptor Dectin-1 upon formation of a /`phagocytic synapse/'. *Nature* 472(7344):471-475.
213. Shukla NM, Malladi SS, Mutz CA, Balakrishna R, & David SA (2010) Structure−Activity Relationships in Human Toll-Like Receptor 7-Active Imidazoquinoline Analogues. *Journal of Medicinal Chemistry* 53(11):4450-4465.
214. Joffre OP, Segura E, Savina A, & Amigorena S (Cross-presentation by dendritic cells. *Nat Rev Immunol* 12(8):557-569.
215. Oh JZ, Kurche JS, Burchill MA, & Kedl RM (*TLR7 enables cross-presentation by multiple dendritic cell subsets through a type I IFN-dependent pathway* pp 3028-3038.
216. Oh JZ & Kedl RM. The Capacity To Induce Cross-Presentation Dictates the Success of a TLR7 Agonist-Conjugate Vaccine for Eliciting Cellular Immunity. *The Journal of Immunology* 185(8):4602-4608.
217. Harshyne LA, Zimmer MI, Watkins SC, & Barratt-Boyes SM (2003) A Role for Class A Scavenger Receptor in Dendritic Cell Nibbling from Live Cells. *The Journal of Immunology* 170(5):2302-2309.

218. Kortylewski M*, et al.* (2004) Interferon-[gamma]-Mediated Growth Regulation of Melanoma Cells: Involvement of STAT1-Dependent and STAT1-Independent Signals. *J Investig Dermatol* 122(2):414-422.
219. Dobrzanski MJ, Reome JB, & Dutton RW (2001) Immunopotentiating Role of IFN-γ in Early and Late Stages of Type 1 CD8 Effector Cell-Mediated Tumor Rejection. *Clinical Immunology* 98(1):70-84.
220. García-Hernández ML, Hernández-Pando R, Gariglio P, & Berumen J (2002) Interleukin-10 promotes B16-melanoma growth by inhibition of macrophage functions and induction of tumour and vascular cell proliferation. *Immunology* 105(2):231-243.
221. Sharp FA*, et al.* (2009) Uptake of particulate vaccine adjuvants by dendritic cells activates the NALP3 inflammasome. *Proceedings of the National Academy of Sciences* 106(3):870-875.
222. Zamarin D*, et al.* (2014) Localized Oncolytic Virotherapy Overcomes Systemic Tumor Resistance to Immune Checkpoint Blockade Immunotherapy. *Science Translational Medicine* 6(226):226ra232.
223. Russell SJ, Peng K-W, & Bell JC (2012) Oncolytic virotherapy. *Nat Biotech* 30(7):658-670.
224. Izutsu K-i, C. Heller M, W. Randolph T, & F. Carpenter J (1998) Effect of salts and sugars on phase separation of polyvinylpyrrolidone-dextran solutions induced by freeze-concentration. *Journal of the Chemical Society, Faraday Transactions* 94(3):411-417.
225. Reddy ST*, et al.* (2007) Exploiting lymphatic transport and complement activation in nanoparticle vaccines. *Nat Biotech* 25(10):1159-1164.
226. Shpilberg O & Jackisch C. Subcutaneous administration of rituximab (MabThera) and trastuzumab (Herceptin) using hyaluronidase. (Translated from eng) *Br J Cancer* 109(6):1556-1561 (in eng).
227. Shultz LD, Brehm MA, Garcia-Martinez JV, & Greiner DL. Humanized mice for immune system investigation: progress, promise and challenges. *Nat Rev Immunol* 12(11):786-798.